
Astrophysical Applications of Scattering in Interstellar and Intracluster Gases

Conrad K. Cramphorn



München 2004

Astrophysical Applications of Scattering in Interstellar and Intracluster Gases

Conrad K. Cramphorn

Dissertation
an der Fakultät für Physik
der Ludwig-Maximilians-Universität
München

vorgelegt von
Conrad K. Cramphorn
aus Dundee in Schottland

München, den 12. Mai 2004

Erstgutachter: Prof. Dr. Rashid A. Sunyaev

Zweitgutachter: Prof. Dr. Ralf Bender

Tag der mündlichen Prüfung: 24. November 2004

Für meine Eltern

Inhaltsverzeichnis

Zusammenfassung (Summary in German)	3
Summary	5
1 Introduction	9
1.1 Diffuse Gas in the Universe	9
1.2 Supermassive Black Holes in the Centres of Galaxies	11
1.2.1 Sgr A*	13
1.2.2 M31	14
1.2.3 M87	15
1.3 Relativistic Jets	16
1.4 Clusters of Galaxies	17
1.5 The Sunyaev-Zel'dovich Effect	18
2 The X-ray luminosity of the Galactic centre in the recent past	21
2.1 Introduction	22
2.2 Method	25
2.2.1 X-ray Archaeology	25
2.2.2 GMCs in the Galactic disk	28
2.2.3 Scattered flux	31
2.3 Limits on the X-ray luminosity of Sgr A* from Giant Molecular Clouds	35
2.3.1 Response of a single cloud	36
2.3.2 Response of one field of view	40
2.3.3 Response of all fields of view containing at least one GMC .	43
2.4 Limits on the X-ray luminosity of Sgr A* from the interstellar HI distribution	47
2.5 The Milky Way at extragalactic distances	52
2.5.1 Scattered X-ray surface brightness	53
2.5.2 Scattered X-ray luminosity	58
2.5.3 Fluorescent iron K_{α} -line luminosity	62
2.6 Discussion	62

3	Constraining the past X-ray luminosity of AGN in clusters of galaxies	65
3.1	Introduction	66
3.2	Advantage of scattered X-ray lines over the scattered continuum . .	69
3.3	AGN in the centre of a beta-cluster	74
3.3.1	Approximation of isotropic scattering	74
3.3.2	Continuum radiation	74
3.3.3	Resonance lines	82
3.4	Numerical simulations	85
3.4.1	M87	85
3.4.2	Cygnus A	96
3.5	Discussion	99
4	Scattering in the vicinity of relativistic jets	103
4.1	Introduction	103
4.2	The model	106
4.3	Results	112
4.3.1	Single ejection	112
4.3.2	Multiple ejections	121
4.4	Application to M87	130
4.4.1	Observations	130
4.4.2	Constraints on the jet parameters	131
4.5	Discussion	137
5	A correlation between the SZ decrement and the Thomson depth	139
5.1	Scaling relations for clusters of galaxies	140
5.2	The SZ decrement	140
5.3	Scaling relation for gas distributed similarly to dark matter	141
5.4	Isothermal gas in a NFW dark matter potential	144
5.5	Clusters with observed SZ decrements	145
5.6	SZ decrement and Thomson depth for simulated clusters	145
5.7	Results	146
5.8	Discussion	148
6	Concluding remarks	151
	References	156

Zusammenfassung

Diese Arbeit befaßt sich mit astrophysikalischen Anwendungen von Streuprozessen in diffusen Gasen innerhalb von Galaxien bzw. Galaxienhaufen. Anhand von aktuellen Beobachtungsdaten wird versucht, Aussagen über die zurückliegende Entwicklung der Leuchtkraft von astrophysikalischen Objekten, wie supermassiven schwarzen Löchern und relativistischen Jets, zu gewinnen, die innerhalb dieser diffusen Gase Strahlung erzeugen. Die im Rahmen dieser Arbeit relevanten physikalischen Eigenschaften dieser Objekte sind in Kapitel 1 zusammengestellt.

In Kapitel 2 werden Aussagen über die Röntgenleuchtkraft des supermassiven schwarzen Lochs im Zentrum der Milchstraße, Sgr A*, während ungefähr der letzten einhunderttausend Jahre hergeleitet. Hierzu werden die Ergebnisse großflächiger Röntgenbeobachtungen entlang der galaktischen Ebene mit den mittels Radio-beobachtungen von Molekülwolken innerhalb der galaktischen Scheibe gewonnenen Ergebnissen kombiniert.

In Kapitel 3 wird der Frage nachgegangen, inwieweit sich ähnliche Aussagen über die in der Vergangenheit liegende Röntgenleuchtkraft eines supermassiven schwarzen Lochs gewinnen lassen, das im Zentrum einer elliptischen Galaxie oder eines Galaxienhaufens vorhanden ist. Hierbei wird insbesondere die kontinuierliche Streuung an freien Elektronen sowie die Streuung in Resonanzlinien analytisch als auch numerisch unter Verwendung von Monte-Carlo Methoden untersucht.

In Kapitel 4 wird eine anisotrop abstrahlende Strahlungsquelle angenommen, mittels der das von relativistischen Jets erzeugte Strahlungsfeld simuliert wird. Dieses Modell wird auf den relativistischen Jet der aktiven Galaxie M87 angewandt, um Aussagen über den Neigungswinkel dieses Jets relativ zu der Sichtlinie und über den Lorentzfaktor der in diesem Jet strömenden Materie zu gewinnen.

In Kapitel 5 wird eine Korrelation zwischen dem durch den Sunyaev-Zel'dovich Effekt hervorgerufenen Intensitätsdekrement der kosmischen Hintergrundstrahlung in Richtung eines Galaxienhaufens und der Thomsondicke des diffusen Gases innerhalb dieses Galaxienhaufens hergeleitet, die im Rahmen von numerischen Simulationen der Strukturbildung dunkler Materie aufgefunden worden ist.

Kapitel 6 schließt die Arbeit mit einer zusammenfassenden Würdigung der Ergebnisse der vorhergehenden Kapitel.

Zusammenfassung

Summary

This thesis studies the question of how observational data can pose non-trivial constraints on the past activity of such diverse astrophysical objects as the centre of the Milky Way, supermassive black holes in the centres of massive elliptical galaxies and of clusters of galaxies and relativistic jets. In order to set the stage for this study, chapter 1 provides a brief summary of the relevant aspects of the different astrophysical objects in question.

In the first part of this work, i.e. in chapter 2, I focus on the putative supermassive black hole at the centre of the Milky Way. High resolution observations of the motions of stars in the vicinity of the dynamical centre of our Galaxy are most plausibly explained by the presence of such an object with a mass of about $2.6 \times 10^6 M_{\odot}$. Recent measurements with the *Chandra* X-ray satellite detect the associated X-ray source Sgr A* at a mere $2 \times 10^{33} \text{ erg s}^{-1}$, more than ten orders of magnitude below the Eddington luminosity of $3 \times 10^{44} \text{ erg s}^{-1}$ for a black hole of such a mass. This relative dimness being remarkable in itself, raises the question of whether Sgr A* was equally dim in the recent past. I will address this question by applying a method which has been successfully applied to giant molecular clouds (GMCs) in the “immediate” vicinity of the Galactic Centre (GC). It has been proposed, that diffuse, hard X-ray emission observed today in the direction of the giant molecular clouds in the central 100 pc of the Galaxy and especially in the direction of a cloud called Sgr B2 is radiation emitted by Sgr A* in the past, which has been scattered into our line of sight by the molecular gas present in these clouds. In order for the mass of molecular gas present in Sgr B2 ($\sim 6 \times 10^6 M_{\odot}$) to produce the presently observed flux, the X-ray luminosity of Sgr A* must have been of the order of $2 \times 10^{39} \text{ erg s}^{-1}$ about 400 years ago, i.e. six orders of magnitude more luminous than at present. The time delay of 400 years corresponds to the different path lengths for photons, received directly or taking the detour via Sgr B2, which lies at a projected distance of ~ 120 pc from the GC.

The application of the method successfully used in the above described case to constrain the luminosity of Sgr A* in the past is not restricted to GMCs close to the GC. In order to provide nontrivial constraints upon the strength of the activity of the GC in the past by means of this method, one requires a scattering material with

Summary

a sufficient optical depth and an estimate of the scattered flux produced by this material. In the case of our Galaxy two obvious choices which fulfill these criteria are interstellar molecular and atomic hydrogen. CO surveys covering the Galactic plane have shown that about $10^9 M_{\odot}$ of H_2 reside in GMCs on orbits between the GC and the sun, with a peak mass surface density around a galactocentric radius between 4 and 6 kpc, the so called molecular ring (e.g. Dame (1993)). The time delays, i.e. the difference of the arrival times between the primary and the scattered radiation, for clouds located in the molecular ring, range up to about 40.000 years. The HI phase of the interstellar medium (ISM) is more diffusely distributed than H_2 . It extends out to about 16 kpc with an approximately constant mass surface density of about $4 M_{\odot} \text{pc}^{-2}$, corresponding to a total mass of the order of $3 \times 10^9 M_{\odot}$ (e.g. Dame (1993)). The *ASCA* Galactic Plane Survey (Sugizaki et al. 2001), on the other hand, provides upper limits for the diffuse X-ray emission produced by any physical processes and in particular by scattering along lines of sight lying within an *ASCA* field of view. It is obvious that the ratio of the computed scattered flux to the upper limit for the scattered flux given by *ASCA* observations gives us an estimate of the average luminosity of the GC at a time which corresponds to the time delay of the observed GMC. In the second part of this chapter the same method is applied to the Andromeda Galaxy (M31) which exhibits a gas distribution similar to the one of our Galaxy.

Chapter 3 addresses the possibility of constraining the X-ray luminosity in the recent past (up to $\sim 10^6$ years ago) of the nucleus of a cluster dominant galaxy by measuring the contribution of scattered radiation from the central source to the surface brightness of the intracluster gas dominated by thermal emission. As it turns out, resonance X-ray lines present an advantage over the adjacent continuum, because the relative contribution of the scattered component is typically larger in the line case by a significant factor of 3–10. The same method can be applied to distant powerful quasars (at redshifts $z \gtrsim 1$) if they have cluster-like gaseous coronae, as suggested by *Rosat* and *Chandra* observations of active galaxies at $z \lesssim 1$. Their surface brightness profiles in the X-ray continuum above $\sim 10 \text{ keV} \gg kT/(1+z)$ (where T is the gas temperature) should be dominated by redshifted scattered radiation from the quasar. Therefore measurements with forthcoming mirror-optics hard X-ray telescopes could give information on the lifetime of quasars and parameters of the hot gas around them.

In chapter 4 of this work I study electron scattering in the vicinity of relativistic jets of radio loud active galactic nuclei (AGN). As these jets produce highly directed, intense beams of radiation, a fraction of this beamed radiation scatters on the thermal plasma generally surrounding an AGN. The morphology of the scattered emission can thus provide constraints on the physical properties of the jet. I present a model to study the feasibility of constraining the parameters of a

jet, especially its inclination angle and bulk Lorentz factor in this way. The model is applied to the well studied jet of M87 and the surrounding diffuse gas and it is found that the observational limits of the surface brightness measured in the region of the putative counterjet provide the tightest constraints on the jet parameters consistent with constraints derived by other methods. The applicability of the model to other sources exhibiting relativistic motions is discussed briefly.

In a final part of my work I derive a scaling relation between the Sunyaev-Zel'dovich (SZ) decrement and the Thomson depth of a cluster of galaxies of the form $\Delta T_r \propto \tau_T^2$, as has been found in numerical dark matter N-body simulations. The motivation for this study being that several of such scaling relations, which suggest the self-similarity of relaxed clusters of galaxies, have been discovered through an interplay of X-ray observations and theoretical modeling of these objects. Especially interesting, in this respect, is the tight relation between the virial mass of a cluster and the temperature of the intracluster medium (ICM), $M_{\text{vir}} \propto T_e^{3/2}$. With the recent progress in observing the SZ decrement in more than a dozen of clusters of galaxies one obtains another observable parameter to constrain the physics of these objects. The strength of the SZ effect is a measure for a different physical parameter than the X-ray surface brightness or the inferred X-ray luminosity. It primarily depends upon the Thomson depth and not on the virial mass, although they are certainly connected in some way. In analogy with well known scaling relations it is reasonable to expect a power law dependence between the SZ decrement and the Thomson depth of a cluster of the form $\Delta T_r \propto \tau_T^\alpha$. Combining this relation with temperature estimates of the ICM through X-ray observations provides direct information about the Thomson depth and about the dependence of T_e on τ_T . Therefore, the Thomson depth of a cluster might become an important scaling parameter for tests of the models of clusters of galaxies.

Chapters 2, 3, 4 and 5 have been or are in the process of being published in Cramphorn (2001), Cramphorn & Sunyaev (2002), Sazonov et al. (2002b) and Cramphorn et al. (2004).

Summary

Die Nachtstunde schlug; ich hüllte mich in meine abenteuerliche Vermummung, nahm die Pike und das Horn zur Hand, ging in die Finsternis hinaus und rief die Stunde ab, nachdem ich mich durch ein Kreuz gegen die bösen Geister geschützt hatte.

Bonaventura, "Nachtwachen"

1

Introduction

1.1 Diffuse Gas in the Universe

Although a nearly perfect vacuum by earthly standards, interstellar space is by no means empty. Large amounts of diffuse gas and dust span the vast distances between the stars of the Milky Way. This so-called interstellar medium probably accounts for a mass of several billion solar masses in our Galaxy. Thus, the mass of the material between the stars is a non-negligible fraction - a few percent - of the mass of all the visible stars in the Galaxy. Yet the presence of interstellar matter is much less obvious than the presence of stars, since the mass contained in ordinary stars has been compacted by self-gravity into a readily observable dense state. It, thus, seems little surprising that, although diffuse gas is found in many different forms throughout the universe and probably constitutes the dominant baryonic form of matter therein, it has eluded the attention of astronomy for a long time, as astronomers were slow to realize its importance for the life-cycles of stars and galaxies.

Historically, the conclusive evidence for the existence of interstellar gas was presented somewhat earlier than the evidence for interstellar dust. In 1904, Hartmann discovered that a set of absorption lines of once-ionised calcium did not undergo the periodic Doppler shifts of the absorption lines in the spectrum of a spectroscopic binary. In other words, whereas the wavelengths of the absorption lines from the photospheres of the stars in the binary system shifted back and forth as the stars revolved in their orbits, there were also absorption lines whose wavelengths

1 Introduction

remained stationary. Hartmann concluded that the “stationary lines” arose from absorption produced by a cold interstellar cloud of gas which lay between the binary system and Earth.

Hartmann’s hypothesis of an intervening gas cloud did not gain immediate acceptance, because the absorbing gas might have resided near the star in question rather than a long distance away. This issue of whether the absorbing gas is “circumstellar” or “interstellar” remains difficult to resolve in any case, even today. However, the “interstellar” interpretation was demonstrated by such people as Plaskett, Struve, Eddington, and Bok, who showed that the ionisation stages, the Galactic distribution, or the velocities of the “stationary lines” were often incompatible with a “circumstellar” interpretation.

Further insights into the interstellar gas originated from later observations that showed that many stars exhibit multiple interstellar absorption lines, i.e. the same lines of e.g. once-ionised calcium at several different Doppler velocities. Moreover, the interstellar lines were relatively narrow in comparison with the absorption lines produced in the photospheres of the stars in question. These facts indicated that the gas producing the interstellar absorption lines must be relatively cold and diffuse, and must come in discrete lumps (“clouds”), which move more or less coherently as a unit. This notion, that interstellar space is not empty but is filled with moving clouds of gas, remains the central concept underlying most studies of the medium between the stars.

It is now well known that the dust and the gas in interstellar space are intimately mixed, and that both generally reside in clouds or complexes of clouds. The ratio of dust mass to gas mass in the Galaxy is about 1 percent. Since the gas itself is only a few percent of the mass of the stars in the Galaxy, interstellar dust constitutes a very minor fraction of the total mass of our Galaxy. Nevertheless, this dust has a great influence on how the Galaxy is observed, because it obscures so much starlight in many directions.

Most of the gas in the Galaxy is confined to the Galactic plane and moves in circular orbits about the Galactic centre, the inward force of gravitational attraction being balanced by centrifugal forces. The gas moves in the gravitational potential defined by the mass distribution of the stars and the Galactic dark matter. The kinematics of the interstellar gas therefore acts as a probe of the gravitational potential of the Galaxy, and the velocities of interstellar neutral hydrogen and molecules provide among the best information about the distribution of mass in the Galaxy.

Unfortunately, the conditions in a spiral galaxy where centrifugal forces support a widespread distribution of gas do not represent well the conditions of gas in early-type, i.e. elliptical, galaxies or in clusters. In order that gas is widely distributed in those cases, its speed of sound must be comparable with the local velocity

1.2 Supermassive Black Holes in the Centres of Galaxies

dispersion, i.e. speeds of a few hundred km s^{-1} and temperatures of $10^6 - 10^7$ K in galaxies or $500 - 1.200 \text{ km s}^{-1}$ and $10^7 - 10^8$ K in clusters. Such gas mainly emits at X-ray wavelengths. Whereas the mass of gas in a normal spiral galaxy represents less than about ten percent of the mass in stars, the fraction becomes of the order of 1 to 10 for clusters of galaxies. The intracluster gas exerts a measurable influence on the galaxies and may prove to be the best probe of the underlying dark matter.

There are strong arguments for the existence of an intergalactic gas as well, since it would be surprising if galaxy formation was 100 per cent efficient. Indeed, most of the baryons in the Universe probably reside in intergalactic gas, where gas is most clearly observed in clouds, which absorb the light of distant quasars.

1.2 Supermassive Black Holes in the Centres of Galaxies

The most powerful energy sources we know of in the Universe are located in the centres of certain galaxies referred to collectively as Active Galactic Nuclei or AGN. They are among the most spectacular objects in the sky, because they produce prodigious luminosities (in some cases apparently as much as 10^4 times the luminosity of a typical galaxy) in tiny volumes (probably $\ll 1 \text{ pc}^3$). This radiation can emerge over an extraordinary broad range of frequencies. In some cases the luminosity per logarithmic frequency interval has been observed to be roughly constant across thirteen orders of magnitude in frequency. The salient observational signatures of AGN, which most often but not always are fulfilled in a given AGN are a very small angular size, Galactic or greater luminosity, a broad-band continuum, strong emission lines, variability and a weak polarisation.

There are many different types of AGN which, broadly speaking, can be divided into groups according to their radio power, their luminosity and their optical spectral lines. As the name implies, radio-loud AGN have very strong radio emission when compared to the optical, whereas radio-quiet objects have relatively little or no measurable radio flux. In low-luminosity objects, which include starburst galaxies and Seyferts, the host galaxy can be seen around the active nucleus. The more distant and energetic quasars lie so far away that generally the surrounding galaxy can no longer be seen, yet the nucleus is so powerful that it outshines the galaxy and appears star-like on the sky. However, the improved imaging capabilities of the *Hubble Space Telescope* have allowed to observe the host galaxies of quasars up to redshifts of the order of 1. If broad spectral lines are seen in the optical spectrum of an AGN, these indicate that one observes high-velocity gas moving at velocities between 1.000 and 10.000 km s^{-1} , presumably from the so-

1 Introduction

called broad line region. These objects are known as type 1 AGN, e.g. Seyfert 1s and type 1 quasars. However, if only narrow lines are observed, one is seeing low velocity gas from the narrow line region (between about 100 and 1.000 km s⁻¹), either because the high velocity gas is obscured perhaps by the molecular torus or because it is simply not there. These objects are called type 2 AGN.

Attempts have been made to unify the apparently disparate components of the world of active galaxies. The basic idea behind this so-called unified model of AGN is that all AGN essentially exhibit the same internal structure in their nucleus driving different observational phenomena. All the differences that we see are caused primarily by the angle of the system, i.e. the plane in which the accretion disc, the outer parts of the broad line region and the molecular torus lie, with respect to the distant observer. It has been proposed that there are basically two parallel sequences, one for radio-loud AGN where the radio jets are very strong and extend into the surrounding galaxy, and another for the radio-quiet AGN where the radio emission is relatively weak. However, there is a strong consensus that the prime mover behind all these objects and the observed phenomena is a supermassive black hole.

A characteristic length scale of a black hole of mass M_{BH} is the gravitational radius

$$R_g = \frac{GM_{\text{BH}}}{c^2} \approx 1.5 \text{ km} \left(\frac{M_{\text{BH}}}{M_\odot} \right). \quad (1.1)$$

For a non-rotating black hole the Schwarzschild radius is twice the gravitational radius, $R_s = 2R_g$. This length scale corresponds to a characteristic timescale of

$$t_s = \frac{R_s}{c} \approx 10^{-5} \text{ s} \left(\frac{M_{\text{BH}}}{M_\odot} \right). \quad (1.2)$$

For supermassive black holes with masses in the range from 10^6 to $10^9 M_\odot$ this corresponds to times from about 10 seconds to 3 hours. Since the radiative force as well as gravity depend on distance from a central source of radiation and gravitation in exactly the same way, there exists a limit for the steady state luminosity of such an object, i.e. the so-called Eddington limit:

$$L_{\text{Edd}} = \frac{4\pi c GM_{\text{BH}}}{\sigma_T} \approx 1.5 \times 10^{38} \text{ erg s}^{-1} \left(\frac{M_{\text{BH}}}{M_\odot} \right). \quad (1.3)$$

That is, for any given mass, there is a critical luminosity, the Eddington luminosity L_{Edd} , beyond which the radiation force must overpower gravity. It immediately follows that the large luminosities one observes from AGN, anywhere from $10^{43} - 10^{47} \text{ erg s}^{-1}$, demand minimum central masses in the range of $10^5 - 10^9 M_\odot$, providing an additional argument on behalf of AGN requiring masses in this range.

1.2 Supermassive Black Holes in the Centres of Galaxies

Several billion years after the Big Bang, the Universe went through a “quasar era” when high-energy AGN were more than ten thousand times as numerous as they are now. Quasars must then have been standard equipment in most large galaxies. Since that time, AGN have been dying out. Now quasars are exceedingly rare, and even medium-luminosity AGN such as Seyfert galaxies are rather uncommon. The only remaining nuclear activity that still occurs in many galaxies is weak. As outlined above, AGN engines are believed to be supermassive black holes that accrete gas and stars and so transform gravitational potential energy into radiation. Since most quasars have switched off, dim or dead “engines” - starving black holes - should be hiding in many nearby galaxies. A search for supermassive black holes, therefore, does not need to be confined to active galaxies that motivated it in the first place. In fact, definite conclusions are much more likely if objects can be observed in which one is not dazzled by a “a searchlight in ones eyes”. Also these searches had to start with the nearest galaxies, because only then one could see close enough to the centre, so that the dynamics of the stars are dominated by the central black hole. Since AGN are rare, nearby galaxies are not particularly active. For these reasons, it is no surprise that the search for supermassive black holes first succeeded in nearby, inactive galaxies including the centre of the Milky Way.

1.2.1 Sgr A*

Our Galaxy has long been known to contain the exceedingly compact radio source Sgr A*. Interferometric measurements give its diameter as $63 R_s$ by less than $17 R_s$, where $R_s = 0.06 \text{ AU} = 8.6 \times 10^{11} \text{ cm}$ is the Schwarzschild radius of a $2.6 \times 10^6 M_\odot$ black hole. As an AGN Sgr A* is feeble, shining with a radio luminosity of only $10^{34} \text{ erg s}^{-1}$. The infrared and high-energy luminosities are higher, but there is no compelling need for a supermassive black hole on energetic grounds.

Our Galactic disk, which we see in the sky as the Milky Way, contains enough dust to block all but about 10^{-14} of the optical light from the Galactic Centre. Measurements of the region around Sgr A* had to await the advent of suitable infrared detectors. Much of the infrared radiation in turn is absorbed by the Earth’s atmosphere, but there is a useful transmission window at a wavelength of 2.2 microns. At this wavelength the extinction towards the Galactic Centre turns out to be a factor of about 20, which is still large but manageable. Early infrared measurements showed a rotation velocity of 100 km s^{-1} and a small rise in velocity dispersion to $\leq 120 \text{ km s}^{-1}$ at the centre. These values were best fit with a black hole of 10^6 solar masses, but the evidence was not compelling. Since then, a series of spectacular technical advances have made it possible to probe closer to the centre. As a result, the strongest case for a black hole in any galaxy is now

1 Introduction

our own, i.e. the Milky Way.

Most remarkably, two independent groups, i.e. Genzel et al. (1997) and Ghez et al. (1998), have used speckle imaging to measure proper motions - the velocity components perpendicular to the line of sight - in a cluster of stars at radii $r = 0.02$ pc from Sgr A*. When combined with complementary measurements at larger radii, the result is that the one-dimensional velocity dispersion increases smoothly to 420 km s^{-1} at about 0.01 pc. Stars at this radius revolve around the Galactic Centre in a human lifetime. Inside of this radius the mass has to be $2.6 \times 10^6 M_{\odot}$.

1.2.2 M31

The Andromeda Galaxy (M31) is very similar to the Milky Way in most respects. At a distance of about 2 million light years, it is one of our “nearest” neighbours. The nucleus of M31 is also believed to harbour a supermassive black hole. However, at the present time the black hole in M31 appears to be in a quiescent phase, exhibiting none of the exotic phenomena seen near the nucleus of our own Galaxy. The existence of a supermassive black hole in M31 has been convincingly demonstrated through a long series of very precise spectroscopic measurements carried out mainly at the Canada-France-Hawaii telescope.

Spectroscopic measurements show that the velocity dispersion, i.e. random motions of the stars in the nucleus of M31, is very sharply peaked about the centre of M31. Similarly, the rotation curve is very narrowly confined to the nuclear region of Andromeda. The velocity dispersion is measured by looking at the width of individual spectral lines. The observed spectrum is a composite of the spectra of all the stars. The composite integrated spectrum is thus broadened because the random motions of individual stars cause slight shifts in the position of a given absorption line. On the other hand, the rotation of the stars about the axis of symmetry of the disk produces a systematic red shift on one side of the nucleus and a blue shift on the other side of the spectral lines.

These observations (Kormendy & Bender 1999) clearly show that there is a very large increase in the mass-to-light ratio towards the centre of M31. This implies that the mass must be quite “dark”. These data cannot prove unambiguously that a supermassive black hole is the cause for the motions of the stars in the nucleus of Andromeda, but after careful examination of all conceivable alternatives, there is general acknowledgement that a supermassive black hole is the simplest and most consistent explanation of the observed phenomena. The observations are well explained by a supermassive black hole having a mass of about $3 \times 10^7 M_{\odot}$.

1.2.3 M87

One of the major goals of the *Hubble Space Telescope* (HST) has been to establish or refute the existence of supermassive black holes in active galaxies by probing the dynamics of AGN at much smaller radii than can be achieved from the ground. Already persuasive evidence has been found that apparently quiescent nearby galaxies contain black holes, but locally there are few candidate galaxies which might harbour a supermassive black hole large enough to have sustained quasar type activity earlier in their evolution. M87 is the nearest and brightest elliptical believed to host such a supermassive black hole.

Since observations as early as 1917, astronomers have suspected that unusual activity was taking place in the centre of M87. They discovered a long “finger” of energy, later termed jet, emanating from the nucleus. Investigations using radio telescopes in the 1950s detected large emissions of energy from the galaxy. This made it clear that the bright optical jet and radio source were the result of energy released by something in the centre of the galaxy.

M87, the dominant giant elliptical galaxy at the centre of the Virgo cluster, was the first galaxy for which tenable stellar dynamical and photometric evidence was advanced for the presence of a supermassive black hole. Subsequent stellar dynamical models showed however that the projected stellar density and the observed rise in velocity dispersion did not necessarily imply the presence of a supermassive black hole, but could still be explained by the presence of a stellar core with an anisotropic velocity distribution.

An important step in the quest to verify the existence of a supermassive black hole in M87 have been the HST emission line and continuum images of a circumnuclear disk of ionised gas which is oriented approximately perpendicular to the synchrotron jet. This cloud of gas is composed mostly of hydrogen. The hydrogen atoms have been ionised, or stripped of their single electron, possibly by radiation originating near the black hole. Similar gaseous disks have also been found in the nuclei of a number of other massive galaxies. Because of surface brightness limitations on stellar dynamical studies at HST resolutions, the kinematics of such disks are in practice likely to be the only way to prove the existence of a central supermassive black hole in all but the very nearest galaxies.

HST spectroscopic observations of the gaseous disk at several discrete locations on opposite sides of the nucleus showed a velocity difference of $> 1.000 \text{ km s}^{-1}$. Under the assumption that these motions arise in a thin rotating Keplerian disk, this leads to central dark mass of M87 in the range of 1 to $3.5 \times 10^9 M_{\odot}$. An important shortcoming of this estimate is the assumption about the inclination of the disk with respect to the line of sight which cannot be properly determined neither by using the few velocities derived from the spectroscopic observations

1 Introduction

nor from the imaging data. Implicit in this measurement of the mass of the central object is also the assumption that the gas motions in the innermost regions reflect a Keplerian rotation and not the effects of non-gravitational forces such as interactions with the jet which are known to dominate the gas motions in the inner regions of many AGN. The current best estimate for the mass of the black hole in the nucleus of M87 taking these considerations into account is $3.2 \times 10^9 M_{\odot}$ (Macchetto et al. 1997).

1.3 Relativistic Jets

Almost one century ago H. D. Curtis noted a “curious straight ray” in M87 which was “apparently connected with the nucleus by a thin line of matter”. This observation marked the first discovery of an extragalactic jet, though its physical nature as well as that of its host nebula would remain obscure for several more decades. Later, Virgo A would be one of the first discrete sources discovered by the “new” radio astronomy, and its association with M87 and the “curious straight ray” observed by Baade and Minkowski, were quickly recognised. Eventually radio interferometer images revealed the bright radio lobes and the optical jet itself. Similarly, the jet would be detected at X-ray frequencies, once the resolution was adequate to separate it from the bright thermal emission. While several hundred jets have now been discovered, M87 remains one of the nearest examples, making it an ideal target for study of the extragalactic jet phenomenon. Only one other extragalactic jet is substantially closer, and that is Centaurus A which is at a very low declination and therefore is difficult to study with northern radio interferometers.

Although radio-loud AGN account for a small fraction of all AGN numerically, these objects present the greatest physical challenges. All the main features of radio-quiet AGN (nuclear continuum and emission lines) are present, but in addition there is the phenomenon of a transport of energy over colossal scales. These are perhaps the largest distinct entities found in nature, and certainly one of the most striking. The ability to obtain spatially resolved data has contributed immensely to their understanding although even now many questions remain open.

Powerful extended extragalactic radio sources pose two vexing astrophysical problems. First, from what energy reservoir do they draw their large radio luminosities (as much as 10^{45} erg s⁻¹ between 10 MHz and 100 GHz)? Second, how does the active centre in the parent galaxy or Quasar supply as much as 10^{61} erg in relativistic particles and fields to radio lobes up to several hundred kiloparsecs outside the optical object?

Double radio sources are known to be fueled by the associated active galactic

nuclei via narrow jets. A fluid model is generally adopted and radio emission is produced by synchrotron radiation from relativistic electrons accelerated in situ. Within the extended radio source, the lower power jets, classified as Fanaroff-Riley (FR) type I, are typically two-sided and thought to be sub- or transonic; the higher power one-sided jets, classified as Fanaroff-Riley type II, are believed to be supersonic and, at least mildly relativistic. VLBI observations of the compact radio source often reveal miniature jets within which features appear to be moving superluminally with speeds of five to ten times the speed of light. These are conventionally interpreted as relativistic jets directed towards us with Lorentz factors up to ten.

In FRI sources, the regions of highest surface brightness lie closest to the nucleus, whereas in FR II sources the hotspots lie at the outer edges. The FR morphological division is also a division in radio power: FR II sources have $P \gtrsim 10^{24}$. This suggests that jets come with a variety of outputs, and that some are too puny to penetrate the intergalactic medium (IGM) in their vicinity. The jets in FRI sources resemble a turbulent plume, whereas the jets in FR II sources are very narrow, with opening angles of only a few degrees. It is plausible that FRI jets dissipate their kinetic energy by entraining IGM material, whereas FR II jets maintain their integrity until they impact on the IGM in a shock. The hotspots are therefore to be interpreted as a rather complex working surface.

1.4 Clusters of Galaxies

Most galaxies in the Universe do not exist in isolation, but are gravitationally bound with other galaxies. Small associations, called groups, may exhibit a few dozen galaxies which extend over a million of light years, the Local Group being an example of such an association. Larger and more rare associations may have thousands of galaxies which cover a spatial extension of millions of light years. The nearest cluster to our own is the Virgo Cluster hosting the giant elliptical galaxy M87. However, even richer in galaxies is the Coma cluster of galaxies several 100 million light years away. Such clusters of galaxies are great astrophysical laboratories in particular because of the following reasons:

- Clusters change very slowly (it takes almost as long as the age of the Universe, i.e. the Hubble time, for significant changes to occur in clusters), thus clusters retain an imprint of how they were formed which makes them a good probe of the history of structure and galaxy formation.
- Through their gravitational influence clusters tend to hold onto the gas in their systems, unlike galaxies, where the gas is forced out through galactic

1 Introduction

winds or supernova explosions. In other words, clusters are closed systems. By studying the chemical composition of clusters, it is possible to study the history of nucleosynthesis in the Universe.

In the 1960s galaxy clusters were first detected as X-ray sources. The detection of emission lines in the X-ray spectra of clusters in the 1970s confirmed that the observed X-ray emission arises from hot (10 to 100 million degrees) intracluster gas trapped within the gravitational potential well of the cluster. The mass of this intracluster medium (ICM) is usually 2 to 10 times that of the galaxies. Most of the ICM is believed to be primordial, either part of the cluster when it first formed or accreted afterwards. However, the metal abundance of the gas in clusters, as measured by X-ray spectra, is usually around 30% that of the Sun. Since the only known way to produce elements besides hydrogen and helium is in stars, it is thought that the metals were formed by the stars within the galaxies of the cluster and were driven out into the ICM by galactic winds produced by supernovae within the galaxies.

Estimates of the total mass of clusters based on the velocity distribution of the galaxies, the X-ray temperature and density profile give values by factors between 10 to 30 larger than can be accounted for by the visible matter in the galaxies and gas. These values are confirmed by the results derived from the analysis of gravitational lensing effects produced by a cluster. Hence, clusters are believed to contain another component, dark matter, in addition to the baryonic component, i.e. the ordinary matter the stars and the ICM are made up of. Up to the present day the properties of dark matter are not well understood and its presence can only be detected through its gravitational influence.

1.5 The Sunyaev-Zel'dovich Effect

As clusters of galaxies are filled by a hot thermal plasma, these objects represent giant reservoirs of free electrons. These hot electrons that initially had been revealed by X-ray observations may be detected in ways other than their thermal bremsstrahlung emission. Photons passing through the cluster will undergo Compton scattering by collisions with the electrons in the ionised ICM, causing distortions in the spectrum of the emergent radiation. The place where one can hope to detect these distortions most readily is in the cosmic microwave background (CMB). The effect of Compton scattering on the photon energy distribution is governed by the so-called Kompaneets equation.

For X-ray gas in clusters the optical depth is low enough that each photon can be considered to scatter only once. In this case one can integrate the Kompaneets

1.5 The Sunyaev-Zel'dovich Effect

equation to obtain a solution for the differential change of the intensity

$$\frac{\Delta I_\nu}{I_\nu} = -y \frac{x e^x}{e^x - 1} \left[4 - x \coth \left(\frac{x}{2} \right) \right], \quad (1.4)$$

with $x = h\nu/(kT_{\text{rad}})$ and the dimensionless Compton y -parameter

$$y = \int \sigma_{\text{T}} n_e \frac{kT_{\text{gas}}}{m_e c^2} dl. \quad (1.5)$$

The above solution has made use of the fact that in this case the gas temperature is much larger than the radiation temperature, i.e. $T_{\text{gas}} \gg T_{\text{rad}}$. Eq. 1.4 describes the frequency dependent Sunyaev-Zel'dovich (SZ) effect, which can be expressed also in terms of the brightness temperature:

$$I_\nu = \frac{2k\nu^2}{c^2} T_{\text{b}} \quad (1.6)$$

At low frequencies, in the Rayleigh-Jeans tail, the effect is a fractional cooling of the background by

$$\frac{\Delta I_\nu}{I_\nu} = \frac{\Delta T_{\text{b}}}{T_{\text{b}}} = -2y \quad (1.7)$$

This effect is not due to the mean shift in photon energy alone, but to a combination of the shift and the convolving effect of the scattering. At high frequencies, beyond the peak of the CMB spectrum, the SZ effect changes sign, offering a clear observational signature. The low frequency effect has been detected in a number of clusters (e.g. Carlstrom et al. (1999)), and is a valuable diagnostic for two reasons. First, being proportional to n_e , it constrains the possible effect of clumping on X-ray emission, which scales as n_e^2 . Second, the method has a different dependence on h than results from X-ray observations, thereby offering a method to determine the Hubble constant.

1 Introduction

*J'aime les nuages ... les nuages qui passent ...
là-bas ... là-bas ... les merveilleux nuages!*

Charles Baudelaire, "Paris Spleen"

2

The X-ray luminosity of the Galactic centre in the recent past

Abstract

Information about the X-ray luminosity of the supermassive black hole located at the Galactic centre (GC), Sgr A*, and its temporal variations in the past is imprinted in the scattered emission observed today in the direction towards giant molecular clouds (GMCs) located in our Galaxy. Due to light travel time effects these clouds probe the activity of Sgr A* at different times in the past depending on their position relative to the GC and the observer. In this chapter we combine results of recent *ASCA* observations along the Galactic plane, providing upper limits for the scattered flux in the 4-10 keV range produced in a given direction, with data from CO surveys of the same regions. These CO surveys map the position and mass of the molecular gas which the GMCs are made up of. Demanding the scattered flux to be not larger than the observed one, this data enables us to derive upper limits for the 4-10 keV luminosity of Sgr A* at certain times during the last 40.000 years down to about $8 \times 10^{40} \text{ erg s}^{-1}$. At other times the limits are less tight, of the order of $10^{41} - 10^{42} \text{ erg s}^{-1}$. For two periods of time of about 2.000 and 4.000 years duration 8.000 and 14.000 years ago the currently available CO data is insensitive to any enhanced activity of the GC. Flares lasting longer than 3.000 years fill these time gaps and therefore can be excluded to have occurred during the last 40.000 years with a luminosity larger than a few $10^{42} \text{ erg s}^{-1}$. The more extended and continuous HI distribution in the

2 The X-ray luminosity of the Galactic centre in the recent past

Galactic disk, which also scatters the radiation emitted by Sgr A*, allows us to extend the time coverage further into the past, back to about 110,000 years, albeit the limits are becoming less tight. We thereby can rule out a long term X-ray activity phase of Sgr A* at one per cent of its Eddington level ending less than about 80,000 years ago. The limits presented in this chapter can be improved by observations of emission in the fluorescent iron K_α -line. We study the feasibility of these methods to investigate past nuclear activity in other spiral galaxies observed with the angular resolution of X-ray telescopes like *Chandra* and *XMM-Newton*.

2.1 Introduction

High spatial resolution observations of the stars in the vicinity of the Galactic centre (GC) strongly suggest the presence of a supermassive black hole having a mass of $2.6 \times 10^6 M_\odot$ (Genzel et al. (1997); Ghez et al. (1998)). Recent *Chandra* measurements (Baganoff et al. 2003) detect the associated X-ray source Sgr A* at a mere $2 \times 10^{33} \text{ erg s}^{-1}$, more than ten orders of magnitude below the Eddington luminosity of $3 \times 10^{44} \text{ erg s}^{-1}$ for a black hole of such a mass. This relative dimness being remarkable in itself raises the question whether Sgr A* was equally dim in the past.

Granat spacecraft observations of the region surrounding the GC have revealed a close resemblance between the morphology of the diffuse X-ray emission above 10 keV and the spatial distribution of molecular gas as inferred from CO observations. Sunyaev et al. (1993) proposed that the diffuse, hard X-ray emission observed today in the direction of giant molecular clouds (GMCs) in the central 100 pc of the Galaxy and especially in the direction of Sgr B2 is radiation emitted by Sgr A* in the past scattered into our line of sight by the molecular gas. They predicted the presence of a strong iron fluorescent K_α -line at 6.4 keV with an equivalent width of the order of 1 keV. This line is a signature of scattering of hard X-ray photons on neutral matter when the primary photon source does not contribute to the observed emission, by either falling outside of the observing beam or being currently not active (Vainshtein & Sunyaev 1980).

In order for the mass of molecular gas ($\sim 6 \times 10^6 M_\odot$) present in Sgr B2 to produce the observed flux, the X-ray luminosity of Sgr A* must have been of the order of $2 \times 10^{39} \text{ erg s}^{-1}$ about 400 years ago. This time delay corresponds to the different path lengths for photons received directly or taking the detour via Sgr B2, which lies at a projected distance of ~ 120 pc from the GC.

Evidence for the scattering scenario has been discovered with the spectroscopic imaging capabilities of the *ASCA* satellite (Koyama et al. (1996); Sunyaev et al.

(1998); Murakami et al. (2000)). The X-ray spectrum of Sgr B2 exhibits strong emission in the iron K_α -line at 6.4 keV confirming the prediction of Sunyaev et al. (1993). Murakami et al. (2001b) have recently observed another GMC close to the GC, Sgr C, to be bright in the K_α -line, strengthening the case for the scattering scenario. These authors call Sgr B2 and Sgr C “X-ray reflection nebulae”. Recent *Chandra* observations (Murakami et al. 2001a) confirm the *ASCA* results about Sgr B2 and the nature of the 6.4 keV K_α -line emission.

The application of the method successfully used in the above described cases to constrain the luminosity of Sgr A* in the past is not restricted to GMCs close to the GC. For it to provide nontrivial constraints upon the strength of the activity of the GC one needs a scattering material with a sufficient optical depth and an estimate of the scattered flux produced by this material. In the case of our Galaxy two obvious choices which fulfil these criteria are interstellar molecular and atomic hydrogen:

- a) CO surveys covering the Galactic plane have shown that about $10^9 M_\odot$ of H_2 reside in GMCs on orbits between the GC and the sun with a peak mass surface density around a galactocentric radius between 4 and 6 kpc, the so called molecular ring (e.g. Dame (1993)). The time delays, i.e. the difference of the arrival times between the primary and the scattered radiation, for clouds located in the molecular ring range up to about 40.000 years.

In this chapter we will compute the scattered flux produced by a GMC in response to a strong flare of Sgr A*. This flux is detectable by current X-ray telescopes even if it was relatively short, with a duration of the order of years. Turning this argument around one infers from the observed relative dimness of GMCs today that there could not have been a strong flare of Sgr A* at those times in the past, which correspond to the time delays of massive GMCs in our Galaxy.

The good temporal “resolution” with an uncertainty of the occurrence of a flare of the order of years comes about because the mass of a GMC is rather concentrated with a very dense core. We are therefore in principle able to pinpoint past flares of Sgr A* during the last 40.000 years very well, if there exists a GMC with a corresponding time delay.

The drawback of this “accurate” timing is that because there only exist a finite number of GMCs in our Galaxy it is not possible to cover the whole time interval from 40.000 years ago corresponding the time delay of the most distant clouds up to “today”. For the analysis presented in this chapter it was only possible to use the CO data from the first Galactic quadrant. This means that we are missing all the GMCs, which are located in the fourth

2 The X-ray luminosity of the Galactic centre in the recent past

Galactic quadrant and which should be equally numerous. This additional data would probably improve the “filling factor” of our sample but still leave several time gaps and not extend the time coverage beyond 40.000 years. The possibility thus always exists that a short flare of Sgr A* occurred during the last 40.000 years unnoticed by us, because there is no GMC which could respond to this flare right now. If we take only the available CO data into account, the coverage becomes complete for flares longer than about 3.000 years and we can thereby rule out any flare brighter than a few 10^{42} erg s⁻¹ during the last 40.000 years of such a or a longer duration.

- b) The HI phase of the interstellar medium (ISM) is more diffusely distributed than H₂. It extends out to about 16 kpc with an approximately constant mass surface density of about $4 M_{\odot} \text{pc}^{-2}$, corresponding to a total mass of the order of $3 \times 10^9 M_{\odot}$ (e.g. Dame (1993)). This implies that the total mass of neutral hydrogen in a field of view of the *ASCA* instrument is larger than the mass of any GMC even those near the GC. For a Galactic longitude of 10° it is about $2 \times 10^7 M_{\odot}$.

Due to its more continuous distribution the response of the HI distribution to flares of Sgr A* will be spread out over a longer time interval. Therefore we are unable to locate the time, when a flare happened. A strong flare longer ago can produce the same response as a weak flare not so long ago. Nevertheless, due to the larger extent of HI in the Galactic disk we can extend the time coverage to about 110.000 years back into the past. We will show that for example the switch off case from 1% of the Eddington luminosity of Sgr A* (the whole Galactic disk is illuminated by Sgr A*, which suddenly “switches off” at a time t_o) can be ruled out to have ended less than about 80 000 years ago.

The *ASCA* Galactic Plane Survey (Sugizaki et al. 2001) provides upper limits for the diffuse X-ray emission produced by scattering along certain directions. In this chapter we compute the expected scattered flux for an assumed Eddington luminosity of 3×10^{44} erg s⁻¹ in the 4-10 keV range. Although this value is rather large, the results can be rescaled to any input luminosity because the scattered flux just scales linearly with the assumed luminosity of the radiation source. It is obvious that the ratio of the computed scattered flux to the upper limit for the scattered flux as given by *ASCA* observations, $f = F_{\text{sc}}/F_{\text{obs}}$, yields an estimate of the average luminosity of the GC, $L_{\text{GC}} \lesssim f^{-1} L_{\text{Edd}}$, at a time in the past corresponding to the time delay of the observed GMC.

This chapter is structured as follows. In the following section we recall the basic ideas and relations of X-ray archaeology. We describe how we extracted the CO

and X-ray data necessary for our purposes from the literature. In section 2.3 we will derive constraints for the past X-ray luminosity of Sgr A* using a specific sample of GMCs in the Galaxy. In section 2.4 we will describe the corresponding limits the Galactic HI distribution can provide. The possibility to use the same methods to study past nuclear activity in other spiral galaxies is studied in section 2.5. In section 2.6 we close with a discussion of our results.

2.2 Method

2.2.1 X-ray Archaeology

The scenario we have in mind is sketched in Figure 2.1. An outburst of duration Δ has occurred at the GC a time t_o ago, as measured by the earth bound observer. As time evolves this signal moves radially outwards from the GC and starts illuminating GMCs at larger and larger galactocentric distances. These clouds scatter a fraction of the incident radiation into the direction of the observer.

The loci of scattering sites giving a fixed time delay form an ellipsoid with foci at the source and the observer. Since the system is symmetric around the line connecting the GC and the observer this ellipsoid is fully described by two parameters which depend upon the time that has passed since the detection of the burst $t - t_o$, where t is the time of observation. In this section we will assume from now on $t_o = 0$ to simplify the following formulae.

Choosing a cartesian coordinate system (see Figure 2.1) with the GC and the Sun at $z = R_o/2$ and $z = -R_o/2$ respectively, the ellipsoid can be expressed as

$$\frac{z^2}{a^2} + \frac{x^2 + y^2}{b^2} = 1, \quad (2.1)$$

where the lengths of the major and minor axis are $a = (ct + R_o)/2$ and $b = \sqrt{(ct)^2 + 2ctR_o}/2$, with c the speed of light and R_o the distance to the GC.

An alternative description of the ellipsoid can be given in polar coordinates R, ϕ (defined in Figure 2.1):

$$R(\phi) = \frac{p}{1 + e \cos \phi}, \quad (2.2)$$

with $p = b^2/a$ and $e = R_o/(2a)$. Note that in the limit of the observer at infinity ($R_o \rightarrow \infty, p \rightarrow ct, e \rightarrow 1$) this ellipsoid becomes a paraboloid described by

$$R(\phi) = \frac{ct}{1 + \cos \phi}. \quad (2.3)$$

2 The X-ray luminosity of the Galactic centre in the recent past

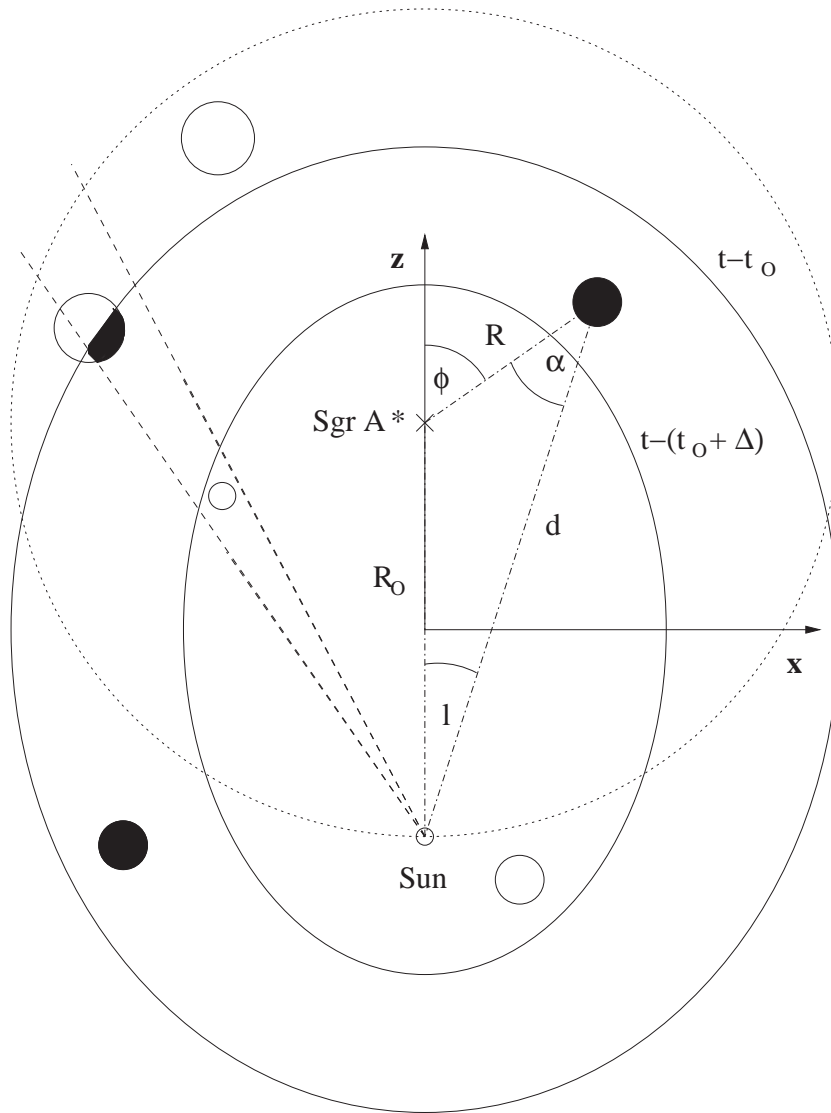


Figure 2.1: A sketch of the scenario studied in this chapter projected onto the Galactic plane. A time t_0 ago the luminosity of Sgr A* (marked by a cross) flared. This enhanced activity lasted for a period Δ . Relative to the earth bound observer (small circle), observing at a time t and orbiting Sgr A* on the dotted circle, the GMCs that lie between the two ellipsoids corresponding to the beginning and the end of the flare are exposed to this enhanced emission. For other GMCs the period of enhanced irradiation already has passed or has not started yet. The boundaries of an exemplary observational field of view are sketched by dashed lines. Inside this field of view one cloud has already faded away and another one is partially covered by the flare. Two possible photon paths between Sgr A* and the observer are marked by dot-dashed lines (the direct path from Sgr A* to the observer is covered half way by the z-axis). The ellipsoids are rotationally symmetric about the z-axis.

The paraboloid approximation is valid e.g. for GMCs at the GC ($R_o \gg ct$) and has been studied in the context of Sgr B2 by Sunyaev & Churazov (1998).¹ In cartesian coordinates the paraboloid is described by:

$$z = \frac{1}{2} \left(ct - \frac{x^2 + y^2}{ct} \right) + \frac{R_o}{2}. \quad (2.4)$$

The velocities of the surfaces of constant time delay along the major and minor axes of the ellipsoid are obtained by differentiation of the formulae for a and b with respect to time. The major axis increases at a constant speed of $c/2$. The velocity along the minor axes depends upon time as follows

$$\dot{b} = \frac{c}{2} \frac{ct + R_o}{\sqrt{(ct)^2 + 2ctR_o}}. \quad (2.5)$$

At times small compared to R_o/c this velocity is larger than the velocity of light and approaches the value $c/2$ for $ct \gg R_o$. Inside of the Galaxy, where most of the GMCs lie inside the solar circle ($R < R_o$), this velocity is always larger than $(2/\sqrt{3})(c/2) \approx 0.58c$.

The velocity in a general direction ϕ is given by the temporal derivative of Equation 2.2 which yields

$$\dot{R}(\phi) = \frac{c}{2} \frac{c^2 t^2 + 2R_o(ct + R_o)(1 + \cos \phi)}{(ct + R_o(1 + \cos \phi))^2}. \quad (2.6)$$

In the paraboloid approximation this becomes, by either differentiating Equation 2.3 with respect to t or by taking the limit $R_o \gg ct$ of Equation 2.6,

$$\dot{R}(\phi) = \frac{c}{1 + \cos \phi}. \quad (2.7)$$

The apparent velocity is given by the projection onto the plane of the sky, which reads

$$v_{\text{app}} = \frac{c \sin \phi}{1 + \cos \phi}. \quad (2.8)$$

¹The study of light echoes has a long history, starting with an explanation of observations of Nova Persei 1901 by Couderc (1939). Since then it has been applied to several astrophysical objects, e.g. supernova lightcurves (Morrison & Sartori 1969), scattering by interstellar dust (Alcock & Hatchett 1978), scattering of an isotropic (Sunyaev 1982) or anisotropic radio source (Gilfanov et al. 1987a) by the thermal gas in a cluster of galaxies, reverberation mapping in AGN (e.g. Peterson (1993)) and Compton echoes from gamma-ray bursts (Madau et al. 2000) to name a few.

2 The X-ray luminosity of the Galactic centre in the recent past

This equation is equivalent to the formula for apparent superluminal motion of matter having velocities close to the speed of light, which is normally expressed in terms of the angle $\theta = \pi - \phi$ (Rees 1967). The formula for the apparent velocity in the Galactic plane in the ellipsoid case is given by

$$v_{\text{app}} = \frac{c}{2} \frac{c^2 t^2 + 2R_o(ct + R_o)(1 + \cos \phi)}{(ct + R_o(1 + \cos \phi))^2} \sin(\phi - l). \quad (2.9)$$

One obtains an additional dependence upon l , because the projection angle for a given direction ϕ depends upon galactocentric distance R and therefore upon time.

The average time delay of photons scattered by a cloud with galactocentric radius R and distance from the observer d is given by:

$$\delta = (R + d - R_o)/c. \quad (2.10)$$

It is obvious that for clouds with a constant galactocentric distance R those, which lie behind the GC, produce the largest time delay $\delta_{\text{max}}(R = \text{const.}) = 2R/c$. For clouds with a distance of 6 kpc to the GC, the edge of the molecular ring, the largest time delay is about 40.000 years. The more diffuse HI phase of the interstellar medium (ISM) extends up to radii of about 16 kpc (Dame 1993). Matter at these distances can in principle probe the activity of the GC up to a time of about 110.000 years ago.

2.2.2 GMCs in the Galactic disk

The results of several CO surveys have been published over the last decades. These surveys map the CO brightness temperature as a function of Galactic longitude l , Galactic latitude b and radial velocity component v_r , differing in resolution and area surveyed.

Solomon et al. (1987), henceforth SRBY87, have published a list (see Table 1 in their paper) of 273 molecular clouds detected with the Massachusetts-Stony Brook CO Galactic Plane Survey of the first Galactic quadrant. These clouds were extracted from the three dimensional (l, b, v_r) data cube by locating surfaces of equal brightness temperature. The distances were computed from the radial velocity component of the centroids under the usual assumption (see e.g. Binney & Merrifield (1998)) that clouds move on circular orbits with a constant circular velocity of $\Theta_o = 220 \text{ km s}^{-1}$.

The assumption of circular orbits with a constant rotational velocity is a fair approximation for clouds inside of the solar circle but breaks down at small galactocentric radii because the orbits are probably highly non circular in this region.

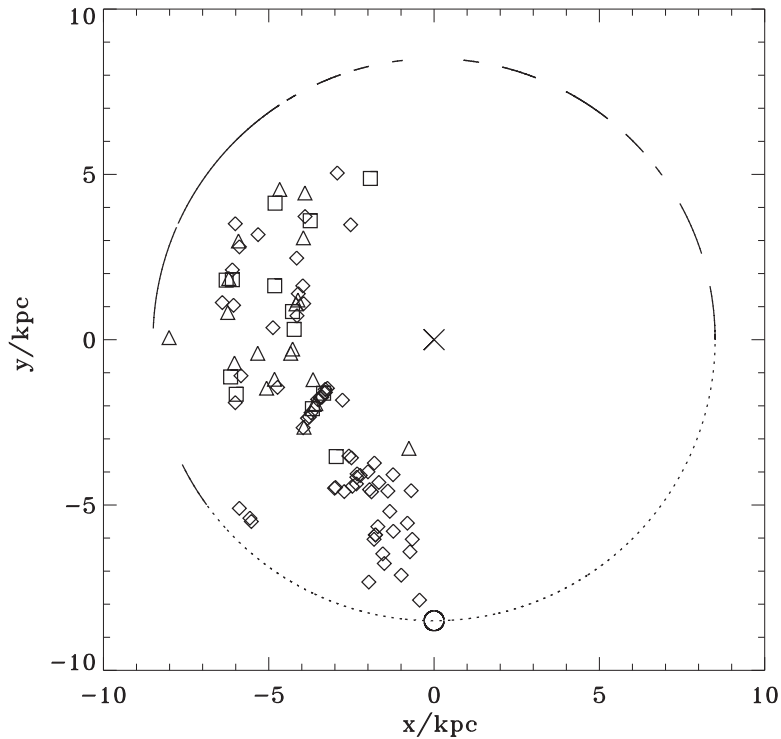


Figure 2.2: The spatial distribution of GMCs selected from SRBY87 for this work. The GMCs cover a range of Galactic longitudes of $8^\circ \leq l \leq 60^\circ$. The position of the GC is marked by a cross. The position of the sun (marked by a small circle) is at coordinates $(-8.5, 0.0)$. For Galactic longitudes covered by *ASCA* observations the solar circle is marked by solid arcs. For Galactic longitudes falling outside of the *ASCA* survey the solar circle is marked by a dotted line. The different symbols denote different cloud masses: $M_{\text{cl}} \leq 5 \times 10^5 M_\odot$ (diamonds), $5 \times 10^5 M_\odot < M_{\text{cl}} \leq 10^6 M_\odot$ (triangles) and $M_{\text{cl}} > 10^6 M_\odot$ (squares).

For GMCs inside the solar circle a ambiguity is inherent to this method of distance determination. A cloud with a given measured radial velocity component can either lie on the near or the far side of the circular orbit it is assumed to travel around the GC. SRBY87 were able to overcome this ambiguity by several methods described in their paper.

This data set is not the most recent one (for more recent surveys of this area see, e.g. Dame et al. (2001) and Lee et al. (2001)) but to our knowledge up to today the only one where mass estimates of a large number of individual GMCs

2 The X-ray luminosity of the Galactic centre in the recent past

GMC	l/deg	b/deg	R/kpc	d/kpc	δ^{a}	M_{cl}^{b}	r_{cl}/pc	t_{cl}^{a}	F_{sc}^{c}	$F_{\text{obs}}^{\text{d}}$	L_{GC}^{e}
003	08.30	+0.00	3.4	5.3	669	55.6	19.3	44	71	19	8.0×10^{40}
014	10.00	-0.04	4.6	4.0	335	11.3	5.8	12	12	15	3.8×10^{41}
059	17.20	-0.20	5.2	12.7	31449	199.1	29.7	353	9.4	17	5.4×10^{41}
080	20.75	+0.10	4.2	5.1	2677	21.6	8.9	39	10	15	4.5×10^{41}
085	21.75	+0.00	4.6	4.5	2007	36.4	9.4	37	16	16	3.0×10^{41}
089	22.05	+0.20	5.4	3.6	1673	33.7	11.9	38	25	16	1.9×10^{41}
116	24.60	-0.15	4.4	10.3	20743	106.7	13.4	126	5.2	15	8.7×10^{41}
122	25.65	-0.10	4.2	9.8	18401	202.6	28.2	283	17	18	3.2×10^{41}
128	25.90	-0.15	3.8	7.7	10037	107.5	17.2	133	12	17	4.3×10^{41}
151	28.30	-0.10	4.8	4.9	4015	41.7	12.5	54	13	14	3.2×10^{41}
152	28.60	+0.05	4.3	7.5	11041	63.3	11.7	90	5.4	14	7.8×10^{41}
158	29.00	+0.05	4.3	7.5	11041	48.9	18.0	145	6.4	15	7.0×10^{41}
162	29.85	-0.05	4.3	7.4	10706	85.1	15.8	127	8.5	15	5.3×10^{41}
171	30.80	-0.05	4.6	5.8	6357	119.3	22.1	107	23	13	1.7×10^{41}
191	33.90	+0.10	4.8	7.1	11375	54.8	15.6	119	6.0	10	5.0×10^{41}
193	34.25	+0.10	6.1	3.1	2342	39.4	9.3	42	16	10	1.9×10^{41}
201	35.20	-0.10	7.9	0.8	669	2.0	3.4	18	16	9.1	1.7×10^{41}
206	36.40	-0.10	6.3	3.1	3011	23.2	8.8	42	11	10	2.7×10^{41}
214	39.85	-0.20	6.3	9.6	24758	375.3	47.4	469	16	7.7	1.4×10^{41}
217	41.15	-0.20	6.2	9.1	22750	201.2	22.4	215	6.7	8.6	3.9×10^{41}

^a Time delay δ and time for the ellipsoid to cross the cloud t_{cl} in units of years

^b Mass of cloud in units of $10^4 M_{\odot}$

^c Scattered flux in the 4-10 keV range in units of $10^{-9} \text{ erg cm}^{-2} \text{ s}^{-1}$ for the whole cloud covered by a flare

^d Flux in the 4-10 keV range observed by *ASCA* in units of $10^{-12} \text{ erg cm}^{-2} \text{ s}^{-1}$

^e Upper limit for the luminosity of Sgr A* in the 4-10 keV range in units of erg s^{-1} a time δ ago

Table 2.1: Selected parameters, i.e. number of cloud in SRBY87 sample, Galactic longitude, Galactic latitude, galactocentric distance, distance, time delay, mass, radius, time it takes the ellipsoid to cross the cloud, scattered flux, observed flux and upper limit for the luminosity of Sgr A* for twenty GMCs from our sample.

have been presented.

Not all of the clouds listed in SRBY87 fall into one of the fields of view of the *ASCA* Galactic Plane Survey. These are clouds located at longitudes larger than 60° or at latitudes larger than 0.3° . Combining the two data sets leaves one with 96 clouds out of 273. The spatial distribution of these clouds in the Galactic plane is plotted in Figure 2.2, symbolised according to their mass (for

the spatial distribution of the full set of clouds see Solomon & Rivolo (1989)). Although a spiral structure only might be marginally discernible in this figure, the concentration of GMCs along the molecular ring is clearly visible.

The cloud properties required for this work are the Galactic longitude l , the galactocentric radius R , the distance from the observer d , the radius r_{cl} and the mass M_{cl} of a cloud, which was computed with the observed velocity dispersion and should thus not be affected by recalibrations of the $\text{I}(\text{CO})/\text{N}(\text{H}_2)$ ratio. For the chosen subsample of clouds these parameters fall in the ranges of $1.9 \times 10^4 M_{\odot} \lesssim M_{\text{cl}} \lesssim 3.8 \times 10^6 M_{\odot}$, $2.5 \lesssim r_{\text{cl}} \lesssim 47$ pc and $3 \times 10^2 \text{years} \lesssim \delta \lesssim 4 \times 10^4 \text{years}$. Note that in SRBY87 a distance of the sun to the GC of 10 kpc was assumed. We have rescaled the distances and derived cloud properties to $R_{\odot} = 8.5$ kpc. In Table 2.1 (columns 1-8) we list the important parameters for twenty exemplary clouds out of our sample. Note that the GMCs in SRBY87 have been ordered and numbered according to their respective Galactic longitude.

2.2.3 Scattered flux

The *ASCA* observations of the Galactic plane ($b \approx 0^\circ$) in the longitude range $-45^\circ \leq l \leq 63^\circ$ have been compiled and analysed by Sugizaki et al. (2001). In Figure 2.2 we have tried to illustrate the range of longitudes covered by the *ASCA* Galactic Plane Survey by plotting solid arcs at a distance R_{\odot} from the GC, where observations have been made. It is obvious that we are missing the CO data from the fourth Galactic quadrant. As mentioned before surveys of this area exist (e.g. Dame et al. (2001)) but to our knowledge this data has not yet been fully analysed. The distribution of GMCs should be symmetric between the Galactic quadrants I and IV. We should therefore expect a similar number of GMCs in the fourth Galactic quadrant.

The *ASCA* observations have been presented in three energy bands. Most interesting for this work because least affected by photoelectric absorption is the X-ray surface brightness in the hardest, i.e. the 4-10 keV, spectral band. The corresponding fluxes at all longitudes are all of a similar order of magnitude. Not even one cloud seems to be especially bright “at the moment”.

Even if the diffuse X-ray flux observed in one field of view originates from a different physical process than scattering, it is still an upper limit for the flux produced through scattering by gas distributed along this beam: $F_{\text{sc}} \leq F_{\text{obs}}$.

The clouds in our sample have optical depths for Thomson scattering up to $\tau_{\text{T}} \approx 10^{-1}$. We therefore are considering scattering in the optically thin limit. Our treatment of absorption is described in a following section (2.2.3.1). Nearly the whole Galaxy is transparent to X-rays with energies above 4 keV, except some regions around the GC. But even here optically thick GMCs do not shield the

2 The X-ray luminosity of the Galactic centre in the recent past

whole disk of the Galaxy from the illumination by Sgr A*. The covering fraction is probably rather small.

In the optically thin case the scattered surface brightness in a given direction at energy E and time of observation t is given by

$$I_{\text{sc}}(E, t) = \int_{s_{\text{min}}(t)}^{s_{\text{max}}(t)} n(s) \frac{L_{\text{GC}}(E, t_{\text{ret}})}{4\pi R(s)^2} \left(\frac{d\sigma}{d\Omega} \right) ds, \quad (2.11)$$

where s_{min} and s_{max} are the boundaries of integration, $n(s)$ is the number density of the scattering gas at a distance s from the observer, $t_{\text{ret}} = t - (R(s) + s)/c$ the “retarded” time, R the distance to the GC and $(d\sigma/d\Omega)$ the differential scattering cross-section. The time dependent integration limits are the points of intersection of the line of sight with the ellipsoids corresponding to the beginning and the end of a flare.

The scattered flux is given by the integration of the surface brightness over the field of view of the *ASCA* instrument:

$$F_{\text{sc}}(E, t) = \int I_{\text{sc}}(E, t) d\Omega. \quad (2.12)$$

We are taking into account the cases when parts of a cloud fall outside the field of view, as sketched in Figure 2.1, or when the field of view is larger than a cloud. However, we are neglecting here the iron K_{α} -line production and the corresponding iron K-edge absorption. The detailed *ASCA* spectral data are not yet publicly available. *XMM-Newton* will provide much improved data including K_{α} -line limits, which will improve the limits for the X-ray luminosity of Sgr A* derived in the following sections.

In the optical thin case the scattered luminosity is proportional to the mass of the illuminated scattering material. An order of magnitude estimate of the above integrals to demonstrate the scaling yields

$$L_{\text{sc}} \sim \frac{3}{16\pi} \frac{\sigma_{\text{T}}}{R^2} \frac{M_{\text{cl}}}{m_{\text{p}}} L_{\text{GC}}. \quad (2.13)$$

This formula neglects the spatial extension of the scattering gas and the angular dependence of the differential scattering cross-section and assumes that the whole cloud is covered by the flare, implying that all of the mass contributes to the scattered emission. For typical cloud parameters one obtains a scattered luminosity of

$$L_{\text{sc}} \sim 6 \times 10^{37} \text{ erg s}^{-1} \left(\frac{L_{\text{GC}}}{L_{\text{Edd}}} \right) \left(\frac{M_{\text{cl}}}{10^6 M_{\odot}} \right) \left(\frac{5 \text{ kpc}}{R} \right)^2, \quad (2.14)$$

which for $L_{\text{GC}} \sim L_{\text{Edd}}$ is comparable to the luminosity of the brightest X-ray binaries in the Galaxy, thereby certainly contradicting the observations.

If the flare duration Δ is shorter than the time for the ellipsoid to sweep across the cloud one has to multiply Equation 2.14 by an additional factor

$$\left(\frac{\Delta}{2r_{\text{cl}}/v_{\text{ell}}}\right), \quad (2.15)$$

where v_{ell} is the velocity of the ellipsoid across the cloud, which can be superluminal depending on the relative orientation of the cloud with respect to the GC and the observer. This additional factor takes into account that only a fraction $\sim \Delta/(2r_{\text{cl}}/v_{\text{ell}})$ of the mass of the cloud is illuminated.

2.2.3.1 Absorption

As X-ray photons of energy E traverse the ISM a fraction $\tau_{\text{ph}}(E)$ of them is absorbed by the heavy elements of the interstellar gas, again assuming optically thin conditions. Therefore a GMC will be exposed to a flux $(L_{\text{gc}}(E, t_{\text{ret}})/4\pi R^2) \exp[-\tau'_{\text{ph}}(E)]$, where $\tau'_{\text{ph}}(E)$ is the optical depth for photoelectric absorption at energy E between the GC and the GMC. The observer will measure a flux $F_{\text{sc}}(E, t) \exp[-\tau_{\text{ph}}(E)]$. The optical depth due to photoelectric absorption is proportional to the hydrogen column density N_{H}

$$\tau_{\text{ph}}(E) = N_{\text{H}}\sigma_{\text{ph}}(E), \quad (2.16)$$

where $\sigma_{\text{ph}}(E)$ is the photoelectric absorption cross-section per hydrogen atom, which we compute with an analytic fit by Morrison & McCammon (1983).

We estimate N_{H} with the average mass surface density of a GMC given by $\Sigma_{\text{cl}} \approx M_{\text{cl}}/r_{\text{cl}}^2\pi$, which leads to $N_{\text{H}} \approx (3/4)(\Sigma_{\text{cl}}/m_{\text{p}})$. Since we have no better knowledge about the hydrogen column density between the GC and a cloud, we furthermore assume $N'_{\text{H}} = N_{\text{H}}$.

2.2.3.2 Differential scattering cross-section for a mixture of H₂ and He

In the following sections we will assume that the GMCs in our sample are composed of 70% molecular hydrogen and 30% helium. It is known (e.g. Sunyaev & Churazov (1996)) that in the energy range in question scattering by the bound electrons of molecular hydrogen and helium is important, because for small scattering angles the differential scattering cross-section per electron for Rayleigh scattering on molecular hydrogen and helium can become two times larger than the one for hydrogen atoms, which at these energies is identical to the Thomson differential cross-section. The angular dependence for Thomson scattering is proportional to $(1+\cos^2\theta_{\text{sc}})$, where θ_{sc} is the scattering angle of the photon, which is approximately given by the angle α defined in Figure 2.1.

2 The X-ray luminosity of the Galactic centre in the recent past

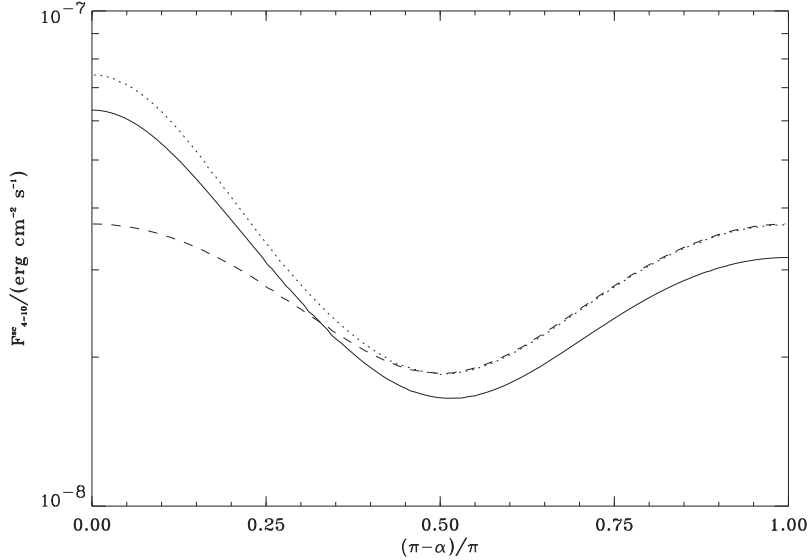


Figure 2.3: The scattered flux in the 4-10 keV range as a function of the angle α (defined in Figure 2.1) for a cloud of $10^6 M_{\odot}$ at 5 kpc distance from the GC and the observer fully illuminated by an Eddington flare of Sgr A*. Note that $\alpha = \pi$ corresponds to the case of forward scattering. The lines mark different mass compositions of the cloud: 70% H_2 + 30% He (solid line), atomic hydrogen (dashed) and molecular hydrogen (dotted).

In Figure 2.3 we plot the scattered flux for a single cloud of $10^6 M_{\odot}$ composed of pure molecular hydrogen, a mixture of 70% molecular hydrogen and 30% helium and pure atomic hydrogen as a function of the angle α ($\alpha = \pi$ corresponds to the case of forward scattering). We chose a galactocentric distance and a distance to the observer of 5 kpc. We used the differential scattering cross-section for scattering by atomic, molecular hydrogen and helium as a function of photon energy and scattering angle as presented in Sunyaev et al. (1999).

The scattered flux for the compositions including molecular hydrogen are larger than the one for atomic hydrogen because for small scattering angles ($\alpha \lesssim \pi$) the two electrons present in molecular hydrogen and helium scatter coherently. The scattered flux for the chosen mixture of molecular hydrogen and helium is smaller than the one for pure molecular hydrogen because in this case there are only 0.85 electrons per nucleon compared to 1 electron per nucleon for pure hydrogen, atomic or molecular.

2.3 Limits on the X-ray luminosity of Sgr A* from Giant Molecular Clouds

There exist several characteristic variability timescales for a supermassive black hole such as Sgr A*. The shortest possible timescale is related to the linear size of the region, where the bulk of energy is released in the accretion disk around a black hole (Shakura & Sunyaev 1973): $t_{\text{bh}} \sim 10R_g/c \sim 300\text{ s}$ for Sgr A*, where R_g is the Schwarzschild radius of the black hole. Tidal disruption events are believed to produce an Eddington level flare over a period $t_{\text{tidal}} \sim \text{years}$ (Rees 1988). The lifetimes of active galactic nuclei (AGN) are believed to be of the order of $10^7 - 10^8$ years. The detailed temporal evolution of the luminosity of Sgr A* is probably rather complex, possibly varying on all of the above timescales.

In this study it is our aim to constrain the past luminosity of Sgr A* from information about the reprocessing system, i.e. the spatially distributed GMCs in the Galactic disk, and the output signal at one point in time, i.e. the scattered flux observed today. Such an approach is reminiscent of the methods used in reverberation mapping of AGN (see e.g. Peterson (1993)). By applying these methods, one tries to gain information about the geometry and kinematics of the emission-line region (the reprocessing system) by monitoring the continuum variations (the input) and the resulting emission-line response (the output). Mathematically this is described by a transfer function Ψ , which applied to our problem can be written as:

$$F_{\text{sc}}(t) = \int_{-\infty}^{\infty} \Psi(t')L_{\text{GC}}(t - t') dt' \quad (2.17)$$

The scattered flux observed at a time t is the response of our system to the activity of the GC in the past. In reverberation mapping of AGN one determines the transfer function Ψ using Fourier transforms of the input and the output over a certain period of time. In our case this is not possible because the scattered flux or an upper limit thereof is known only at one moment in time, i.e. “today”.

If the cloud had no spatial extension at all, i.e. a “point mass”, the transfer function would be just a δ -function having an amplitude proportional to the mass of the cloud. The transfer function for several point mass clouds with different time delays would be a sum of δ -functions. In such cases it would be possible to ascribe an unique X-ray luminosity of Sgr A* to an observed scattered flux.

Due to the spatial extension of a GMC with an internal density distribution this δ -function is smeared out in time. This means that the scattered flux observed at one moment in time depends upon the luminosity of the GC over a certain period of time in the past. The correspondence between the observed scattered flux and the luminosity of the GC is therefore not one to one anymore.

2 The X-ray luminosity of the Galactic centre in the recent past

What one can do to constrain the luminosity of Sgr A* in this case is to assume some input, a “test function”, and compare the resulting output with the observations. Should the output be inconsistent with the observed flux then the initial input must be wrong.

We assume the temporal and spectral behaviour of the luminosity of Sgr A* to be of the following form

$$L_{GC}(E, t) = \begin{cases} L_o(E_o/E) & t_{\text{on}} \leq t \leq t_{\text{off}} \\ 0 & \text{else,} \end{cases} \quad (2.18)$$

with $t_{\text{on}} = t_o - \Delta/2$ and $t_{\text{off}} = t_o + \Delta/2$. This choice of spectral behaviour implies a photon index of 2, which is representative of observed AGN spectra in the 4-10 keV range. Note that here we define for the sake of symmetry t_o as the time half way through the flare, whereas in Section 2.1 t_o was defined as the beginning of the flare.

Different inputs can produce the same output because as mentioned above there does not exist a one to one relation between the luminosity and the scattered flux. It is therefore impossible to constrain the past luminosity at one moment in time. The important quantity is thus actually the emitted energy over a period T

$$Q = \int_T L_{GC}(t') dt', \quad (2.19)$$

where T is given by the minimum of the flare duration and the time for the ellipsoid to cross the cloud. The limits we are deriving in the following sections are therefore constraints upon a time averaged luminosity of Sgr A*, viz. $\hat{L}_{GC} \lesssim L_{\text{max}}$ with $\hat{L}_{GC} = Q/T$.

2.3.1 Response of a single cloud

Observations of molecular tracers of H_2 (see e.g. Blitz & Williams (1999)) show that GMCs are far from being spherically symmetric objects. They are highly structured being made out of clumps with high density variations from one point to another. Due to their amorphous nature without a clear central peak the density profile is often difficult to define observationally. Another difficulty is that different tracers of H_2 turn optically thick at different densities. Nevertheless Williams et al. (1995) were able to determine a density distribution of the form $\rho \propto r^{-2}$ for dense clumps in the Rosette molecular cloud. We therefore adopt this radial dependence as our profile A:

$$\rho_{\text{cl}}(r) = \begin{cases} \rho_o(r_o/r)^2 & r \leq r_{\text{cl}} \\ 0 & r > r_{\text{cl}}. \end{cases} \quad (2.20)$$

2.3 Limits on the X-ray luminosity of Sgr A* from Giant Molecular Clouds

The normalisation ρ_o is chosen in such a way, that the mass contained inside the radius of the cloud corresponds to the one given in SRBY87. The cutoff is required to obtain a finite mass.

Besides the response of the cloud with density profile A we have also computed the response for a different profile to study the influence of the mass distribution inside a cloud upon our results. We choose as our profile B the following one:

$$\rho_{\text{cl}}(r) = \frac{\rho_o}{(1 + (r/r_o)^2)^2}. \quad (2.21)$$

This profile has a constant core density up to a radius of the order r_o , which we choose to be $0.1r_{\text{cl}}$. Most of the mass of this profile is provided by matter located at these radii.

Having specified the input (Equation 2.18) and an internal density distribution for a cloud (Equations 2.20 and 2.21) we can integrate Equations 2.11 and 2.12 numerically to compute the scattered flux produced by a cloud out of our sample. As an illustrative example we chose cloud 116 from the SRBY87 sample (see Table 2.1) and computed its response to Eddington flares of Sgr A* of durations of 1, 10, 100 and 300 years as a function of time. Figure 2.4 displays the results of these computations.²

Figure 2.4 shows that an Eddington flare of the GC lasting for one year 20 764 years ago, the time delay δ of cloud 116, “today” would produce a scattered flux of about $2 \times 10^{-10} \text{ erg cm}^{-2} \text{ s}^{-1}$ for profile A and $4 \times 10^{-11} \text{ erg cm}^{-2} \text{ s}^{-1}$ for profile B in the *ASCA* field of view cloud 116 is located in. Since the observational limit for this field of view is below these values, thus falsifying the initial assumption, there could not have been an Eddington flare of Sgr A* of a duration of one year or longer 20.764 years ago. A one year flare occurring 100 years earlier or later can not be excluded by cloud 116, because the scattered fluxes would be below the observational limits.

²Note that Figure 2.4 (and the following figures depicting a dependence upon $t - t_o$) can be read in two ways:

1. Regarding t , the time of observation, as the independent variable and keeping t_o , the time half way through the flare, fixed (e. g. $t_o = -\delta$) the different curves mark the scattered flux as a function of observing time t in response to a flare of Sgr A* at $t_o = -\delta$. One tracks the response of a single flare as time evolves.
2. Considering t_o as the independent variable and keeping t , the time of observation, fixed (e. g. $t = 0$) the different curves mark the scattered flux observable at a time $t = 0$ as a function of the time half way through the flare t_o . At one moment in time one observes the response of flares occurring at different times t_o . This case applies to what is done in this chapter to constrain the past luminosity of Sgr A*.

2 The X-ray luminosity of the Galactic centre in the recent past

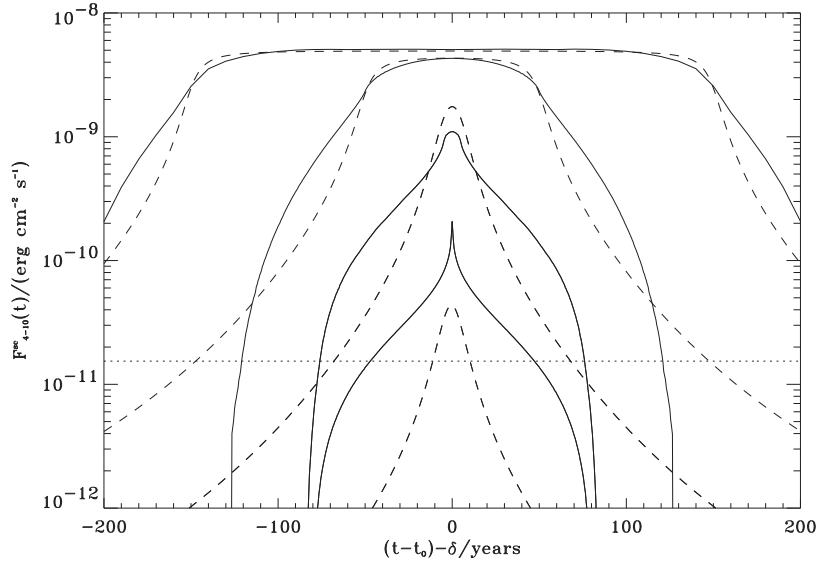


Figure 2.4: The scattered flux in the 4-10 keV range observable at a time t produced by a single cloud (number 116 in Table 2.1) in response to an Edington flare of Sgr A* of 1, 10, 100 and 300 years duration (from bottom to top) occurring around a time t_0 for two different density profiles of the cloud given by Equation 2.20 (solid lines, profile A) and Equation 2.21 (dashed lines, profile B). The observational limit for the scattered flux produced in the field of view the cloud is located in is marked by a dotted line. The time delay δ for this cloud is 20.764 years, the radius of the cloud is 13.4 pc and the time for the ellipsoid to cross the cloud about 126 years, which corresponds to a cloud crossing velocity of $v_{\text{ell}} \approx 0.8c$ (for the other cloud parameters see Table 2.1).

Because especially for short flares the shape of the lightcurve mainly depends upon how the mass is distributed inside a cloud, the responses for the density profiles A and B differ in these cases.

The response of a cloud with density profile A to the one year flare illustrates that a cloud whose mass is centrally concentrated will produce a light curve with a very sharp maximum. This comes about because for short flare durations the space between the two ellipsoids covers only a small part of the cloud. This illuminated region sweeps along the cloud and produces a maximum flux when it covers the most dense, central part of the cloud. Increasing the flare duration one encloses more and more mass between the two ellipsoids, corresponding to the beginning and the end of the flare. This increases the scattered flux, which is proportional to the mass, and averages out density contrasts at different radii. The central spike

2.3 Limits on the X-ray luminosity of Sgr A* from Giant Molecular Clouds

produced by the one year flare therefore vanishes for longer flare durations. The steep decline of the scattered flux observable for density profile A comes about because of the cutoff of the profile at $r = r_{\text{cl}}$.

For density profile B, which approximately corresponds to a constant density inside r_o , the main contribution to the total mass of the cloud is provided by matter at radii $r \sim r_o$. Because the one year flare covers a region smaller than this size, there is more mass probed by the one year flare in the central region of profile A than profile B. The largest scattered flux produced for a one year flare by a cloud with density profile A is therefore larger than the one for a cloud with density profile B. For flares of longer duration larger parts of the cloud will be covered and the fluxes will reach a similar level, because both density profiles are normalised in such a way that the total mass contained inside of a radius r_{cl} is equal for both profiles.

If the duration of the flare increases, the whole cloud will be covered at one point. From this point on an increase of flare duration will no more produce a larger flux, because all of the cloud is already enclosed between the two ellipsoids. This “saturation” time t_{cl} , i.e. the flare duration for which the maximum flux is achieved or equivalently the time for the ellipsoid to sweep across the cloud, depends obviously on the radius of the cloud but also on the position of the cloud relative to the GC and the observer. This position determines the time travel effects and the different velocities of the ellipsoid sweeping across the cloud. For example in the extreme case, when the cloud lies exactly behind the source the time it takes an ellipsoid to cross the cloud is $4r_{\text{cl}}/c$. On the contrary, in the case when the cloud lies half way between the GC and the observer at a small Galactic longitude, the time to sweep across the cloud is of the order of $(r_{\text{cl}}/R_o)r_{\text{cl}}/c$, which is obviously much smaller than the value given above. Thus, if the cloud is located closer to the observer than the source of the flare, the whole cloud will be scanned much quicker than the light crossing time of the cloud. For the cloud behind the source the temporal evolution will be slowest. For the GMCs in our sample the values lie somewhere between these two extreme cases.

We have computed lightcurves similar to Figure 2.4 for all the GMCs in our sample. With these lightcurves we are able to estimate the saturation time and the maximum scattered flux. The saturation time t_{cl} of a cloud and its radius yield an estimate for the velocity of the ellipsoid sweeping across the GMC: $v_{\text{ell}} \sim (2r_{\text{cl}}/c)/t_{\text{cl}}$. In column 9 of Table 2.1 we have listed the saturation times for twenty GMCs from our sample. The cloud crossing velocities for these clouds lie in the range of $0.6c \lesssim v_{\text{ell}} \lesssim 3.2c$.

The maximum scattered flux produced by a cloud yields an upper limit for the luminosity of the GC via the following argument. In our models we are computing the scattered flux in response to an Eddington flare of Sgr A* some time ago, which

2 The X-ray luminosity of the Galactic centre in the recent past

enables us to estimate the ratio $F_{\text{sc}}/F_{\text{obs}}$. Consistency with observations demand the scattered flux to be smaller than the actually observed one: $F_{\text{sc}}/F_{\text{obs}} \leq 1$. Since the computed scattered flux just scales linearly with the assumed input luminosity we can find the luminosity of the GC for which this inequality is fulfilled:

$$L_{\text{GC}} \lesssim \frac{F_{\text{obs}}}{F_{\text{sc}}} L_{\text{Edd}}. \quad (2.22)$$

For twenty clouds selected from our sample we have listed the scattered flux, the observed flux and the derived upper limit upon the past luminosity of Sgr A* in columns 10 to 12 of Table 2.1.

If the duration of a flare increases beyond t_{cl} then the flux will stay at a constant level and the curves will extend to times $t - t_o \approx \delta \pm \Delta/2$ as is illustrated in Figure 2.4 by the responses to the flare lasting 300 years. An even further increase of the flare duration will have the result that at one point several clouds along one line of sight can be illuminated by one flare and their scattered fluxes begin to overlap, producing a larger total flux. This case will be discussed further below.

As mentioned in the beginning of this section observations show that the above assumed spherically symmetric density profiles are too simplistic. The curves in Figure 2.4 for a “real” GMC will probably look quite differently. They will be “noisier”, exhibit maybe several peaks because of different density maxima and will not display this symmetry. However, as we have shown, the choice of the density distribution mainly determines the shape of the lightcurves, i.e. the scattered flux as a function of time, but not the level of the maximum scattered flux, which depends mainly on the total mass and the position of the cloud once it is fully covered by a flare. As long as the CO observations provide us with a good estimate of the total mass of a GMC we are, therefore, fairly confident that our computations, especially of the maximum scattered flux and the derived limit, are fairly “correct”, albeit the mentioned uncertainties about the density distribution inside a GMC.

2.3.2 Response of one field of view

The *ASCA* field of view has a diameter of about 40' and thus subtends a solid angle of 0.35 deg^2 . This diameter corresponds to a linear scale of about 100 pc at the distance of the GC. Figure 2.2 shows that several clouds are located at similar Galactic longitudes. Their angular separations are often smaller than the diameter of the *ASCA* field of view. In most fields of view one finds therefore more than one cloud. Since we have a total of 96 GMCs distributed over 49 *ASCA* fields of view there are about two clouds per field of view on average. For one of these fields of view ($l = 27.51^\circ$), in which five clouds are located, the maximum number

2.3 Limits on the X-ray luminosity of Sgr A* from Giant Molecular Clouds

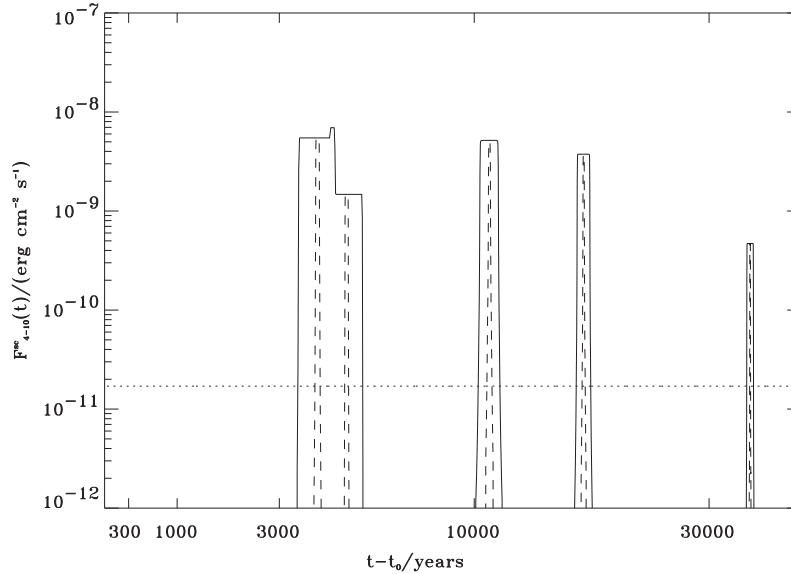


Figure 2.5: The scattered flux in the 4-10 keV range observable at a time t produced by five GMCs located in one *ASCA* field of view pointing at a Galactic longitude of $l = 27.51^\circ$ in response to an Eddington flare of Sgr A* of 100 (dashed) and 1,000 (solid) years duration occurring around a time t_0 . The observational limit for the scattered flux produced in this field of view is marked by the dotted line. Note how the scattered fluxes of two GMCs begin to overlap for the 1,000 year flare because both clouds are illuminated at a given point in time.

of clouds in one field of view, we plot the scattered flux as a function of time in Figure 2.5.³

Due to the different combinations of galactocentric and heliocentric distances of these five clouds they have different time delays, i.e. they respond to activity of the GC at different times. For every cloud we get a response similar to that displayed in Figure 2.4 at the time delay corresponding to each cloud. Figure 2.5 shows that all five clouds already have reached their maximum flux for a 100 year

³The plots presented in this and the following sections have to cover a period of time of 40,000 years and also should resolve flares on the timescale of years. In order to be more illustrative we are plotting the total scattered flux as a function of a different time coordinate defined by

$$t \rightarrow \log \left(1 + \frac{t}{t_s} \right),$$

where we have chosen $t_s = 3,000$ years. This choice ensures a linear behaviour for times small and a logarithmic one for times large compared to t_s .

2 The X-ray luminosity of the Galactic centre in the recent past

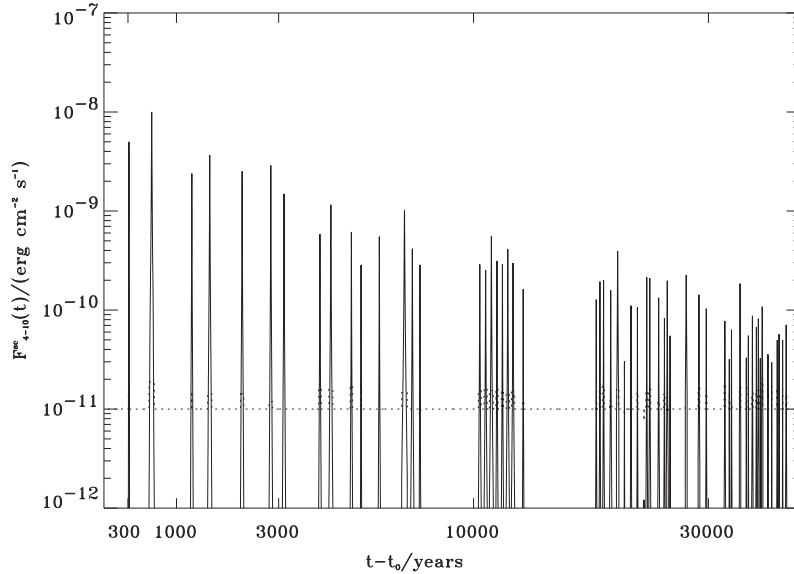


Figure 2.6: The maximum of the scattered flux in the 4-10 keV range observable at a time t in all the fields of view produced by all 96 GMCs from our sample in response to an Eddington flare of Sgr A* of 1 year duration occurring around a time t_0 . The observational limits for the scattered flux are marked by a dotted line.

flare. For this duration all the clouds are already covered and their saturation time is therefore smaller than 100 years. For a 1.000 year flare the scattered fluxes from two clouds start to overlap. This happens when the duration of a flare is longer than the time needed for the ellipsoid to cross the distance between these two clouds. Despite the fact that Figure 2.5 restricts the luminosity of Sgr A* much more than Figure 2.4 it is obvious that there are large time gaps during the last 40.000 years where these 5 clouds are insensitive to the luminosity of Sgr A*.

Spatial overlapping of the clouds in the field of view and absorption should not be a problem because the dense cores with large column depths lie in different directions. Certainly there should be further clouds of smaller size, below the detection threshold of the CO survey, present but these do provide only little scattered flux because of their much smaller masses. Since we have GMCs not only in one field of view one can combine the limits from all fields of view, which is done below.

2.3 Limits on the X-ray luminosity of Sgr A* from Giant Molecular Clouds

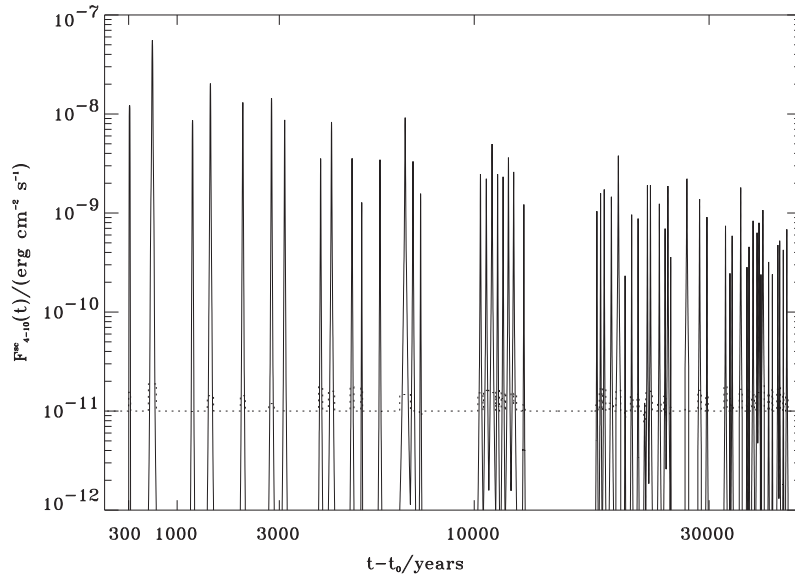


Figure 2.7: The maximum of the scattered flux in the 4-10 keV range observable at a time t in all the fields of view produced by all 96 GMCs from our sample in response to an Eddington flare of Sgr A* of 10 years duration occurring around a time t_0 . The observational limits for the scattered flux are marked by a dotted line.

2.3.3 Response of all fields of view containing at least one GMC

In total there are 49 *ASCA* fields of view covering at least one cloud out of the SRBY87 sample. The scattered flux produced in these fields of view will be similar to the one shown in Figure 2.5 with a peak for every cloud roughly proportional to the mass of the cloud. The peaks are centred around the time delay for the cloud and their temporal extent is of the order of $\Delta/2$, if the duration of the flare is longer than the cloud crossing time.

To combine the information from all 49 fields of view we proceeded in the following way. We computed the expected scattered flux for each field of view for a temporal grid covering the last 40,000 years with a sufficient time resolution to resolve the response of individual clouds. From these 49 lightcurves we select at each temporal grid point the largest scattered flux produced in response to the assumed input. As the observational limit at that time we choose the limit for that *ASCA* field of view, in which the largest scattered flux is produced. In Figures 2.6 to 2.9 the result of this procedure is shown, viz. the temporal response of all fields

2 The X-ray luminosity of the Galactic centre in the recent past

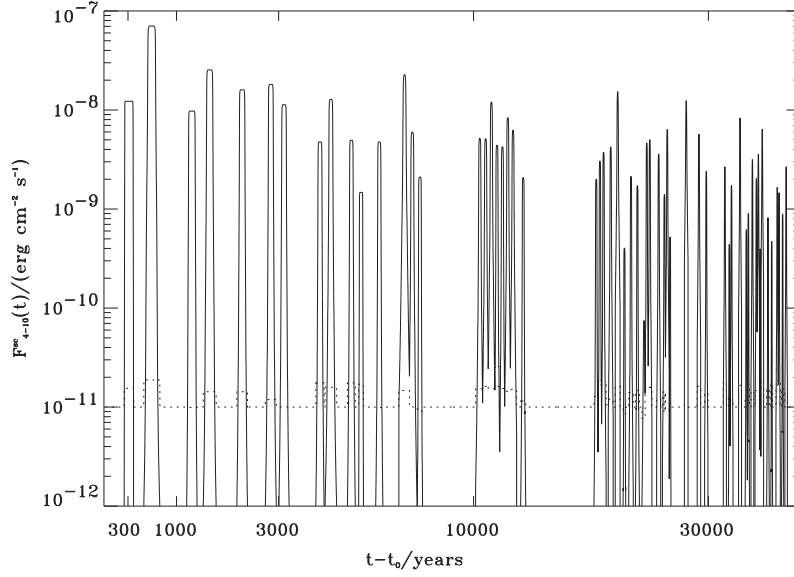


Figure 2.8: The maximum of the scattered flux in the 4-10 keV range observable at a time t in all the fields of view produced by all 96 GMCs from our sample in response to an Eddington flare of Sgr A* of 100 years duration occurring around a time t_0 . The observational limits for the scattered flux are marked by a dotted line.

of view to an Eddington flare of Sgr A* of 1, 10, 100 and 1.000 years duration.

As one progresses from short to long flare durations a larger and larger portion of the last 40.000 years is covered by the GMCs. Increasing the flare duration by an order of magnitude results in an increase of the scattered flux by approximately the same factor (this factor depends upon the density profile) as long as the flare duration is smaller than the “saturation time” for a given cloud.

The first spike is produced by a GMC having a time delay of about 335 years (cloud 014 in Table 2.1). Remarkable about this cloud is that it attains its maximum scattered flux for a flare duration of only about 12 years. With its radius of 5.8 pc one can estimate that the ellipsoid sweeps across the cloud with a “velocity” of about $3.2c$. This rather large velocity is the result of the position of this GMC. It lies nearly half way between the GC and the observer at an longitude of only 10° . In a previous section (2.3.1) we showed that clouds near the line between the GC and the observer can have very small cloud crossing times, because the motion of the ellipsoid is highly superluminal.

The largest scattered flux is produced by a GMC with a time delay of 669 years (cloud 003 in Table 2.1). To make the maximum scattered flux produced by this

2.3 Limits on the X-ray luminosity of Sgr A* from Giant Molecular Clouds

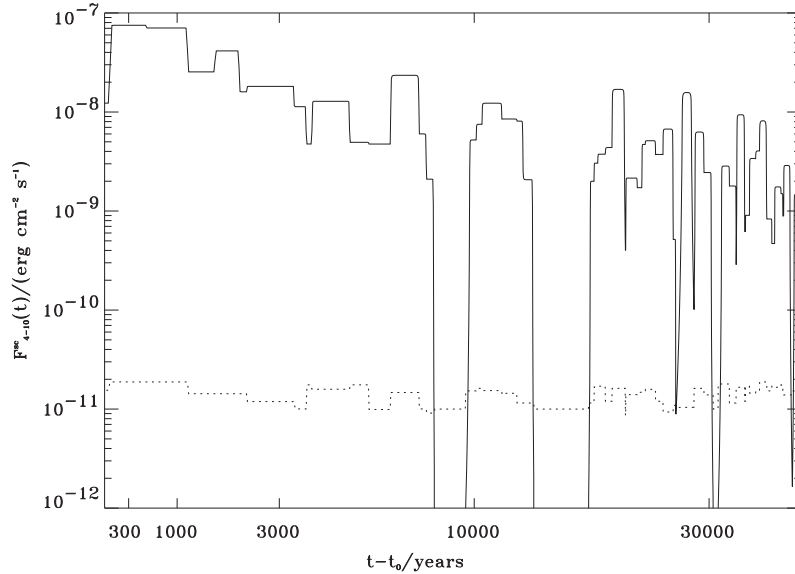


Figure 2.9: The maximum of the scattered flux in the 4-10 keV range observable at a time t in all the fields of view produced by all 96 GMCs from our sample in response to an Eddington flare of Sgr A* of 1.000 years duration occurring around a time t_0 . The observational limits for the scattered flux are marked by a dotted line.

cloud ($\sim 7 \times 10^{-8} \text{ erg cm}^{-2} \text{ s}^{-1}$) consistent with the observational limits ($\sim 2 \times 10^{-11} \text{ erg cm}^{-2} \text{ s}^{-1}$) a burst must have been $\sim 3 \times 10^{-4}$ times below the Eddington luminosity, corresponding to a luminosity of Sgr A* of at most $\sim 8 \times 10^{40} \text{ erg s}^{-1}$. For the smaller peaks one derives less tight limits (see also Table 2.1).

For short flare durations the flux from clouds with smaller time delays is larger than the one from clouds with large time delays. By increasing the flare duration, these clouds attain comparable fluxes. This is mainly a consequence of the fact that the position of these clouds relative to the GC and the observer, determines not only their time delay but also the time it takes the ellipsoid to cross the cloud. As we have seen the velocity of the ellipsoid is smallest for clouds “behind” the GC, which are also the clouds with large time delays.

Although the times when there is no observable scattered flux shrink with increasing flare duration there are still some time gaps as shown in Figure 2.9 even for an assumed flare duration of 1.000 years. The two most pronounced time gaps lie around about 8.000 and 14.000 years. It is obvious from the observable trend in Figures 2.6 to 2.9 that by further increasing the assumed flare duration at one point the whole period of the last 40.000 years will be covered. This happens for

2 The X-ray luminosity of the Galactic centre in the recent past

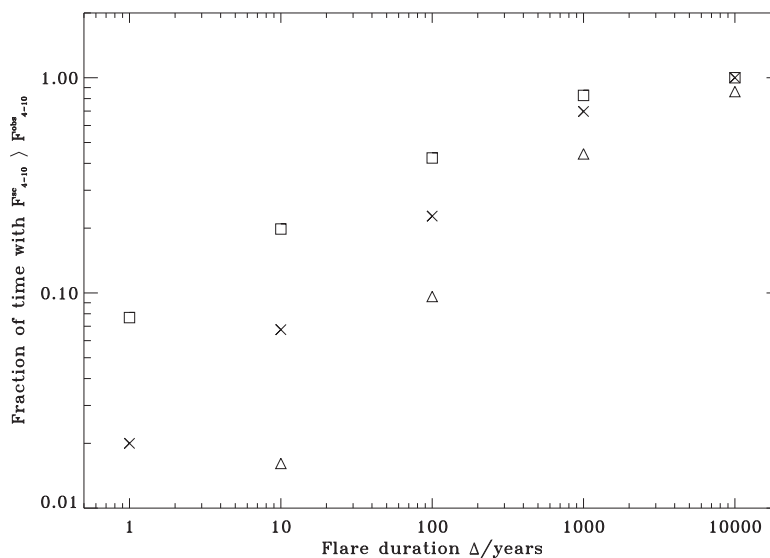


Figure 2.10: The fraction of time the scattered flux is larger than the observed upper limits during the last 40.000 years as a function of the duration of the flare for different luminosities of Sgr A*: $10^{40} \text{ erg s}^{-1}$ (triangles), $10^{42} \text{ erg s}^{-1}$ (crosses) and $3 \times 10^{44} \text{ erg s}^{-1}$ (squares). This quantity is an approximate estimate of the probability to detect a flare of duration Δ occurring during the last 40.000 years.

flare durations longer than about 3.000 years. This means that we can exclude a flare lasting longer than 3.000 years of a luminosity larger than a few $10^{42} \text{ erg s}^{-1}$ to have happened during the last 40.000 years. A similar conclusion can be drawn from Figure 2.10, where we have tried to address the question of what is the chance that there was a strong flare of duration Δ during the last 40.000 years unnoticed by us.

For the clouds from the SRBY87 sample Figure 2.10 shows the fraction of time the scattered flux was larger than the observational limits during the last 40.000 years for different flare durations. This quantity should be an approximate estimate of the probability to detect a flare as a function of flare duration Δ . The curves should be continuous but we computed them only for several durations of the flare. It is obvious that this simple estimate does not take into account the level of the scattered flux above the observational limits. From this picture we conclude that an Eddington level flare of duration longer than about 300 years occurring any time during the last 40.000 years is rather unlikely and one of duration longer than 3.000 years can be excluded. Since as mentioned above we only were able to use the data from one Galactic quadrant the values shown in Figure

2.4 Limits on the X-ray luminosity of Sgr A* from the interstellar HI distribution

2.10 should actually be regarded as lower limits to the probability.

2.4 Limits on the X-ray luminosity of Sgr A* from the interstellar HI distribution

Another major component of the ISM of the Milky Way is neutral, atomic hydrogen. Its total mass is about three times larger than that of molecular hydrogen. This is due to the larger extent of the HI disk.

As shown in the previous section our sample of GMCs is insensitive to the activity of the GC during the last 40.000 years for a few time windows, in particular two periods of 2.000 and 4.000 years duration about 8.000 and 14.000 years ago for flares of about 1.000 years duration. For shorter flare durations these temporal gaps become larger and more numerous. They are as mentioned in section 2.1 a result of the concentration of GMCs towards the molecular ring, their finite number in the Galactic disk, their finite size of about 10 pc and probably the fact that we are missing the necessary data about GMCs located in the fourth Galactic quadrant. In this respect the more continuous HI distribution is of greater value. It provides less tight limits but extends further back into the past without large gaps in the temporal coverage.

Interstellar neutral hydrogen is concentrated in clouds, which are much less massive ($\lesssim 10^4 M_\odot$) than GMCs. Their total number is thus much larger. In the model of the Galactic ISM of McKee & Ostriker (1977) the mean separation between individual HI clouds λ is of the order of 88 pc. Applied to our problem there exist two obvious limits for the response of these clouds distributed in the Galactic disk to a flare of Sgr A* depending on its duration:

- a) If the flare duration Δ is longer than the time for the ellipsoid to travel the mean distance between HI clouds, $\lambda/c \approx 290$ years, the flare scatters on a quasi continuous background medium. Because the gas is optically thin all the mass illuminated by the flare, i.e. the mass enclosed between the two ellipsoids, contributes to the scattered flux.
- b) For a flare duration shorter than the time it takes the ellipsoid to travel across the mean cloud separation we are dealing with individual clouds and the problem becomes more complex, in which each HI cloud gives some contribution to the total scattered flux.

The HI distribution is rather thin with a scale height of about 100 pc (e.g. Dickey & Lockman (1990)) for galactocentric distances smaller than R_\odot . Beyond the solar

2 The X-ray luminosity of the Galactic centre in the recent past

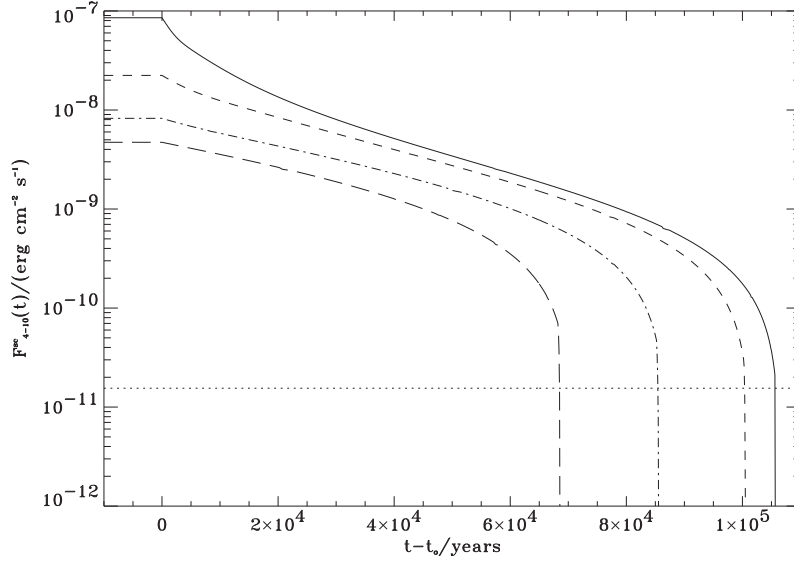


Figure 2.11: The scattered flux in the 4-10 keV range observable at a time t produced by the Galactic HI distributed along one of the *ASCA* fields of view in response to Sgr A* switching off from Eddington luminosity at a time t_0 . The different lines mark fields of view pointing at different Galactic longitudes: $\pm 10^\circ$ (solid), $\pm 30^\circ$ (dashed), $\pm 60^\circ$ (dot-dashed) and $\pm 90^\circ$ (long dashed). The observational limit for the flux in the *ASCA* field of view pointing at $l = 10^\circ$ is marked by the dotted line.

circle the HI scale height seems to increase due to a possible warp of the Galactic disk. For distances larger than $\sim R_o$ most of the disk is practically inside the *ASCA* field of view of $40'$. For our purposes it is therefore valid to neglect the distribution of HI with height above the disk and to assume the HI to be concentrated in the Galactic disk. Since the HI mass surface density is approximately constant out to a radius of 16 kpc, we assume the following profile:

$$\Sigma_{\text{HI}}(R) = \begin{cases} 4 M_\odot \text{ pc}^{-2} & R \leq R_{\text{max}} \\ 0 & R > R_{\text{max}}, \end{cases} \quad (2.23)$$

with $R_{\text{max}} = 16$ kpc. In this section we want to compute how the HI distributed in our Galaxy according to this profile responds to different types of activity of Sgr A*. The forms of activity we have in mind are:

- **Switch off:** Sgr A* was active at a level L_{Edd} up to a time t_0 and then switched off.⁴

⁴ Note that in this and in the following section t_0 marks the end of the assumed activity.

2.4 Limits on the X-ray luminosity of Sgr A* from the interstellar HI distribution

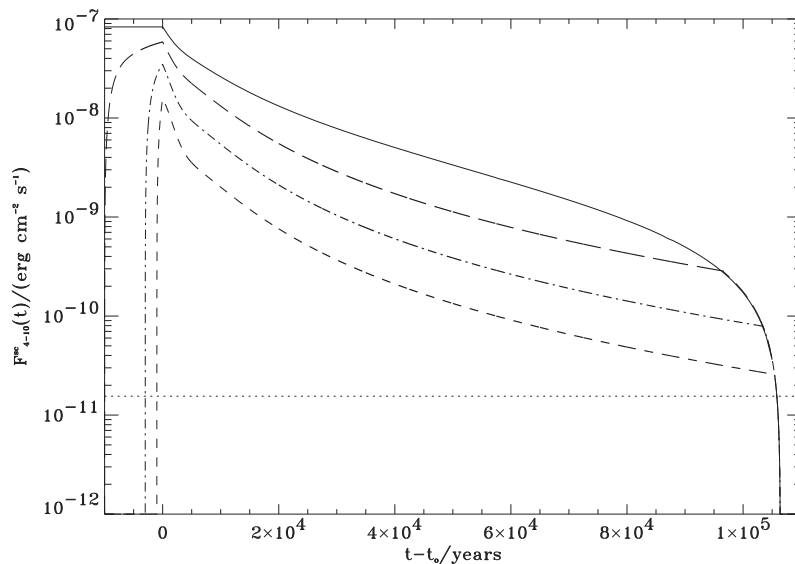


Figure 2.12: The scattered flux in the 4-10 keV range observable at a time t produced by the Galactic HI distributed along one of the *ASCA* fields of view pointing at a Galactic longitude $l = 10^\circ$ in response to Eddington flares of Sgr A* of different durations ending at a time t_0 : switch off (solid), 10,000 years (long dashed), 3,000 years (dot-dashed) and 1,000 years (dashed). The observational limit for the flux in the *ASCA* field of view pointing at 10° is marked by the dotted line.

- **Flare:** A flare lasting for a duration Δ at a level L_{Edd} ended at a time t_0 .

For the Milky Way the switch off scenario is equivalent to a “flare” with a duration longer than about 110,000 years because the whole disk out to 16 kpc would be illuminated and thus scattering in this case.

For the mass surface density profile given by Equation 2.23 the mass of hydrogen distributed along the *ASCA* beam pointing at a longitude of 10° is of the order of $2 \times 10^7 M_\odot$, which is about an order of magnitude larger than the most massive GMCs in our sample. It is therefore of no surprise that if all of this gas is illuminated, the total scattered flux will be substantially higher than in the case of a single GMC as discussed in the previous section. The maximal optical depth for Thomson scattering along an *ASCA* beam is of the order of 5×10^{-2} . The main photoelectric absorption by heavy elements should be caused by GMCs along the way. One should therefore look for an *ASCA* field not “contaminated” by a massive GMC.

In Figure 2.11 we plot the scattered flux produced at a time t by the HI dis-

2 The X-ray luminosity of the Galactic centre in the recent past

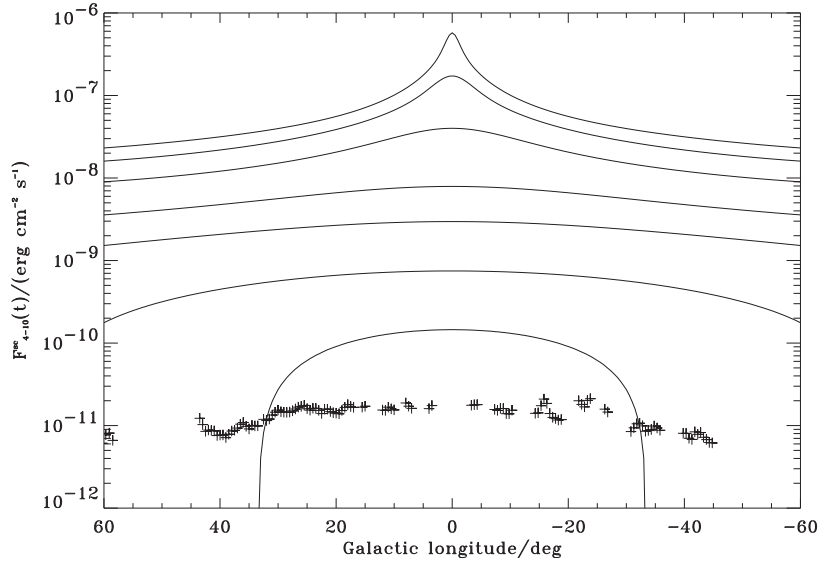


Figure 2.13: The scattered flux in the 4-10 keV range produced by the Galactic HI distributed along one *ASCA* field of view in response to Sgr A* switching off from Eddington luminosity at a time t_0 as a function of Galactic longitude l . The different lines mark the scattered flux observable at different times after the switch off of Sgr A*: 1.000, 3.000, 10.000, 30.000, 50.000, 80.000 and 100.000 years (from top to bottom). The observational *ASCA* limits are marked by crosses.

tributed along *ASCA* beams pointing at four different Galactic longitudes in response to a switch off of Sgr A* at a time t_0 . The further away one looks from the GC the less mass will be located inside the field of view. This is the main reason for the differences of the scattered fluxes for different longitudes at times before the switch off. The cutoff of the curves at late times is due to the ellipsoid leaving the disk. For larger Galactic longitudes, where the line of sight through the disk is smaller, this occurs at earlier times, e.g. for 90° this happens after about 70.000 years, whereas for 10° this happens after 100.000 years.

Figure 2.12 shows the same quantities plotted for one Galactic longitude, but for different durations of the flare. As can be taken from this figure, obviously a switch off of Sgr A* from Eddington level less than about 100.000 years ago is inconsistent with the observational limits. For a typical luminosity of an AGN hosted by a spiral galaxy of $10^{43} \text{ erg s}^{-1}$ a switch off could not have happened less than about 80.000 years ago. Remarkable about this figure is that even a flare of a duration of 1.000 years happening 100.000 years ago would produce a

2.4 Limits on the X-ray luminosity of Sgr A* from the interstellar HI distribution

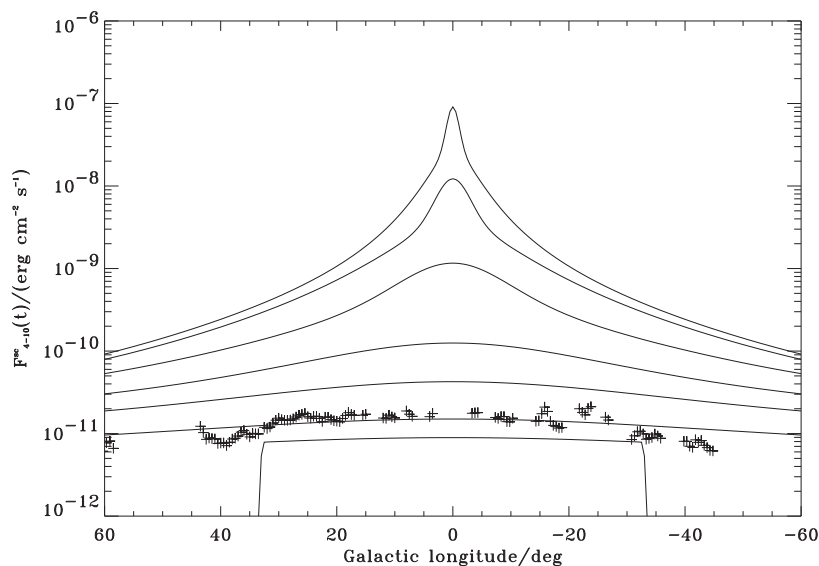


Figure 2.14: The scattered flux in the 4-10 keV range produced by the Galactic HI distributed along one *ASCA* field of view in response to an Eddington flare of Sgr A* of 300 years duration ending at a time t_0 as a function of Galactic longitude l . The different lines mark the scattered flux observable at different times after the end of the flare: 1.000, 3.000, 10.000, 30.000, 50.000, 80.000 and 100.000 years (from top to bottom). The observational *ASCA* limits are marked by crosses. It is possible for the flare to reach large longitudes because it moves with highly superluminal motion at early times.

scattered flux larger than currently observed upper limits. A similar conclusion can be drawn from the following two figures.

Figure 2.13 shows the dependence of the scattered flux in an *ASCA* field of view at different times after the end of the activity in the longitude range $-60^\circ \leq l \leq 60^\circ$. Due to our assumed axially symmetric mass surface density profile the curves are obviously symmetric in the Galactic plane about the direction towards the GC. At small longitudes the scattered flux is large because one looks through a lot of gas and also the distance of the gas to Sgr A* is smaller than for larger longitudes. The scattered fluxes are rather large, because for the switch off case the whole disk is scattering at early times after the demise of the nuclear activity. The cutoff observable for the scattered flux 100.000 years after the switch off at Galactic longitudes $|l| \gtrsim 35^\circ$ is again a result of the ellipsoid growing beyond the outer edge of the HI disk and therefore leaving no illuminated matter along that direction.

2 The X-ray luminosity of the Galactic centre in the recent past

For a shorter flare the flux will be obviously less, because only the illuminated parts of the disk will scatter the incident radiation. In Figure 2.14 we plot the expected flux for a flare of 300 years duration. As argued above flares of such a or a longer duration should scatter on a “continuous” HI background.

The dependence of the flux scattered by the Galactic HI upon Galactic longitude in response to a flare with a suitable choice of duration, time elapsed since the fading of the flare and luminosity is similar to the X-ray emission of the Galactic ridge as observed by *ASCA*. This scenario might therefore be a possible explanation for the hard component of the X-ray emission of the Galactic ridge. Under the assumption that the flare of Sgr A* had a hard enough spectrum the scattered emission might contribute to the hard component of the emission of the Galactic ridge detected above 10 keV by *RXTE* (Valinia & Marshall 1998) and *OSSE* up to energies of 600 keV (Skibo et al. 1997). There is one crucial test for this model. If we really observe scattered radiation from Sgr A* then a narrow iron K_{α} -line at 6.4 keV must be present with an equivalent width of the order of 1 keV (Vainshtein & Sunyaev 1980).

The detection of emission in the 6.7 keV line from the Galactic ridge by *Tenma* was reported by Koyama et al. (1986). This fact shows that the upper limits from *ASCA* we are using are coming from the detection of the non scattered component. The detection of the neutral iron K_{α} -line intensity in the same direction might give us much stronger limits than presented in this chapter. *XMM-Newton* is certainly able to separate the 6.4 and 6.7 keV lines much better than *Tenma*. Therefore we will get this information in the coming years and will be able to improve on the results of this chapter.

Obviously spiral arms or other large scale structures, e.g. a warp of the Galactic disk, will change the simple picture described above. Said structure would lead to increased scattering for some directions, e.g. for large column densities along spiral arms, and thereby provide additional information about these deviations from a constant disk. If for example the density contrast of HI inside and outside of spiral arms is substantial one would get an additional time dependence as the ellipsoid scans across spiral arms and the regions between them. Despite the above-mentioned possible complications we nevertheless decided to adopt the simplified density distribution given by Equation 2.23 in this section.

2.5 The Milky Way at extragalactic distances

It is well known that other spiral galaxies contain an ISM similar to the one of the Milky Way. CO and 21 cm observations have revealed the spatial distribution of H_2 and HI in many nearby spiral and irregular galaxies. M31 for example, containing

2.5 The Milky Way at extragalactic distances

a supermassive black hole of about $4.5 \times 10^7 M_{\odot}$ in its centre (see e.g. Kormendy & Gebhardt (2001)), has a HI mass similar to the one of the Milky Way, which is very concentrated in a ring at about 12 kpc from the nucleus (Sofue & Kato 1981). Although its H₂ mass is less than the one of the Milky Way it is also located in a ring at about the same radius (Nieten 2001). Since there have been and will be *Chandra* (Garcia et al. 2000) and *XMM-Newton* (Shirey et al. 2001) observations of this object, M31 might be a promising target for the methods and results presented in this section. Many other nearby spiral galaxies have been observed by *Chandra* already, e.g. M100 (Kaaret 2001), M101 (Pence et al. 2001), NGC 1068 (Young et al. 2001) and NGC 4151 (Yang et al. 2001) to name a few.

Many of these spiral galaxies also seem to harbour a supermassive black hole at their centres (Kormendy & Gebhardt 2001) with some of them demonstrating AGN activity. Spiral galaxies are believed to be the host galaxies of certain classes of AGN, in particular Seyfert I and II galaxies. The luminosities of their nuclei are typically of the order of $10^{42} - 10^{44} \text{ erg s}^{-1}$. It is therefore an interesting question to ask how interstellar gas responds to activity of the AGN and what observational signs it should produce when the AGN switches off. We want to address these questions using the methods presented in the previous sections.

To demonstrate solely the effects of scattering by a gas disk we decided not to model a specific galaxy with an observed density distribution of its neutral gas, but rather to show how the scattered emission of the Milky Way would look like at extragalactic distances. We therefore assume the same simple mass surface density profile as in the previous section (Equation 2.23).

2.5.1 Scattered X-ray surface brightness

If a galaxy is close enough to be resolved by the *Chandra* X-ray telescope then it is possible to map its scattered surface brightness as a function of position on the sky. The basic formula to compute this quantity along a given line of sight is Equation 2.11. In this section we are using the paraboloid approximation (see Sunyaev & Churazov (1998) or Section 2.1) to compute the integration boundaries $s_{\min}(t)$ and $s_{\max}(t)$. The paraboloid approximation is valid in this case given the larger distances of extragalactic objects.

In Figure 2.15 we plot the surface brightness of the scattered emission produced by a gas disk with a central, isotropic radiation source of luminosity $L_{\text{agn}} = 10^{44} \text{ erg s}^{-1}$ that turned off 10,000 years ago. The disk has an inclination of $i = 60^\circ$, with i defined as the angle between the line of sight and the normal direction of the disk. The figure shows that a part of the disk exhibits no brightness at all,

2 The X-ray luminosity of the Galactic centre in the recent past

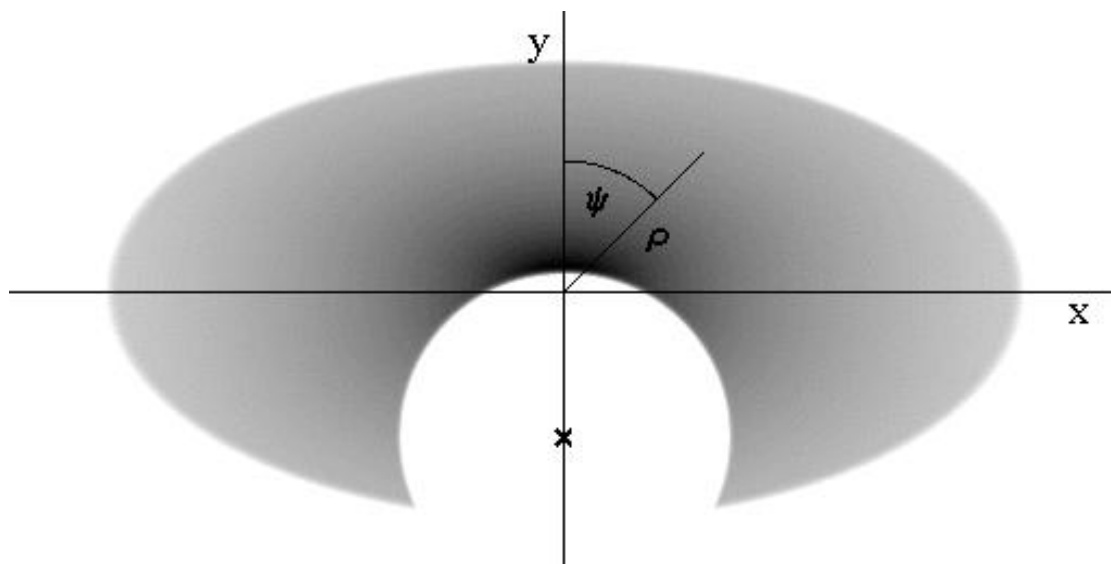


Figure 2.15: The surface brightness of the scattered emission in the plane of the sky (specified by x and y or ρ and ψ) produced by a fully illuminated gas disk of constant mass surface density 10.000 years after the central source has turned off. The inclination angle of the disk is $i = 60^\circ$. The physical radius of the disk is 16 kpc. The centre of the circle (marked by a cross) which marks the boundary between the illuminated and the not illuminated parts of the disk moves with a velocity of $1.73c$ in the direction given by $\psi = \pi$. Its radius has a size of about 6 kpc and grows with time at a rate $2c$.

because it is not illuminated anymore⁵. The boundary of this region, which is the projection of the intersection of the paraboloid at a time $t - t_o$ with the disk onto the plane of the sky, is a circle. As time progresses this boundary moves radially outwards from the nucleus with an apparent velocity

$$\dot{\rho}(\psi) = \frac{c \cos i}{1 + \cos \psi \sin i}. \quad (2.24)$$

This velocity depends upon the position angle ψ , which is defined in Figure 2.15. The maximum velocity of $c \cos i / (1 - \sin i)$ is given for $\psi = \pi$ and the minimum velocity of $c \cos i / (1 + \sin i)$ for $\psi = 0$. This “motion” has the effect that the centre of the circle (marked by a cross in Figure 2.15) moves in the direction $\psi = \pi$ while it is growing in size. The velocity of its centre is given by $v_o = (\dot{\rho}(\pi) - \dot{\rho}(0))/2 = c \tan i$, which is superluminal for inclination angles larger than

⁵Note that the “negative” of Figure 2.15 corresponds to the case 10.000 years after a switch on of the AGN.

2.5 The Milky Way at extragalactic distances

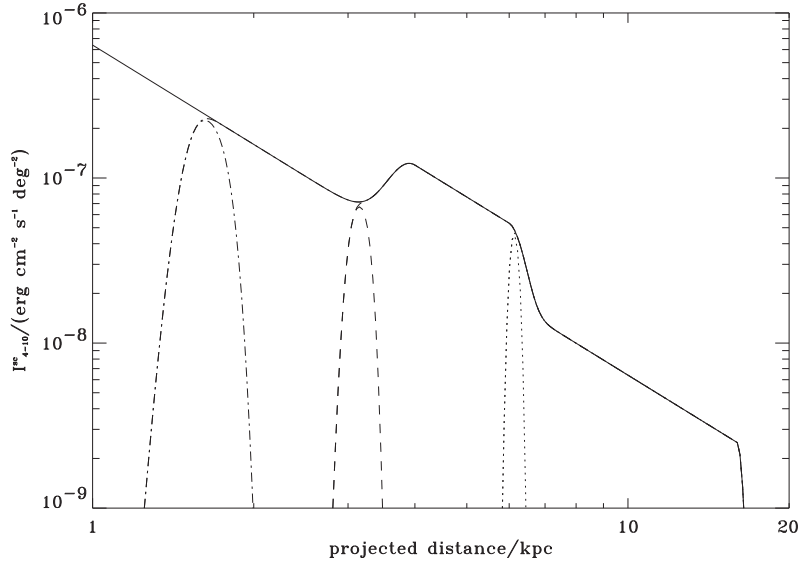


Figure 2.16: The scattered X-ray surface brightness in the 4-10 keV range as a function of projected distance from the nucleus along a fixed position angle of $\psi = \pi/2$. The solid line marks the surface brightness for the fully illuminated disk. The other lines mark the switch off (Figure 2.15) and the 1.000 year flare case (Figure 2.19) 5.000 (dot-dashed), 10.000 (dashed) and 20.000 (dotted) years after the end of the nuclear activity. The switch off case corresponds to the curves which show no brightness below a certain distance and then join on to the solution for the fully illuminated disk. The increase in surface brightness between 4 and 6 kpc is due to the molecular ring which is located at these radii. The ρ^{-2} dependence described by Equation 2.25 is visible.

45° . For an inclination of $i = 60^\circ$ this velocity is $v_o \approx 1.73c$. The radius of the circle grows with time as $ct/\cos i$.

The motion of this circle and the boundary between the illuminated and the not illuminated parts of the disk is an example of apparent superluminal motion produced by scattering on suitable shaped screens. This subject has been discussed in the literature by e.g. Blandford et al. (1977).

For a face on disk ($i = 0^\circ$) with a constant mass surface density it is easy to see from Equation 2.11 that the surface brightness drops with distance from the nucleus as $\propto \rho^{-2}$. This is still valid in the case of an inclined disk. In the limit of a uniform disk with a constant mass surface density restricted by $r = r_{\max}$ one can derive an analytic solution for the surface brightness of the illuminated parts of a disk with inclination i . It is necessary to express the factor $(1 + \cos^2 \theta_{sc})/r^2$

2 The X-ray luminosity of the Galactic centre in the recent past

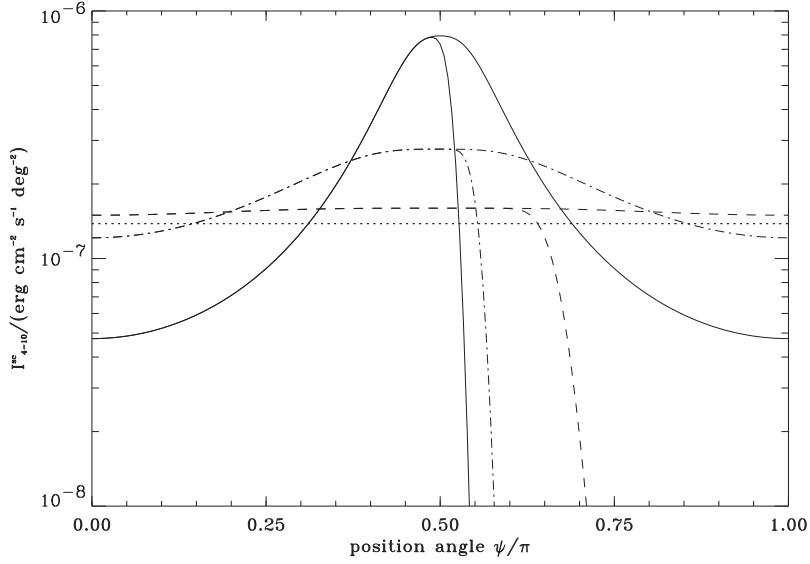


Figure 2.17: The scattered X-ray surface brightness in the 4-10 keV range as a function of position angle at a fixed projected distance of 2 kpc from the nucleus. The different lines mark different inclination angles of the disk for the fully illuminated disk and 5.000 years after switch off: $i = 0^\circ$ (dotted), $i = 30^\circ$ (dashed), $i = 60^\circ$ (dash-dotted) and $i = 80^\circ$ (solid). The switch off leads to disappearance of the illuminated region at large position angles.

appearing in Equation 2.11, where θ_{sc} is the scattering angle and r the physical distance from the nucleus, as a function of the projected radius ρ , the position angle ψ and the inclination angle i which yields

$$I_\nu = \frac{\Sigma_{HI}}{\cos i} \frac{L_{agn}}{4\pi\rho^2} \frac{3\sigma_T}{16\pi} \frac{1 + 2 \cos^2 \psi \tan^2 i}{(1 + \cos^2 \psi \tan^2 i)^2}. \quad (2.25)$$

As can be taken from Figure 2.15, the scattered surface brightness cuts off beyond a certain position angle, because these parts of the disk are not illuminated anymore by the central source. This angle is given by:

$$\psi_{max} = \arccos \left(\frac{c^2 t^2 - \rho^2}{2 c t \rho \tan i} \right). \quad (2.26)$$

Besides this more qualitative picture we present in Figures 2.16, 2.17 and 2.18 the surface brightness along several cuts of the partly illuminated disk shown in Figure 2.15. These figures confirm the validity of the above formulae, viz. Equations 2.25 and 2.26.

2.5 The Milky Way at extragalactic distances

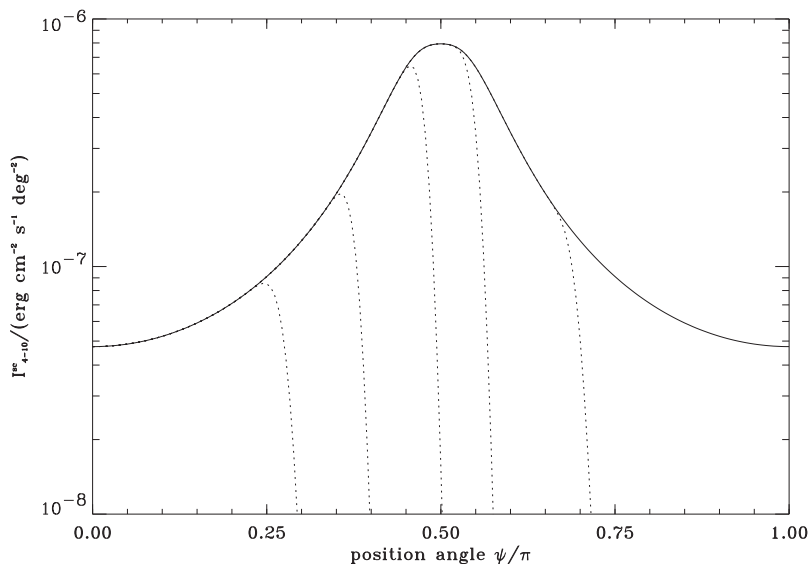


Figure 2.18: The scattered X-ray surface brightness in the 4-10 keV range as a function of position angle at a fixed projected distance of 2 kpc from the nucleus. The inclination of the disk is $i = 80^\circ$. We plot the surface brightness for the fully illuminated disk (solid line) and 1,000, 3,000, 10,000, 30,000 and 50,000 years (dotted lines from right to left) after the switch off of the central radiation source.

In Figure 2.16 we plot the scattered surface brightness as a function of projected radius ρ for a fixed position angle of $\psi = \pi/2$. The curve for the fully illuminated disk shows the ρ^{-2} dependence of the surface brightness given by Equation 2.25. Note that in this computation we have included a molecular ring with a two times larger mass surface density between about 4 and 6 kpc, which causes the bump between these radii. The surface brightness cuts off beyond the maximal disk radius of 16 kpc. Furthermore plotted in this figure are the surface brightness for the switch off (full picture given in Figure 2.15) and the flare scenario (full picture given in Figure 2.19) at different times after the end of the nuclear activity. The curves showing the surface brightness for the the flare scenario move with a velocity of about c to larger projected distances as given by Equation 2.24 for a position angle of $\psi = \pi/2$.

Figures 2.17 and 2.18 show the scattered surface brightness at a fixed projected distance of $\rho = 2$ kpc from the nucleus as a function of position angle. For clarity no molecular ring was assumed in these two plots.

In Figure 2.17 we plot the surface brightness of the scattered emission for differ-

2 The X-ray luminosity of the Galactic centre in the recent past

ent inclinations of the disk for the fully illuminated case and the switch off case. The brightness contrast for large inclination angles of the disk mainly comes about because the same projected distance at position angles $\psi = 0$ and $\psi = \pi/2$ corresponds to physical distances from the nucleus differing by a factor of $(\cos i)^{-1}$. Furthermore the average scattering angle for material at a position angle of $\psi = 0$ is $\theta_{sc} \approx \pi/2 + i$ compared to $\theta_{sc} \approx \pi/2$ for a position angle of $\psi = \pi/2$. The angular dependence of the curves presented in Figure 2.17 is well described by Equation 2.25.

Figure 2.18 shows the same quantities plotted for a disk with a large inclination of $i = 80^\circ$ at different times after the switch off of the central source. With increasing time the not illuminated part of the disk “works” its way towards smaller position angles. The angle where the brightness cuts off is given by Equation 2.26.

In Figure 2.19 we show how structure in the same disk as in the previous figures is probed by a flare of the nucleus. This case might be relevant for spiral galaxies like Andromeda, where the neutral gas is very concentrated in a ring. We map the surface brightness of the scattered emission produced by a gas disk with a 2 kpc broad molecular ring at 5 kpc, with a mass surface density two times larger than the other parts of the disk, illuminated by a flare of the central source of 1.000 years duration at different times after the end of the flare. The velocity of the light front behind (or above) the nucleus is much smaller than the superluminal one in front (or below) of the source. As time progresses the light front scans along the molecular ring. GMCs will lighten up and produce flares in response. With the spatial resolution of *Chandra* one should be able to resolve these clouds in a galaxy up to a distance of about 10 Mpc. The characteristic time of these events is rather short.

At a certain point the lower, faster light front reaches the edge of the gas disk. The “ring” will start to break up and a luminous arc travels upwards, slowly fading away as it reaches larger distances.

Obviously a flare due to the tidal disruption of a star in the nucleus with a duration of the order of a few years will produce a feature in the scattered surface brightness distribution of smaller width than the one shown in Figure 2.19. If the tidal disruption rate is large enough, of the order of $10^{-4} \text{ year}^{-1}$, one might find several of such arcs per galaxy.

2.5.2 Scattered X-ray luminosity

For a source too distant to be resolved by X-ray telescopes, the measurable quantity is the scattered flux, from which a scattered luminosity can be derived. In this section we compute the scattered luminosity of a spiral galaxy with the same neutral gas distribution as our Galaxy in response to the above assumed forms of

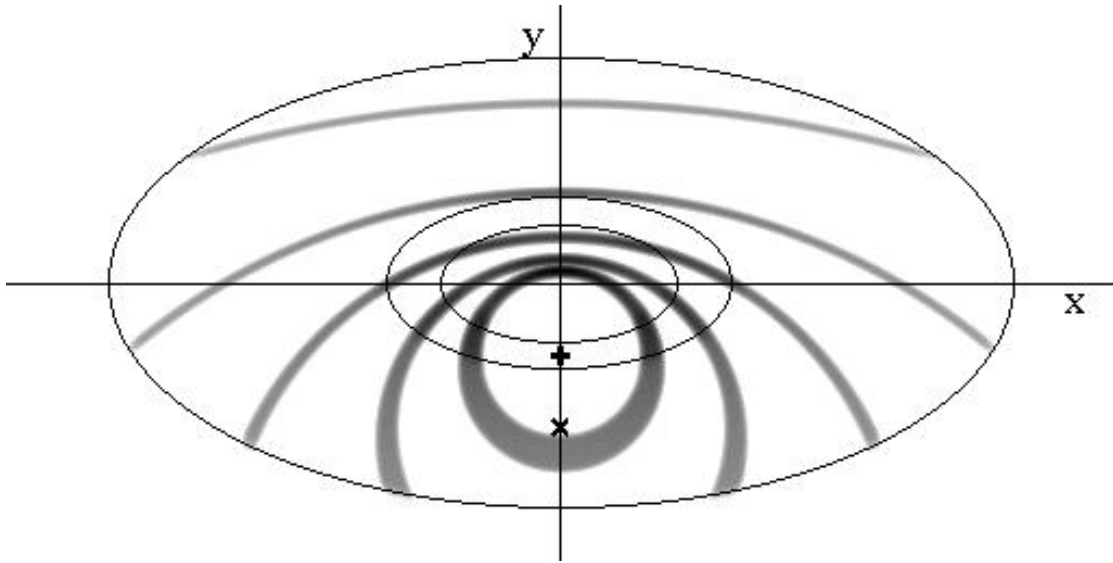


Figure 2.19: The surface brightness of the scattered emission produced by a gas disk with a 2 kpc broad molecular ring at 5 kpc illuminated by a flare of the central source of 1.000 years duration having occurred 5.000, 10.000, 20.000, 40.000 and 60.000 years ago. The edges of the gas disk at 16 kpc and the molecular ring at 4 and 6 kpc are marked by solid ellipses. The inclination angle of the disk is $i = 60^\circ$. The centres of the “rings” 5.000 and 10.000 years after the end of the flare have been marked by a plus sign and a cross. Note how with progressing time the flare scans along the molecular ring. The highest surface brightness regions, besides the one close to the nucleus, are where the flare intersects the molecular ring.

activity of its nucleus.

Figure 2.20 shows the scattered luminosity after the AGN has switched off as a function of time for different inclinations of the disk. As parameters we choose as before $L_{\text{agn}} = 10^{44} \text{ erg s}^{-1}$ and a constant HI distribution $\Sigma_{\text{HI}} = 4 M_{\odot} \text{ pc}^{-2}$ up to 16 kpc. The different luminosities for different inclinations at times $t - t_0 \leq 0$, when the whole disk is illuminated, come about because of the angular dependence of the differential scattering cross-section. For a face on disk $i = 0^\circ$ the scattering angle is obviously $\pi/2$. Because the differential cross-section for Thomson scattering is minimal for an angle of $\pi/2$ the face on disk has the smallest scattered luminosity. The much stronger differences at larger times are due to the superluminal motion of the light front. It leads to the strong effects in the low luminosity tail. Note the similarity of these curves with the ones of the scattered flux produced by the Galactic HI distribution in response to a switch off or a flare of Sgr A* (Figures 2.11

2 The X-ray luminosity of the Galactic centre in the recent past

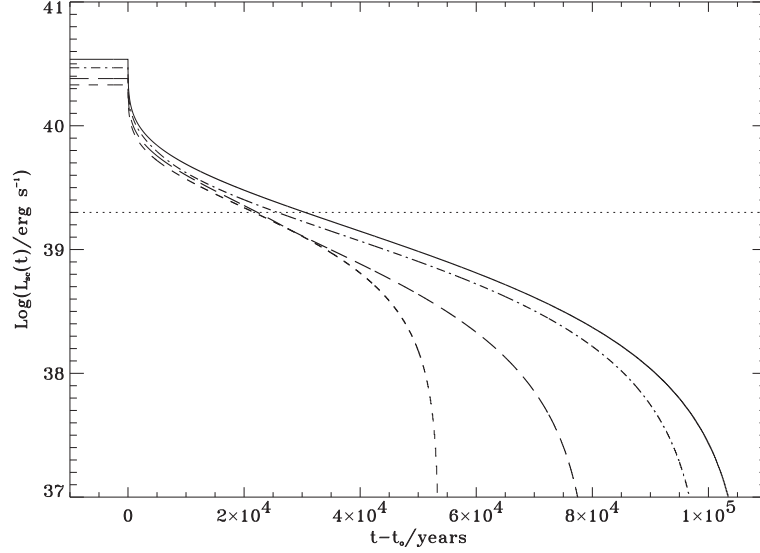


Figure 2.20: The scattered X-ray luminosity observable at a time t produced by a spiral galaxy with the HI distribution of the Milky Way in response to its central radiation source switching off at a time t_0 . The assumed luminosity of the AGN is $10^{44} \text{ erg s}^{-1}$. The different curves are for an inclination angle of the disk of 90° [edge on] (solid), 60° (dot-dashed), 30° (long dashed) and 0° [face on] (dashed). The dotted line marks the luminosity produced by the Galactic population of X-ray binaries.

and 2.12). The edge on case ($i = 90^\circ$) is similar to the case of the observer located inside the Milky Way looking at small Galactic longitudes. The X-ray binary population of the Milky Way produces a luminosity of about $2 \times 10^{39} \text{ erg s}^{-1}$ in the 2-10 keV range (Grimm et al. 2002). It will be therefore difficult to detect the scattered signal below such a limit.

For the face on disk ($i = 0^\circ$) one can derive a simple analytic solution for the scattered luminosity as a function of time. In this case the illuminated and not illuminated parts are concentric disks (switch off or switch on scenario) or annuli (flare scenario). The problem therefore is axially symmetric and the projected distance ρ is equivalent to the physical distance r from the nucleus. Imagine the disk to be made up of small mass elements $dM = \Sigma(\rho) dA = \Sigma(\rho) 2\pi\rho d\rho$. If the mass element is illuminated it contributes a fraction $dL \propto dM/\rho^2$ (Eq. 2.14) to the scattered luminosity. The total scattered luminosity at a time t is just the integral

2.5 The Milky Way at extragalactic distances

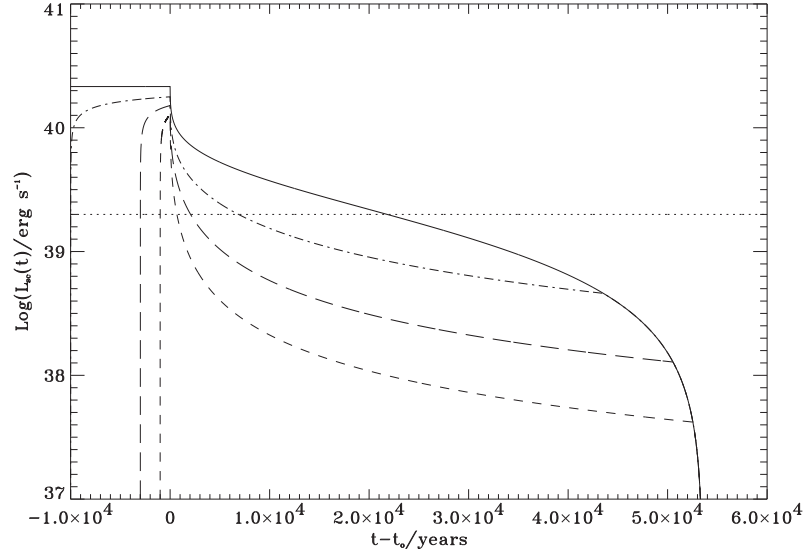


Figure 2.21: The scattered X-ray luminosity observable at a time t produced by a face on disk ($i = 0^\circ$) with the HI distribution of the Milky Way in response to flares of the central radiation source of different durations ending at a time t_0 : 1.000 years (dashed), 3.000 years (long dashed) and 10.000 years (dot-dashed). The solid line shows the switch off case. The assumed luminosity of the AGN is $10^{44} \text{ erg s}^{-1}$. The dotted line marks the luminosity produced by the Galactic population of X-ray binaries.

over all the illuminated mass elements

$$L_{\text{sc}}(t) = \int dL \propto \int_{a(t)}^{b(t)} \frac{\Sigma(\rho) d\rho}{\rho}. \quad (2.27)$$

For a constant mass surface density $\Sigma(\rho) = \Sigma_{\text{HI}}$ one obtains the simple solution

$$L_{\text{sc}}(t) = L_o^{\text{sc}} \ln \frac{b(t)}{a(t)}, \quad (2.28)$$

with

$$L_o^{\text{sc}} = 2 \times 10^{39} \text{ erg s}^{-1} \left(\frac{L_{\text{agn}}}{10^{44} \text{ erg s}^{-1}} \right) \left(\frac{\Sigma_{\text{HI}}}{4 M_\odot \text{ pc}^{-2}} \right).$$

For the face on disk the ellipsoids travel radially outward with the velocity of light and the inner and outer radius can be described as $a(t) = ct$ and $b(t) = c(t + \Delta)$ for the flare scenario. For the switch off scenario one has $b(t) = \rho_{\text{max}}$ and for the

2 The X-ray luminosity of the Galactic centre in the recent past

switch on case $a(t) = 0$. This simple analytic formula helps to understand the behaviour of the curves presented in Figure 2.21, which are the results of our numerical integration. For large times the flare solutions join with the switch off solution. This happens when only the outer parts of the disk of size corresponding to the flare duration are still scattering.

2.5.3 Fluorescent iron K_α -line luminosity

Scattering of X-rays produced by a powerful AGN is accompanied by X-ray photo absorption by heavy elements and emission in the narrow fluorescent K_α -lines. The iron K_α -line at 6.4 keV is the brightest spectral emission feature in the scattered radiation. Its equivalent width in the scattered X-ray flux is close to 1 keV for a normal cosmic abundance of iron (Vainshtein & Sunyaev 1980). The time dependence of the K_α -line luminosity should repeat that of the scattered continuum. The main difference is that scattering in the K_α -line is isotropic. The results for the K_α -line fluorescence line should therefore differ by a factor of two or less and follow similar trends as presented in the previous figures. For example if we would plot the luminosity in the K_α -line in Figure 2.20 the differences for times before the switch off would disappear and one would get the same luminosity for all disks independent of inclination. Since the narrow K_α -line originating in Galactic X-ray binaries has a very low equivalent width, observations of the fluorescent, iron K_α -line are a more promising way to detect the scattered radiation produced by a faded flare of Sgr A* or an AGN.

2.6 Discussion

In this chapter we have presented upper limits on the hard X-ray luminosity of Sgr A* in the recent past. As scattering material we have considered the molecular and neutral atomic hydrogen present in the Galactic Disk. The CO and X-ray data we had access to, have allowed us to derive limits for the 4-10 keV luminosity of Sgr A* down to about $8 \times 10^{40} \text{ erg s}^{-1}$ at specific times. For other times the limits are of the order of $10^{41} - 10^{42} \text{ erg s}^{-1}$. Now we want to briefly address a few points which demand some further discussion:

a) Anisotropy of the X-ray emission of Sgr A:*

In simulating the activity of the GC we made the assumption that the emission of Sgr A* was isotropic. Studies of AGN show that their radiation field is often anisotropic due to the presence of a relativistic jet or as a result of shielding by a molecular torus. A jet produced by Sgr A* would probably

point away from the Galactic plane. This would make our derived limits weaker.

b) *Chandra observations of the Galactic Ridge:*

Ebisawa et al. (2001) have reported the results of a deep *Chandra* observation of a Galactic plane region ($l = 28.45^\circ, b = -0.2^\circ$), which is devoid of known X-ray point sources. The total X-ray flux in the 2-10 keV range is determined to be $\sim 1.1 \times 10^{-10} \text{ erg s}^{-1} \text{ deg}^{-2}$. About ten per cent of this flux is accounted for by point sources resolved by *Chandra*. These are extragalactic sources seen through the Galactic disk. 90% of the observed flux is due to diffuse emission at the level of the sensitivity and the angular resolution of *Chandra*. This diffuse flux is within a factor of two of the ones measured by *ASCA* in nearby fields, which are of the order of $\sim 6 \times 10^{-11} \text{ erg s}^{-1} \text{ deg}^{-2}$ (Suzgizaki et al. 2001). Unfortunately none of the GMCs listed in the SRBY87 sample lies in this field, but the HI column density in this direction is about $2 \times 10^{22} \text{ cm}^{-2}$, similar to the one in the *ASCA* fields. Improvements might result from the spectral data obtained by *XMM-Newton*. If *XMM-Newton* will be able to detect the K_α -line of neutral iron in the same field this will open the possibility to separate the scattering contribution.

c) *Chandra observations of the Orion Nebula:*

The Trapezium region ($l = 209.01^\circ, b = -19.38^\circ$) of the Orion Nebula has recently been observed by *Chandra* (Schulz et al. 2001). An upper limit for the diffuse emission in the energy range 0.1-10 keV of $2 \times 10^{28} \text{ erg s}^{-1} \text{ arc sec}^{-2}$ is derived, which corresponds to a diffuse flux of $\sim 1 \times 10^{-8} \text{ erg s}^{-1} \text{ deg}^{-2}$. The distance towards the Orion nebula is $\approx 440 \text{ pc}$, corresponding to a time delay of ~ 2.400 years. The galactocentric distance of Orion is $R \sim 8.8 \text{ kpc}$. The measured H_2 column density in this direction is $3.2 \times 10^{22} \text{ cm}^{-2}$, which translates into an upper limit for the luminosity of Sgr A* of $3 \times 10^{41} \text{ ergs}^{-1}$. So GMCs in our vicinity might give comparable limits to the ones derivable from GMCs located in the molecular ring, but their time delays will be only of the order of their distances.

An obvious next step would be to apply this method to constrain the luminosity of Sgr A* in the past to GMCs and HI gas with still larger distances from the GC and thereby to extend the time coverage. However, since the scattered luminosity is proportional to M_{gas}/R^2 , there certainly will be a limit up to what distances one will obtain meaningful results using this method.

A reservoir of neutral gas which has the potential to scatter the radiation from Sgr A* at even larger distances and therefore longer time delays than galactic GMCs is the LMC. With a distance of $\sim 50 \text{ kpc}$ from the sun the time delay for

2 The X-ray luminosity of the Galactic centre in the recent past

the LMC turns out to be ~ 250.000 years. Unfortunately the data of the LMC existing in the literature does not permit to obtain interesting limits upon the X-ray luminosity of Sgr A*. We should therefore wait for *XMM-Newton* observations of the iron K_α -line in the direction towards massive gas complexes in the LMC.

*I would like to know the stars again as the Chaldeans
knew them, two thousand years before Christ.*

D. H. Lawrence, “Apocalypse”

3

Constraining the past X-ray luminosity of AGN in clusters of galaxies

Abstract

Only a small fraction of the galactic nuclei in the nearby universe are luminous; most of them are currently dim. We investigate the feasibility of constraining the X-ray luminosity in the recent past (up to $\sim 10^6$ years ago) of the nucleus of a cluster dominant galaxy by measuring the contribution of scattered radiation from the central source to the surface brightness of the intracluster gas dominated by thermal emission. We show that resonance X-ray lines present an advantage over the adjacent continuum, because the relative contribution of the scattered component is typically larger in the line case by a significant factor of 3–10. As an example, we estimate the level of constraint that could be derived from future fine spectroscopic observations on the past X-ray luminosity of the nearby M87 and Cygnus A active galaxies. For instance, scattered line radiation should be detectable from the Virgo cluster if the X-ray luminosity of M87 was a few times 10^{44} erg s $^{-1}$, or 10^{-3} of its Eddington luminosity, until a few times 10^5 years ago. For comparison, upper limits inferred from the available *XMM-Newton* and *Chandra* X-ray continuum data are typically 1–2 orders of magnitude weaker. The same method can be applied to distant powerful quasars (at redshifts $z \gtrsim 1$) if they have cluster-like gaseous coronae, as suggested by *Rosat* and *Chandra*

3 Constraining the past X-ray luminosity of AGN in clusters of galaxies

observations of active galaxies at $z \lesssim 1$. Their surface brightness profiles in the X-ray continuum above $\sim 10 \text{ keV} \gg kT/(1+z)$ (where T is the gas temperature) should be dominated by redshifted scattered radiation from the quasar. Therefore, measurements with forthcoming mirror-optics hard X-ray telescopes could give information on the lifetime of quasars and parameters of the hot gas around them.

3.1 Introduction

It is commonly believed that active galactic nuclei (AGN) are powered by accretion onto a supermassive black hole. However, a detailed description of this process is still missing. One of the principal obstacles to making progress here is that we know very little from observations about the variability of AGN on timescales longer than a few tens of years.

Nuclear variability on the longest timescales up to the Hubble time is expected to be governed by the supply of gas from galactic scales to the central kpc. Such transport can be triggered by mergers and interactions of galaxies (e.g. Hernquist (1989)). There are reasons to believe that AGN can be strongly variable on timescales much shorter than the Hubble time. For example, Ciotti & Ostriker (1997, 2001), in a follow-up to Binney & Tabor (1995), have suggested a mechanism for elliptical galaxies in which an accreting central black hole heats the ambient gas to the point at which the accretion stops, then fuelling resumes after the gas has cooled. In this model, strong outbursts during which the AGN luminosity approaches the Eddington critical value can occur every $10^8 - 10^9$ years. A similar outburst behaviour but on shorter timescales of typically 10^6 years can result from thermal-viscous instability expected to operate in AGN accretion disks (Lin & Shields 1986; Mineshige & Shields 1990; Siemiginowska et al. 1996; Burderi et al. 1998). We may also mention tidal disruption of stars by supermassive black holes, which can give rise to rare (every $10^4 - 10^5$ years per galaxy), short (months to years) and bright (sub-Eddington) flares (Rees 1988).

Since we are unable to explore directly the long-term variability of galactic nuclei, some indirect methods are in need. A feasible way would be to observe radiation which was emitted in the past by a galactic nucleus and later scattered toward us by the interstellar medium. Since the characteristic size of a galaxy is a few tens kpc, we could see the “echo” of previous AGN activity $\sim 10^5$ years after the central source turned off. This idea has been put forward by Sunyaev et al. (1993) in relation to our Galaxy. It was suggested that the diffuse, hard X-ray emission observed today in the direction of giant molecular complexes in the central 100 pc of the Milky Way is scattered radiation emitted by Sgr A* in

the past. This hypothesis has been confirmed by the detection with the *ASCA* and *Chandra* satellites of diffuse emission in the 6.4 keV fluorescence iron line from the Sgr B2 cloud (Koyama et al. 1996; Murakami et al. 2001a). Cramphorn & Sunyaev (2002) have recently elaborated on this problem and derived upper limits on the X-ray luminosity of Sgr A* during the past 10^5 years (see chapter 2).

It seems natural to extend the above approach to elliptical galaxies and in particular to cluster dominant galaxies. Recent observations with the Hubble Space Telescope and ground-based telescopes have confirmed previous suggestions that (i) powerful low-redshift ($z < 0.5$) AGN are found in luminous and preferentially early-type galaxies (Bahcall et al. 1997; Hooper et al. 1997; Boyce et al. 1998; McLure et al. 1999; Schade et al. 2000) and (ii) they are generally located in cluster environments (McLure & Dunlop 2001). Since cluster cores typically have sizes $r_c \sim 100$ kpc, we could hope to detect radiation emitted by the nucleus (plus possibly by a jet) of a cluster dominant galaxy until a few times $r_c/c \sim 10^6$ years ago and scattered by the hot intracluster gas toward us. Up to $\sim 1\%$ of the radiation of the central source can be Thomson scattered by free electrons within the gas.

Previous theoretical efforts in this direction have focused on the prospects for detecting scattered (strongly polarised) AGN radiation at radio and optical wavelengths (Sunyaev 1982; Gilfanov et al. 1987a; Sholomitskii & Yaskovich 1990; Wise & Sarazin 1990a,b; Sarazin & Wise 1993; Murphy & Chernoff 1993). However, it would be particularly interesting to get information on the history of the central source from observations of X-ray scattered radiation, since the bulk of the AGN X-ray emission is believed to originate within a few gravitational radii of the central black hole.

One feasible way to detect the scattered X-rays against the thermal emission of the hot gas would be to perform observations at $E \gg kT$, where E is the photon energy and $kT \sim 1\text{--}10$ keV is the gas temperature. Indeed, the AGN spectrum is a power-law, $F_{\text{AGN}} \propto E^{-\alpha}$ with $\alpha \sim 1$, while the plasma bremsstrahlung spectrum is exponentially declining, $F_{\text{gas}} \propto \exp(-E/kT)$, at $E \gg kT$. Unfortunately, the angular resolution and sensitivity of present-day hard X-ray telescopes are not sufficient for mapping clusters of galaxies and detecting scattered AGN radiation. However, the situation may improve dramatically with the advent of grazing incidence X-ray telescopes sensitive up to ~ 40 keV, such as those under consideration for the projected *Constellation-X*¹ and *XEUS*² missions. Furthermore, given the huge collecting area (several square meters) of these planned telescopes in the standard X-ray band, it should become possible to search for scattered X-rays from distant quasars (at redshifts $z \gtrsim 1$). Indeed, since the ra-

¹<http://constellation.gsfc.nasa.gov/docs/main.html>

²http://astro.esa.int/SA-general/Projects/XEUS/main/xeus_main.html

3 Constraining the past X-ray luminosity of AGN in clusters of galaxies

diation from a quasar gets redshifted on its way to us, a significant gain in the ratio $F_{\text{AGN}}/F_{\text{gas}} \propto [E(1+z)]^{-\alpha} \exp[E(1+z)/kT]$ could be achieved already at $E \sim 10$ keV. Such observations would permit one to constrain the lifetime of quasars and the parameters of the hot gas around them. This possibility is one of the issues discussed in the present chapter (particularly in section 3.3.2).

On the observational side, evidence has been accumulated over recent years that AGN are often surrounded by gas atmospheres typical of clusters of galaxies. Early ROSAT observations indicated the presence of luminous extended X-ray emission around several powerful quasars with redshifts out to $z = 0.73$ (Crawford et al. 1999; Hardcastle & Worrall 1999). More recently, the *Chandra* observatory clearly resolved extended hot gas around several relatively nearby AGN, including 3C295 ($z = 0.461$, Harris et al. (2000a)), 3C220.1 ($z = 0.62$, Worrall et al. (2001)), 3C123 ($z = 0.2177$, Hardcastle et al. (2001)), Cyg A ($z = 0.0562$, Smith et al. (2002)), and H1821+643 ($z = 0.297$, Fang et al. (2002)).

Chandra has also detected luminous extended (to radii ~ 100 kpc) X-ray emission surrounding two high-redshift powerful radio galaxies 3C294 at $z = 1.786$ (Fabian et al. 2001) and PKS 1138–262 at $z = 2.156$ (Carilli et al. 2002). Assuming for these objects that the emission of the central source is isotropic and its X-ray luminosity has been the same in the past as it is now (\sim a few 10^{45} erg s^{-1}), we are able to estimate (see section 3.3.2) that the gas surface brightness should be dominated by scattered power-law radiation from the AGN already at $E \gtrsim 10$ keV.

In this chapter we also discuss another possibility of detecting scattered AGN X-ray radiation. We will show in sections 3.2 and 3.3.3 that at least for nearby AGN located in cluster dominant galaxies or in isolated giant elliptical galaxies, one can gain significantly by measuring the scattered surface brightness in resonance X-ray lines rather than in the continuum. Such observations would ideally require high (\sim a few eV) spectral resolution in order to separate the resonance lines from other lines. The resolution needed together with high sensitivity can be achieved with future high-energy astrophysics observatories such as *Astro-E2*³, *Constellation-X* and *XEUS*. As an example, we estimate (in section 3.4) the level of constraints it should be possible to derive on the past X-ray luminosity of the nearby M87 and Cyg A active galaxies. Yet better constraints could be obtained by measuring the polarisation of the scattered X-ray resonance line radiation (see section 3.5).

³<http://www.astro.isas.ac.jp/astroe/index-e.html>

3.2 Advantage of scattered X-ray lines over the scattered continuum

Consider an AGN surrounded by hot ($T \gtrsim 10^7$ K) gas. The following emission components will contribute to the X-ray surface brightness of the gas:

- First, there is X-ray emission (line plus continuum) of the hot plasma in which collisional ionisation and excitation dominate. However, a bright AGN may additionally photoionize the plasma. In our calculations below we fully neglect this effect, although it can be important when the AGN luminosity is very high, i.e. quasar-like.
- Second, there is radiation emitted by the AGN and Thomson scattered by free electrons in the gas. This scattered radiation contributes to the surface brightness in the spectral continuum.
- Finally, AGN photons with energies falling within the cores of X-ray lines of ions of heavy elements can resonantly scatter on these ions, thus contributing to the surface brightness in the lines.

Consider an optically thin volume of gas with electron temperature T and number density n_e , exposed to an external spectral flux $F_E(E)$ (measured in units of $\text{erg cm}^{-2} \text{s}^{-1} \text{keV}^{-1}$).

The plasma continuum spectral emissivity due to bremsstrahlung is given by (e.g. Zombeck (1990))

$$\epsilon_{E,\text{cont}}(E) = 2.3 \times 10^{-20} T^{-1/2} \exp(-E/kT) n_e^2 g_B(T, E) \quad (\text{erg cm}^{-3} \text{s}^{-1} \text{keV}^{-1}), \quad (3.1)$$

where g_B is the corresponding Gaunt factor.

The energy-integrated emissivity in a resonance line by ions of type z due to electron collisional excitation of an electron from the ground level i to an excited level k is given by (e.g. Zombeck (1990))

$$\begin{aligned} \epsilon_{\text{line}} &= 2.7 \times 10^{-15} T^{-1/2} \exp(-E_{ik}/kT) \\ &\times n_e n_z(T) f_{ik} g_{ik}(T) \quad (\text{erg cm}^{-3} \text{s}^{-1}), \end{aligned} \quad (3.2)$$

where n_z is the ion number density, which depends on the gas temperature. The remaining quantities appearing in equation (3.2), namely E_{ik} , f_{ik} and g_{ik} , characterise the line itself, denoting its energy, oscillator strength and excitation Gaunt factor, respectively.

3 Constraining the past X-ray luminosity of AGN in clusters of galaxies

The rate (per unit volume) of Thomson scattering of the external radiation, integrated over the scattering angle θ , is

$$\begin{aligned}\epsilon_{E,\text{cont}}^{\text{scat}}(E) &= \frac{3}{8} \int_{-1}^1 d \cos \theta (1 + \cos^2 \theta) \epsilon_{E,\theta,\text{cont}}^{\text{scat}}(E, \theta) \\ &= F_E(E) n_e \sigma_T \text{ (erg cm}^{-3} \text{ s}^{-1} \text{ keV}^{-1})\end{aligned}\quad (3.3)$$

where $\sigma_T = 6.65 \times 10^{-25}$ is the Thomson scattering cross section. Note that we ignore throughout the Klein–Nishina correction to the scattering cross section as well as the change in the photon energy by scattering, which is justifiable if $E \ll mc^2$ and $kT \ll mc^2$, where $mc^2 = 511$ keV is the electron rest energy.

The energy-integrated rate of resonant scattering (integrated over the scattering angle) of the external radiation in the line $i \rightarrow k$ by ions z is

$$\begin{aligned}\epsilon_{\text{line}}^{\text{scat}} &= 4.1 \times 10^{-18} \pi \\ &\times F_E(E_{ik}) n_z(T) r_e c f_{ik} \text{ (erg cm}^{-3} \text{ s}^{-1}),\end{aligned}\quad (3.4)$$

where $r_e = 2.82 \times 10^{-13}$ cm is the classical electron radius, c is the speed of light, and the numerical coefficient accounts for the unit transition from Hz to keV.

From equations (3.1) and (3.3) we can find the ratio of the Thomson scattering rate to the bremsstrahlung emissivity:

$$\begin{aligned}\frac{\epsilon_{E,\text{cont}}^{\text{scat}}}{\epsilon_{E,\text{cont}}}(E) &= 2.9 \times 10^{-5} \\ &\times F_E(E) T^{1/2} \exp(E/kT) n_e^{-1} g_B^{-1}(T, E).\end{aligned}\quad (3.5)$$

The ratio of the resonant scattering rate to the emissivity in the line $i \rightarrow k$ is given by a similar expression, which follows from equations (3.2) and (3.4),

$$\begin{aligned}\frac{\epsilon_{\text{line}}^{\text{scat}}}{\epsilon_{\text{line}}} &= 4.1 \times 10^{-5} \\ &\times F_E(E_{ik}) T^{1/2} \exp(E_{ik}/kT) n_e^{-1} g_{ik}^{-1}(T).\end{aligned}\quad (3.6)$$

We can now compare the ratios (3.6) and (3.5) for $E = E_{ik}$:

$$R \equiv \frac{\epsilon_{\text{line}}^{\text{scat}}}{\epsilon_{\text{line}}} / \frac{\epsilon_{E,\text{cont}}^{\text{scat}}}{\epsilon_{E,\text{cont}}} = 1.4 \frac{g_B(T, E_{ik})}{g_{ik}(T)}.\quad (3.7)$$

In the low-temperature limit ($kT \ll E_{ik}$), the excitation Gaunt factor g_{ik} ranges between 0.1 and 0.25 for most interesting lines; it slowly increases with temperature and reaches 0.2–0.3 at $kT \sim E_{ik}$ (e.g. Mewe et al. (1985)). The bremsstrahlung

3.2 Advantage of scattered X-ray lines over the scattered continuum

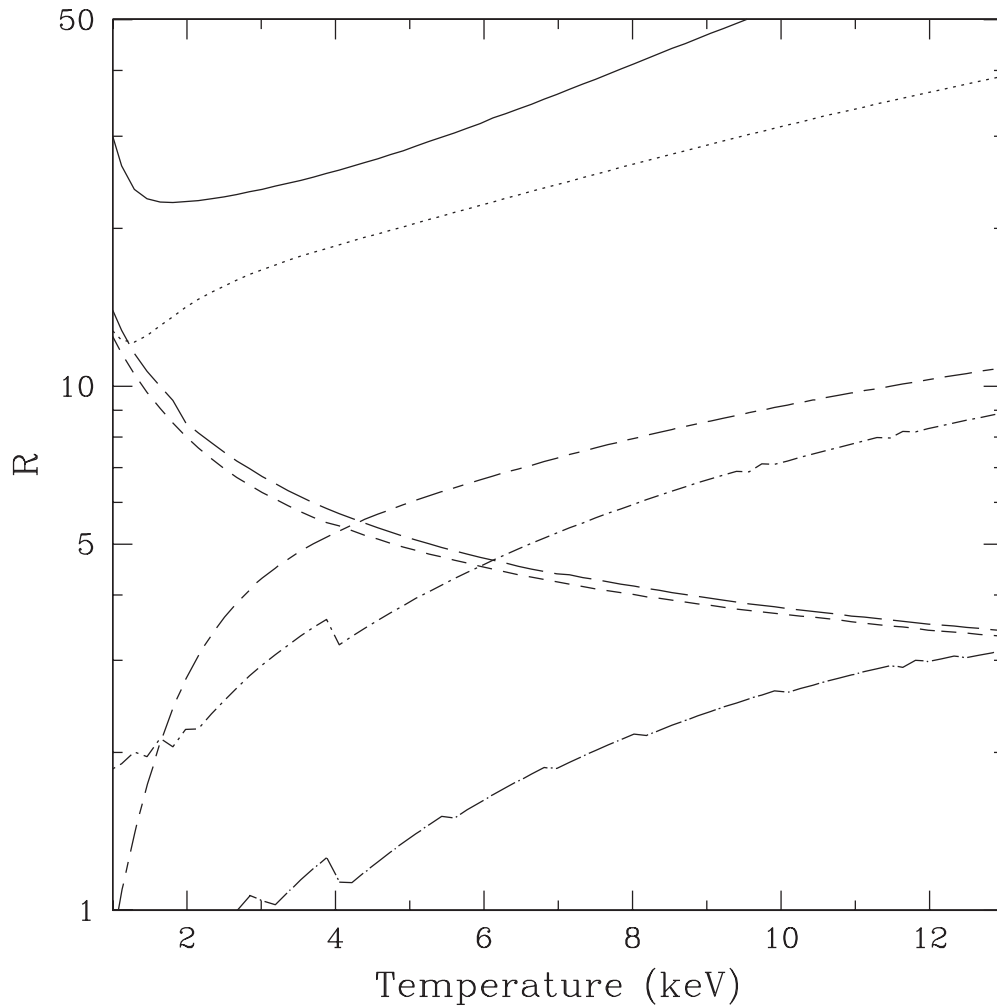


Figure 3.1: Ratio R defined by Eq. 3.7 as a function of plasma temperature for various resonance X-ray lines: Fe XXIII L-shell line at 1.13 keV (solid), Fe XXIV L-shell line at 1.17 keV (dotted), Si XIII $K\alpha$ line at 1.86 keV (short-dashed), S XV $K\alpha$ line at 2.46 keV (long-dashed), Fe XXV $K\alpha$ line at 6.70 keV (dot-short-dashed), Fe XXVI $Ly\alpha$ line at 6.97 keV (dot-long-dashed), and Fe XXV $K\beta$ line at 7.88 keV (short-dash-long-dashed).

3 Constraining the past X-ray luminosity of AGN in clusters of galaxies

Gaunt factor also is a weak function of temperature: $g_B = (kT/E)^{0.4}$ when $E \sim kT$. Summarising these facts, we may simply write

$$R \sim 6 \text{ for } kT \sim E_{ik}. \quad (3.8)$$

This approximate relation is accurate to within a factor of 3 for all resonance X-ray lines of interest to us. Fig. 3.1 shows, for several resonance lines, the dependence $R(T)$ computed using the MEKAL plasma emission code in combination with other atomic data sources (see section 3.4 for details). In these computations the contribution to ϵ_{line} of unresolved (defined as those with energies within one Doppler width of the resonance energy) satellite lines was taken into account. This effectively leads to a smaller value of R compared to the definition (3.7). However, this reduction is only significant for the 6.70 keV and 6.97 keV $K\alpha$ lines of iron when $kT \ll E_{ik}$. We should note that the large values ($R \sim 20$ at $kT \sim E_{ik}$) obtained for the iron L-shell lines at 1.13 keV and 1.17 keV may be partly the result of the different values for the oscillation strengths being used in the MEKAL code with which we compute ϵ_{line} and in the list of resonance lines of Verner et al. (1996) which we use to compute $\epsilon_{\text{line}}^{\text{scat}}$. We do not attempt in this chapter to correct for this and possibly other inconsistencies caused by the simultaneous use of several sources of atomic data. However, we estimate that some of our computational results obtained in section 3.4 below may contain a relative systematic error of $\lesssim 2$.

We point out that R is typically several times smaller for intercombination lines than for resonance lines and $R \approx 0$ for forbidden lines. For this reason we consider only resonance lines throughout.

We have thus found that for a given resonance line with energy E_{ik} , the relative contribution of scattered external radiation to the volume X-ray emissivity of hot gas is typically larger by a significant factor of the order of 3–10 than for the continuum at E_{ik} . We also know that for typical cluster temperatures $kT \sim$ a few keV the combined surface brightness of the intracluster gas in the resonance X-ray lines with $E_{ik} \sim kT$ is comparable to that in the continuum. We therefore arrive at the conclusion that resonance X-ray lines present a significant advantage over the continuum for searches of scattered AGN radiation in clusters of galaxies and elliptical galaxies performed at $E \sim kT$.

After we have introduced the R factor in equation (3.7) and shown that this factor is only weakly dependent on the resonance line and on gas temperature, we can continue our treatment in parallel for continuum and line emission.

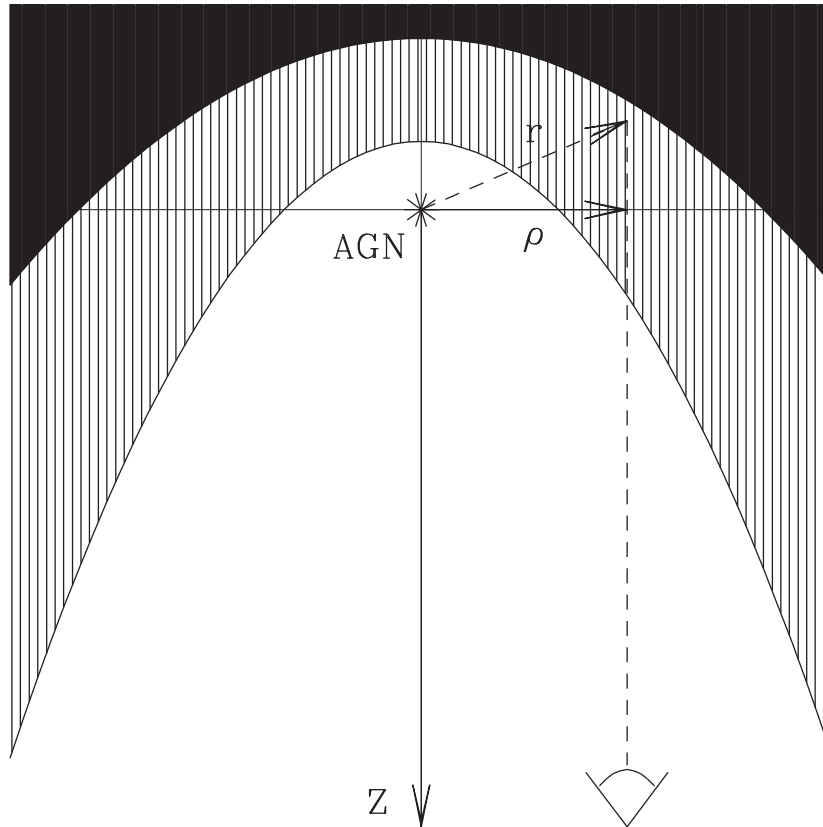


Figure 3.2: Sketch of the model. The points with equal travel time from the AGN to the observer lie on a paraboloid. In the switch-off case, the thermal plasma located in the grey and black regions is scattering the radiation emitted by the AGN. In the case of a flare of the AGN, only the grey area is filled by photons and contributing to the scattered emission. A possible path for a photon scattered into the line of sight of the observer is marked by a dashed line. The system is rotationally symmetric about the z-axis.

3.3 AGN in the centre of a beta-cluster

We shall now consider the following model (see Fig. 3.2). A supermassive black hole is located in the centre of a cluster of galaxies containing hot gas with a beta-law radial density profile (Cavaliere & Fusco-Femiano 1976):

$$n_e = n_0(1 + r^2/r_c^2)^{-3\beta/2}, \quad (3.9)$$

where n_0 is the central electron number density and r_c is the core-radius. The gas temperature T and element abundances are constant over the cluster.

At a moment $t_{\text{on}} = -\Delta$ (as measured by an earth bound observer) the central source switches on (i.e. becomes an AGN) and at a later moment $t_{\text{off}} = 0$ it switches off. The AGN emits isotropically X-ray radiation having a power-law spectrum of photon index γ , at a constant luminosity L_X in the energy band $[E_1, E_2]$:

$$L_X = A \int_{E_1}^{E_2} E^{-\gamma} E dE = A \frac{E_2^{2-\gamma} - E_1^{2-\gamma}}{2 - \gamma}. \quad (3.10)$$

The spectral flux at a given distance r from the AGN is therefore

$$F_E = \frac{(2 - \gamma)L_X}{4\pi(E_2^{2-\gamma} - E_1^{2-\gamma})r^2} E^{1-\gamma}. \quad (3.11)$$

Our goal is to find the surface brightness profile of the cluster, including the contribution of scattered AGN radiation, at a given moment of time $t > t_{\text{on}}$.

3.3.1 Approximation of isotropic scattering

We shall use throughout this chapter the approximation of isotropic scattering. This simplifies the treatment but requires explanation. We know that in reality Thomson scattering occurs according to the Rayleigh phase function $p(\cos\theta) = 3(1 + \cos^2\theta)/8$. In the case of resonant scattering, the phase function depends on the line and generally can be represented as a weighted sum of the Rayleigh phase function and the isotropic function $p(\cos\theta) = 1/2$ (see e.g. Chandrasekhar (1950)). However, for our given geometry of the problem the resulting brightness profiles depend only weakly (typically by less than 10%) on the phase function. For this reason, the approximation of isotropic scattering is quite reasonable.

3.3.2 Continuum radiation

We shall first consider the X-ray spectral continuum, for which the relevant scattering mechanism is Thomson scattering. Since the Thomson optical depths of

3.3 AGN in the centre of a beta-cluster

clusters of galaxies and elliptical galaxies are small, $\tau_T \lesssim 0.01$, we can use the single-scattering approximation and make some analytic estimates.

The continuum (bremsstrahlung) surface brightness of a beta-cluster is described, as a function of projected distance ρ from the nucleus, by the well-known formula, which can be obtained by integrating the plasma emission along a given line of sight (i.e. along the coordinate z – see Fig. 3.2) using equations (3.1) and (3.9):

$$\begin{aligned}
 B_{E,\text{cont}} &\equiv \int_{-\infty}^{\infty} \frac{\epsilon_{E,\text{cont}}(r)}{4\pi} dz \\
 &= 2.9 \times 10^{-5} \frac{\Gamma(3\beta - 1/2)}{\Gamma(3\beta)} \left(\frac{n_0}{0.01 \text{ cm}^{-3}} \right)^2 \frac{r_c}{100 \text{ kpc}} \\
 &\times \left(\frac{kT}{1 \text{ keV}} \right)^{-1/2} (E/kT)^{-0.4} \exp(-E/kT) \\
 &\times (1 + \rho^2/r_c^2)^{-3\beta+1/2} \\
 &\quad (\text{erg cm}^{-2} \text{ s}^{-1} \text{ sr}^{-1} \text{ keV}^{-1}), \tag{3.12}
 \end{aligned}$$

where $r = (\rho^2 + z^2)^{1/2}$ and we have adopted $g_B(T, E) = (E/kT)^{-0.4}$.

The surface brightness of the Thomson scattered AGN radiation is given by

$$B_{E,\text{cont}}^{\text{scat}} \equiv \int_{z_1}^{z_2} \frac{\epsilon_{E,\text{cont}}^{\text{scat}}(r)}{4\pi} dz = \frac{\sigma_T}{4\pi} \int_{z_1}^{z_2} F_E(r) n_e(r) dz, \tag{3.13}$$

where we have used equation (3.3) and our assumption of isotropic scattering.

The time-dependent integration limits $z_1(t, \rho)$ and $z_2(t, \rho)$ in equation (3.13) are determined by the loci of scattering sites giving a fixed time delay \tilde{t} . If the distance between the emitter and the observer is much larger than the characteristic size of the scattering cloud, which is true in our case, the constant-delay surface is a paraboloid with its focus at the position of the source (see e.g. Sunyaev & Churazov (1998) and references therein to earlier work considering similar light-echo problems):

$$z(\tilde{t}, \rho) = \frac{1}{2} \left(\frac{\rho^2}{c\tilde{t}} - c\tilde{t} \right). \tag{3.14}$$

Therefore,

$$z_1(t, \rho) = \frac{1}{2} \left[\frac{\rho^2}{c(t + \Delta)} - c(t + \Delta) \right], \tag{3.15}$$

$$z_2(t, \rho) = \begin{cases} (\rho^2/ct - ct)/2 & \text{if } 0 < t \\ \infty & \text{if } -\Delta < t < 0. \end{cases} \tag{3.16}$$

The integration limits in equation (3.13) depend on the outburst duration Δ . We shall first consider two limiting cases for which an analytic treatment is possible.

3 Constraining the past X-ray luminosity of AGN in clusters of galaxies

3.3.2.1 Stationary case

Let the AGN be a persistent source. The limits of the integral $\int_{z_1}^{z_2} \epsilon_{E,\text{cont}}^{\text{scat}} dz$ are then $z_1(t, \rho) = -\infty$ and $z_2(t, \rho) = \infty$, and it is possible, using equation (3.9) for $n_e(r)$ and equation (3.11) for F_E , to express the integral through hypergeometric functions. In the particular interesting case of $\beta = 2/3$, the scattered surface brightness is

$$B_{E,\text{cont}}^{\text{scat}}(\beta = 2/3) = 6.0 \times 10^{-5} \frac{L_X}{L_{\text{Edd}}} \frac{M_{\text{BH}}}{10^9 M_\odot} \frac{n_0}{0.01 \text{ cm}^{-3}} \\ \times \frac{100 \text{ kpc}}{r_c} \frac{2 - \gamma}{10^{2-\gamma} - 1} \left[r_c/\rho - (1 + \rho^2/r_c^2)^{-1/2} \right] E^{1-\gamma} \\ (\text{erg cm}^{-2} \text{ s}^{-1} \text{ sr}^{-1} \text{ keV}^{-1}), \quad (3.17)$$

where M_{BH} is the mass of the central black hole, $L_{\text{Edd}} = 1.4 \times 10^{38} M_{\text{BH}}/M_\odot$ is the corresponding Eddington luminosity, L_X is the AGN luminosity in the energy range 1–10 keV, and E is measured in keV.

The ratio of the scattered surface brightness to the intrinsic surface brightness of the gas in the continuum is

$$\frac{B_{E,\text{cont}}^{\text{scat}}}{B_{E,\text{cont}}}(\beta = 2/3) = 2.3 \frac{L_X}{L_{\text{Edd}}} \frac{M_{\text{BH}}}{10^9 M_\odot} \frac{0.01 \text{ cm}^{-3}}{n_0} \\ \times \left(\frac{100 \text{ kpc}}{r_c} \right)^2 \left(\frac{kT}{1 \text{ keV}} \right)^{0.1} \frac{2 - \gamma}{10^{2-\gamma} - 1} \\ \times (1 + \rho^2/r_c^2)^{3/2} \left[r_c/\rho - (1 + \rho^2/r_c^2)^{-1/2} \right] \\ \times E^{1.4-\gamma} \exp(E/kT). \quad (3.18)$$

We can also write down asymptotic expressions applicable in the limit of $\rho \gg r_c$ for arbitrary values of β :

$$B_{E,\text{cont}}^{\text{scat}}(\rho \gg r_c) = 3.2 \times 10^{-5} \frac{\Gamma(3\beta/2 + 1/2)}{\Gamma(3\beta/2 + 1)} \frac{L_X}{L_{\text{Edd}}} \frac{M_{\text{BH}}}{10^9 M_\odot} \\ \times \frac{n_0}{0.01 \text{ cm}^{-3}} \frac{100 \text{ kpc}}{r_c} \frac{2 - \gamma}{10^{2-\gamma} - 1} (\rho/r_c)^{-3\beta-1} E^{\gamma-1} \\ (\text{erg cm}^{-2} \text{ s}^{-1} \text{ sr}^{-1} \text{ keV}^{-1}); \quad (3.19)$$

$$\frac{B_{E,\text{cont}}^{\text{scat}}}{B_{E,\text{cont}}}(\rho \gg r_c) = 1.1 \frac{\Gamma(3\beta/2 + 1/2)\Gamma(3\beta)}{\Gamma(3\beta/2 + 1)\Gamma(3\beta - 1/2)} \frac{L_X}{L_{\text{Edd}}} \\ \times \frac{M_{\text{BH}}}{10^9 M_\odot} \frac{0.01 \text{ cm}^{-3}}{n_0} \left(\frac{100 \text{ kpc}}{r_c} \right)^2 \left(\frac{kT}{1 \text{ keV}} \right)^{0.1}$$

3.3 AGN in the centre of a beta-cluster

$$\times \frac{2-\gamma}{10^{2-\gamma}-1} (\rho/r_c)^{3\beta-2} E^{1.4-\gamma} \exp(E/kT). \quad (3.20)$$

It can also be shown that within the core of the cluster, $B_{E,\text{cont}}^{\text{scat}} \propto \rho^{-1}$ and $B_{E,\text{cont}}^{\text{scat}}/B_{E,\text{cont}} \propto \rho^{-1}$ for any β . This can be directly verified for $\beta = 2/3$ using equation (3.18).

Fig. 3.3a demonstrates the dependence of the surface brightness profile of a cluster with a central AGN on the β parameter. The scattered surface brightness profiles were derived by numerical integration of equation (3.13). Fig. 3.4 shows the corresponding plots for the ratio of the scattered surface brightness to the intrinsic surface brightness of the intracluster gas. We see both from Fig. 3.4 and equation (3.20) that outside the core region (at $\rho \gtrsim r_c$), the relative contribution of scattered AGN radiation to the surface brightness increases with ρ when $\beta > 2/3$.

The $\beta = 1/3$ case presented in Figs. 3.3a and 3.4 corresponds to cluster cooling flows. Typically, the gas density grows $\propto r^{-1}$ towards the centre of the cooling flow, which roughly corresponds to a beta-model with a small r_c , large n_0 and $\beta \approx 1/3$. We then find from equations (3.12) and (3.19) that $B_{E,\text{cont}} \propto \rho^{-1}$ and $B_{E,\text{cont}}^{\text{scat}} \propto \rho^{-2}$ (assuming a constant temperature) for cooling flows. Interestingly, the surface brightness profile of scattered AGN radiation within the core of a beta-cluster (see above) is similar ($\propto \rho^{-1}$) to the intrinsic brightness profile of an (isothermal) cooling flow. Of course, a cluster core dominated by scattered emission from a central powerful quasar will have a very different spectrum (power law) than a cooling flow.

The energy dependent factor $E^{1.4-\gamma} \exp(E/kT)$ appearing in equations (3.18) and (3.20) has a minimum (for $\gamma > 1.4$) at $E = (\gamma - 1.4)kT$ and increases exponentially when $E \gg kT$. The origin of this dependence is obvious: we are comparing the slowly declining (power-law) spectrum of the AGN emission with the exponentially decaying efficiency of collisional radiative mechanisms operating in the intracluster gas. It is clear that for a given AGN luminosity and parameters of the gas, a significant gain (in terms of the relative contribution of scattered AGN radiation to the surface brightness) can be achieved by performing observations at $E \gg kT$, like in our examples in Figs. 3.3 and 3.4. A cautionary note is necessary here. If one wants to constrain the past luminosity of an AGN by mapping its host elliptical galaxy in hard X-rays, a restriction will appear due to a significant contribution to the measured surface brightness from the (unresolved) X-ray binaries of the galaxy. We estimate that in practice it should be very difficult to obtain limits better than $L_X \sim 10^{-3}L_{\text{Edd}}$. Of course, this complication is irrelevant for surface brightness measurements carried out over regions of a galaxy cluster that are almost devoid of point X-ray sources, say at distances ~ 100 kpc from the nucleus of a central dominant galaxy.

3 Constraining the past X-ray luminosity of AGN in clusters of galaxies

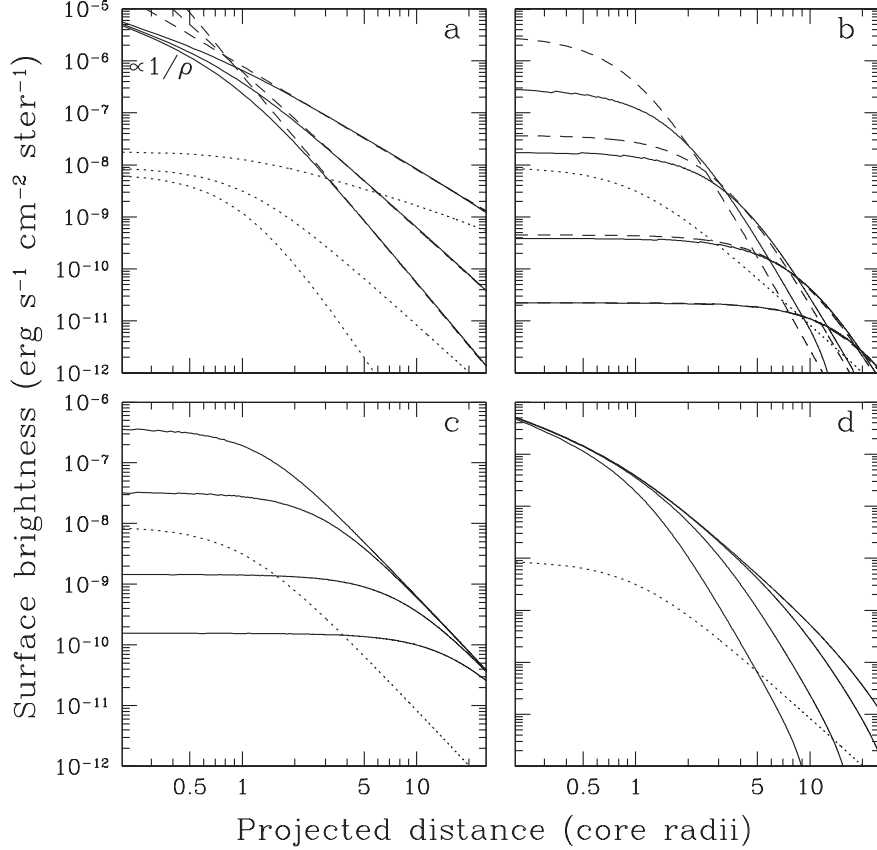


Figure 3.3: **a)** Surface brightness profiles of scattered AGN radiation (solid lines) and plasma thermal emission (dotted lines) in the X-ray continuum at $E = 20$ keV, for a model in which a central $10^9 M_\odot$ black hole is a persistent X-ray source with $L_X = L_{\text{Edd}}$ and $\gamma = 2$. The host cluster has the following parameters: $r_c = 100$ kpc, $n_0 = 0.01 \text{ cm}^{-3}$, $kT = 3$ keV, and (from top to bottom) $\beta = 1/3, 2/3$ and 1 , and is local ($z \ll 1$). The dashed lines are $\rho \gg r_c$ asymptotes given by Eq. 3.19, applicable at $\rho \gtrsim 2r_c$. In the opposite limit of $\rho \ll 1$ the scattered surface brightness is proportional to ρ^{-1} and is independent of β , as indicated in the upper left corner of the figure. **b)** Surface brightness profiles of scattered AGN radiation (solid lines) at $E = 20$ keV, measured at different times ($t = r_c/c, 3r_c/c, 9r_c/c$ and $19r_c/c$ – from top to bottom) after the end of a short ($\Delta = r_c/c$) flare with $L_X = L_{\text{Edd}}$. For the same values of the parameters as in (a) and $\beta = 2/3$. The dashed lines are $\rho, ct \gg r_c$ asymptotes given by Eq. 3.22. The dotted line is the surface brightness profile of plasma thermal emission. **c)** Same as (b), but for the case where the central source was on ($L_X = L_{\text{Edd}}$) until $t_{\text{off}} = 0$ (profiles order from top to bottom). **d)** Same as (c), but for the case where the central AGN switched on at $t = 0$ (profiles order from bottom to top).

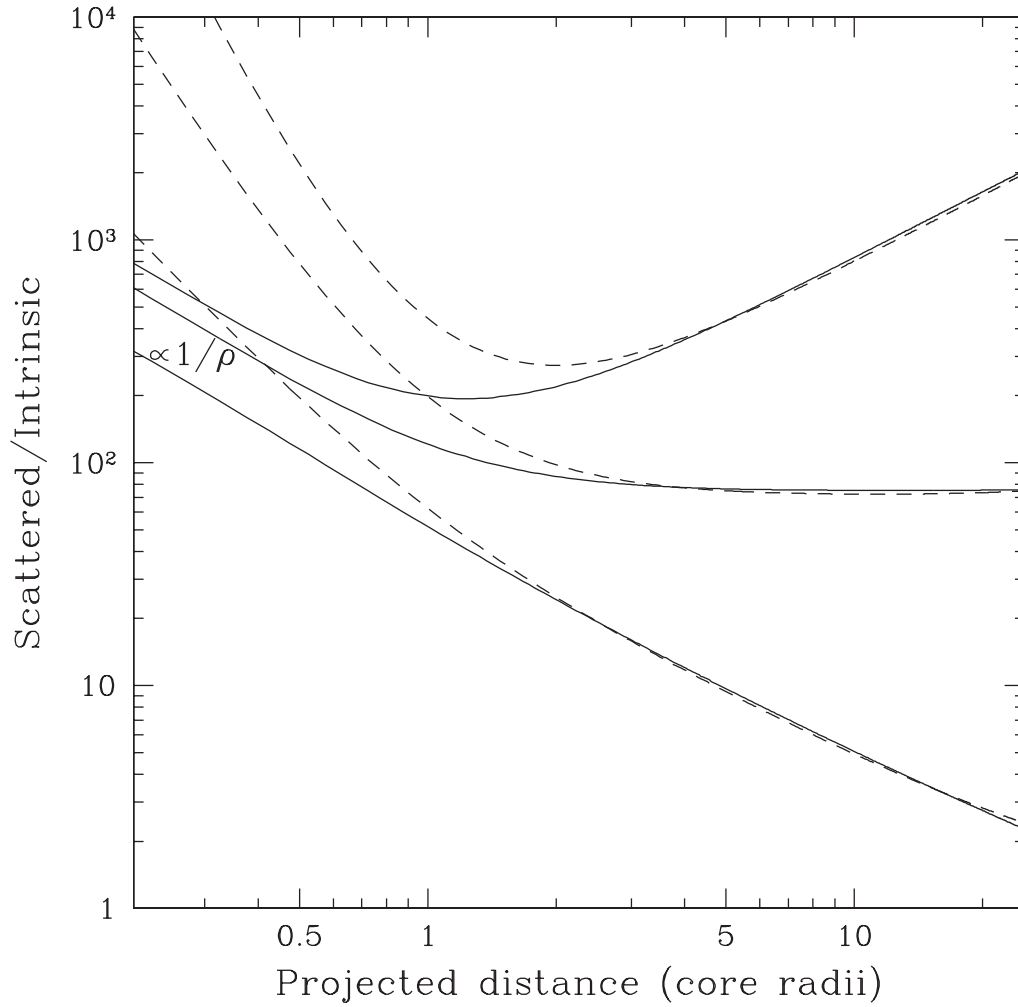


Figure 3.4: Radial profiles of the ratio of the surface brightness of scattered AGN radiation to the intrinsic brightness of the beta-cluster gas, for the same model as in Fig. 3.3a. The solid lines correspond (from bottom to top) to $\beta = 1/3, 2/3$ and 1. The dashed lines are the corresponding $\rho \gg r_c$ asymptotes given by Eq. 3.20.

3 Constraining the past X-ray luminosity of AGN in clusters of galaxies

3.3.2.2 The case of a high-redshift AGN

Furthermore, if a powerful quasar is observed at high redshift z , the relevant factor will be $[E(1+z)]^{1.4-\gamma} \exp[E(1+z)/kT]$. Consider for example the radio galaxy 3C294 located at $z = 1.786$, for which a surrounding intracluster medium has recently been revealed with *Chandra* (Fabian et al. 2001). Since the total number of counts registered from the source in the 20 ksec *Chandra* observation was small, ~ 100 , of which only ~ 30 are from the central AGN, it is only possible to make rough estimates in this case. Fabian et al. find that the gas temperature is ~ 5 keV, the 2–10 keV rest-frame luminosity of the hot gas is $\sim 2.5 \times 10^{44}$ erg s $^{-1}$, the corresponding (isotropic) luminosity of the AGN is $\sim 1.1 \times 10^{45}$ erg s $^{-1}$, the photon index for the AGN emission $\gamma \sim 2$ and the radial Thomson depth of the cluster is ~ 0.004 .

We can then estimate that the ratio of the flux of scattered AGN radiation to that of thermal bremsstrahlung emission from the gas is only $\sim 1\%$ at $E \lesssim 2$ keV, $\sim 3\%$ at 5 keV, $\sim 30\%$ at 10 keV, ~ 1 at 12 keV and ~ 4 at 15 keV. These estimates assume that the central source is isotropic and its luminosity has been the same in the recent past (over \sim a few 10^5 years), and are made for the total flux from the whole observed X-ray halo (of ~ 15 arcsec, or equivalently ~ 100 kpc radius). We thus see that it is desirable to go to energies above 10 keV in searching for scattered AGN radiation around the 3C294 galaxy. However, photon statistics then becomes a limiting factor. We can roughly estimate that the *XEUS* observatory with its effective area of ~ 2 m 2 at 10 keV and angular resolution of a few arcsec should be able to detect only a total of ~ 10 scattered AGN photons above 10 keV in a 100 ks observation of 3C294. This, combined with much more accurate measurements of the surface brightness of the intracluster gas in the standard X-ray band, could be only about enough to put constraints on the past history of the central X-ray luminosity of 3C294.

Another similar example is the radio galaxy PKS 1138–262 at $z = 2.2$, for which *Chandra* also has observed luminous extended X-ray emission (Carilli et al. 2002). In this case, the gas X-ray luminosity is similar to that of the 3C294 cluster (unfortunately, the gas temperature is unconstrained), but the inferred 2–10 keV (rest-frame) luminosity of the central source is four times higher, $\sim 4 \times 10^{45}$ erg s $^{-1}$. Moreover, in this case the gas emission is likely dominated by scattered AGN radiation already at $E \gtrsim 5$ keV (due to the higher redshift and luminosity), so that a few hundred scattered AGN photons could be detected above 5 keV in a 100 ks *XEUS-2* observation of PKS 1138–262 (taking into account the larger collecting area of the telescope at lower energies).

We note that photon statistics should be less of a problem for more nearby AGN and quasars such as 3C 273 located at $z = 0.158$. In fact, it is possible, given the

3.3 AGN in the centre of a beta-cluster

huge X-ray luminosity of 3C 273, $\sim 2 \times 10^{46}$ erg s $^{-1}$ (e.g. Yaqoob & Serlemitsos (2000)), that a hot intracluster medium surrounding it, if any, will be first observed in scattered emission rather than its own X-ray emission.

3.3.2.3 Short AGN flare

Suppose now that an AGN experienced an outburst in the past, between $t_{\text{on}} = -\Delta$ and $t_{\text{off}} = 0$. Here “short” means that the line-of-sight depth of the illuminated (see Fig. 3.2) zone of the cluster must be much smaller than the characteristic size at a given projection radius. Therefore, one of the following conditions must be fulfilled: $\Delta \ll r_c/c$ if $\rho \lesssim r_c$ or $\Delta \ll \rho/c$ if $\rho \gtrsim r_c$. Then, as follows from equations (3.15) and (3.16),

$$\delta z(t, \rho) \equiv z_2 - z_1 \approx \frac{c\Delta}{2}(1 + \rho^2/c^2t^2), \quad (3.21)$$

and $\int_{z_1}^{z_2} \epsilon_{E,\text{cont}}^{\text{scat}}(\rho, z) dz \approx \epsilon_{E,\text{cont}}^{\text{scat}}(\rho, z_2)\delta z(\rho)$. We then find in the limit of $\rho, ct \gg r_c$

$$\begin{aligned} B_{E,\text{cont}}^{\text{scat}} &= 3.2 \times 10^{-5} \times 4^{3\beta/2} \frac{L_X}{L_{\text{Edd}}} \frac{M_{\text{BH}}}{10^9 M_\odot} \\ &\times \frac{n_0}{0.01 \text{ cm}^{-3}} \frac{100 \text{ kpc}}{r_c} \frac{2 - \gamma}{10^{2-\gamma} - 1} \\ &\times (\Delta/t)(r_c/ct)^{3\beta+1}(1 + \rho^2/c^2t^2)^{-3\beta-1} E^{1-\gamma} \\ &(\text{erg cm}^{-2} \text{ s}^{-1} \text{ sr}^{-1} \text{ keV}^{-1}); \end{aligned} \quad (3.22)$$

$$\begin{aligned} \frac{B_{E,\text{cont}}^{\text{scat}}}{B_{E,\text{cont}}} &= 1.2 \times 4^{3\beta/2} \frac{\Gamma(3\beta)}{\Gamma(3\beta - 1/2)} \frac{L_X}{L_{\text{Edd}}} \frac{M_{\text{BH}}}{10^9 M_\odot} \\ &\times \frac{0.01 \text{ cm}^{-3}}{n_0} \left(\frac{100 \text{ kpc}}{r_c}\right)^2 \left(\frac{kT}{1 \text{ keV}}\right)^{0.1} \frac{2 - \gamma}{10^{2-\gamma} - 1} \\ &\times (\Delta/t)(ct/r_c)^{3\beta-2}(\rho/ct)^{6\beta-1}(1 + \rho^2/c^2t^2)^{-3\beta-1} \\ &\times E^{1.4-\gamma} \exp(E/kT). \end{aligned} \quad (3.23)$$

Comparing equations (3.23) and (3.20), we see that for a given luminosity L_X the contribution of scattered AGN radiation to the surface brightness at $\rho \sim ct$ is smaller by a factor of Δ/t for the flare compared to the stationary case. This happens because in the former case the scattered radiation comes from a gas layer of depth $\delta z \sim c\Delta$ along the line of sight, whereas $\delta z \sim \rho \sim ct$ in the latter case.

Fig. 3.3b shows a sequence of scattered surface brightness profiles that would be measured at different times after a short AGN outburst. We see that distant

3 Constraining the past X-ray luminosity of AGN in clusters of galaxies

regions of the cluster reveal no scattered light early on after the flare but become progressively brighter as time goes by and photons of the flare propagate through the gas. The ratio $B_{E,\text{cont}}^{\text{scat}}/B_{E,\text{cont}}$ has a maximum at $\rho_{\text{max}} \sim ct$, as indicated by equation (3.23). For example, $\rho_{\text{max}} = r_c$ when $\beta = 2/3$. Therefore, the zone of largest contribution of scattered AGN radiation propagates outward at an apparent velocity equal to the speed of light. It is important for observations that this zone is broad — $\delta\rho_{\text{eff}} \sim \rho_{\text{max}} \sim ct$.

We also notice that the amplitude of the effect is proportional to the product $L_X\Delta$, i.e. to the total energy emitted by the AGN during the flare. Thus, for example, a 10^5 -year outburst at $L_X = 0.01L_{\text{Edd}}$ would produce the same scattered surface brightness profile (at $\rho, ct \gg r_c$) as a 10^4 -year flare at $L_X = 0.1L_{\text{Edd}}$.

3.3.2.4 Switch-off and switch-on scenarios

We next consider a scenario in which the central source was persistently (over a time that is longer than the characteristic light travel time of the cluster) bright in the past until it suddenly turned off. A sequence of resulting scattered surface brightness profiles corresponding to different times after the switch-off ($t > 0$) is shown in Fig. 3.3c. One can see that these profiles differ markedly from those corresponding to the flare case (see Fig. 3.3b). In particular, as time goes by the surface brightness decreases in the central region, while it remains practically unchanged in more distant parts of the cluster for a long time $\sim \rho/c$ after the switch-off. This gives rise to a broad ($\delta\rho \sim \rho$) maximum of the scattered/intrinsic brightness ratio, which propagates outward at an apparent speed of light.

Another interesting situation takes place when the central source is bright at the time of observation and has turned on just recently. This “switch-on” case may actually correspond to observed quasars, which may have been luminous for a time short compared to the light travel time of the gas around them. This situation is depicted in Fig. 3.3d. One can see that the radial distribution of scattered AGN radiation is effectively truncated at a certain radius $\sim c(t - t_{\text{on}})$. This opens the possibility to estimate the time during which the quasar has been active.

3.3.3 Resonance lines

The results obtained above can be directly extended to the case of resonance lines provided that the intracluster gas is optically thin ($\tau \ll 1$) to resonant scattering. We shall consider this limit below and then point out in section 3.3.3.1 differences that may arise when $\tau \gtrsim 1$.

3.3 AGN in the centre of a beta-cluster

In the absence of external illumination, the equivalent width of a line would be

$$\begin{aligned}
 EW_0 &= \int_{-\infty}^{\infty} \epsilon_{\text{line}} dz / \int_{-\infty}^{\infty} \epsilon_{E,\text{cont}}(E_{ik}) dz \\
 &= 1.2 \times 10^5 \frac{n_z(T)}{n_e} f_{ik} \frac{g_{ik}(T)}{g_B(T, E_{ik})} \text{ (keV)}, \tag{3.24}
 \end{aligned}$$

under our assumption of constant temperature and constant element abundances.

Resonant scattering of the AGN photons leads to an increase of the equivalent width. At the same time, Thomson scattering of the AGN radiation tends to enhance the continuum near the line and thus to decrease its equivalent width. As we know from section 3.2, the first effect is a factor of $R \sim 6$ larger than the second, hence the net effect of scattering of AGN emission in the intracluster gas should be increased equivalent widths of the resonance lines. We can thus write:

$$\begin{aligned}
 EW &= \left(\int_{-\infty}^{\infty} \epsilon_{\text{line}} dz + \int_{z_1}^{z_2} \epsilon_{\text{line}}^{\text{scat}} dz \right) / \\
 &\quad \left(\int_{-\infty}^{\infty} \epsilon_{E,\text{cont}} dz + \int_{z_1}^{z_2} \epsilon_{E,\text{cont}}^{\text{scat}} dz \right) \\
 &= EW_0 \frac{1 + R \int_{z_1}^{z_2} \epsilon_{E,\text{cont}}^{\text{scat}} dz / \int_{-\infty}^{\infty} \epsilon_{E,\text{cont}} dz}{1 + \int_{z_1}^{z_2} \epsilon_{E,\text{cont}}^{\text{scat}} dz / \int_{-\infty}^{\infty} \epsilon_{E,\text{cont}} dz}. \tag{3.25}
 \end{aligned}$$

If the contribution of scattered AGN radiation to the surface brightness of the cluster is small, the fractional increase of the equivalent line width will be

$$\begin{aligned}
 \frac{\Delta EW}{EW_0} &\equiv \frac{EW - EW_0}{EW_0} \approx \\
 &= \frac{R - 1}{5} \frac{\int_{z_1}^{z_2} \epsilon_{E,\text{cont}}^{\text{scat}}(E_{ik}) dz}{\int_{-\infty}^{\infty} \epsilon_{E,\text{cont}}(E_{ik}) dz}. \tag{3.26}
 \end{aligned}$$

Using equation (3.26), one can readily apply all the results of section 3.3.2 to optically thin resonance lines.

It should be emphasised that equation (3.26) is strictly valid only in the case where both the plasma temperature (which affects the ionisation balance and plasma emissivity) and the element abundances are constant along the line of sight corresponding to a given projected distance ρ . Indeed, only when these conditions are met, $\epsilon_{\text{line}}(r) \propto \epsilon_{\text{cont}}(r)$ and $\epsilon_{\text{line}}^{\text{scat}}(r) \propto \epsilon_{\text{cont}}^{\text{scat}}(r)$ – see equations (3.1)–(3.4). In the general case, a coefficient somewhat different than $R - 1$ will relate the ratios $\Delta EW/EW_0$ and $\int_{z_1}^{z_2} \epsilon_{E,\text{cont}}^{\text{scat}} dz / \int_{-\infty}^{\infty} \epsilon_{E,\text{cont}} dz$.

We should also remind the reader that we ignore throughout the effect of the AGN on the ionisation balance (n_z) in the intracluster medium. The irradiation

3 Constraining the past X-ray luminosity of AGN in clusters of galaxies

of the gas by a very bright central source will first of all alter the equivalent width of the emission line relative to the value predicted by equation (3.24); it will also affect (however to a smaller degree, because both ϵ_{line} and $\epsilon_{\text{line}}^{\text{scat}}$ are proportional to n_z) the ratio $\Delta EW/EW_0$.

3.3.3.1 Finite depth effects

The intracluster gas may be moderately optically thick in the stronger X-ray lines ($\tau \gtrsim 1$, e.g. Gilfanov et al. (1987b)), so that the analytic results obtained above will be only approximately valid in this case.

The optical depth at the centre of a resonance line along a given direction \vec{l} through the cluster is

$$\tau_0 = \int \sigma_0 n_z(r) dl. \quad (3.27)$$

At plasma temperatures typical of galaxy clusters ($kT \sim 1\text{--}10$ keV), all interesting X-ray lines have nearly Doppler absorption profiles whose width is determined by the velocities of thermal and turbulent motions, because the line natural width is relatively small. Therefore, the cross section at line centre is

$$\sigma_0 = \frac{\sqrt{\pi} h r_e c f_{ik}}{\Delta E_D} \quad (3.28)$$

(h is Planck's constant), with the Doppler width being

$$\begin{aligned} \Delta E_D &= E_{ik} \left(\frac{2kT}{Am_p c^2} + \frac{V_{\text{turb}}^2}{c^2} \right)^{1/2} \\ &= E_{ik} \left[\frac{2kT}{Am_p c^2} (1 + 1.4AM^2) \right]^{1/2}, \end{aligned} \quad (3.29)$$

where A is the element atomic mass, m_p is the proton mass, V_{turb} is the characteristic turbulent velocity and M is the corresponding Mach number. The role of the additional line broadening due to turbulence becomes more important with increasing A .

Taking into account turbulence line broadening is important for two reasons. First, this phenomenon may cause some resonance lines, which would otherwise have $\tau \gtrsim 1$, to become optically thin. Secondly, some satellite lines may fall within the core of the resonance line, thereby effectively reducing the factor R defined in equation (3.7). As was noted in section 3.2, this effect is particularly important for the $K\alpha$ lines of H-like and He-like iron at $kT \sim 1$ keV.

If τ_0 is non-negligible, first of all the intrinsic surface brightness profile of the intracluster gas will be distorted due to the diffusion of photons from the central

region to the outer parts of the cluster. The equivalent line width will be somewhat smaller than predicted by equation (3.24) at $\rho \lesssim r_c$, and larger at $\rho \gtrsim r_c$ (Gilfanov et al. 1987b). Note that this effect takes place already at $\tau_0 < 1$, when only single resonant scattering is important, and becomes more pronounced when $\tau_0 > 1$.

When the optical depth becomes larger than unity, multiple resonant scatterings come into play. In the stationary scenario, the surface brightness profile of the scattered AGN emission in a line with $\tau_0 \gtrsim 1$ will be flatter in the cluster core compared to a $1/\rho$ profile in the $\tau_0 \ll 1$ case. Also, the total flux of AGN photons scattered toward us from the core region will be smaller than calculated in the single-scattering approximation by a factor $\sim \tau_0$. However, due to the rather similar effects taking place for thermal gas emission (see above), the net correction to the ratio EW/EW_0 is expected to be fairly small for $\tau_0 \gtrsim 1$.

Multiple resonant scatterings also delay the escape of AGN photons from the cluster core. As a result, the time-dependent scattered surface brightness profiles arising in the outburst scenario will be affected.

3.4 Numerical simulations

As a next step, we have performed numerical simulations for two actual clusters. We used a combination of (i) a Monte-Carlo code to simulate the diffusion of photons (both those emitted by the AGN and by the gas) through multiple resonant scatterings and (ii) the MEKAL code (Kaastra 1992) as implemented in the software package XSPEC v10 (Arnaud 1996) to calculate the plasma emissivity in lines. The line energies and oscillator strengths were taken from the list of strong resonance lines of Verner et al. (1996) and the solar abundances of elements from Anders & Grevesse (1989). The ionisation fractions were calculated using collisional ionisation rate fits from Voronov (1997), radiative recombination rates from Verner & Ferland (1996) and dielectronic recombination rates from Aldrovandi & Pequignot (1973), Shull & van Steenberg (1982) and Arnaud & Rothenflug (1985).

3.4.1 M87

One of the most promising targets in the sky for observing the discussed effect is M87. This is a giant elliptical galaxy located near the centre of the nearest (16 Mpc – 1 arcmin corresponds to 4.7 kpc) rich cluster of galaxies Virgo. M87 hosts a central black hole of mass $3 \times 10^9 M_\odot$ (Macchetto et al. 1997; Marconi et al. 1997), which is the largest reliably measured black hole mass. The corresponding Eddington luminosity is $L_{\text{Edd}} = 4 \times 10^{47} \text{ erg s}^{-1}$.

M87 demonstrates AGN activity. In particular, observations at different energy

3 Constraining the past X-ray luminosity of AGN in clusters of galaxies

Table 3.1: The brightest X-ray and extreme UV resonance lines of the M87/Virgo intracluster gas.

Ion	Energy (keV)	Equivalent width (eV)	Optical depth
Fe XXIV	0.049	1	3.0
Fe XXIV	0.065	2	6.0
Fe XXIII	0.093	3	8.5
O VIII	0.654	20	0.6
Ne X	1.021	30	0.9
Fe XXIII	1.129	10	3.2
Fe XXIV	1.166	30	2.7
Si XIII	1.865	10	1.3
Si XIV	2.005	60	1.3
S XV	2.461	20	1.3
Ar XVII	3.140	20	0.4
Fe XXV	6.700	740	1.2
Fe XXV	7.881	110	0.2

bands reveal an unresolved nucleus and a one-sided jet. The combined bolometric luminosity of the nucleus and jet is $\sim 10^{42}$ erg s $^{-1}$ (e.g. Biretta et al. (1991)), or $\sim 10^{-6}$ of the Eddington luminosity. This is an amazingly small value given the fact that the nucleus is located in the centre of a dense cooling flow. The average power input in the form of relativistic plasma from the jet into a large-scale radio halo around M87 is estimated (Owen et al. 2000) to have been $\sim 10^{44}$ erg s $^{-1}$ over the past $\sim 10^8$ years, which is still a small fraction of the Eddington luminosity.

Both the nucleus and the jet (whose brightest knot is at a distance of ~ 1 kpc from the nucleus) have recently been observed in X-rays with the *XMM-Newton* (Böhringer et al. 2001) and *Chandra* (Wilson & Yang 2002) satellites. The X-ray spectrum is a power-law with values for the photon index ranging between 2 and 2.9 for the nucleus and different knots in the jet. The inferred X-ray (1–10 keV) luminosities of the nucleus and the jet are $\sim 3 \times 10^{40}$ and 8×10^{40} erg s $^{-1}$, respectively (Böhringer et al. 2001).

In our simulations, we modelled the distribution of the intracluster gas surrounding M87 based on the results of recent analyses of the XMM observations by Böhringer et al. (2001); Finoguenov et al. (2002) and Matsushita et al. (2002). We assumed the distribution of gas to be spherically symmetric around M87 and restricted our consideration to the central region within a radius of 250 kpc. The

3.4 Numerical simulations

electron density radial profile was represented by a sum of two beta-models (3.9) with the following parameters: $n_0 = 0.13 \text{ cm}^{-3}$, $r_c = 1.7 \text{ kpc}$, $\beta = 0.42$ and $n_0 = 0.011 \text{ cm}^{-3}$, $r_c = 22 \text{ kpc}$, $\beta = 0.47$. We adopted a constant temperature $kT = 1 \text{ keV}$ within the central 1 kpc, the dependence $kT = 1.5(r/5 \text{ kpc})^{0.22} \text{ keV}$ between 1 and 50 kpc, and a constant $kT = 2.5 \text{ keV}$ at larger radii. The last value approximately corresponds to temperatures measured with *ASCA* (Shibata et al. 2001) in different parts of the Virgo cluster within $\sim 300 \text{ kpc}$ from M87. The element abundances were taken to be constant at $r < 10 \text{ kpc}$, with $A(\text{O}) = 0.4$, $A(\text{Si}) = 1.0$, $A(\text{S}) = 1.0$, $A(\text{Ar}) = 1.0$ and $A(\text{Fe}) = 0.8$ (in units of solar abundances), then gradually declining to $A(\text{O}) = 0.4$, $A(\text{Si}) = 0.6$, $A(\text{S}) = 0.6$, $A(\text{Ar}) = 0.6$ and $A(\text{Fe}) = 0.4$ at $r = 40 \text{ kpc}$, and constant thereafter.

Table 3.1 lists the resonance X-ray and extreme UV lines that we estimate to be the strongest emission lines of the M87 gas. All of these lines have substantial optical depths from the centre to the boundary of the gas cloud, assuming negligible turbulence.

Using equation (3.20), we can estimate for the stationary scenario the contribution of scattered AGN radiation to the surface brightness of M87/Virgo in the X-ray continuum:

$$\begin{aligned} \frac{B_{E,\text{cont}}^{\text{scat}}}{B_{E,\text{cont}}} &= 4 \times 10^2 \frac{L_X}{L_{\text{Edd}}} E^{-0.6} \exp(E/1.5 \text{ keV}) \\ &\times \left(\frac{\rho}{1.7 \text{ kpc}} \right)^{-0.7}, \quad 1.7 \text{ kpc} \ll \rho \ll 22 \text{ kpc}; \end{aligned} \quad (3.30)$$

$$\begin{aligned} \frac{B_{E,\text{cont}}^{\text{scat}}}{B_{E,\text{cont}}} &= 40 \frac{L_X}{L_{\text{Edd}}} E^{-0.6} \exp(E/2 \text{ keV}) \\ &\times \left(\frac{\rho}{22 \text{ kpc}} \right)^{-0.6}, \quad \rho \gg 22 \text{ kpc}. \end{aligned} \quad (3.31)$$

Here we have assumed constant temperatures of $kT = 1.5 \text{ keV}$ and $kT = 2 \text{ keV}$ for equations (3.30) and (3.31), respectively, and $\gamma = 2$.

The corresponding dependences for the equivalent width of a resonance line with $\tau_0 \ll 1$ can be found from equations (3.30) and (3.31) assuming constant element abundances for a given ρ as $\Delta EW/EW_0 = (R - 1) B_{E,\text{cont}}^{\text{scat}}(E_{ik})/B_{E,\text{cont}}(E_{ik})$.

Now we proceed to discussing the results of our computations, which do not use the assumption of small optical depth.

3 Constraining the past X-ray luminosity of AGN in clusters of galaxies

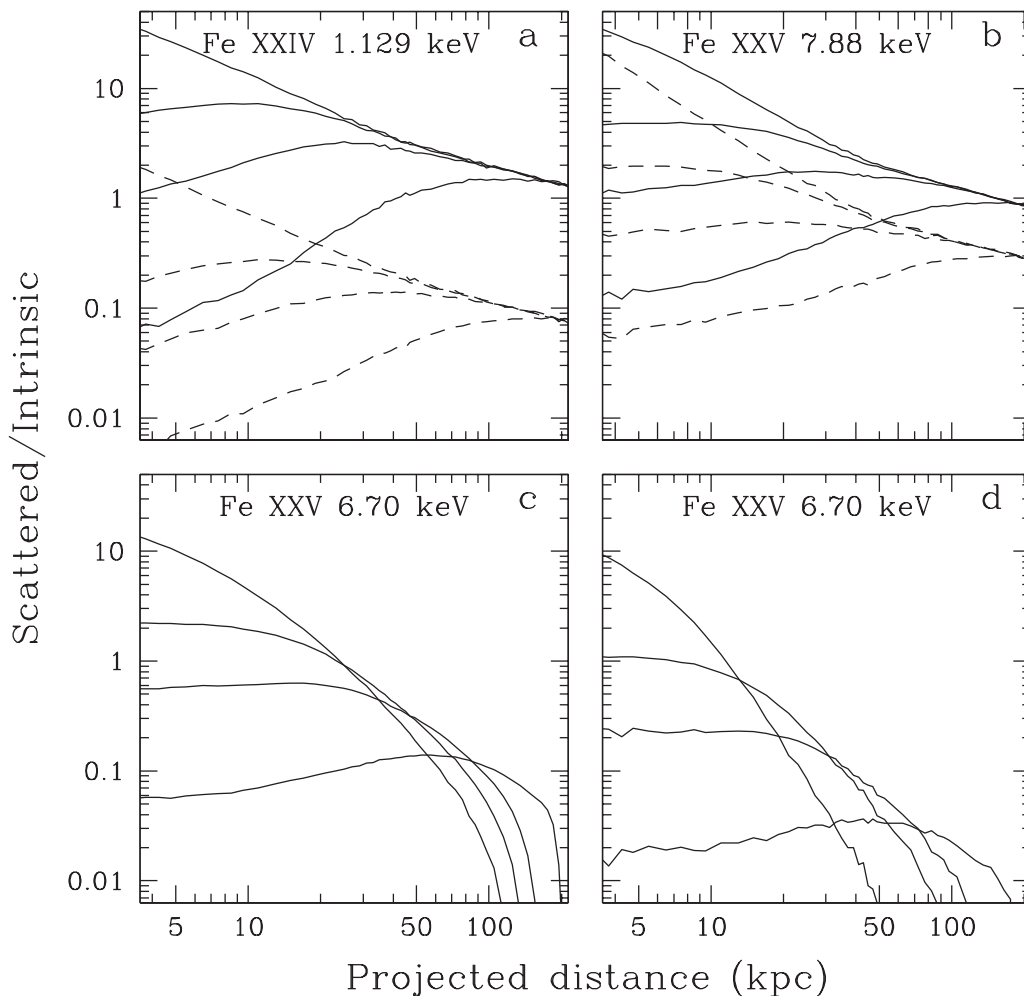


Figure 3.5: **a)** Ratio of the surface brightness of scattered AGN radiation to the intrinsic brightness of the hot gas in the iron 1.13 keV resonance line, in the switch-off scenario for M87, at different times after AGN switch-off as a function of projected radius. The AGN emitted $L_X = 0.01L_{\text{Edd}}$ in the past. The different solid lines correspond, from top to bottom, to elapsed times of 5, 50, 100 and 250 thousand years. The dashed lines are the corresponding profiles for the spectral continuum at the energy of the resonance line. **b)** Same as (a), but for the iron Fe 7.88 keV line. **c)** Same as (a), but for the iron 6.70 keV line and a 10^5 -year outburst ($L_X = 0.01L_{\text{Edd}}$). **d)** Same as (c), but for a 2×10^4 -year outburst.

3.4.1.1 Switch-off scenario

We first consider a scenario in which M87 was bright in the past for a long time (at least \sim a million years) until it suddenly turned off (actually switched to its present low-luminosity state) at $t_{\text{off}} = 0$. We have plotted in Figs. 3.5a and 3.5b for two resonance lines the computed contribution of scattered radiation from the AGN to the surface brightness as a function of projected radius as would be measured by observers living in various epochs $t > 0$ after the switch-off. Also shown are the corresponding profiles for the continuum emission near the lines. The relative contribution of scattered AGN emission is a factor of $R \sim 6$ (with a scatter of ~ 3 between the lines) larger for the lines than for the continuum, in agreement with the result of section 3.2. We adopted $L_X = 0.01L_{\text{Edd}}$ for our examples. Since the discussed effect is proportional to L_X , the results can be easily recomputed for any AGN luminosity.

Fig. 3.6 compares the surface brightness profiles of scattered AGN radiation and thermal emission in the iron 6.7 keV line, which has the largest equivalent width in our sample. It is essential that photon statistics is not expected to impose strong restrictions on the prospects of detecting scattered AGN radiation from the Virgo cluster out to ~ 1 Mpc from M87 with the next generation of X-ray spectrometers.

The finite depth effects that were discussed in section 3.3.3.1 play in the M87 case only a minor role for the X-ray lines, because for them $\tau_0 < 3$ (see Table 3.1). Fig. 3.7 compares two cases, $M = 0$ (no turbulence) and $M = 0.5$ (significant turbulence), for the iron 1.13 keV line. The increased turbulence leads to a decrease from $\tau_0 = 3.2$ to $\tau_0 = 0.7$. We see that the relative contribution of scattered AGN emission to the surface brightness in the central ~ 10 kpc is several times larger in the former (optically-thick) case, except for the early moments. This increase is mainly due to the delayed escape of photons.

We can now address the principal question of our study: what constraints can X-ray observations place on the past luminosity of the M87 central source? Suppose that it is possible in an experiment to map the distribution of the equivalent width of a particular line over M87/Virgo with $\delta = 10\%$ accuracy, which we consider a realistic value (see the discussion in section 3.5). Should then the relative contribution of scattered AGN emission exceed δ at least at some projected radius (i.e. at least at the maximum of EW/EW_0 in Fig. 3.5), it will be possible to estimate the past AGN luminosity. The resulting dependence of the minimum detectable past luminosity of M87 on time after the switch-off is plotted in Fig. 3.8a.

We see that in order to have a 10% contribution of scattered radiation from the AGN whose luminosity in the past was $L_X = 10^{-4}L_{\text{Edd}} = 4 \times 10^{43}$ erg s $^{-1}$ (i.e. several hundred times higher than the combined X-ray luminosity of the nucleus

3 Constraining the past X-ray luminosity of AGN in clusters of galaxies

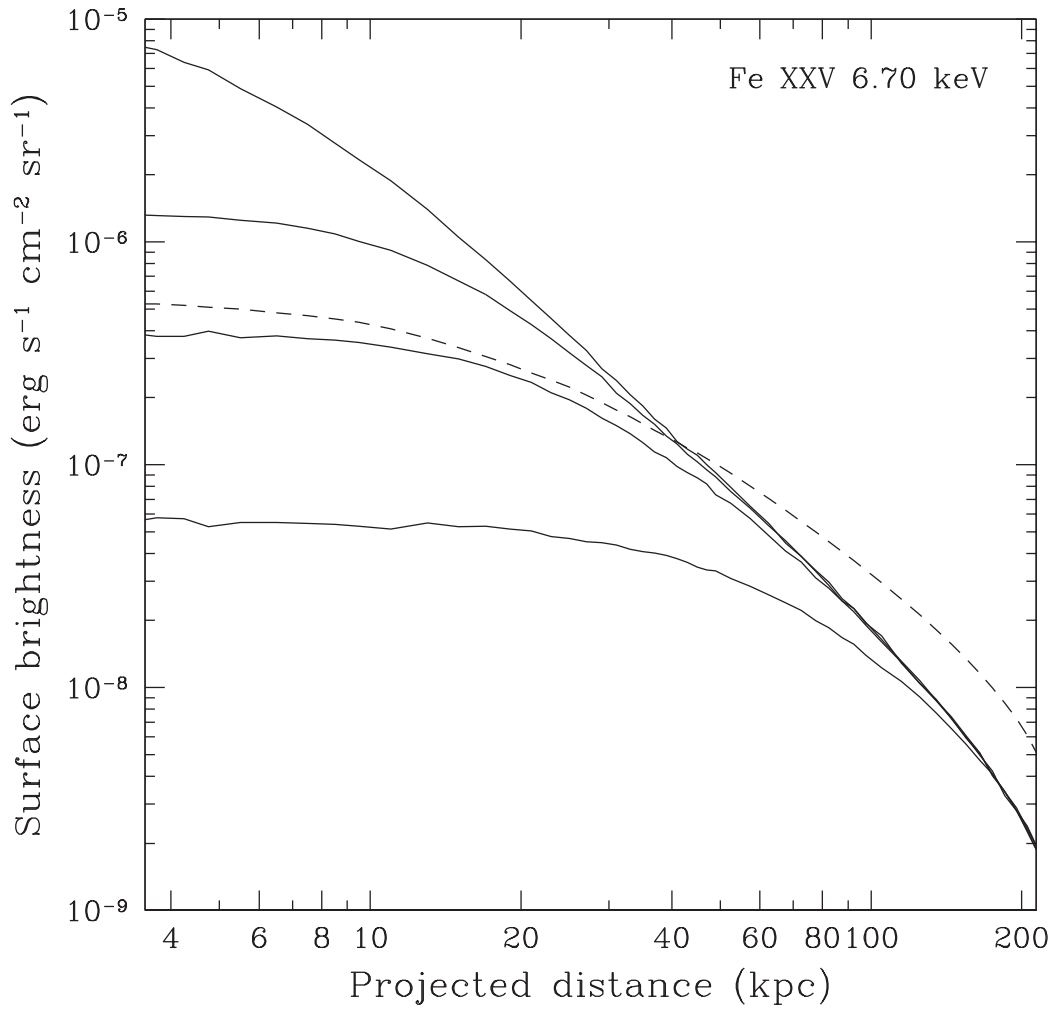


Figure 3.6: M87/Virgo surface brightness of scattered AGN radiation (solid lines) in the iron 6.70 keV resonance line at different times (as in Fig. 3.5) after the AGN switch-off. The dashed line shows the intrinsic surface brightness profile of the hot gas in the 6.70 keV line, which also is distorted by resonant scattering. The AGN emitted $L_X = 0.01L_{\text{Edd}}$ in the past.

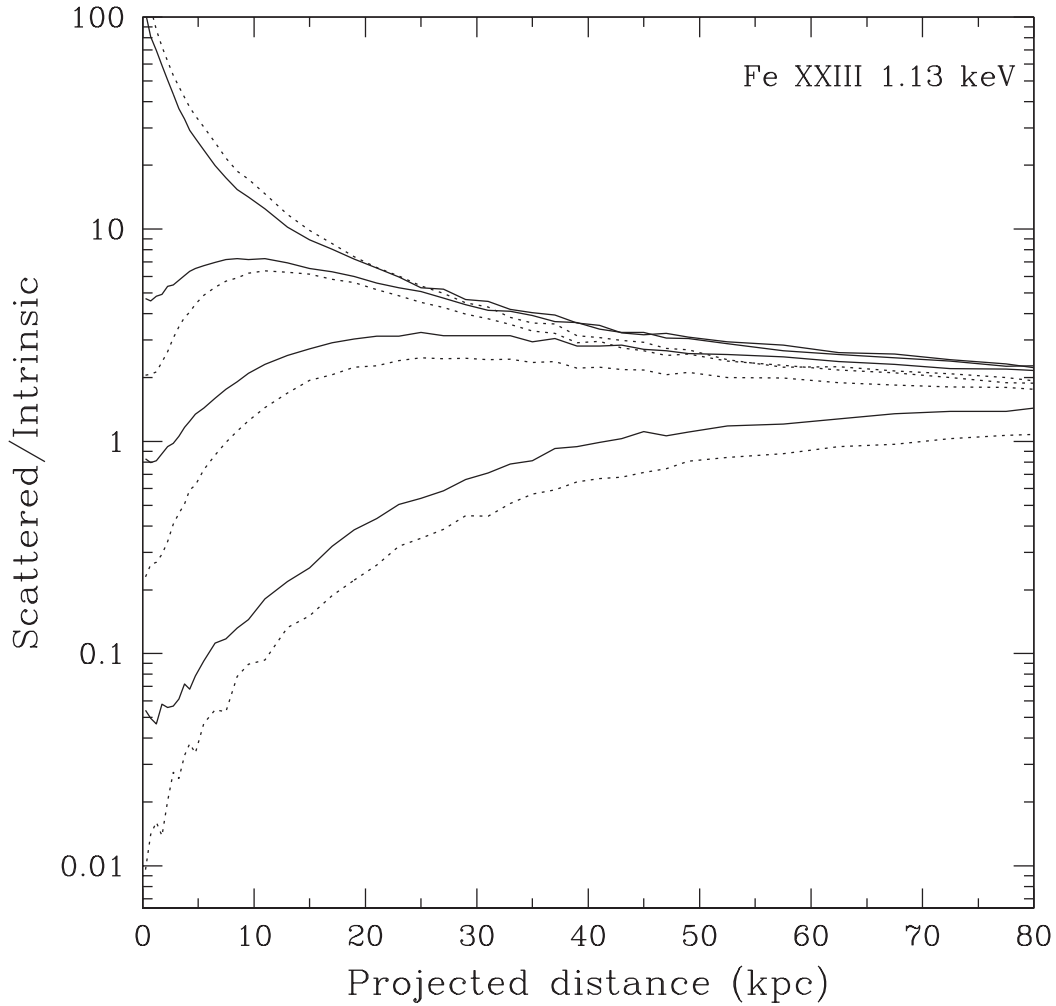


Figure 3.7: Ratio of the surface brightness of scattered AGN radiation to the intrinsic brightness of the hot gas in the iron 1.13 keV resonance line, in the switch-off scenario for M87, as a function of projected radius. The sampled times are as in Fig. 3.5. The solid lines correspond to the case of negligible turbulence, and the dotted lines to $M = 0.5$. Note the linear scaling chosen for the projected radius, as opposed to the logarithmic scaling in Fig. 3.5.

3 Constraining the past X-ray luminosity of AGN in clusters of galaxies

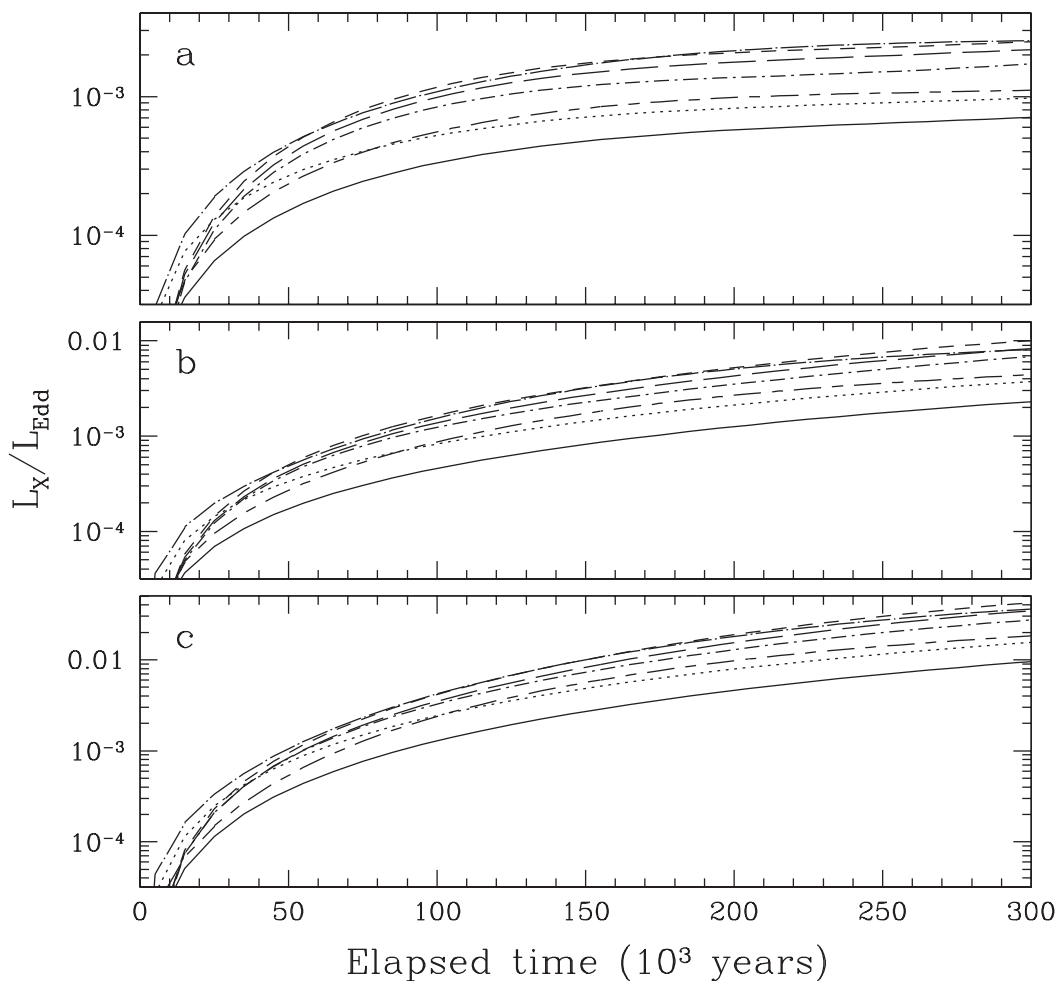


Figure 3.8: **a)** Minimum detectable (for $\delta = 10\%$ – see text) past X-ray luminosity as a function of elapsed time in the switch-off scenario for M87. The different curves correspond to mapping M87/Virgo in different lines: Fe 1.13 keV line (solid), Fe 1.17 keV line (dotted), Si 1.86 keV line (short-dashed), S 2.46 keV line (long-dashed), Ar 3.14 keV line (dot-short-dashed), Fe 6.70 keV line (dot-long-dashed) and Fe 7.88 keV line (short-dash-long-dashed). **b)** Same as (a), but for a 10^5 -year flare. **c)** Same as (b), but for a 2×10^4 -year flare.

and jet now), we should be not later than $\sim 3 \times 10^4$ years after the switch-off and look with X-ray telescopes into the M87 core region ($\rho \lesssim 10$ kpc ~ 2 arcmin in the plane of the sky), as is clear from Fig. 3.5. If the luminosity in the past was higher, $L_X = 10^{-3}L_{\text{Edd}} = 4 \times 10^{44}$ erg s $^{-1}$, we must live no later than $\sim 2 \times 10^5$ years after the switch-off and look further out (at $\rho \sim 50 - 200$ kpc ~ 20 arcmin from the AGN). The nearly flat ($\propto t^{-0.6}$) shape of the curves in Fig. 3.8a, which have been truncated at $t = 3 \times 10^5$ years to minimize the effects of the finite size of our model gas cloud, suggests that if the X-ray luminosity of M87 was \sim a few $10^{-3}L_{\text{Edd}} \sim 10^{45}$ erg s $^{-1}$ in the past, the maximum allowed elapsed time would only be restricted by the extent of the gas in the Virgo cluster (~ 1 Mpc), the effective area of the detector and the field of view of the telescope.

We may therefore conclude that it should be possible with future X-ray spectrometers to measure or obtain fairly tight limits on the past X-ray luminosity of the central source in M87. For comparison, we can use the available data of *XMM-Newton* observations of the M87/Virgo core to derive some weaker limits already now. Böhringer et al. (2001) have analysed X-ray spectra taken from a sequence of rings centred on the M87 nucleus. The most distant ring has an outer radius $r_{\text{out}} \approx 60$ kpc, and the innermost circle has $r_{\text{in}} \approx 1.25$ kpc. Except for the spectrum of the central circle to which the direct emission from the AGN contributes, the individual spectra correspond to optically thin thermal emission from the gas. The quality of the spectra is apparently good up to ~ 7 keV. We can therefore suggest that the surface brightness of scattered AGN radiation (having a power-law spectrum) does not exceed the actually measured surface brightness in the X-ray continuum at 7 keV nowhere between $\rho = 1.25$ kpc and 60 kpc. From this condition we can find an upper limit on the past X-ray luminosity of M87 as a function of time after the switch-off, similarly as we derived the limits presented in Fig. 3.8a based on the resonance line computations. However, in the previous case we did not impose any limitations on the projected radius and we adopted a value $\delta = 10\%$, rather than $\delta = 100\%$ to be used now. The resulting dependence is shown in Fig. 3.9.

We see that the current limits based on the spectral continuum data are rather weak. For example, the average X-ray luminosity of the M87 AGN over a long period of $\gtrsim 10^5$ years ending 5×10^4 years ago was not higher than $5 \times 10^{-3}L_{\text{Edd}} = 2 \times 10^{45}$ erg s $^{-1}$. By comparing Fig. 3.9 with Fig. 3.8a, we see that the current limits could be improved by at least an order of magnitude by means of fine X-ray spectroscopy. Alternatively, much tighter limits could be obtained by measuring the surface brightness of M87/Virgo in the hard X-ray continuum. To illustrate this possibility, we have repeated our analysis for $E = 20$ keV – see the result in Fig. 3.9. Going from $E = 7$ keV to 20 keV (again assuming a $\delta = 100\%$ scattered contribution relative to the bremsstrahlung emission) leads to a factor of ~ 200

3 Constraining the past X-ray luminosity of AGN in clusters of galaxies

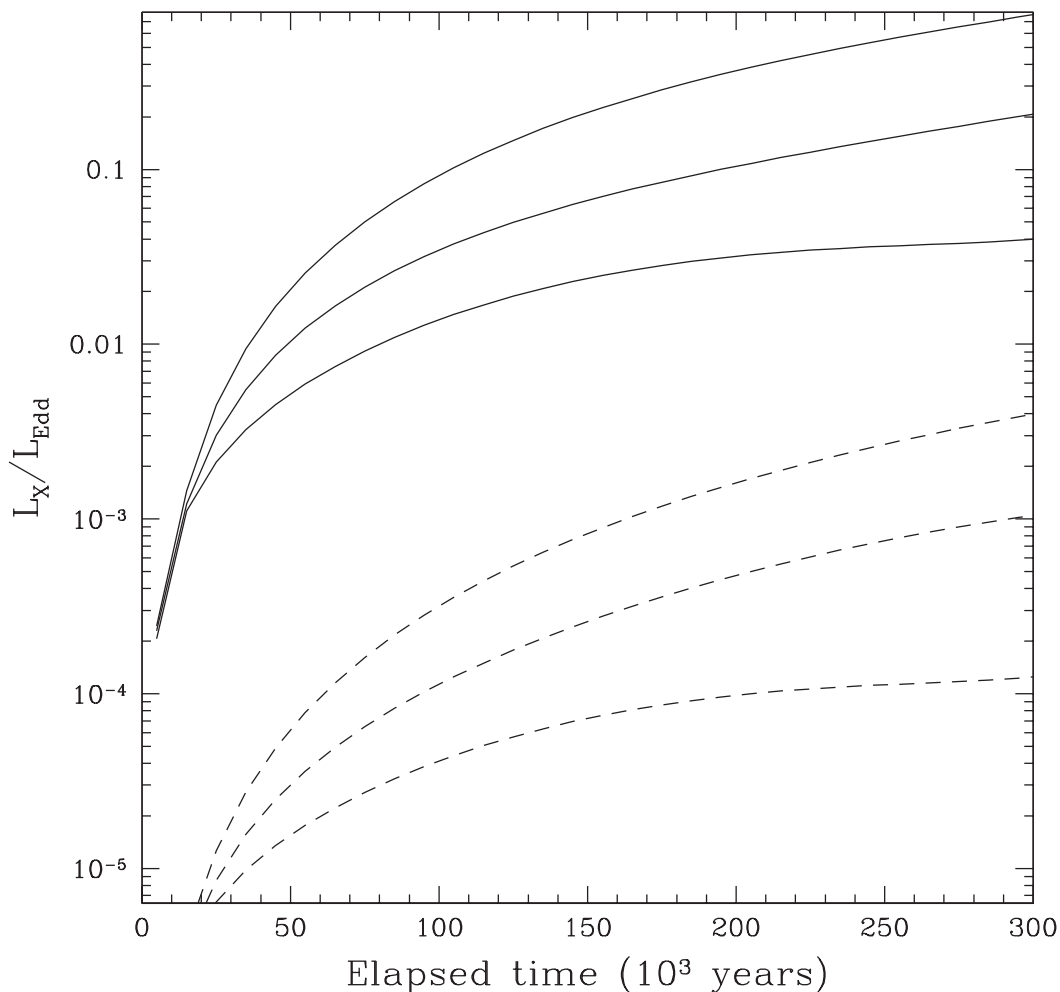


Figure 3.9: Upper limits (for $\delta = 100\%$) on the past X-ray luminosity of the M87 AGN as a function of elapsed time, derived from *XMM-Newton* observations of the M87/Virgo central region in the X-ray spectral continuum below 7 keV, for three cases: switch-off, a 10^5 -year flare and a 2×10^4 -year flare (solid lines from bottom to top). For comparison shown (dashed lines) are the limits obtainable if it were possible to map M87/Virgo at $E = 20$ keV.

3.4 Numerical simulations

Table 3.2: The brightest resonance X-ray and extreme UV lines of the Cyg A intracluster gas.

Ion	Energy (keV)	Equivalent width (eV)	Optical depth
Fe XXIV	0.049	1	0.9
Fe XXIV	0.065	2	1.8
Fe XXV	6.70	250	1.8
Fe XXV	7.88	40	0.3
Fe XXVI	6.97	200	0.3

(!) stronger limits.

3.4.1.2 Flare scenario

Suppose now that some time ago M87 experienced an outburst that was short compared to the characteristic light crossing time of the gas cloud, i.e. $\Delta \ll 10^6$ years. Some analytic estimates for this case were obtained in section 3.3.2.3. Figs. 3.5c and 3.5d show the computed time evolution of the scattered/thermal brightness ratio profile for the Fe XXV $K\alpha$ line for outburst durations $\Delta = 10^5$ years and $\Delta = 2 \times 10^4$ years, respectively, and an AGN luminosity $L_X = 0.01L_{\text{Edd}}$. Note that for $t \gg \Delta$ the scattered surface brightness profile depends on the product $L_X\Delta$, rather than on L_X and Δ separately.

Figs. 3.8b and 3.8c show the minimum detectable (for 10% scattered contribution) AGN outburst luminosity as a function of elapsed time for the two considered scenarios. These dependences should be compared with Fig. 3.8a representing the switch-off scenario. We see that until a certain moment $t_{\text{crit}} \sim \Delta$ the minimum detectable luminosity is only a little smaller in the flare case than in the switch-off case. This is expected, because the characteristic line-of-sight depth of the illuminated volume at $t = t_{\text{crit}}$ is about the same, $\delta\rho \sim ct_{\text{crit}}$, in both cases. Only at $t \gg \Delta$, does the minimum detectable luminosity become much larger (by a factor of Δ/t) for short outbursts. This directly follows from comparison of equations (3.20) and (3.23).

Fig. 3.9 shows upper limits for the same outburst scenarios but obtained using the *XMM-Newton* data on the X-ray continuum emission from M87/Virgo.

3 Constraining the past X-ray luminosity of AGN in clusters of galaxies

3.4.2 Cygnus A

Our second example is Cyg A. This is a well-known nearby ($z = 0.0562$, i.e. about 20 times more distant than M87 – 1 arcmin approximately corresponds to 100 kpc) powerful radio galaxy. Cyg A has recently been observed with the *Chandra* satellite, and detailed information was obtained on the morphology of X-ray emission from the galaxy (Young et al. 2002) as well on the intracluster gas surrounding it (Smith et al. 2002).

In the *Chandra* and quasi-simultaneous *RXTE* observations (Young et al. 2002), hard (up to 100 keV), spatially unresolved X-ray emission was detected from the position of the radio and infrared nucleus of Cyg A. The energy spectrum of this radiation is power law with photon index $\gamma = 1.5$, heavily absorbed below a few keV. The inferred unabsorbed 1–10 keV luminosity of the nucleus is $L_X \sim 5 \times 10^{44}$ erg s $^{-1}$. This is four orders of magnitude larger than the X-ray luminosity of the M87 nucleus.

The *Chandra* observations clearly reveal an intracluster medium. The gas has a complex structure within the central ~ 100 kpc, which apparently is the result of an interaction with the relativistic material produced by AGN activity. In contrast, the morphology of the gas is simple at larger radii ($\gtrsim 100$ kpc), namely the gas appears to be spherical within at least 700 kpc of the nucleus, and nearly isothermal with $kT \sim 7 - 8$ keV. The total luminosity of the intracluster gas is $\sim 10^{45}$ erg s $^{-1}$, which is comparable to the X-ray luminosity of the central AGN and is a typical value for rich clusters of galaxies.

Given the above observational facts, we can estimate the contribution of scattered emission from the AGN to the X-ray surface brightness outside the central 100 kpc of the Cyg A cluster. Due to the highly irregular distribution of gas in the innermost region of Cyg A, our simulations will not be aimed at this zone. Based on these considerations and the results of Smith et al. (2002), we model the radial distribution of gas density by a beta-model with $n_0 = 0.05$ cm $^{-3}$, $r_c = 30$ kpc and $\beta = 0.5$. The temperature is assumed to be constant, $kT = 5$ keV, within the central 50 kpc and also at $r > 150$ kpc, $kT = 7.5$ keV. The abundance of iron is taken to be 0.35 solar. Our model cloud of gas has an outer boundary at $r = 1$ Mpc.

Table 3.2 lists the strongest emission lines of the Cyg A cluster, as implied by our model. The *Chandra* and *RXTE* data do reveal two strong lines, one near 6.7 keV (Fe K α) and another near 7.9 keV (Fe K β plus possibly Ni K α). It appears (see Fig. 7 in Smith et al. (2002)) that the measured (with moderate energy resolution) spectra also do not contradict the presence of a strong line at the position of Fe Ly α (6.97 keV).

We can estimate from equation (3.20) the stationary contribution of scattered

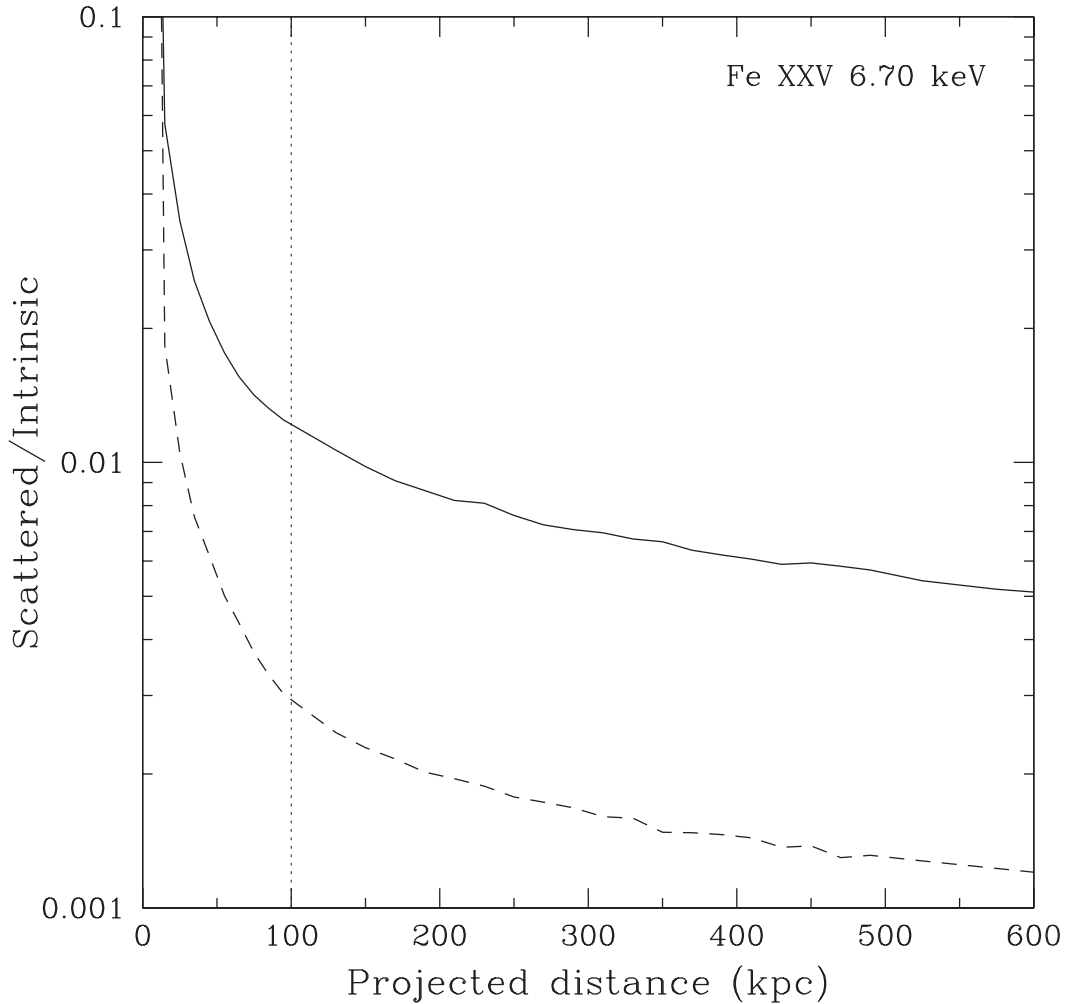


Figure 3.10: Ratio of the surface brightness of scattered AGN radiation to the intrinsic brightness of the hot gas in the iron 6.70 keV resonance line, in the stationary scenario for Cyg A, as a function of projected radius (the solid line). The AGN X-ray luminosity is assumed to be equal to its present-day value, $L_X = 5 \times 10^{44} \text{ erg s}^{-1}$. The dashed line shows the corresponding profile for the spectral continuum at the resonance energy. The vertical dotted line indicates that the results to the left of it are not reliable.

3 Constraining the past X-ray luminosity of AGN in clusters of galaxies

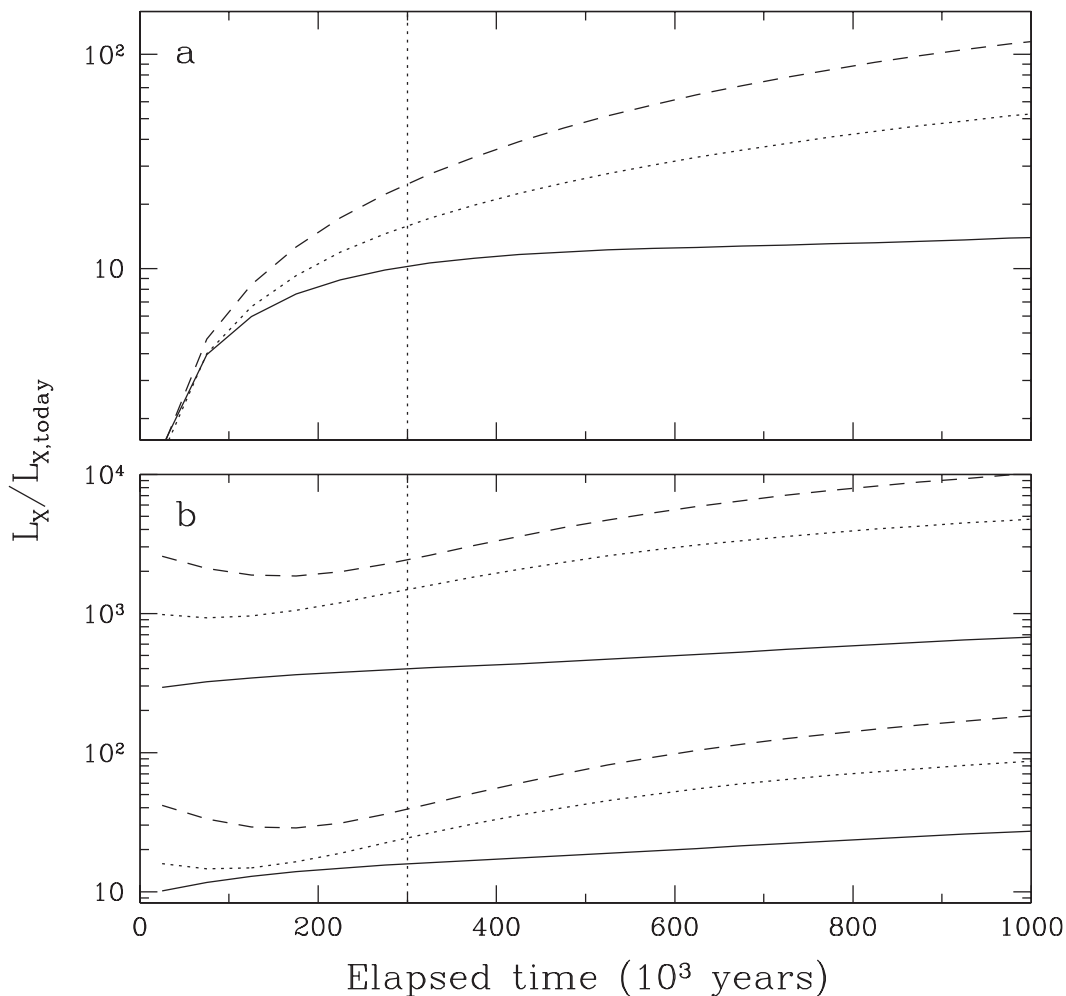


Figure 3.11: **a)** Minimum detectable (for $\delta = 10\%$ – see text) past X-ray luminosity of Cyg A as a function of elapsed time. The surface brightness is measured in the iron 6.70 keV line. The solid line corresponds to the switch-off case ($\Delta \rightarrow \infty$). The dotted and dashed lines correspond to outbursts of duration $\Delta = 5 \times 10^5$ years and $\Delta = 2 \times 10^5$ years, respectively. The luminosity is normalised to the present-day X-ray luminosity of the Cyg A nucleus. The vertical dotted line indicates that the results to the left of it are not reliable. **b)** Same as (a), but derived from *Chandra* observations of the Cyg A cluster in the X-ray spectral continuum below 8 keV (for $\delta = 100\%$). For comparison shown (the lower set of lines) are the limits that could be obtained if it were possible to map the Cyg A cluster at $E = 40$ keV.

AGN radiation to the surface brightness of the Cyg A cluster in the X-ray continuum:

$$\frac{B_{E,\text{cont}}^{\text{scat}}}{B_{E,\text{cont}}} = 2 \times 10^{-3} \frac{L_X}{5 \times 10^{44} \text{ ergs}^{-1}} E^{-0.1} \exp(E/7.5 \text{ keV}) \times \left(\frac{\rho}{30 \text{ kpc}} \right)^{-0.5}, \quad (3.32)$$

where we have normalised the X-ray luminosity of the Cyg A nucleus to its present-day value and used $\gamma = 1.5$.

Fig. 3.10 shows a computed Cyg A radial profile of the scattered/thermal surface brightness ratio for the iron 6.7 keV line, assuming that the AGN X-ray luminosity has remained for a few million years the same as it is now (the stationary scenario). We see that scattered AGN emission contributes of the order of 1% at $\rho \sim 200$ kpc. It then follows that the Cyg A luminosity should have been an order of magnitude higher in the past (i.e. $L_X \sim 5 \times 10^{45} \text{ erg s}^{-1}$) for scattered AGN radiation to contribute $\sim 10\%$ to the strong X-ray lines observed from the intracluster gas (see Fig. 3.11).

We can also use the available *Chandra* data on the X-ray continuum emission from the Cyg A cluster to find upper limits on the past X-ray luminosity of its central source. We adopt the following parameters for this analysis: $E = 8$ keV – the maximum photon energy at which thermal bremsstrahlung emission is still detected, and $\rho_{\text{min}} = 10^2$ kpc and $\rho_{\text{max}} = 6 \times 10^2$ kpc – the boundaries of the region that is well explored with *Chandra*. We plot the resulting upper limits in Fig. 3.11b. We see that the current constraints are very weak because of the high temperature (~ 7 keV) of the intracluster gas. For comparison (see Fig. 3.11b), arcminute-resolution observations of the Cyg A cluster at $E \sim 40$ keV could provide limits on its past luminosity similar to those obtainable by mapping the cluster in resonance lines (see Fig. 3.11a).

3.5 Discussion

The main results of this chapter are as follows.

- We have demonstrated that there are two viable observational strategies for constraining the past X-ray luminosity of galactic nuclei with the next generation of X-ray telescopes. One is to search for scattered AGN radiation in the spectral continuum at high energies $E \gg kT(1+z)$, and the other is to perform imaging in bright resonance X-ray lines. The first approach appears to be particularly promising for studying distant (at $z \gtrsim 0.5$) powerful quasars and their environments (section 3.3.2).

3 Constraining the past X-ray luminosity of AGN in clusters of galaxies

- We have shown that the relative contribution of scattered radiation is typically larger by a significant factor of 3–10 in a resonance line than in the neighbouring continuum (section 3.2).
- We have estimated the level of constraints that could be derived from future observations on the past X-ray luminosity of the nearby M87 and Cyg A active galaxies (section 3.4). The upper limits imposed by the available *XMM-Newton* and *Chandra* X-ray continuum data are typically 1–2 orders of magnitude weaker.

Although we have been mostly discussing clusters of galaxies and their central dominant galaxies, the same method can also be applied to groups of galaxies and isolated giant elliptical galaxies, which also are large reservoirs of hot ionised gas capable of scattering AGN radiation. The main advantage of clusters is the larger extent of intracluster gas, which enables studying previous galactic activity on longer timescales (up to a few times 10^6 years for the richest clusters) than in the case of groups of galaxies and early-type galaxies (up to a few times 10^5 years). On the other hand, the latter two classes of objects have their own advantage that typical gas temperatures for them are $kT \sim 1$ keV and the factor $\exp(E/kT)$ becomes significant already in the standard X-ray band (< 10 keV). In particular, one can use the $K\alpha$ line of He-like iron at 6.7 keV. Indeed, the corresponding ions (Fe XXV) are still abundant at such low temperatures, but collisional excitation of the ions leading to emission in the line is already inefficient.

Although we have only considered the case where the AGN is an isotropic source, in reality angular anisotropy at some level is expected. Therefore, the contribution of scattered emission from the AGN to the surface brightness may be larger or smaller in some regions than predicted assuming source isotropy. We refer the reader to chapter 4 and the papers by Gilfanov et al. (1987a) and Wise & Sarazin (1990b) for a detailed discussion of scattered surface brightness profiles that may arise in the case of beamed source emission.

In the discussion of our simulations for the M87 and Cyg A galaxies and the associated clusters of galaxies we used a fiducial value of 10% as the minimum detectable contribution of scattered AGN emission to a resonance line. We realize that significant efforts will be required to achieve this or better detection level experimentally. One difficulty is that the measured surface brightness is the integral of emission (thermal plus scattered) along a given line of sight, and there may be present gas with different temperatures and element abundances along this line of sight. Both types of variations will have an effect on the equivalent line width. In principle it should be possible to determine and subtract the underlying temperature and abundance radial trends from a careful analysis of the spectral-imaging data. The remaining uncertainties are expected to be largest for

cluster central regions, where both the gas temperature and element abundances vary significantly, for example in the M87 case. On the other hand, this problem is not expected to be severe outside cluster cores. For example, in the Cyg A cluster the gas appears to be nearly isotropic outside the central ~ 200 kpc (see Smith et al. (2002)), whereas the equivalent width of the 6.7 keV iron emission line changes by only $\sim 10\%$ when the gas temperature varies by 0.5 keV around $kT \sim 7.5$ keV. Therefore, achieving the 10% detection level appears realistic.

It is clear that the potential of the method can be fully realized only when it is possible to resolve the interesting resonance lines from neighbouring lines. Indeed, lines other than resonance lines can contribute significantly to the intrinsic emission of the gas, but little to the scattered AGN emission. Moreover, it is desirable that all important lines in blends be resolved, such as the permitted, intercombination and forbidden lines in the complex around the 6.7 keV (Fe XXV $K\alpha$) line. Even a small contribution of scattered emission from the AGN could then be made manifest by comparing the surface brightness profiles measured in these lines. We are therefore looking forward to future high-energy astrophysics missions such as *Astro-E2*, *Constellation-X* and *XEUS* that will provide the required energy resolution (\sim a few eV).

Finally, we would like to note that the constraints on the past AGN X-ray luminosity could be further improved by means of X-ray polarimetry, especially if it became possible to measure polarisation in X-ray resonance lines. The radiation of a central source gets strongly polarised upon scattering in a beta-cluster (with a typical resulting degree of polarisation $P \sim 60\%$, Sunyaev 1982), whereas the intrinsic emission of the intracluster gas in X-ray resonance lines is also polarised but to a much lesser degree ($P \lesssim 10\%$, Sazonov et al. 2002). Thus, even a few per cent contribution of scattered AGN radiation to the surface brightness in a resonance line would be manifest in polarimetric observations.

3 Constraining the past X-ray luminosity of AGN in clusters of galaxies

Ihr Leben werde von Anfang an in einer Welt der Märchen hingelebt, und sie sprächen ebenso leicht von den wilden Feenpalästen hinter den Bergen wie von dem stummen Gewaltigen in der Wolke, der großen Macht, die dort oben im Raume haust und Sterne kaut.

Knut Hamsun, “Mysterien”

4

Scattering in the vicinity of relativistic jets

Abstract

Relativistic jets of radio loud active galactic nuclei (AGN) produce highly directed, intense beams of radiation. A fraction of this beamed radiation scatters on the thermal plasma generally surrounding an AGN. The morphology of the scattered emission can thus provide constraints on the physical properties of the jet. We present a model to study the feasibility of constraining the parameters of a jet, especially its inclination angle and bulk Lorentz factor in this way. We apply our model to the well studied jet of M87 and the surrounding diffuse gas and find that the observational limits of the surface brightness measured in the region of the putative counterjet provide the tightest constraints on the jet parameters consistent with constraints derived by other methods. We briefly discuss the applicability of our model to other sources exhibiting relativistic motions.

4.1 Introduction

Giant ellipticals in the central parts of clusters of galaxies often harbour an active galactic nucleus (AGN) which is believed to be powered by a supermassive black hole. X-ray observations have revealed that these AGN are surrounded by an atmosphere consisting of a hot and tenuous thermal plasma that fills the intracluster

4 Scattering in the vicinity of relativistic jets

space. The optical depth for Thomson scattering due to the free electrons present in this plasma reaches values of the order of $10^{-3} - 10^{-2}$. Therefore, up to one per cent of the luminosity of an AGN radiating in such an environment will be scattered on the free thermal electrons and this scattered radiation will be highly polarised (Sunyaev 1982).

A rather interesting situation arises in the case of an AGN powering a radio galaxy through a pair of relativistic jets which emit synchrotron radiation. The radiation produced by the relativistic particles gyrating along the magnetic fields of the jet is strongly beamed, i.e. the radiation field is highly anisotropic in the vicinity of the jets, due to well known relativistic effects.

The free electrons present in the hot thermal plasma, on the other hand, are distributed in a more or less spherically symmetrical way around the AGN. The electrons located close to the jet are exposed to the largest radiative flux and, therefore, will be the strongest sources of scattered radiation. Thus, the surface brightness profile of the electron scattered component should reflect the anisotropy of the jet emission and could provide information about the intrinsic jet properties. Combining this information with knowledge about the density distribution of the scattering gas, which for instance is obtainable through X-ray observations, might enable one to gain information about such parameters as the inclination angle of the jet axis towards the line of sight and the bulk Lorentz factor of the jet flow. The feasibility of this method will be studied in this chapter.

The “standard model” of extragalactic jets (Blandford & Rees (1974); Scheuer (1974)) describes such objects as intrinsically symmetric structures. The different appearances of the jet pointing towards the observer in comparison with the one pointing away from the observer, the so-called counterjet, stems primarily from the orientation of the oppositely directed axes of these jets with respect to the observer. In the case of a small inclination angle and a large Lorentz factor the counterjet might be rendered practically invisible, as is presumably the case in e.g. M87, offering only indirect evidence for its existence in the form of e.g. corresponding hotspots and radio lobes.

With respect to the question addressed in this chapter, however, it is important to note that the electrons being illuminated by the counterjet are exposed to and scatter as much radiation as the electrons located on the side of the jet. The only difference obviously being that the photons scattered by electrons located on the side of the counterjet have to travel larger distances in order to reach the distant observer than photons scattered by electrons located on the side of the jet.

The observational problem related to the detection of the discussed effect against the “background” produced by other sources of radio emission, e.g. the jets themselves, radio lobes etc., should be least demanding in the region of the counterjet. In fact one can envisage a situation where the jet pointing away from the observer

is beamed so strongly out of our direction that the jet is rendered practically invisible. However, the scattered light produced by the counterjet might still be visible and, thus, revealing its presence.

This idea was put forth by Gilfanov, Sunyaev & Churazov (1987a, henceforth GSC87) in a study of the scattered radiation originating from a point source, which was modeled to vary over time and to radiate non isotropically. It was shown that a highly directional compact source can produce extended jet-like structures in the surface brightness distribution of the scattered radiation. Furthermore, GSC87 demonstrated that in addition to a temporal variability a rotation as well as a precession of the directional radiation diagram of the central point source give rise to a large amount of morphological variety of the diffuse sources of radiation.

In the context of similar studies Wise & Sarazin (1990b) and Sarazin & Wise (1993) point out that observations of electron scattered profiles in cluster radio sources would provide a test of theories, which seek to unify disparate types of AGN, viz. the hypothesis that Fanaroff-Riley Class I (FR I) radio galaxies are the parent population of BL Lac objects. The radiation beam produced by a FR I radio source, which is pointing towards us in a BL Lac object, should be observable by means of the scattered radiation it produces.

For the purposes of the above-cited studies it was appropriate to model the radiation field produced by a relativistic jet as two oppositely directed radiation cones of constant intensity with a half-opening angle $\sim 1/\gamma$, where γ is the bulk Lorentz factor of the jet flow. Although this approximation certainly is valid on scales much larger than the jet itself (as will be confirmed by the results of this chapter), the effects caused by the exact shape of the beamed radiation pattern as well as by the motion of the radiation source itself should become noticeable as one “approaches” the jet, i.e. as one wants to study the behaviour of the scattered radiation in the vicinity of the jet. It is, therefore, one object of this chapter to study how well said approximation works on length scales which are comparable to the size of the jet itself.

This chapter is structured as follows. In Section 4.2 we describe our model and the accompanying equations. We apply our model to two scenarios in Section 4.3 and present the numerically obtained solutions thereof. We use these results in Section 4.4 to try to derive constraints on the inclination angle and the bulk Lorentz factor for the observationally well studied jet of M87. Section 4.5 closes with a summary of our results.

4.2 The model

Radio observations have revealed the complex structure of extragalactic jets (e.g. Bridle & Perley (1984)). Bright patches moving with apparent superluminal motion often alternate with fainter regions along a given jet. The origin of these bright patches, so-called knots, is still not fully understood. The most popular model at present, the internal shock model (Rees 1978), regards these knots as jet plasma excited by shocks moving along the jet. Particles are accelerated by these shocks and emit radiation by the synchrotron process as they gyrate along the magnetic field of the jet. According to this model, the velocity of a knot does not necessarily equal the actual velocity of the underlying fluid flow, should, however, represent an upper limit thereof.

In a different, somewhat less popular model these knots are interpreted as magnetised clouds of relativistic electrons, so-called plasmoids or blobs, being ejected out of the centre of an AGN by a cataclysmic event along the jet axes (e.g. van der Laan (1963)). The velocity of these blobs by definition corresponds to the velocity of the jet flow.

Irrespective of which of the above models is “correct”, in the following sections it is our aim to construct a simple albeit realistic model of the radiation field produced by a two-sided, symmetric relativistic jet. According to our model the jet spans an inclination angle towards the line of sight θ , exhibits a bulk Lorentz factor γ and radiates with an intrinsic luminosity L_{jet} . We imagine the jet to be made up of several point sources moving along the jet axis, which we will henceforth call “blobs”.

We choose our system of coordinates as shown in Fig. 4.1. The electron number density $n_e(r)$ is distributed in a spherically symmetrical way about the centre of the AGN. The x- and y-axis span the plane of the sky, with the x-axis being the projection of the jet axis onto the plane of the sky. The z-axis is pointing towards the observer. The jet is inclined with respect to the line of sight by an angle θ and the counterjet by an angle $\pi - \theta$, respectively.

At a time $t = 0$ a first pair of blobs is created inside the nucleus of the AGN. Information about this event reaches the observer, located at a distance d along the z-axis, after a time $t = d/c$, where c is the speed of light. The blobs are assumed to move ballistically with a velocity $v = \beta c$ along the jet and the counterjet, respectively, wherein β is given by $\beta = \sqrt{1 - 1/\gamma^2}$. The motion of a blob can be described in the chosen coordinate system as

$$\mathbf{r}_{\text{blob}}(t) = \mathbf{r}_o + \mathbf{v}t = (x_o + v_x t, 0, z_o + v_z t), \quad (4.1)$$

with the projections of the blob velocity onto the coordinate axes $v_x = v \sin \theta$ and $v_z = v \cos \theta$, respectively. For a single pair of blobs x_o and z_o could be omitted.

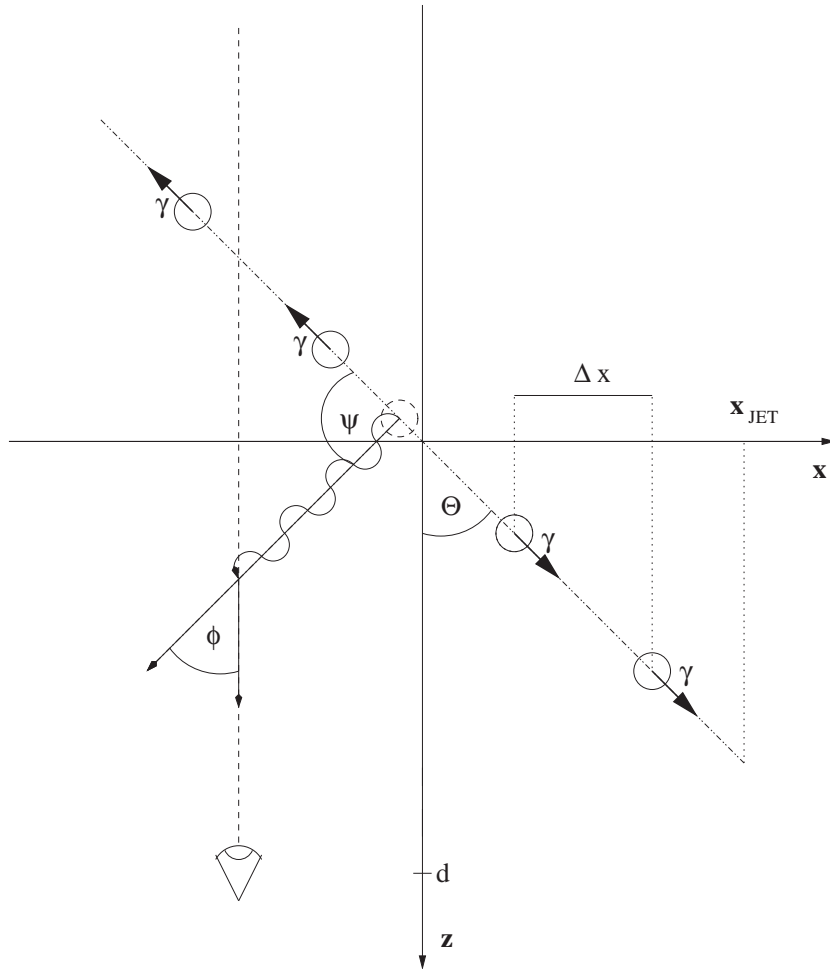


Figure 4.1: A sketch of the scenario studied in this chapter. An AGN situated at the origin produces a two-sided, symmetric jet lying in the (x,z) -plane. The jet’s radiation field is modeled by a chain of “blobs” ejected by the AGN at a constant rate along directions spanning an angle of θ and $\pi - \theta$ with the line of sight of the observer, who is located at a distance d along the z -axis. These blobs (in this case two blobs on each side) travel with a relativistic velocity βc corresponding to a Lorentz factor γ along the respective jet axes. The blobs are separated by a projected physical distance Δx . The actual observed apparent distance between the blobs Δx_{app} differs for the two sides of the jet. After a blob has traveled a projected distance of x_{jet} away from the AGN, according to our model the blob ceases radiating. An exemplary photon (curly line), which was produced by one of the blobs at a time when the blob was closer to the nucleus (position marked by a dashed circle), is emitted along a direction making an angle ψ with the direction of the blob motion along the counterjet. Further along its path the photon is scattered through an angle ϕ into the direction of the distant observer and received by him at a distance d .

4 Scattering in the vicinity of relativistic jets

However, these quantities become necessary once one wishes to keep track of several pairs of blobs over time as described in the later sections of this chapter.

The apparent velocity v_{app} of the blobs in the plane of the sky, as seen by the distant observer, is given by the well known formula for superluminal motion (Rees 1967)

$$v_{\text{app}} = \frac{v \sin \theta}{1 \mp \beta \cos \theta}. \quad (4.2)$$

After the blobs have traveled a physical distance l_{jet} corresponding to a projected distance $x_{\text{jet}} = l_{\text{jet}} \sin \theta$ along the jet and counterjet they cease radiating. The lifetime of these blobs is therefore given by $\tau = l_{\text{jet}}/v$. Due to time travel effects the apparent lifetime τ_{app} of the approaching blob differs from the one of the receding blob, which can be expressed as (e.g. Ryle & Longair (1967))

$$\tau_{\text{app}} = \tau(1 \mp \beta \cos \theta). \quad (4.3)$$

The lifetime in the reference frame of a blob would introduce an additional factor of γ because of the transversal Doppler effect.

After a period of time T a second pair of blobs is emitted in our model and so forth. If the AGN keeps producing blobs at such a constant rate, the spatial separation between blobs will remain constant. The apparent distance between two successive blobs Δx_{app} is simply the product of their apparent velocity and the period of the blob ejection cycle, viz.

$$\Delta x_{\text{app}} = v_{\text{app}} T = \frac{\Delta x}{1 \mp \beta \cos \theta}. \quad (4.4)$$

Obviously, the number of blobs per unit length of jet scales inversely proportional to this quantity. Since we are assuming the jet and the counterjet to be of equal lengths, this quantity is also proportional to the number of apparently active blobs at a given moment in time.

In the following sections the above-mentioned quantities are required in order to compute the apparent luminosity of the jet and the counterjet. The total intrinsic jet luminosity is just the sum of the individual blob luminosities of existing blobs. In our model we try to approach the limit of the radiation field produced by a continuous jet by increasing the number of blobs per unit length of the jet while keeping the assumed luminosity of the jet constant.

For optical thin conditions, which should be a valid approximation in the present case, the scattered surface brightness at coordinates x, y on the plane of the sky and at a time of observation t is given by the integral over the emissivity due to scattering along the corresponding line of sight

$$I_{\nu}^{\text{sc}}(x, y, t) = \int_{z_{\text{min}}}^{z_{\text{max}}} j_{\nu}^{\text{sc}}(\mathbf{r}, t) dz, \quad (4.5)$$

where \mathbf{r} is the radius vector of the point of scattering and z_{\min} and z_{\max} are the boundaries of integration, which as will be described in more detail further below depend themselves upon the position on the plane of the sky and the time of observation, i.e. x , y and t .

In the optical thin approximation the emissivity due to scattering can be expressed as

$$j_{\nu}^{\text{sc}}(\mathbf{r}, t) = n_e(\mathbf{r}) \sum_{\text{blobs}} \frac{P_{\nu}(\mathbf{n}, t')}{|\mathbf{r} - \mathbf{r}_{\text{blob}}(t')|^2} \left(\frac{d\sigma}{d\Omega} \right), \quad (4.6)$$

where $n_e(\mathbf{r})$ is the electron number density at the position \mathbf{r} , $P_{\nu}(\mathbf{n}, t')$ the spectral power per unit solid angle emitted by a blob at a “retarded time” t' at a position $\mathbf{r}_{\text{blob}}(t')$ into a direction defined by the unit vector \mathbf{n} and $(d\sigma/d\Omega)$ the differential scattering cross section. The unit vector pointing from the retarded position of the blob towards the point of scattering is given by

$$\mathbf{n} = \frac{\mathbf{r} - \mathbf{r}_{\text{blob}}(t')}{|\mathbf{r} - \mathbf{r}_{\text{blob}}(t')|}. \quad (4.7)$$

In order to evaluate the scattered surface brightness at a time of observation t , the corresponding retarded time t' has to be computed. The received photon must have traveled from its point of emission, i.e. the position of the blob at a time t' , via the point of scattering to the distant observer. The relation between the time of observation t and the retarded time t' , therefore, is given by the following expression

$$c(t - t') = d - z + |\mathbf{r} - \mathbf{r}_{\text{blob}}(t')|. \quad (4.8)$$

Solving this implicit equation for t' yields

$$t' = \gamma^2 \frac{A - \sqrt{A^2 - c^2 B / \gamma^2}}{c^2}, \quad (4.9)$$

with

$$A = c^2 t - v_x(x - x_o) - v_z(z - z_o) - c(d - z)$$

and

$$B = (ct - (d - z))^2 - ((x - x_o)^2 + y^2 + (z - z_o)^2).$$

Eq. 4.9 enables one to compute the position of the blob at a time t' as a function of the time of observation t and the point of scattering with coordinates x , y and z .

4 Scattering in the vicinity of relativistic jets

We assume a blob to emit synchrotron radiation with a spectral index α (in the following sections we will adopt a value of $\alpha = 0.5$, which is commonly observed in the spectra of radio jets). Thus, the spectral luminosity is given by

$$L_\nu = L_\nu^o \left(\frac{\nu_o}{\nu} \right)^\alpha. \quad (4.10)$$

Each blob radiates at an intrinsic rate of $L_\nu^o = 4\pi P_\nu^o$. We assume the intrinsic luminosity of a blob to remain constant over its lifetime. The relation between the spectral luminosity per unit solid angle in the observer's frame, i.e. the rest frame of the scattering electron or equivalently the rest frame of the distant observer, and in the rest frame of a blob is given by (e.g. Rybicki & Lightman (1979))

$$P_\nu(\mathbf{n}) = \delta^{3+\alpha} P_\nu^o = \left(\frac{1}{\gamma(1 - \beta \cos \psi)} \right)^{3+\alpha} P_\nu^o, \quad (4.11)$$

where δ is the Doppler or beaming factor.

The angle between the direction of motion of the blob and the line connecting the retarded position of the blob, i.e. the position of the blob at a time t' , and the point of scattering ψ can be computed as follows. The cosine of this angle is given by the scalar product of \mathbf{n} and the unit vector along the jet axis given by $\mathbf{e}_{\text{jet}} = (\sin \theta, 0, \cos \theta)$. One thus obtains

$$\cos \psi = \frac{\sin \theta (x - x_{\text{blob}}) + \cos \theta (z - z_{\text{blob}})}{\sqrt{(x - x_{\text{blob}})^2 + y^2 + (z - z_{\text{blob}})^2}}, \quad (4.12)$$

where x_{blob} and z_{blob} are computed according to Eq. 4.1.

Since we are considering photons produced by the synchrotron process and since the scattering electrons have a temperature of several keVs, it is appropriate to use the differential cross section for Thomson scattering, i.e.

$$\left(\frac{d\sigma}{d\Omega} \right) = \frac{3\sigma_{\text{T}}}{16\pi} (1 + \cos^2 \phi), \quad (4.13)$$

where σ_{T} is the Thomson cross section.

The angle between the line connecting the retarded blob position and the line of sight can be computed analogously to the angle ψ . The relation $\cos \phi = \mathbf{e}_z \cdot \mathbf{n}$, where \mathbf{e}_z denotes the unit vector along the z-axis, yields

$$\cos \phi = \frac{z - z_{\text{blob}}}{\sqrt{(x - x_{\text{blob}})^2 + y^2 + (z - z_{\text{blob}})^2}}. \quad (4.14)$$

The density profile of the hot electron gas surrounding an AGN located inside a central galaxy of a cluster can be derived by means of the observed X-ray surface brightness profile produced by this gas. Since the computations in our model are generally performed numerically, any density distribution could be used in principle. However, for the sake of simplicity we are assuming for the time being a density distribution according to the widely used beta profile (Cavaliere & Fusco-Femiano 1976)

$$n_e(r) = \frac{n_e^o}{(1 + (r/r_c)^2)^{\frac{3}{2}\beta_c}}, \quad (4.15)$$

which is fully parametrised by the normalisation of the electron number density n_e^o , the core radius r_c and the β_c parameter. The application of our results to the jet of M87 in a later section, however, will use a recently determined density profile for this object.

Finally the integration boundaries z_{\min} and z_{\max} of the integral occurring in Eq. 4.5 have to be computed. These quantities are functions of the position on the plane of the sky x, y and the time of observation t and can be considered as two surfaces evolving with time. These surfaces are defined as the loci of scattering sites giving a fixed time delay for photons traveling from their point of emission to the distant observer, which divide space into three distinct regions: one region that scatters photons originating from the blob during its existence and two regions that cannot scatter any photons since either the source has not turned on yet or has already switched off.

For a stationary source of radiation the shape of these surfaces is that of a paraboloid¹ with the radiation source at the apex, which can be described e.g. by the following formula (e.g. Sunyaev & Churazov (1998))

$$z = \frac{1}{2} \left(\frac{x^2 + y^2}{ct} - c^2(t - d/c)^2 \right). \quad (4.16)$$

In the case of a moving radiation source z_{\min} and z_{\max} can be computed by setting Eq. 4.9 equal to t'_{\min} and t'_{\max} , respectively, where t'_{\min} is the time the blob started radiating and t'_{\max} the time the blob stopped radiating. Solving this equation for z_{\min} and z_{\max} , respectively, it turns out that z_{\min} also can be described by Eq. 4.16. This, however, is actually not surprising, because our model was set up in a way that a blob is created in the nucleus of the AGN corresponding to our origin of coordinates.

¹It should be noted that the paraboloid is an approximation to the more general case of an ellipsoid, which is valid for the case of the source of radiation and the scattering site being at large distances from the observer. The more general case has been applied in chapter 2, i.e. the study of the scattering of radiation produced by the supermassive black hole at the centre of the Milky Way by giant molecular clouds located in the Galactic molecular ring.

4 Scattering in the vicinity of relativistic jets

Concerning z_{\max} the result is just a generalisation of Eq. 4.16 describing the loci of equal travel times from a stationary source located at the origin to the observer, i.e.

$$z_{\max} = \frac{1}{2} \left(\frac{(x - x_{\text{blob}}(t'_{\max}))^2 + y^2 + z_{\text{blob}}(t'_{\max})^2}{ct} - c^2(t'_{\max} - (t - d/c))^2 \right). \quad (4.17)$$

This equation describes a similar paraboloid as Eq. 4.16 except that its apex corresponds to the point in space where the blob ceases radiating.

With the above equations at hand the remaining problem turns out to be a function of the variables x , y , and t , the free parameters being the intrinsic spectral luminosity of the blob or jet L_{ν}° , the bulk Lorentz factor γ , the inclination angle θ , the parameters of the electron density distribution, i.e. n_e° , β_c and r_c , and the length of the jet l_{jet} , which together with a given Lorentz factor corresponds to a given lifetime of a blob.

4.3 Results

Using Eq. 4.5 one is now in a position to compute the surface brightness of the diffuse scattered emission for a given scenario as a function of the position on the plane of the sky and the time of observation. In the following sections we will use the brightness temperature more commonly used in radio astronomy to express our results, i.e.

$$T_{\text{b}}^{\text{sc}} = \frac{\lambda^2}{2k_{\text{B}}} I_{\nu}^{\text{sc}}, \quad (4.18)$$

where k_{B} is Boltzmann's constant. A wavelength of observation of 6 cm is assumed corresponding to a frequency of about 5 GHz.

4.3.1 Single ejection

A first scenario to apply our model to is the single ejection of a pair of blobs. In order to compare the results of the present section with the results of later sections we have chosen the following set of parameters as a reference model which may be representative of an ‘‘average’’ jet originating in the nucleus of the central galaxy of an ‘‘average’’ cluster of galaxies: $\gamma = 5$, $\theta = 30^{\circ}$, $L_{\nu}^{\circ} = 10^{32} \text{ erg s}^{-1} \text{ Hz}^{-1}$, $l_{\text{jet}} = 2 \text{ kpc}$, $n_e^{\circ} = 10^{-3} \text{ cm}^{-3}$, $\beta_c = 2/3$ and $r_c = 10 \text{ kpc}$. Furthermore, we place the source at a distance of 16 Mpc from the observer. The corresponding observed flux is about $8.5 \times 10^2 \text{ Jy}$. For the chosen set of parameters the blobs have a ‘‘lifetime’’ of about 6.800 years corresponding to an apparent lifetime of the approaching blob

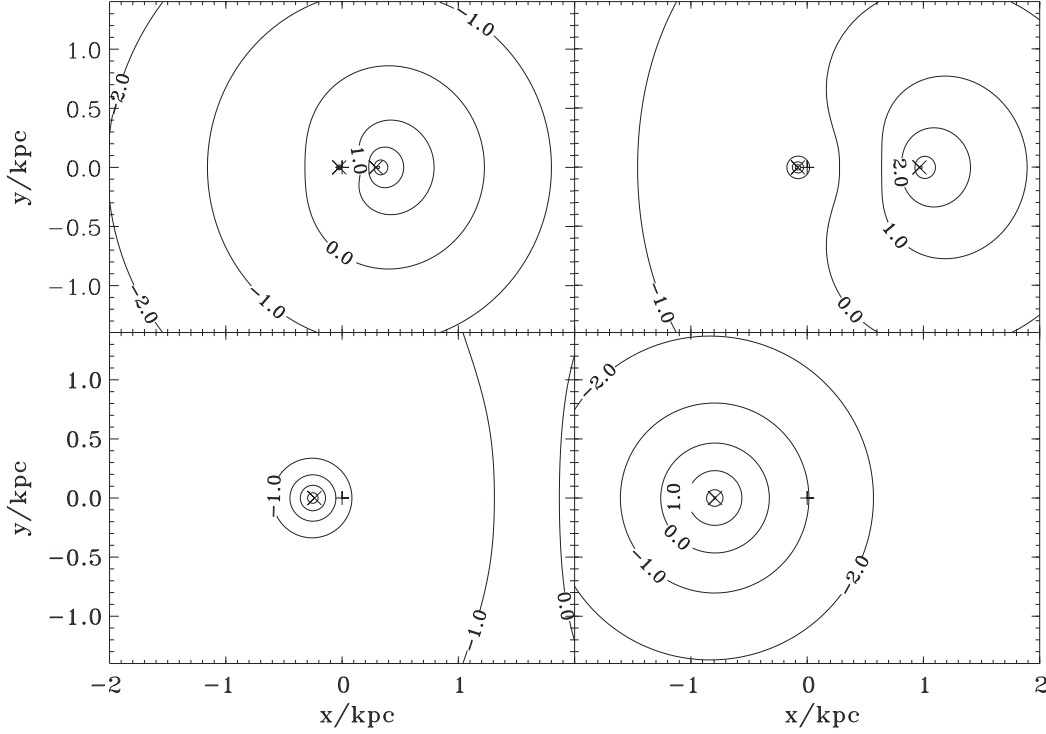


Figure 4.2: Contour plots of the brightness temperature of the scattered radiation three hundred (upper left), one thousand (upper right), three thousand (lower left) and ten thousand (lower right) years after the ejection of a pair of blobs with an inclination angle of $\theta = 30^\circ$ and a Lorentz factor of $\gamma = 5$. The blob moving to the right is approaching the observer. Beyond a projected distance of 1 kpc from the nucleus the blobs cease to radiate. The positions of the nucleus and the approaching and the receding blob are marked by a plus sign and by crosses, respectively. Logarithmic contour levels are shown down to $\log T_b = -2$.

of about 1.000 and of the receding blob of about 12.000 years, respectively. Using Eq. 4.2 the apparent velocities can be computed and turn out to be $3.23c$ (about 1.000 parsec per 1.000 years) for the approaching blob and $0.27c$ (about 80 parsec per 1.000 years) for the receding blob, respectively. As can be taken from Eqs. 4.5 and 4.6 our results easily can be converted to a different density normalisation or a different intrinsic luminosity, since the scattered surface brightness just scales linearly with these quantities.

4 Scattering in the vicinity of relativistic jets

4.3.1.1 Brightness Temperature

In Fig. 4.2 we are plotting contours of equal brightness temperature of the scattered radiation in the plane of the sky three hundred, one thousand, three thousand and ten thousand years after the ejection of a pair of blobs out of the nucleus of an AGN for the above chosen set of parameters. The two blobs travel a projected distance of 1 kpc along the positive and negative x-axis, respectively, and then stop to radiate, wherein the blob moving to the right is approaching the observer.

In the first snapshot three hundred years after the ejection of the pair of blobs the scattered radiation due to the approaching blob is already rather extended, whereas the scattered radiation produced by the receding blob is barely visible at the centre. The scattered surface brightness stemming from the approaching blob has already reached a maximum value of more than 10^4 Kelvin and the position of this maximum coincides with the apparent position of the approaching blob. This maximum is about 300 pc distant from the nucleus. Although the distribution of the scattered surface brightness due to the approaching blob is symmetric with respect to the x-axis, such a symmetry is not given with respect to the direction perpendicular thereto. Rather some contour lines of the scattered radiation produced by the approaching blob adopt a more “kidney-like” shape, which becomes even more pronounced in the following snapshot seven hundred years later. We have observed this shape in our numerical computations in particular for the cases of small inclination angles and large Lorentz factors. However, the contour lines at further distances from the nucleus exhibit a spherically symmetric shape.

The second snapshot one thousand years after the ejection of the pair of blobs shows the morphology of the brightness temperature of the scattered emission at a time just before the approaching blob switches off, i.e. reaches a projected distance of 1 kpc from the nucleus. Compared with the previous snapshot the pattern of scattered radiation produced by the approaching blob has spread out further, while the maximum brightness temperature has decreased somewhat. Close to the nucleus the scattered radiation originating from the receding blob is just starting to become more extended, but already has reached a maximum brightness temperature of almost 10^4 Kelvin. As can be taken from this and especially the two following snapshots the scattering pattern produced by the receding blob exhibits a more spherically symmetric shape than the scattering pattern produced by the approaching blob.

Two thousand years later, i.e. three thousand years after the ejection of the pair of blobs, the maximum of scattered radiation due to the approaching blob has already moved beyond the scales of Fig. 4.2, i.e. to distances more than 2 kpc away from the nucleus. Only a single contour line corresponding to a brightness temperature of 1 Kelvin is still visible on the right side of the plot. As the ap-

proaching blob already has switched off, this “afterglow” of scattered radiation keeps on moving away from the nucleus with the same apparent velocity as the approaching blob during its existence. The maximum of this afterglow actually is about 3 kpc distant from the nucleus and will keep on moving to even larger distances, as time progresses further, while at the same time decreasing in brightness until completely fading away. The scattered radiation of the receding blob, on the other hand, still can be seen centered at a distance of about 250 pc to the left of the nucleus.

Finally, after ten thousand years the scattered radiation produced by the approaching blob fully has disappeared (the maximum would be located at a distance of almost 10 kpc from the nucleus now) and only the pattern of scattered radiation produced by the receding blob can be observed. In the meantime, this pattern of scattered radiation due to the receding blob has become more extended, while traveling out to a distance of about 800 pc. It should be noted that as in the case of the approaching blob, at still later times one can observe an “afterglow” of scattered radiation produced by the receding blob even after this blob has stopped radiating. Also this pattern of scattered radiation on the side of the receding blob keeps on moving with the same apparent velocity as the receding blob itself.

As already mentioned and as can be taken from Fig. 4.2 the respective maxima of the scattered surface brightnesses coincide with the respective apparent blob positions and, thus, both move with the same apparent velocity. We have verified that this holds true even for very large Lorentz factors, i.e. that the highest brightness temperature is found at the apparent position of a blob. For large Lorentz factors the scattered emission tends to become more “concentrated” around a blob.

The above results differ somewhat from the findings of GSC87, who found that for the approximation of two oppositely directed radiation cones a burst (equivalent to our blob lifetime) produces two pronounced maxima in the brightness distribution (see Fig. 2 of GSC87), wherein the maximum on the side of the cone pointing in the direction of the observer is fainter than the one on the side of the radiation cone pointing away from the observer. Such a behaviour was not observed in our computations. Furthermore, it was shown in GSC87, that using the adopted approximation the velocities of the fainter maximum and the brighter maximum can be given by a formula depending only on the inclination angle. Obviously, this approximation does not allow to derive any dependence on the Lorentz factor. As we have seen in our computations, however, the velocity of the scattering pattern produced by a blob is given by Eq. 4.2.

4 Scattering in the vicinity of relativistic jets

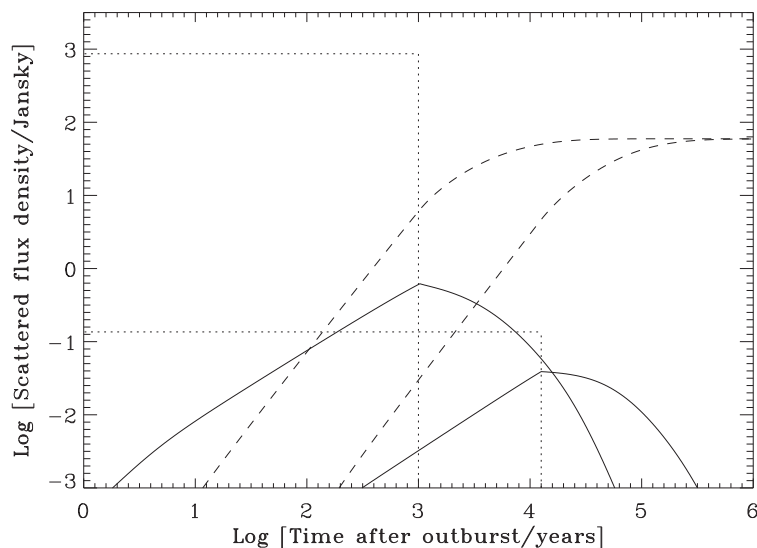


Figure 4.3: Temporal evolution of the scattered flux densities (solid lines), the apparent flux densities (dotted lines) and the fluences of scattered flux (dashed lines) for the approaching and the receding blob shown in Fig. 4.2. As long as the approaching blob keeps on radiating the ratio of its apparent flux density to its scattered flux density is larger than three orders of magnitude. After the blobs switch off (reflected by the kinks in the lightcurves of the scattered flux and the drop off of the apparent direct flux) an “afterglow” of scattered radiation remains. The fluence of the scattered flux for both the approaching as well as for the receding blob reaches a maximum value of about $2.4 \times 10^{-16} \text{ erg cm}^{-2} \text{ Hz}^{-1}$.

4.3.1.2 Flux and Fluence

With respect to our model a physically somewhat more “global” quantity than the scattered surface brightness is the total scattered flux originating from a blob. In Fig. 4.3 we are plotting the scattered flux densities, the apparent flux densities and the fluences produced by each blob of the pair of blobs shown in Fig. 4.2 as a function of time up to 10^6 years after the ejection. The fluxes are measured in units of Janskys, where 1 Jy corresponds to a flux of $10^{-23} \text{ erg cm}^{-2} \text{ s}^{-1} \text{ Hz}^{-1}$.

The general behaviour of the two blobs in time as exhibited in the contour plots shown in Fig. 4.2 and as described in the previous section is also reflected by the scattered fluxes produced by these blobs. Initially, the scattered flux due to the approaching blob dominates and increases linearly in time. About one thousand years after the ejection corresponding to the time when the approaching blob switches off, its scattered flux peaks at a maximum value of about 600 mJy. After

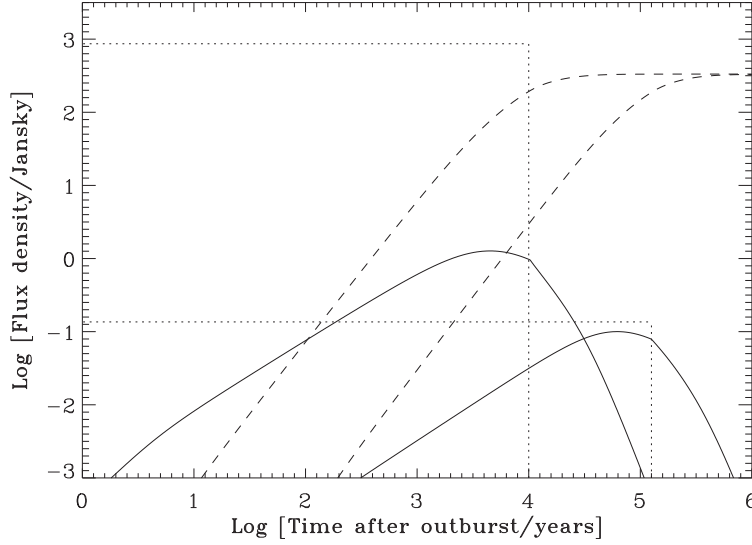


Figure 4.4: Temporal evolution of the scattered flux densities (solid lines), the apparent flux densities (dotted lines) and the fluences of scattered flux (dashed lines) for the same parameters as in Fig. 4.3 except that a jet length of 20 kpc has been chosen, i.e. the blobs have a lifetime that is an order of magnitude longer than the blobs shown in Fig. 4.3. For the receding blob the ratio of the scattered flux to the apparent direct flux approaches almost unity when its scattered flux density reaches its maximum value. The fluence of the scattered flux for both the approaching as well as for the receding blob reaches a maximum value of about $1.7 \times 10^{-15} \text{ erg cm}^{-2} \text{ Hz}^{-1}$.

the switch off an “afterglow” of scattered radiation remains for some time at a similar level of flux.

The lightcurve corresponding to the scattered flux due to the receding blob is similar in shape, however, peaks at a smaller maximum value and is shifted to later times. The scattered flux produced by the receding blob reaches its maximum value of about 40 mJy about 12,000 years after the ejection and remains at a similar flux level for almost 10^5 years after the switch off of the receding blob.

In order to estimate a characteristic size of the distribution of the scattered radiation produced by these blobs, i.e. the size of the region where the bulk of the scattered flux originates from, we have computed the flux coming from a circle of radius r as a function of this radius, wherein the circle is centered on the position of the blob or equivalently on the position of the maximum of the surface brightness distribution of the scattered radiation. Our results show that the size of this

4 Scattering in the vicinity of relativistic jets

characteristic region grows with time, remains, however, smaller than about 1 kpc for about 3×10^3 years for the approaching blob and for about 3×10^4 years for the receding blob.

In order to set the values for the scattered fluxes into context, we have plotted the apparent “direct” fluxes received from the approaching blob as well as from the receding blob for a comparison. Obviously these direct fluxes vanish once the blobs stop to radiate, as reflected by the drop off in flux after about 1.000 years and 12.000 years, respectively. While the approaching blob is active, i.e. radiating, the ratio of its apparent direct flux to its scattered flux is about 1.400. For the receding blob the ratio of the apparent direct flux to the scattered flux turns out to be about a factor of 3.

Fig. 4.4 is equivalent to Fig. 4.3 except that the blobs travel out to a physical distance which is an order of magnitude larger, i.e. $l_{\text{jet}} = 20$ kpc, before they stop radiating. Thus, compared with the pair of blobs of Fig. 4.3 also their lifetime is increased by an order of magnitude. Whereas the scattered fluxes of the blobs in Fig. 4.3 break off at a point in time when the scattered flux is still increasing, the scattered flux in Fig. 4.4 reaches a maximum and thereafter gradually declines before breaking off because of the switch off of the blobs. This decline is due to the decreasing density beyond distances of the order of the core radius of the density distribution, which in this case has been chosen to be 10 kpc. As the magnitude of the maximum scattered flux becomes larger in comparison to Fig. 4.3, the ratio of the apparent flux to the maximum scattered flux becomes correspondingly smaller. For the receding blob this ratio is approaching unity.

As we have seen the approaching and the receding blob exhibit a different behaviour, when studying the surface brightness profiles produced by these blobs (Fig. 4.2) or their scattered flux (Figs. 4.3 and 4.4). The brightness temperature of the scattered radiation produced by the approaching blob reaches higher values and is more extended than in the case of the receding blob. Thus, the corresponding scattered flux produced by the approaching blob for a given time is larger than the scattered flux of radiation originating from the receding blob as depicted in Figs. 4.3 and 4.4 given the blobs are still active. However, as also exhibited in Figs. 4.2 to 4.4 the apparent lifetime of the receding blob is correspondingly longer than the apparent lifetime of the approaching blob. It is, thus, interesting to look at the total time integrated fluxes produced by these blobs.

To this end, Figs. 4.3 and 4.4 also show the respective fluences, i.e. the time integrated fluxes, of the approaching and the receding blob. As can be taken from these figures these fluences approach the same values as one would expect. The fluence for the case shown in Fig. 4.4 turns out to be not quite a factor of ten larger than the fluence produced by the blobs shown in Fig. 4.3, because the density drops with distance from the nucleus.

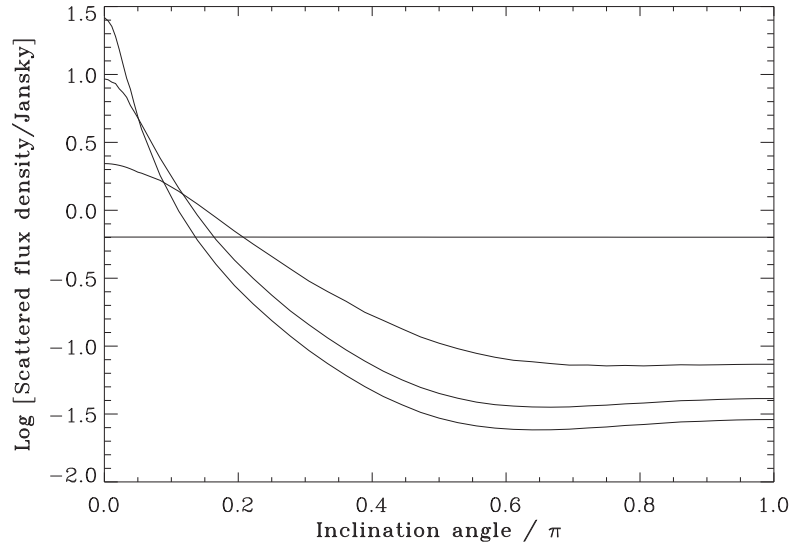


Figure 4.5: Maximum of the scattered flux density produced by a single blob as a function of the inclination angle for four different Lorentz factors, viz. 1 (stationary source), 2, 5 and 10 (the same parameters have been used as before). For small inclination angles the blob moving with a Lorentz factor of 10 is producing the largest scattered flux. Note that for very large inclination angles the maximum of the scattered flux slightly starts to increase again. This effect is caused by the angular dependence of the differential cross section for Thomson scattering which “amplifies” forward as well as backward scattering compared to a scattering at a right angle.

We now turn to the dependency of the maximum scattered flux produced by a single blob on the inclination angle and the Lorentz factor. Fig. 4.5 shows this maximum scattered flux for the case of a stationary blob (which obviously shows no dependence on the inclination angle) and three blobs moving with different Lorentz factors. For small inclination angles the blob with the largest Lorentz factor, i.e. $\gamma = 10$, produces the largest scattered flux, which decreases for larger inclination angles. It is interesting to note, however, that beyond a certain inclination angle the scattered flux slightly starts to increase again. We have verified that this behaviour is caused by the specific angular dependence of the Thomson scattering cross section which enhances forward and backward scattering compared to scatterings at different angles.

In order to be able to address the question, whether the scattered radiation discussed in this section might be observable at all, we have plotted in Fig. 4.6 the

4 Scattering in the vicinity of relativistic jets

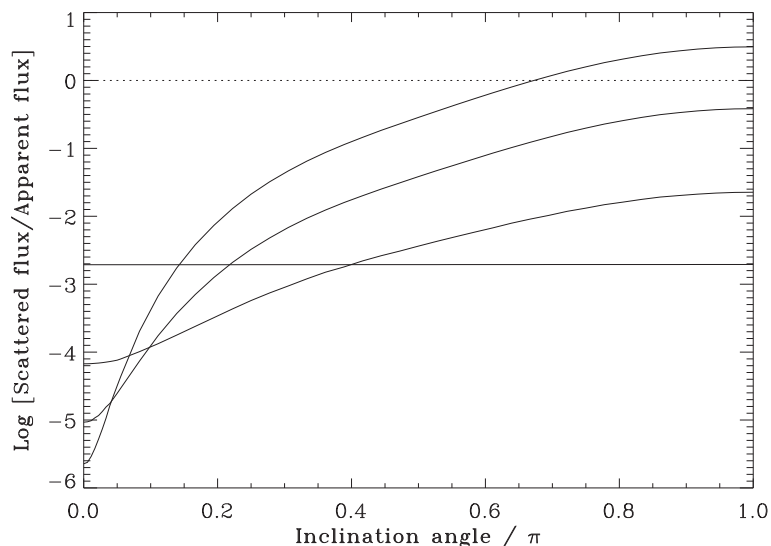


Figure 4.6: Ratio of the maximum of the scattered flux density to the apparent flux for a single blob as a function of the inclination angle of the direction of motion of the blob with respect to the line of sight for four different Lorentz factors, viz. 1, 2, 5 and 10. The ratio for the stationary source is an estimate of the optical depth for Thomson scattering of the surrounding gas, which in this case is about 1.85×10^{-3} . Given the assumed electron density and the corresponding Thomson depth, the ratio of the scattered flux to the apparent flux reaches unity at an inclination angle of about $2/3\pi$ for a Lorentz factor of 10. For even larger inclination angles the scattered flux becomes larger than the apparent flux.

ratio of the total scattered flux produced by a blob to its apparent direct flux as a function of the inclination angle for four different Lorentz factors, viz. 1 (stationary source), 2, 5 and 10. Since for a stationary point source the scattered flux is given by $F_{sc} = \tau_T F_o$ (Sunyaev 1982), this ratio should correspond to the optical depth for Thomson scattering. For the chosen electron density distribution the Thomson depth turns out to be about 1.85×10^{-3} .

Concerning the case of a moving blob, it can be taken from Fig. 4.6 that for small inclination angles the scattered flux is several orders of magnitude smaller than the direct flux, wherein this ratio decreases for larger Lorentz factors. As one goes to larger inclination angles, however, the ratio of the scattered flux to the direct flux increases substantially. For a Lorentz factor of 10 this ratio reaches unity at an inclination angle of about 120° . For even larger inclination angles the

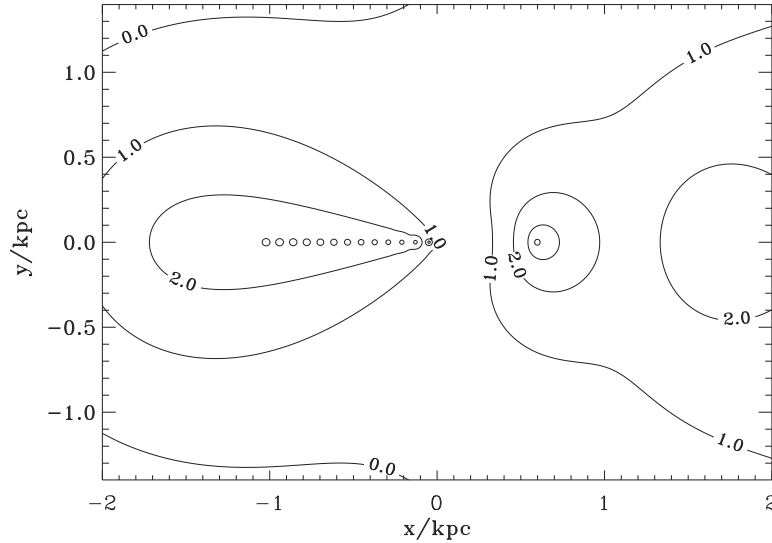


Figure 4.7: Contour plot of the brightness temperature of the scattered radiation about twenty thousand years after the onset of the jet activity, i.e. the ejection of the first pair of blobs. About every 1.000 years a further pair of blobs has been produced. The corresponding apparent distance between individual blobs is about 1 kpc for the approaching blobs on the right side of the nucleus and about 80 pc for the receding blobs on the left side of the nucleus.

flux of scattered radiation becomes larger than the flux of direct radiation given a Lorentz factor of 10. For Lorentz factors of 5 and below the ratio does not reach unity for the chosen set of parameters. However, since the scattered radiation is simply proportional to the electron density and the direct emission does not depend thereon, the ratio of these two quantities scales linearly with the assumed electron density.

4.3.2 Multiple ejections

In this section we will study a multiple blob scenario, i.e. instead of creating only a single pair of blobs a second pair of blobs is ejected after a certain period of time and so forth. If the ejection period is chosen to be short enough, the ambient scattering medium will “sense” no difference to a quasi-continuous ejection of radiating matter moving at relativistic velocities. As will become clear from the results presented in this section and as can be taken from Eqs. 4.5 and 4.6, the problem we are studying is linear in the contribution of each single blob. Thus, the

4 Scattering in the vicinity of relativistic jets

scattering pattern produced by several blobs essentially is just the sum of several spatially and temporally shifted scattering patterns produced by a single blob as illustrated in Fig. 4.2.

4.3.2.1 Brightness Temperature

Fig. 4.7 shows a contour plot of the brightness temperature of the scattered radiation about 20.000 years after the ejection of a first pair of blobs for the multiple blob scenario. A pair of blobs has been ejected every 1.000 years corresponding to an intrinsic spatial blob separation of about 300 pc. Given a Lorentz factor of 5 and an inclination angle of 30° , the apparent distances between two subsequent blobs can be computed according to Eq. 4.4 yielding an apparent distance of about 1 kpc between approaching blobs and about 80 pc between receding blobs, respectively. These different apparent distances between blobs for the jet and the counterjet side are readily apparent in Fig. 4.7. As before, we assume the blobs to switch off after having traveled a projected distance of 1 kpc. As, furthermore, can be taken from Fig. 4.7, the pattern of scattered radiation on the side of the receding blobs looks much “smoother” than the one on the jet side. However, as will become clear from the following figures, by reducing the blob separation further, also the scattering pattern on the side of the approaching blobs will adopt a more or less smooth shape.

In the following it is our aim to study the behaviour exhibited in Fig. 4.7 for a larger number of blobs, for longer times and on larger scales. To this end, we are plotting in Fig. 4.8 the brightness temperature of the scattered radiation as a function of position on the plane of the sky at 10^3 , 10^4 , 10^5 and 10^6 years after the onset of the assumed jet activity. Again, the blobs are ejected with an inclination angle of 30° with respect to the line of sight, move with a velocity corresponding to a Lorentz factor of 5 and stop radiating beyond a projected distance of 1 kpc. An intrinsic spatial separation of the blobs of 50 pc has been chosen corresponding to an ejection of a pair of blobs about every 170 years. Save to the larger spatial dimensions of the field of view, the contour plots shown in this figure are analogous to the contour plots shown in Figs. 4.2 and 4.7.

Over a time span of 10^6 years we are observing the gradual build up of a stationary scattering pattern initially on the side of the jet and thereafter on the side of the counterjet. In particular, it can be taken from the first snapshot in Fig. 4.8 that one thousand years after the onset of the jet activity the scattered radiation pattern begins to develop on the side of the approaching blobs, i.e. the side of the jet. Already at these early times the high brightness temperatures on the side of the approaching blobs adopt an elongated jet-like shape close to the nucleus. The contours of lower brightness temperatures at larger distances from

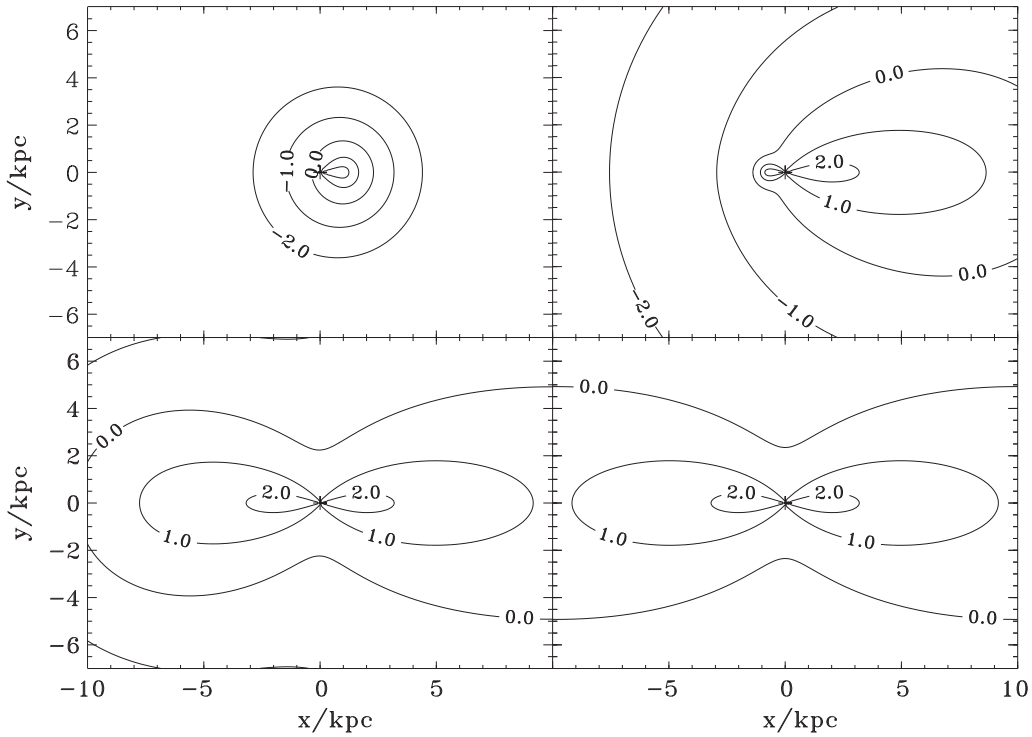


Figure 4.8: Contour plots of the brightness temperature of the scattered radiation 10^3 (upper left), 10^4 (upper right), 10^5 (lower left) and 10^6 (lower right) years after the onset of the jet activity, i.e. the ejection of the first pair of blobs. About every 170 years a further pair of blobs has been ejected. The position of the nucleus is marked by a plus sign. Logarithmic contour levels are shown down to $\log T_b = -2$.

the nucleus exhibit a more symmetric shape. On this scale one cannot discern any contribution to the scattered radiation produced by the blobs on the side of the counterjet yet.

However, 9.000 years later scattered radiation produced by the receding blobs can be observed up to a distance of 1 kpc from the nucleus exhibiting a jet-like shape similar to the one produced on the side of the jet in the earlier snapshot. The scattering pattern on the jet side, on the other hand, has in the meantime almost fully developed on the scales shown, especially in the vicinity of the nucleus. Further generations of approaching blobs will maintain this “steady state”.

One hundred thousand years after the onset of the jet activity, the picture is nearly symmetric with respect to the y -axis, i.e. the scattering patterns on the jet

4 Scattering in the vicinity of relativistic jets

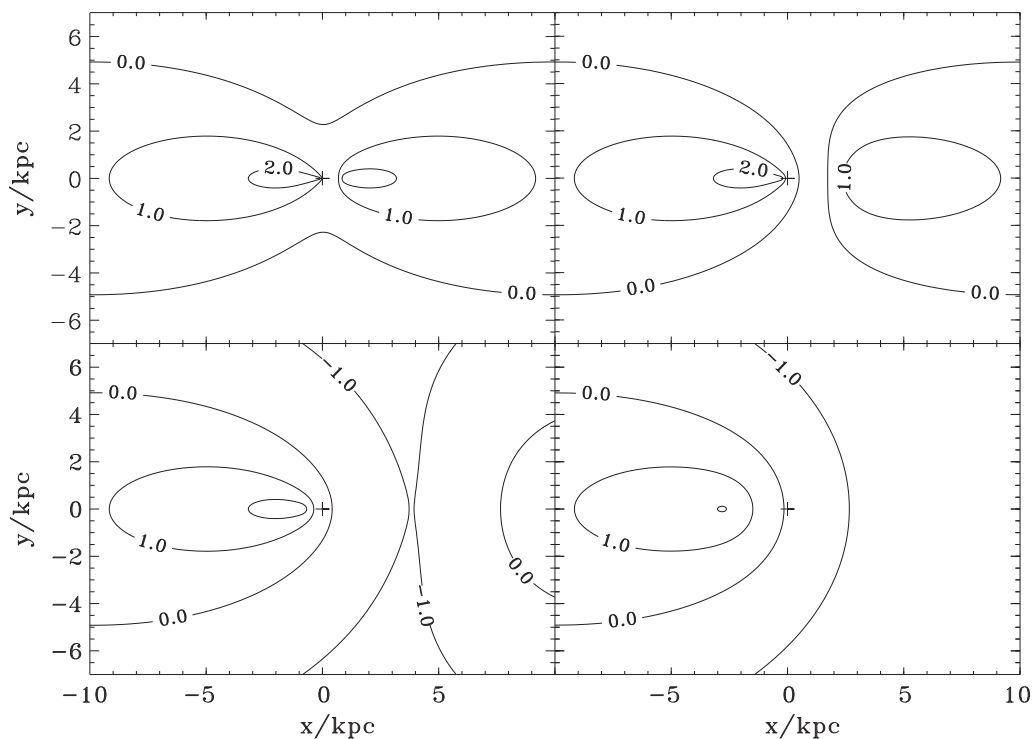


Figure 4.9: Contour plots of the brightness temperature of the scattered radiation one thousand (upper left), three thousand (upper right), ten thousand (lower left) and thirty thousand (lower right) years after the demise of the jet activity, i.e. the ejection of the last pair of blobs, which lasted for 10^6 years (corresponding to the snapshot shown in the lower right of Fig. 4.8). The position of the nucleus is marked by a plus sign. Logarithmic contour levels are shown down to $\log T_b = -2$.

and the counterjet side appear almost identical. Only for distances of about 10 kpc to the left of the nucleus the scattered radiation on the side of the counterjet is still a bit fainter compared with the corresponding regions on the jet side. In other words, the scattering pattern on the side of the counterjet has not “caught up” completely with the scattering pattern on the jet side yet, which as mentioned before by this time already has reached a stationary shape.

In the last snapshot illustrating the situation 10^6 years after the onset of the jet activity the whole pattern of scattered radiation has reached a symmetric, stationary shape. Differently put, if we would keep producing blobs at the adopted rate, the morphology exhibited by the scattered radiation obviously would not

change. This “steady-state” scattering pattern is reminiscent of the plot presented in GSC87 (see their Fig. 1), which was obtained by a point source radiating into two oppositely directed cones. Obviously, on the scales shown in Fig. 4.7 such an approximation produces similar results, since the projected length of the jet and the counterjet of 1 kpc is small compared to the dimensions of the whole system illustrated in this figure. Essentially, one can think of the final snapshot shown in Fig. 4.8 being made up of several “overlapping”, more or less spherically symmetric patterns produced by a single blob as shown in Fig. 4.2.

Now that we have been producing blobs for 10^6 years and the scattered surface brightness exhibits a symmetric shape, we want to study what happens in case the jet switches off, i.e. in case no more blobs are being ejected. Fig. 4.9 shows the effect of such a switch off by means of contour plots of the brightness temperature of the scattered radiation one thousand, three thousand, ten thousand and thirty thousand years after the demise of the jet activity.

Initially, the brightness temperature in the vicinity of the nucleus drops on the side of the jet. As time progresses, this region of reduced brightness moves out to larger distances from the nucleus. After about ten thousand years a similar behaviour can be observed on the side of the counterjet. By the time of thirty thousand years after the demise of the jet activity the scattered emission on the side of the jet has vanished completely. However, regions on the side of the counterjet being more distant from the nucleus still exhibit some brightness, wherein the maximum brightness temperature is located at about 3 kpc to the left of the nucleus. At even later times the maximum of this afterglow of scattered radiation will have traveled to greater distances from the nucleus and will have decreased further in brightness.

4.3.2.2 Flux and Fluence

As in the section discussing the scenario with a single pair of blobs, we now turn to the scattered fluxes in order to study how the general behaviour exhibited in Figs. 4.8 and 4.9 is reflected by these quantities.

Fig. 4.10 being similar to Figs. 4.3 and 4.4 shows the scattered flux, the direct flux and the fluence produced by the jet and the counterjet as a function of time after the onset of the jet activity in our multiple blob scenario. Given the assumed set of parameters, the scattered flux due to the counterjet reaches the same level as the scattered flux due to the jet after about three hundred thousand years corresponding to the stationary scattering pattern illustrated in the snapshot on the lower right of Fig. 4.8. However, as in the case of a single pair of blobs initially the flux due to the approaching blobs dominates over the flux of scattered radiation produced by the receding blobs. It should be noted that the lightcurve shown in

4 Scattering in the vicinity of relativistic jets

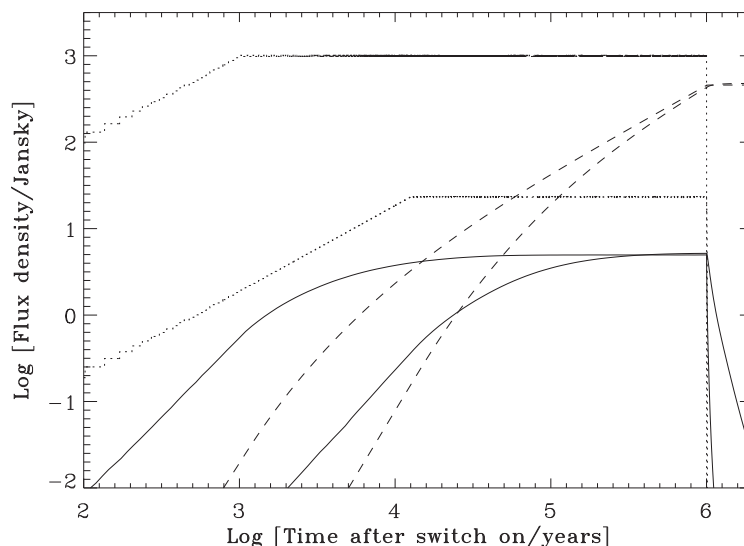


Figure 4.10: Temporal evolution of the scattered flux densities (solid lines), the apparent flux densities (dotted lines) and the fluences of scattered flux (dashed lines) for the jet and the counterjet shown in Figs. 4.8 and 4.9. After a time of about 3×10^5 years the counterjet produces the same amount of scattered flux as the jet as long as the source is active. The fluence of the scattered flux for both the jet as well as for the counterjet reaches a maximum value of about $4.6 \times 10^{-13} \text{ erg cm}^{-2} \text{ Hz}^{-1}$.

Fig. 4.10 is essentially just the sum of the lightcurves for a single blob as shown in Fig. 4.3 shifted by a constant time difference.

The behaviour of the scattered fluxes after the switch off is difficult to assess from Fig. 4.10. We, therefore, have plotted the scattered flux and the apparent flux after the switch-off in Fig. 4.11 using a different time axis. As in the case of a single pair of blobs, one can observe an afterglow of diffuse scattered radiation after the apparent fluxes have died away that lasts substantially longer on the side of the counterjet. Note that in this case the switch-off of the jet is not a simple step function, but rather the sum of multiple step functions shifted in time.

We now want to study the dependence of the quantities discussed above on the inclination angle and the Lorentz factor. To this end Fig. 4.12 shows stationary scattering patterns for four different inclination angles, viz. 15° , 30° , 60° and 90° . The other parameters have been chosen as in the previous examples. The scattering patterns in question that exhibit a symmetry with respect to the x- and the y-axis are reached after a quasi-continuous ejection of blobs for roughly 4×10^5 ,

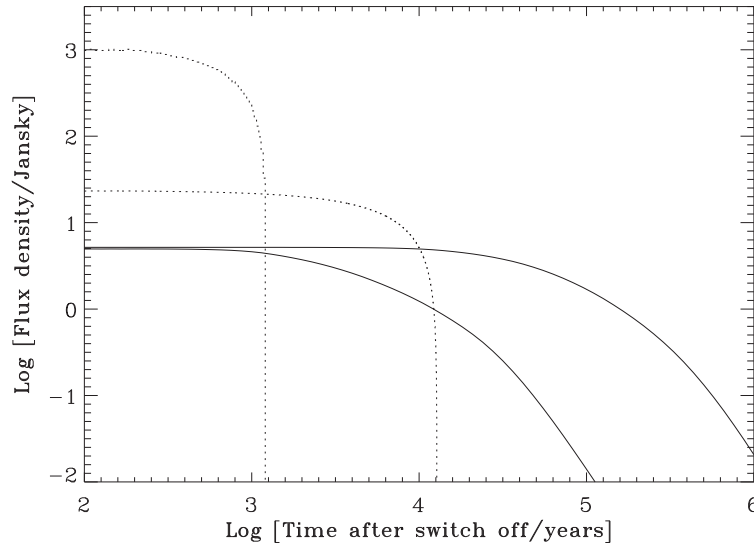


Figure 4.11: Temporal evolution of the scattered flux densities (solid lines) and the apparent flux densities (dotted lines) for the jet and the counterjet shown in Fig. 4.9 after the demise of the jet activity, which lasted for 10^6 years.

2.5×10^5 , 10^5 and 5×10^4 years, respectively. These values were estimated by computing the time, when the flux inside the region shown in the snapshots of Fig. 4.12 reaches and remains at the same constant value on the jet side as well as on the side of the counterjet. For this reason in the case of $\theta = 30^\circ$ the time to reach the steady state is a bit shorter than the time deduced from Fig. 4.10, because in that figure the total scattered flux is shown, to which regions beyond the scales of the snapshots given in Fig. 4.12 contribute.

The time needed to reach the stationary state obviously increases with decreasing inclination angle. The reason for this behaviour is as we have seen in the previous section that for a given Lorentz factor it takes the receding blobs apparently longer to travel out to the projected distance where they stop radiating.

Concerning the overall shape of the distribution of the scattered radiation, these scattering patterns appear more “elongated” along the x-axis for the cases where the jet axis lies close to the plane of the sky, i.e. inclination angles of roughly 90° . In other words, for these cases more flux is contributing to the total scattered flux from regions located at larger distances from the nucleus. It is interesting to compare these plots with the corresponding plots for a point source radiating into two oppositely directed cones as given in GSC87 for the case of $\theta = 90^\circ$ (see their Fig. 1) and by Wise & Sarazin (1990b) for the case of $\theta = 15^\circ$ and also $\theta = 90^\circ$ (see

4 Scattering in the vicinity of relativistic jets

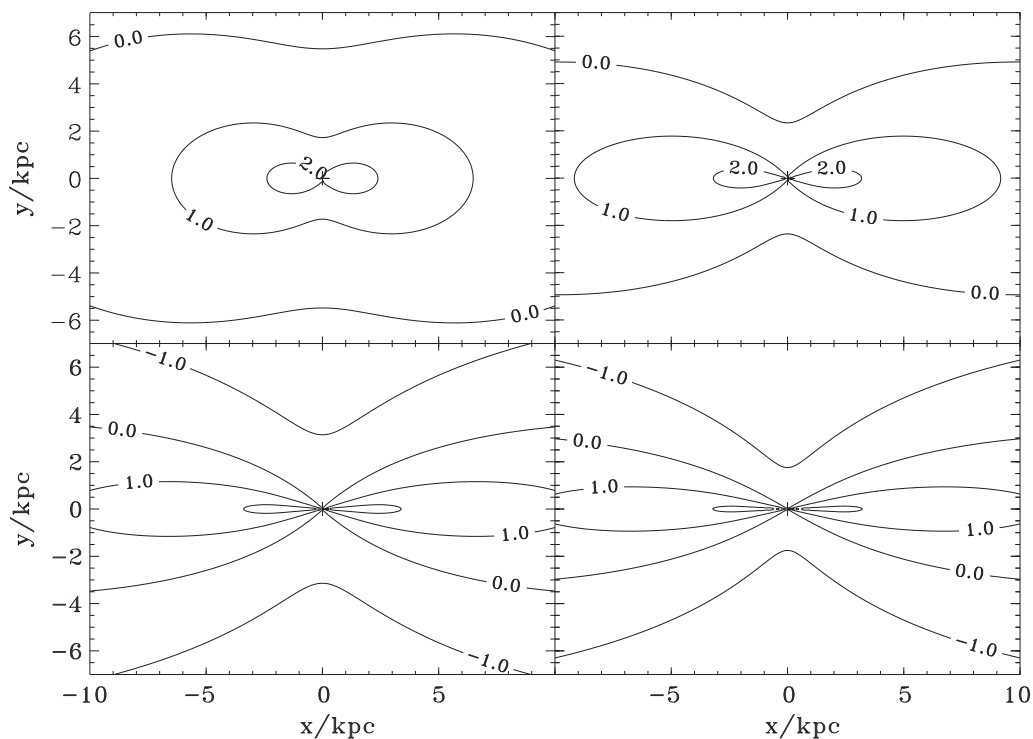


Figure 4.12: Contour plots of the brightness temperature of the scattered radiation for the stationary, symmetric case for an inclination angle of 15° (upper left), 30° (upper right), 60° (lower left) and 90° (lower right). The time required to reach such a stationary state is roughly 4×10^5 , 2.5×10^5 , 10^5 and 5×10^4 years, respectively. The position of the nucleus is marked by a plus sign.

their Fig. 7, assuming an opening angle of the cone having a half angular width of 15°). When looking for instance at the respective surface brightness distributions for the case where the jet axes lie in the plane of the sky it seems that taking into account the actual blob motion has the effect of stretching out the whole scattering pattern along the negative and positive x-axis, respectively. Obviously, the plots provided in the earlier studies cannot provide any brightness temperature for regions lying outside the assumed radiation cones. However, save to the above mentioned difference inside of the radiation cones the results appear qualitatively similar.

The above described behaviour is also apparent when looking at the dependence of the total scattered flux on the Lorentz factor and especially on the inclination angle. Fig. 4.13 shows the maximum of the scattered flux density produced by a

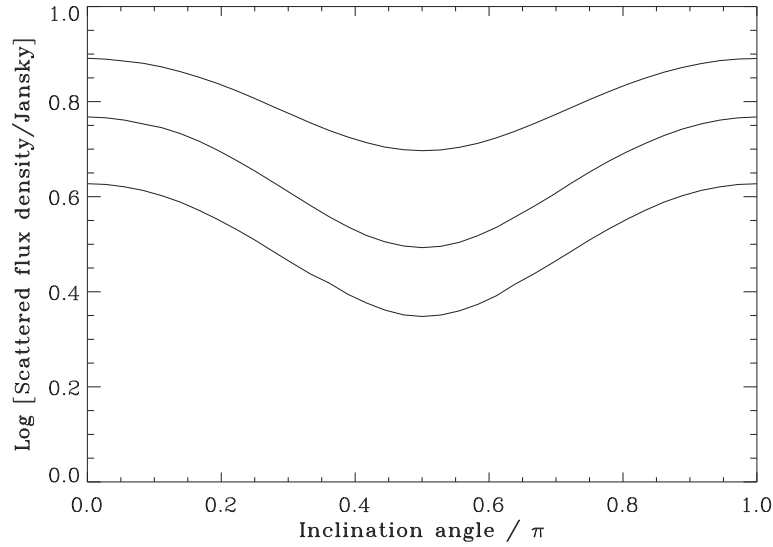


Figure 4.13: Maximum of the scattered flux density produced by a jet as a function of the inclination angle for three different Lorentz factors, viz. 2, 5 and 10 (from top to bottom) for the assumed density distribution.

jet as a function of the inclination angle for three different Lorentz factors. As can be taken from this figure, the total scattered flux does not depend strongly on the Lorentz factor or the inclination angle.

The behaviour exhibited in Fig. 4.13 might seem at first sight a bit surprising, in that the dependency of the total scattered flux on the inclination angle and the Lorentz factor turns out to be so small. However, since essentially the same amount of energy, i.e. the same number of photons, is distributed over more or less the same volume, one would expect no “substantial” differences between the respective total scattered fluxes once the distribution of scattered radiation has settled to a stationary state. We have verified that the small dependency of the total scattered flux on the inclination angle and the Lorentz factor apparent from Fig. 4.13 is primarily due to the angular dependence of the Thomson scattering cross section as well as to a lesser extent on the chosen density distribution.

In Fig. 4.14 we are plotting the ratio of the total scattered flux to the apparent flux for our simulated jet having reached its stationary state as a function of the inclination angle with respect to the line of sight for three different Lorentz factors. The conclusions to be drawn from this figure are rather similar to the results given in Fig. 4.6, in that above a certain inclination angle of in this case about 140° the total scattered flux can dominate the apparent direct flux in the case of a Lorentz

4 Scattering in the vicinity of relativistic jets

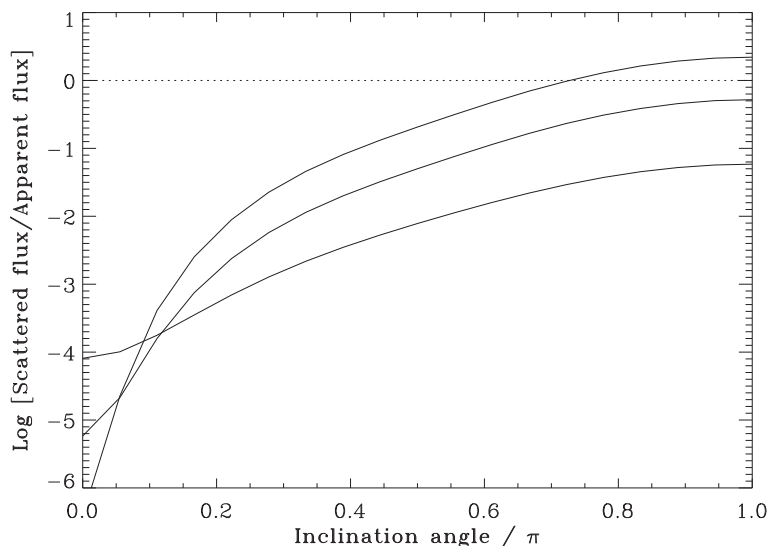


Figure 4.14: Ratio of the maximum of the scattered flux density to the apparent flux for a jet as a function of the inclination angle of the jet with respect to the line of sight for three different Lorentz factors, viz. 2, 5 and 10.

factor of ten or larger. It should, however, be kept in mind that in computing the ratio we have used the total scattered flux, to which as was shown in the previous contour plots regions can contribute of sizes much larger than the jet itself.

For Lorentz factors equal or smaller than five the apparent direct flux dominates the total scattered flux for any inclination angle. These curves do not depend on the assumed intrinsic jet luminosity, but scale linearly with the assumed electron density. Since as we have seen in the previous figure the total scattered flux varies very little with the inclination angle, the strong dependence of the ratio given in Fig. 4.14 on the inclination angle essentially is due to the variation of the beaming factor on the Lorentz factor and the inclination angle. This point will be of importance in the following section where we try to derive constraints on the parameters of the jet of M87 based on the above described models.

4.4 Application to M87

4.4.1 Observations

M87 (NGC 4486) is a giant elliptical galaxy near the centre of the Virgo cluster, which is located at a distance of about 16 Mpc (Tonry (1991); 1 arcsec corresponds

to 78 pc). It contains one of the best studied synchrotron jets as it is one of the nearest examples of this phenomenon (for a general review about the jet in M87 see e.g. Biretta (1993)). M87 is classified as a FR I type radio galaxy, meaning a low-luminosity, centre-brightened source. Its approximately 2.5 kpc long jet exhibits a complex knotty structure and is a prominent source of radio, optical and X-ray emission (Biretta et al. 1991). The jet has a luminosity of $L_{\text{jet}} \sim 10^{43} \text{ erg s}^{-1}$, with the brightest knots contributing a few times $10^{42} \text{ erg s}^{-1}$. This non thermal activity is believed to ultimately be driven by a central black hole of a mass of about $3 \times 10^9 M_{\odot}$ (Macchetto et al. 1997). Although a counterjet has not been observed directly, a feature reminiscent of a hotspot has been detected at optical wavelengths (Sparks et al. 1992).

4.4.2 Constraints on the jet parameters

Radio observations have allowed to derive several constraints on the parameters of the jet of M87. These constraints can be plotted in the parameter space spanned by the Lorentz factor and the inclination angle in order to study which regions thereof are consistent with the observations. In the case of M87 such a plot has been presented by e.g. Biretta et al. (1989). Based on these observations and the constraints derived therewith, the inner jet (from the nucleus to the so-called knot A) is believed to exhibit a Lorentz factor of about 3 to 5 and to be orientated at an inclination angle of about 30° to 40° from the line of sight (Biretta et al. 1995).

4.4.2.1 Constraint based on the flux ratio

In deriving these constraints use was made of the fact that the ratio of the jet flux to the counterjet flux

$$R_1 = \frac{F_{\text{app}}^{\text{jet}}}{F_{\text{app}}^{\text{cjet}}} = \left(\frac{1 + \beta \cos \theta}{1 - \beta \cos \theta} \right)^{2+\alpha} \quad (4.19)$$

has to be at least larger than the observed lower limit for this quantity of 150, wherein $F_{\text{app}}^{\text{jet}}$ and $F_{\text{app}}^{\text{cjet}}$ are the apparent fluxes from the jet and the counterjet, respectively. Obviously, Eq. 4.19 is only valid for the luminosity of the jet and the counterjet being equal. Less conservative estimates for this ratio provided in Biretta et al. (1989) are 740 and 1.600, which were obtained by using a different technique of background subtraction. These estimates were derived by measuring the flux in a 9° wide wedge centered on the jet up to a distance of about 19 arcsec from the nucleus and a corresponding region located opposite of the nucleus was used for the counterjet.

4 Scattering in the vicinity of relativistic jets

The above cited observational lower limits for the flux ratio also set a constraint on the scattered flux produced in the same region located on the side of the counterjet, in that also the ratio

$$R_2 = \frac{F_{\text{app}}^{\text{jet}}}{F_{\text{sc}}^{\text{cjet}}} \quad (4.20)$$

has to be larger than the observational lower limits obtained by Biretta et al. (1989), where $F_{\text{sc}}^{\text{cjet}}$ is the scattered flux in the corresponding region located on the side of the counterjet. The model developed in the previous sections allows us to compute the ratio R_2 for a “grid” of Lorentz factors in the range from 1 to 10 and inclination angles in the range from 0° to 90° using the observational parameters of M87 as follows.

Given specific values for the Lorentz factor and the inclination angle, we set up our model to reproduce the apparent flux measured on the side of the jet, which amounts to about 2.4 Jy (Biretta et al. 1989). Furthermore, we fix the observed projected length of the jet to 1.5 kpc. We model the distribution of intracluster gas around M87 based on the results of a recent analysis of *XMM-Newton* observations by Matsushita et al. (2002). The electrons are distributed according to the sum of two beta-models (see Eq. 4.15) with the following two sets of parameters: $n_e^\circ = 0.13 \text{ cm}^{-3}$, $\beta_c = 0.42$, $r_c = 1.7 \text{ kpc}$ and $n_e^\circ = 0.011 \text{ cm}^{-3}$, $\beta_c = 0.47$, $r_c = 22 \text{ kpc}$. We, furthermore, assume that the jet and the counterjet have been active long enough, to reach a stationary distribution of the scattered surface brightness as shown in Fig. 4.12. Finally, we integrate this scattered surface brightness inside a 9° wide wedge having its tip centered on the nucleus and its symmetry axis coinciding with the axis of the counterjet out to a distance of about 1.5 kpc from the nucleus yielding the scattered flux in this region.

In Fig. 4.15 we are plotting the two constraints R_1 and R_2 in the parameter space spanned by the Lorentz factor and the inclination angle. Obviously, the constraints derived by the methods studied in this chapter and based upon the observational limit for the jet to counterjet flux ratio are less restricting than the constraints obtained by the conventional flux ratio method. This is because the constraint based on R_1 already restricts the jet of M87 to inclination angles of less than about 40° and to Lorentz factors larger than about 1.5, if one adopts the conservative value of 150 as a lower limit for R_1 . For the larger ratios cited in Biretta et al. (1989) the constraints would become correspondingly more tight.

The constraint obtained by using the ratio R_2 , on the other hand, allows us to exclude only a very small region of the parameter space shown in Fig. 4.15 corresponding to Lorentz factors larger than about 8 and inclination angles larger than about 70° . Even if one would adopt the larger observational limits for this ratio, the constraints based on the ratio R_2 would always be less restricting than

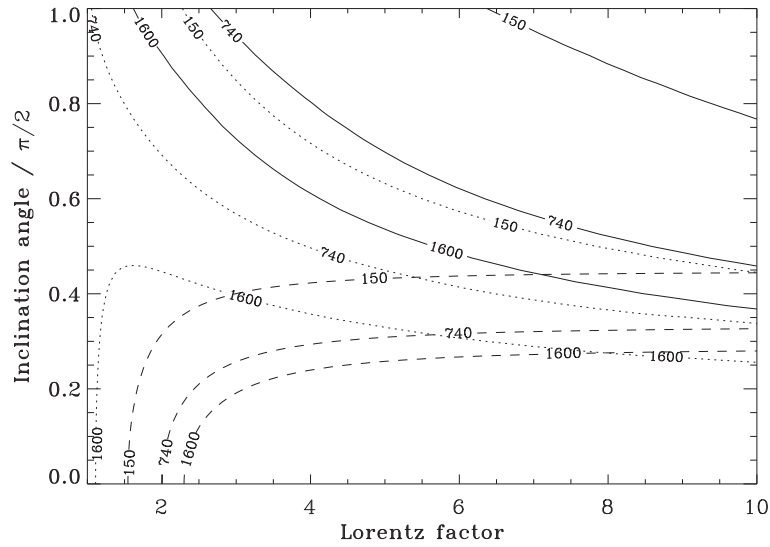


Figure 4.15: Constraints on the jet of M87 in the parameter space spanned by the Lorentz factor and the inclination angle. The solid lines mark the constraints derived by the method described in this chapter based on the ratio R_2 of the apparent jet flux to the scattered flux received from a corresponding region on the side of the counterjet having the shape of a wedge with its tip centered on the nucleus. The estimated lower limits for this ratio of 150, 740 and 1600 have been taken from Biretta et al. (1989). For consistency with observations the parameters of the jet of M87 have to lie in a region above these respective estimates, i.e. “below” the corresponding contours. The dashed lines show the conventional constraint based on the ratio R_1 of the apparent jet flux to the apparent counterjet flux. The dotted lines give the constraints according to the present chapter in case it would be possible to use the total scattered flux.

the constraints based upon the ratio R_1 , because the respective contour lines for the latter ratio correspondingly would exclude more and more of the parameter space.

The reason for the constraints based upon the ratio R_2 being less tight than the ones derived based on the ratio R_1 is that in computing the former ratio we, essentially, are missing a lot of scattered flux. As described above the scattered flux was computed inside a 9° wide wedge out to a distance of about 1.5 kpc. However, when looking for instance at the snapshots presented in Fig. 4.12, one appreciates that a substantial fraction of the total scattered flux originates in regions beyond a distance of 1.5 kpc from the nucleus and also from regions outside of the wedge in the vicinity of the nucleus. This “missing” scattered flux is also reflected in

4 Scattering in the vicinity of relativistic jets

Fig. 4.15, where we, furthermore, have plotted the tightest constraints that could possibly be achieved by the method discussed in this section. Obviously, these “best case” constraints, however, are still less tight than the constraints based on Eq. 4.19 except for very large Lorentz factors of about 10.

4.4.2.2 Constraint based on the brightness temperature

A somewhat more qualitative constraint applying the results of the previous sections of this chapter can be obtained by using the observed brightness temperature in the region of the counterjet and in the vicinity of M87. To this end, we have searched in the literature for appropriate observations and have found two very interesting radio maps of M87 and its environment on two different scales.

Hines et al. (1989) present a radio map at a wavelength of 6 cm of the inner lobes of M87 reaching out to a distance of about 5 kpc from the nucleus. As can be taken from Fig. 4 of their paper the surface brightness in the region of the counterjet lies in the range between 0.38 and 1.52 mJy per beam. It is interesting to note that this relatively dim region starts very close to the nucleus and extends out to distances of about 1.2 kpc therefrom along the axis of the counterjet. Their observation was conducted at a wavelength of 6 cm and had a resolution of 0.4 arcsec.

Concerning the distribution of the surface brightness on larger scales Owen et al. (2000) recently have provided a map of the radio halo of M87 at 90 cm out to a distance of about 40 kpc from the nucleus. The radio map presented in Fig. 3 of their paper exhibits two rather interesting regions for the purposes of the present study. These regions lie on the respective extensions of the jet and the counterjet about 4 to 6 kpc distant from the nucleus on the jet side and about 3 to 10 kpc distant from the nucleus on the side of the counterjet. We estimate the surface brightness in these relatively dim regions “north” of the feature D and “south” of the feature C to be of the order of 20 mJy per beam (Owen et al. (2000), in particular Fig. 3). The beam size of this observation was 7.8×6.2 arcsec².

Since the measurements of the flux obtained by Biretta et al. (1989) and of the surface brightnesses in the above cited observations are given at different wavelengths, viz. 2, 6 and 90 centimetres, one needs an estimate of the spectral index in order to compare these observations at different wavelengths. Harris et al. (2000b) assumed spectral index values of 0.8 and 0.9 to integrate the radio spectrum between 10^7 and 10^{10} Hz in a study comparing extra nuclear X-ray and radio features in M87. The values for the spectral index were obtained from a unpublished spectral index map between 74 and 327 MHz provided by N. Kassim. In a study of the radio lobes of Virgo A at 2.8 cm wavelength Rottmann et al. (1996) find a very steep spectrum in the outer lobes. Values for the spectral index between

1.6 and 2.8 are quoted. Adopting a spectral index of 1, which should represent a conservative choice, we compute the brightness temperatures corresponding to the limits given by Hines et al. (1989) and Owen et al. (2000) to be 25 and 0.07 Kelvin at a wavelength of 2 cm, respectively. Choosing a respective spectral index of 0.5 or 2 instead, would yield respective limits for the brightness temperature of 43 and 0.48 Kelvin as well as 8.3 and 0.002 Kelvin.

Given the above derived observational limits on the surface brightness at a wavelength of 2 cm in two specific regions in the vicinity of M87, we by using the methods presented in this chapter are able to address the question, whether these observational limits are consistent with the scattered surface brightness to be expected from a jet producing the observed direct flux as measured by Biretta et al. (1989). Thus, in computing the respective surface brightness profiles we proceed in a similar way to the previous section while taking the beam sizes of the respective observation into account, i.e. we fix the observed apparent jet flux as well as the observed projected jet length and vary the Lorentz factor and the inclination angle.

Fig. 4.16 shows the results of these computations in that the brightness temperature of the scattered radiation is plotted as a function of the distance from the nucleus along the axis of the counterjet for three different combinations of Lorentz factor and inclination angle, viz. $\gamma = 5$ and $\theta = 30^\circ$, $\gamma = 10$ and $\theta = 30^\circ$ as well as $\gamma = 5$ and $\theta = 60^\circ$. Also shown are the observational upper limits taken as outlined above from Hines et al. (1989) for distances from 0.1 up to 1.2 kpc from the nucleus and from Owen et al. (2000) for distances from 3 kpc up to 10 kpc from the nucleus.

As can be taken from this figure, the presently most favoured model for the jet of M87 having a Lorentz factor between 3 and 5 and an inclination angle between 30° and 40° lies well within our constraints. However, the surface brightness profiles for the other two combinations of Lorentz factor and inclination angle, i.e. $\gamma = 10$ and $\theta = 30^\circ$ as well as $\gamma = 5$ and $\theta = 60^\circ$, do not seem to be consistent with the observations of Owen et al. (2000), in that the scattered brightness temperatures are larger than the ones observed. Obviously, for even larger Lorentz factors and/or inclination angles this inconsistency would become even more striking. Again, it should be noted, that the conclusions to be drawn from Fig. 4.16 are based on the assumption that the counterjet is intrinsically symmetric to the jet and that the jet has been active long enough for the scattered radiation to reach a stationary state as described in the previous sections.

The surface brightness level derived from Owen et al. (2000) represents a fundamental restriction for our method which cannot be overcome by observations with a very high dynamic range, since nowhere inside the large scale lobes of the order of about 40 kpc a lower surface brightness can be found. Furthermore it should be

4 Scattering in the vicinity of relativistic jets

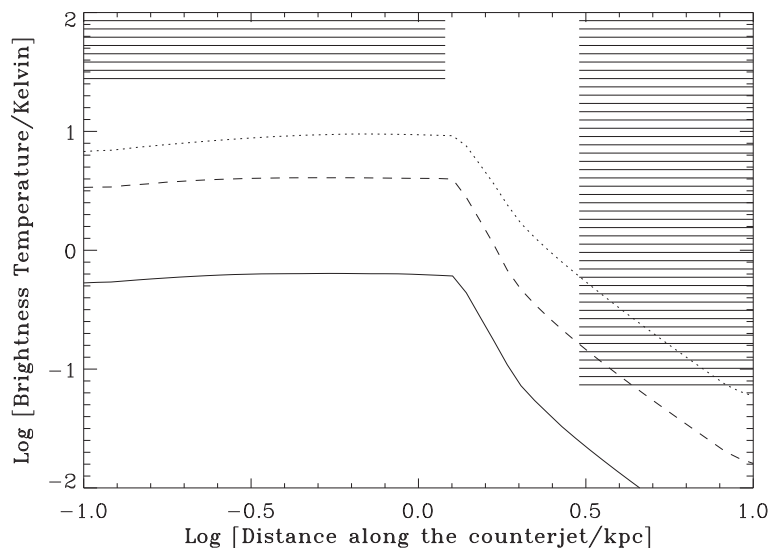


Figure 4.16: Brightness temperature of the scattered radiation as a function of the distance from the nucleus along the axis of the counterjet for the following combinations of Lorentz factor and inclination angle: 5, 30° (solid curve); 10, 30° (dashed curve) and 5, 60° (dotted curve). The observational upper limits marked by rectangles filled by thick horizontal lines are taken from Hines et al. (1989) for distances of 0.1 up to 1.2 kpc from the nucleus and from Owen et al. (2000) for distances from 3 kpc up to 10 kpc from the nucleus.

pointed out that several features in the lobe on the side of the counterjet, i.e. the east lobe, are quite luminous (Hines et al. 1989). The total flux of these sources is about 1.5 Jy. Assuming this radiation to be isotropic the scattered flux should be about 1.5 mJy for the assumed density distribution of M87. The regions studied in this section are located within a circle of at least 1 kpc around this lobe. Assuming that this scattered flux is distributed over such an area in the sky, a conservative upper value for the average brightness temperature of the scattered radiation produced by the features within this eastern radio lobe turns out to be 0.05 Kelvin and thus should not be critical for the method studied here.

For the purposes of this chapter it would be very interesting to obtain an estimate of the scattered surface brightness in the region in the vicinity of M87 we have been focusing on in this section at higher frequencies. This is because the overall synchrotron spectrum of the jet of M87 is characterized by a medium flat radio to optical spectral index of 0.65, a steep cutoff at frequencies beyond a critical value of about 2×10^{15} Hz and some flattening at frequencies below 10^{10} Hz (Meisenheimer

et al. 1996). Given the above mentioned steep spectrum of the outer radio lobes, wherein this region is located, observations at higher frequencies might lead to even better constraints.

4.5 Discussion

In this chapter we have tried to assess the possibility of constraining the parameters of relativistic extragalactic jets by means of a model for the radiation field produced by such jets. Based on this model we have computed the brightness temperature of the scattered radiation as well as the scattered fluxes for several different scenarios.

In a first part of this chapter we have illustrated and discussed the scattered radiation produced by a single pair of blobs being ejected along oppositely directed axes out of the nucleus of an AGN. In a second part we have studied the distribution of the scattered surface brightness produced by multiple blob pairs.

The results of these two sections have been used in a final section of this chapter, where we have tried to derive independent constraints for the jet of M87 based on the observed jet to counterjet flux ratio and based on the surface brightness in two specific regions on the side of the counterjet. We found that the presently most popular model for the jet of M87 lies well within the derived constraints. However, a combination of a very large Lorentz factor and a large inclination angle does not seem to be consistent with the observational limits.

Lorentz factors of up to 10 have been detected in extragalactic jets. As is apparent from the foregoing results, any extragalactic jet located in a cluster with a high electron density might be a promising target for the method presented in this chapter. However, motions with apparent superluminal velocities have been observed in galactic objects as well. For instance the two microquasars GRS 1915+105 and GRO J1655-40 (Mirabel & Rodriguez (1994); Hjellming & Rupen (1995)) have an inferred bulk Lorentz factor of 2.5. However, for these cases, the observations suggest that the single blob scenario should be more appropriate.

Observations of Gamma-Ray Bursts strongly indicate and theoretical models for these objects advocate, the presence of relativistic, well collimated outflows in GRBs. The radiating matter is believed to move initially with Lorentz factors up to $10^2 - 10^3$. From the perspective of the present chapter these objects are very interesting in that the inclination angle is most probably very well constrained, since these objects are believed to be observed very close to the line of sight. In this context it should be stressed, that in principle the method studied in this chapter to constrain relativistic, well collimated outflows is not restricted to radio wavelengths.

4 Scattering in the vicinity of relativistic jets

Jahrtausendlang haben Männer gestrebt und gelitten und gezeugt, und Frauen haben unter Schmerzen geboren. Vor hundert Jahren hat vielleicht ein anderer Mensch an dieser Stelle gesessen; wie Sie hat er mit Furcht und Sehnsucht im Herzen auf das sterbende Licht auf den Gletschern geblickt. Wie Sie war er vom Mann gezeugt und von der Frau geboren. Er hat Schmerz und kurze Wonne empfunden wie Sie. War er jemand anderes? War er nicht Sie selbst?

Erwin Schrödinger

5

A correlation between the SZ decrement and the Thomson depth

Abstract

In a recent study of dark matter N-body simulations a scaling relation between the SZ decrement and the Thomson depth of a cluster of galaxies of the form $\Delta T_r \propto \tau_T^2$ has been found (Diaferio et al. 2000). In this chapter it will be shown that such a scaling relation arises if the intracluster gas is distributed similar to the dark matter density described by the NFW-profile and the finite spatial resolution of the numerical simulation is taken into account. It is furthermore investigated whether the $\Delta T_r \propto \tau_T^2$ relation holds for analytical models of an isothermal gas sphere in the gravitational potential of a dark matter halo distributed according to the NFW-profile, for the available experimental data of SZE observations and for recent results from cosmological gasdynamic simulations of clusters of galaxies. Combining such a relation with temperature estimates from X-ray observations would provide information about the dependence of T_e on τ_T . The Thomson depth might therefore emerge as another important scaling parameter in studies of clusters of galaxies.

5.1 Scaling relations for clusters of galaxies

Through an interplay of X-ray observations and theoretical modelling several scaling relations, which suggest the self-similarity of relaxed clusters of galaxies, have been discovered. Especially interesting is the tight relation between the virial mass of a cluster and the temperature of the intracluster medium (ICM), $M_{\text{vir}} \propto T_e^{3/2}$ (see e.g. Evrard et al. (1996), Horner et al. (1999)).

With the recent progress in observing the SZ decrement in about a dozen of clusters of galaxies (Birkinshaw 1999; Carlstrom et al. 1999) one obtains another observable parameter to constrain the physics of these objects. The magnitude of the SZ effect (SZE) is a measure for a different physical parameter than the X-ray surface brightness or the inferred X-ray luminosity. It primarily depends upon the Thomson depth and not on the virial mass, although they are certainly connected in some way.

In analogy with well known scaling relations it is reasonable to expect a power law dependence between the SZ decrement and the Thomson depth of a cluster of the form $\Delta T_r \propto \tau_T^\alpha$. Combining this relation with temperature estimates of the ICM through X-ray observations provides direct information about the Thomson depth and about the dependence of T_e on τ_T . Therefore the Thomson depth of a cluster might emerge as an important scaling parameter for tests of the models of clusters of galaxies.

5.2 The SZ decrement

The scattering of Cosmic Microwave Background (CMB) photons by the thermal electrons of the ICM leads to a unique distortion of the CMB spectrum (Sunyaev & Zel'dovich (1972, 1980); see Rephaeli (1995) for a recent review). In the Rayleigh-Jeans (RJ) limit the thermal effect causes a temperature decrement given by

$$\frac{\Delta T_r}{T_r} = -2 \int n_e \sigma_T \frac{kT_e}{m_e c^2} dl. \quad (5.1)$$

In an attempt to study the imprint of large-scale motions in superclusters on the CMB Diaferio et al. (2000), henceforth DSN, have analysed high-resolution N-body simulations of a representative volume of a Cold Dark Matter universe. Since the SZE depends upon the properties of the ICM they made the following assumptions about the relation of dark matter to gas:

- The electron number density is simply proportional to the dark matter mass density $n_e = (\rho_{\text{dm}}/m_p)\Omega_b/\Omega_o$, where m_p is the proton mass, Ω_b the baryonic density and Ω_o the gravitating matter density in units of the critical density

5.3 Scaling relation for gas distributed similarly to dark matter

- At any point within the cluster the plasma is thermalized, i.e. $kT_e = \sigma_{\text{dm}}^{\parallel 2} m_p / 2$, where $\sigma_{\text{dm}}^{\parallel}$ is the projected velocity dispersion of the dark matter particles

Note that, since $\beta = (\mu m_p \sigma^{\parallel 2} / kT_e)$, the second assumption implies $\beta = 6/5$ for an abundance with $\mu = 3/5$, as is inferred for clusters of galaxies, if the projected velocity dispersions of dark matter particles and galaxies are equivalent. DSN computed the Thomson depth along a given line of sight through the simulated volume as:

$$\tau_{\text{T}} = \sigma_{\text{T}} \int n_e dl = \sigma_{\text{T}} \frac{\Omega_{\text{b}}}{\Omega_{\text{o}}} \int_0^L \frac{\rho_{\text{dm}}(l)}{m_p} dl, \quad (5.2)$$

with L the linear dimension of the computational box. With their assumptions the thermal SZE in the Rayleigh-Jeans limit can be expressed as

$$\frac{\Delta T_{\text{r}}}{T_{\text{r}}} = -2 \sigma_{\text{T}} \frac{m_p}{m_e} \frac{\Omega_{\text{b}}}{\Omega_{\text{o}}} \int_0^L \frac{\sigma_{\text{dm}}^{\parallel 2}(l)}{2c^2} \frac{\rho_{\text{dm}}(l)}{m_p} dl, \quad (5.3)$$

These two quantities were computed for a large number of clusters and it was found that the SZE scales quadratically with the Thomson depth:

$$\Delta T_{\text{r}} \approx -\tau_{\text{T}}^2 \cdot 2 \times 10^6 \mu\text{K}. \quad (5.4)$$

5.3 Scaling relation for gas distributed similarly to dark matter

In order to compute the Thomson depth as it was done by DSN we assume that the dark matter density profile of a cluster of galaxies is of the form proposed by Navarro et al. (1995), henceforth NFW, i.e.

$$\rho_{\text{dm}}(x) = \frac{\rho_{\text{s}}}{x(1+x)^2}, \quad (5.5)$$

with ρ_{s} being the product of the non-dimensional over-density δ_{c} and the critical density $\rho_{\text{crit}} = 1.88 \times 10^{-29} h^2 \text{ g cm}^{-3}$ ($h = H_{\text{o}}/100 \text{ km s}^{-1} \text{ Mpc}^{-1}$) and $x = r/r_{\text{s}}$ the radius measured in units of the scaling radius. The NFW-profile is self similar, meaning that for dark matter halos of different virial mass the shape of the profile remains the same and just scales with the over-density and the scaling radius. These two quantities are not independent. For a given set of cosmological parameters they can be computed as a function e.g. of the virial mass of a cluster (Navarro et al. 1997). Equation 5.5 therefore represents a one parameter family

5 A correlation between the SZ decrement and the Thomson depth

of profiles. To compute the Thomson depth for the NFW-profile one has to solve the following integral

$$\tau_{\text{T}}(z) = \sigma_{\text{T}} r_{\text{s}} \frac{\Omega_{\text{b}}}{\Omega_{\text{o}}} \frac{\rho_{\text{s}}}{m_{\text{p}}} \int \frac{dl}{x(1+x)^2}, \quad (5.6)$$

where the projected radius z and the coordinate along the line of sight l , both measured in units of the scaling radius, have been introduced. They are related to the radial distance x through $x^2 = z^2 + l^2$. The Thomson depth as computed in Equation 5.6 is just proportional to the surface mass density $\tau_{\text{T}} = \sigma_{\text{T}}(\Omega_{\text{b}}/\Omega_{\text{o}})(\Sigma_{\text{dm}}/m_{\text{p}})$. Since this is an important quantity for studying the effects of gravitational lensing due to a cluster of galaxies it has been computed in this context for the NFW-profile by Bartelmann (1996)

$$\tau_{\text{T}}(z) = \sigma_{\text{T}} r_{\text{s}} \frac{\Omega_{\text{b}}}{\Omega_{\text{o}}} \frac{\rho_{\text{s}}}{m_{\text{p}}} \frac{2f(z)}{z^2 - 1}, \quad (5.7)$$

with

$$f(z) = \begin{cases} 1 - \frac{2}{\sqrt{z^2-1}} \arctan\left(\sqrt{\frac{z-1}{z+1}}\right), & \text{for } z > 1 \\ 0, & \text{for } z = 1 \\ 1 - \frac{2}{\sqrt{1-z^2}} \operatorname{arctanh}\left(\sqrt{\frac{1-z}{1+z}}\right), & \text{for } z < 1 \end{cases}$$

Since $f(z)$ involves only non-dimensional quantities Equation 5.7 implies that for a given cluster with a certain virial mass and therefore given over-density and scaling radius the Thomson depth scales as: $\tau_{\text{T}} \propto \rho_{\text{s}} r_{\text{s}}$.

The temperature profile of the ICM used by DSN can be written as

$$kT_{\text{e}}(r) = \frac{m_{\text{p}} \sigma_{\text{dm}}^{\parallel}(r)^2}{2} = \frac{1}{2} \frac{m_{\text{p}} G M_{\text{dm}}(< r)}{r}. \quad (5.8)$$

The NFW density profile implies a mass profile given by

$$M_{\text{dm}}(< x) = 4\pi \rho_{\text{s}} r_{\text{s}}^3 \left[\ln(1+x) - \frac{x}{1+x} \right]. \quad (5.9)$$

Therefore Equation 5.3 reads as

$$\frac{\Delta T_{\text{r}}}{T_{\text{r}}} = c_1 \rho_{\text{s}}^2 r_{\text{s}}^3 \int \frac{\ln(1+x) - x/(1+x)}{x^2(1+x)^2} dl, \quad (5.10)$$

with the constant

$$c_1 = -\frac{4\pi}{3} \frac{\sigma_{\text{T}} G m_{\text{p}} (\Omega_{\text{b}}/\Omega_{\text{o}})}{m_{\text{e}} c^2}.$$

5.3 Scaling relation for gas distributed similarly to dark matter

This integral (Equation 5.10) cannot be solved analytically for $z > 0$ but does not depend upon the virial mass of a cluster. This implies that the SZ decrement should obey the scaling $\Delta T_r \propto \rho_s^2 r_s^3$. With these scalings one obtains that the ratio $\Delta T_r / \tau_T^2$ should not be constant but rather scale with mass as r_s .

So far the effects of the finite spatial resolution, which are inherent to numerical simulations, upon the relation found by DSN have been neglected. For example the spatial resolution of the OCDM model they found their relation for is $\delta r = 30 h^{-1}$ kpc. This is modelled analytically by folding the computed Thomson depth and SZ decrement with gaussian windows of relative beam-size $a = \delta r / r_s$. This method gives results consistent with a central integration ($z = 0$) with a lower integration boundary $l_{\min} \sim a$. The beam averaged Thomson depth and microwave decrement therefore read as

$$\widehat{\tau}_T(a) = \int_0^\infty \frac{e^{-z^2/2a^2}}{a^2} \tau_T(z) z dz \quad (5.11)$$

and

$$\Delta \widehat{T}_r(a) = \int_0^\infty \frac{e^{-z^2/2a^2}}{a^2} \Delta T_r(z) z dz. \quad (5.12)$$

The important thing to note is that since δr is constant, the relative beam-size a decreases with increasing scaling radius. For a more massive cluster the relative beam-size is therefore smaller and only the more central parts of the cluster are probed in the averaging process. This is essentially the origin of the relation found by DSN.

Working this out one obtains an expression for the normalisation found by DSN and its dependence on the parameters of the model

$$\frac{\Delta \widehat{T}_r}{\widehat{\tau}_T^2} = \frac{4\pi}{3} \frac{Gm_p^2 T}{\sigma_T m_e c^2} \frac{\delta r}{(\Omega_b / \Omega_o)} g(a) \approx 2 \times 10^6 \mu\text{K},$$

where we have used $T_r = 2.725\text{K}$ the CMB temperature (Mather et al. 1999), $\Omega_b = 0.0125 h^{-2}$ (Smith et al. 1993) and $\Omega_o = 0.3$. The dependence on a is collected in the function $g(a)$. Since as mentioned before a depends upon the scaling radius and therewith upon the virial mass of a cluster one can compute the ratio $\Delta \widehat{T}_r / \widehat{\tau}_T^2$ as a function of the virial mass instead of a . The variation of $g(a)$ over the mass range 1×10^{13} to $3 \times 10^{15} M_\odot$ is less than 10%. This explains why DSN found the relation between the SZ decrement and the Thomson depth in their studies.

5.4 Isothermal gas in a NFW dark matter potential

It is an observational fact, that the central parts of relaxed, non cooling flow clusters are close to isothermal. Their surface brightness profile is well fitted by the so called β -profile (Cavaliere & Fusco-Femiano 1978), which implies an electron density profile

$$n_e(r) = \frac{n_e^o}{(1 + (r/r_c)^2)^{3\beta/2}}. \quad (5.13)$$

The connection of the parameters of the β -profile, i.e. n_e^o , r_c and β , to the parameters characterising the NFW-profile, i.e. ρ_s and r_s , is not easy to interpret. Integrating the force balance in hydrostatic equilibrium for the gravitational potential given by the mass distribution (Equation 5.9) of a NFW-profile

$$\frac{dp_g}{dr} = -\frac{GM_{\text{dm}}(< r)}{r^2}\rho_g, \quad (5.14)$$

with p_g the gas pressure, under the assumption of isothermality leads to the following gas density distribution (Makino et al. 1998)

$$\rho_g(x) = \rho_g^o e^{-b} (1+x)^{b/x}, \quad (5.15)$$

where b is given by

$$b = \frac{4\pi G m_p \rho_s r_s^2}{kT_e}. \quad (5.16)$$

It is assumed that the gas is at a temperature given by the virial theorem. To fix the constant of integration the following normalisation of the gas density is used. The ratio of the gas mass to the dark matter mass inside the virial radius is given by the universal baryon fraction

$$\frac{M_{\text{gas}}(< r_{\text{vir}})}{M_{\text{dm}}(< r_{\text{vir}})} = \frac{\Omega_b}{\Omega_o}. \quad (5.17)$$

Using this relation for the normalisation leads to

$$\rho_g^o = \rho_s \frac{\Omega_b}{\Omega_o} \left[\ln(1+c) - \frac{c}{1+c} \right] \times \left[e^{-b} \int_0^c x^2 (1+x)^{b/x} dx \right]^{-1}, \quad (5.18)$$

with $c = r_{\text{vir}}/r_s$ the concentration parameter. The Thomson depth and SZ decrement resulting from this density profile must be computed numerically. Note that the gas density profile (Equation 5.13) is very sensitive to the parameter b , which

depends upon the gas temperature. Although the derived gas density distribution can be well fitted to a β -profile the core radii one obtains are up to one order of magnitude smaller than the observed ones, suggesting that additional physical processes have to be included (Makino et al. 1998).

5.5 Clusters with observed SZ decrements

Recent progress in observational techniques have allowed a significant detection of the SZ decrement in about a dozen of clusters of galaxies. More clusters have been observed, but not all data are published yet. The published data has been compiled e.g. by Cooray (1999), who scaled the observations made with different instruments and therefore at different frequencies to the RJ part of the spectrum and applied relativistic corrections where appropriate. The cluster temperatures as derived from broad-band single-phase plasma fits to *ASCA* data by White (2000) were used. To this sample two high redshift clusters ($z \approx 0.5$) were added for which recent observations of the SZE have been reported: MS 0451.6-0305 (Reese et al. 2000) and RX J0658-5557 (Andreani et al. 1999). The Thomson depth for these clusters were computed with Equation 5.1 under the assumption of isothermality (see Table 5.1).

5.6 SZ decrement and Thomson depth for simulated clusters

In recent years numerical simulations of clusters of galaxies which treat the dark matter and the gas component consistently have been performed by several groups. It was possible to obtain the data necessary for the purposes of this chapter from two sources: the Santa Barbara Cluster Project (Frenk et al. 1999) and the Simulated Cluster Archive (Norman et al. 2000). The Santa Barbara Cluster Project compiled and compared simulations of a cluster with virial mass $1.1 \times 10^{15} M_{\odot}$ by several groups with different codes and found general consistency of the results. The cosmological parameters used in their simulations were: $h = 0.5$, $\Omega = 1.0$, $\Omega_b = 0.1$, $\sigma_8 = 0.9$. We used their best fit gas density and temperature profile to compute the Thomson depth and the SZ decrement.

The Simulated Cluster Archive is a project to make data for several simulated clusters of galaxies publicly available on the Internet. The following cosmological parameters for a Λ CDM model were used in those simulations: $h = 0.7$, $\Omega_0 = 0.3$, $\Omega_b = 0.026$, $\Omega_{\Lambda} = 0.7$, $\sigma_8 = 0.928$. The Thomson depth and the SZ decrement

5 A correlation between the SZ decrement and the Thomson depth

Cluster	$\tau_T/10^{-3}$	T_e/keV	$\Delta T_r/\text{mK}$
A0478	13.13 ± 2.66	06.58 ± 0.26	-0.92 ± 0.15
A0665	11.06 ± 1.64	07.73 ± 0.38	-0.91 ± 0.09
A0773	09.69 ± 1.85	08.63 ± 0.68	-0.89 ± 0.10
A1413	12.32 ± 1.83	07.32 ± 0.25	-0.96 ± 0.11
A1656	05.96 ± 1.20	08.67 ± 0.17	-0.55 ± 0.10
A1689	19.44 ± 3.64	09.23 ± 0.28	-1.91 ± 0.30
A1835	15.41 ± 2.67	08.17 ± 0.50	-1.34 ± 0.15
A2142	09.37 ± 1.79	09.02 ± 0.32	-0.90 ± 0.14
A2163	13.64 ± 2.64	13.29 ± 0.64	-1.93 ± 0.28
A2204	12.51 ± 4.08	07.21 ± 0.25	-0.96 ± 0.28
A2218	12.36 ± 1.99	06.84 ± 0.34	-0.90 ± 0.10
A2256	05.94 ± 1.31	06.96 ± 0.11	-0.44 ± 0.09
Zw3146	13.72 ± 2.84	05.89 ± 0.26	-0.86 ± 0.14
CL0016+16	13.95 ± 3.56	08.15 ± 0.80	-1.21 ± 0.19
MS0451.6-0305	12.91 ± 0.98	10.40 ± 0.90	-1.43 ± 0.10
RXJ0658-5557	07.84 ± 4.22	17.00 ± 4.00	-1.42 ± 0.43

Table 5.1: Thomson depth, electron temperature and SZ decrement for sixteen observed clusters of galaxies

were computed for 16 clusters, having virial masses in the range of 5×10^{14} to $2 \times 10^{15} M_\odot$.

5.7 Results

In this section the results from the previous sections are presented and discussed. The SZ decrement of each cluster from the four samples is plotted against its Thomson depth in Figure 5.1. The solid line is the relation found by DSN: $\Delta T_r \approx -\tau_T^2 \cdot 2 \times 10^6 \mu\text{K}$. The triangles which trace this relation are seven models of a cluster with virial mass in the range from 1×10^{14} to $3 \times 10^{15} M_\odot$. Given the virial mass of the dark matter halo the scaling radius and the over-density were computed, according to the algorithm provided in Navarro et al. (1997). With these parameters the Thomson depth and the microwave decrement were derived as described in section 5.3.

The same method was used for the second sample covering the same virial mass range. The Thomson depth was computed with the gas density distribution given by Equation 5.15. Because this model assumes isothermality the SZ decrement is simply proportional to the Thomson depth. The temperature and its scaling with

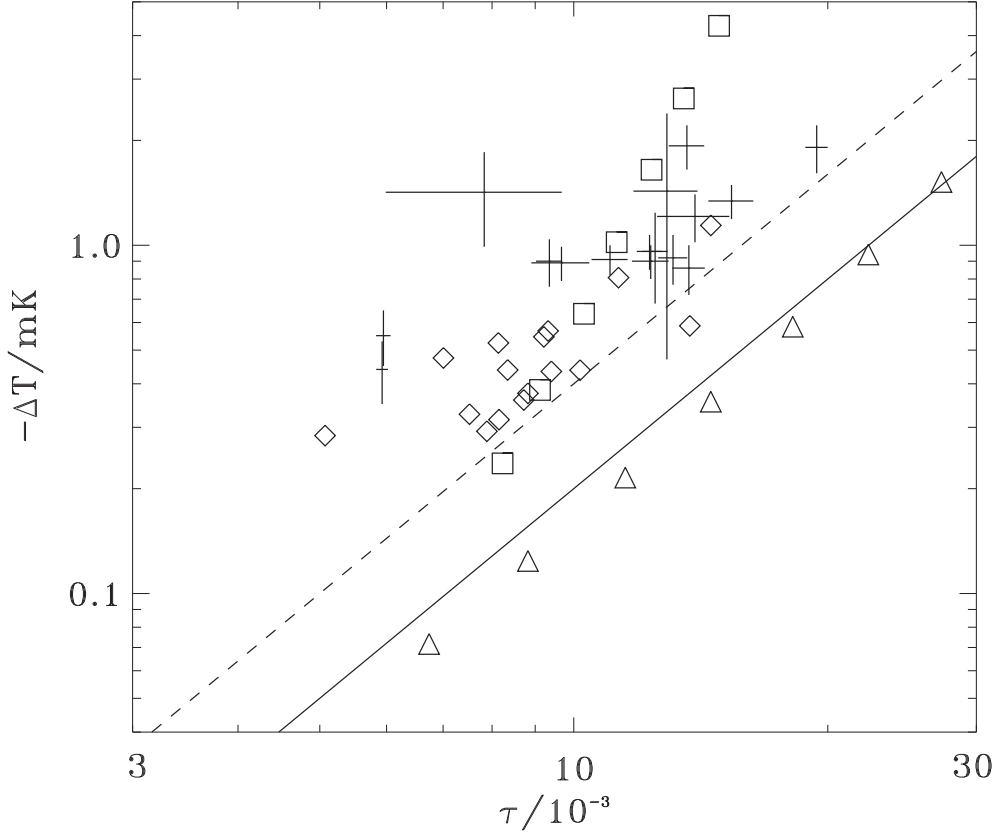


Figure 5.1: SZ decrement as a function of Thomson depth. The two quantities have been computed for a sequence of virial masses from 1×10^{14} to $3 \times 10^{15} M_{\odot}$ for the dark matter sample (triangles) and the gas sample (squares). The positions of the simulated and observed clusters are shown by diamonds and crosses. The solid line is the relation found by DSN $\Delta T = -\tau_{\text{T}}^2 \cdot 2 \times 10^6 \mu\text{K}$. The dashed line is the same relation for $\beta = 3/5$.

virial mass were chosen in such a way, that the parameter b remained constant over the given mass range, corresponding to a fixed $\beta = 2/3$. The position of these clusters in the $\Delta T_{\text{r}}-\tau_{\text{T}}$ plane are marked by squares. It is obvious that for this sample the slope of the relation is much steeper. It is close to $\Delta T_{\text{r}} \propto \tau_{\text{T}}^4$, which would imply a dependence $T_{\text{e}} \propto \tau_{\text{T}}^3$. The significance of this steep dependence is nevertheless doubtful because as mentioned in one of the previous sections there are some inconsistencies related to this gas density distribution. The actual slope of the relation is very sensitive to the scaling of the parameter b with virial mass.

5 A correlation between the SZ decrement and the Thomson depth

Changing the absolute value for b or equivalently β does not change the slope of the relation but mainly shifts the data points to larger Thomson depths.

The positions of the observed clusters are plotted together with their error bars. This sample is obviously strongly biased: the hottest, most massive clusters were chosen to be observed in order to make the detection of the SZE more probable. Future observations with higher sensitivity will detect lower mass clusters and therefore show how the relation extends down to smaller Thomson depths.

Finally the derived Thomson depth and SZ decrement for the simulated clusters are plotted with diamonds. It is obvious that the slope for the observed and simulated clusters is more shallow than a dependence $\Delta T_r \propto \tau_T^2$. A best fit to the combined data set gives a slope of about $3/2$. A different slope is not surprising since gas and dark matter are distributed differently in clusters of galaxies. The simulated and observed clusters lie all above the relation found by DSN. If one assumes a value of $3/5$ for β instead of $6/5$ the normalisation of the relation being proportional to β^{-1} simply doubles (dashed line in Figure 5.1). There is still a discrepancy of about a factor of 2, which might indicate the influence of some neglected physical processes, e.g. non gravitational-heating.

5.8 Discussion

In this chapter an explanation of a relation between the Thomson depth and the CMB decrement caused by the SZE found in studies of dark matter N-body simulations of clusters of galaxies was presented. This relation was derived by assuming that the density profiles of dark matter halos in N-body simulations can be described by the NFW-profile and by modelling the finite spatial resolution of numerical simulations.

An attempt has furthermore been made to investigate if there are hints for the existence and slope of such a relation from other samples of clusters of galaxies. Constructing clusters with a more realistic description of the gas density distribution resulted in a steeper slope of the relation. From the data for the observed and simulated clusters one cannot confirm a relation although a certain trend is discernible, indicating a much shallower slope. Future observations and numerical simulations should allow to test, whether such a relation still holds at and how it extends down to smaller Thomson depths. Although this relation awaits a firm establishment, it is important to mention possible applications. As mentioned earlier a relation between the SZ decrement and the Thomson depth would imply, if clusters are close to isothermal, a relation between T_e and τ_T or equivalently between ΔT_r and T_e . A relation like this would enable one to estimate the temperature of the cluster from the observed SZ decrement. Combining this relation

with the mass temperature relation one could derive a $M_{\text{vir}} - \tau_{\text{T}}$ or equivalently $M_{\text{vir}} - \Delta T_{\text{r}}$ relation for clusters of galaxies, which is rather important since the virial mass is an important but difficult quantity to determine. This might become especially important for high redshift clusters, which are too faint in X-rays.

5 A correlation between the SZ decrement and the Thomson depth

*Gerettet ist das edle Glied
Der Geisterwelt vom Bösen,
Wer immer strebend sich bemüht,
Den können wir erlösen.
Und hat an ihm die Liebe gar
Von oben teilgenommen,
Begegnet ihm die selige Schar
Mit herzlichem Willkommen.*

Johann Wolfgang Goethe, "Faust II"

6

Concluding remarks

Upper limits on the hard X-ray luminosity of Sgr A* during the last 100.000 years have been presented in chapter 2. As scattering material I have considered the molecular and neutral atomic hydrogen present in the Galactic disk. The available CO and X-ray data made it possible to derive limits for the 4-10 keV luminosity of Sgr A* down to about $8 \times 10^{40} \text{ erg s}^{-1}$ at certain times during this period. For other times the limits are of the order of $10^{41} - 10^{42} \text{ erg s}^{-1}$. With respect to the results of chapter 2 a few points require some further discussion.

First, in simulating the activity of the GC it was assumed that the emission of Sgr A* was isotropic. Studies of AGN show that their radiation field is often anisotropic due to the presence of a relativistic jet or as a result of shielding by a molecular torus. A jet produced by Sgr A* would probably point away from the Galactic plane. This would render the derived limits weaker.

Secondly, Ebisawa et al. (2001) have reported the results of a deep *Chandra* observation of a Galactic plane region ($l = 28.45^\circ, b = -0.2^\circ$), which is devoid of known X-ray point sources. The total X-ray flux in the 2-10 keV range is determined to be $\sim 1.1 \times 10^{-10} \text{ erg s}^{-1} \text{ deg}^{-2}$. About ten per cent of this flux is accounted for by point sources resolved by *Chandra*. These are extragalactic sources seen through the Galactic disk. 90 % of the observed flux is due to diffuse emission at the level of the sensitivity and the angular resolution of *Chandra*. This diffuse flux is within a factor of two of those measured by *ASCA* in nearby fields, which are of the order of $\sim 6 \times 10^{-11} \text{ erg s}^{-1} \text{ deg}^{-2}$ (Sugizaki et al. 2001). Unfortunately none of the GMCs listed in the SRBY87 sample lies in this field, but

6 Concluding remarks

the HI column density in this direction is about $2 \times 10^{22} \text{ cm}^{-2}$, similar to the one in the *ASCA* fields. Improvements might result from the spectral data obtained by *XMM-Newton*. If *XMM-Newton* will be able to detect the K_{α} -line of neutral iron in the same field this will open the possibility to separate the scattering contribution.

Finally, the Trapezium region ($l = 209.01^{\circ}, b = -19.38^{\circ}$) of the Orion Nebula has recently been observed by *Chandra* (Schulz et al. 2001). An upper limit for the diffuse emission in the energy range 0.1-10 keV of $2 \times 10^{28} \text{ erg s}^{-1} \text{ arc sec}^{-2}$ is derived, which corresponds to a diffuse flux of $\sim 1 \times 10^{-8} \text{ erg s}^{-1} \text{ deg}^{-2}$. The distance towards the Orion nebula is $\approx 440 \text{ pc}$, corresponding to a time delay of ~ 2.400 years. The galactocentric distance of Orion is $R \sim 8.8 \text{ kpc}$. The measured H_2 column density in this direction is $3.2 \times 10^{22} \text{ cm}^{-2}$, which translates into an upper limit for the luminosity of Sgr A* of $3 \times 10^{41} \text{ erg s}^{-1}$. So GMCs in our vicinity might give comparable limits to the ones derivable from GMCs located in the molecular ring, but their time delays will only be of the order of their distances.

An obvious next step would be to apply the method developed in chapter 2 to constrain the luminosity of Sgr A* in the past to GMCs and HI gas with still larger distances from the GC and thereby to extend the time coverage. However, since the scattered luminosity is proportional to M_{gas}/R^2 , there certainly will be a limit up to what distances one will obtain meaningful results using this method.

A reservoir of neutral gas which has the potential to scatter the radiation from Sgr A* at even larger distances and therefore longer time delays than galactic GMCs is the LMC. With a distance of $\sim 50 \text{ kpc}$ from the sun the time delay for the LMC turns out to be ~ 250.000 years. Unfortunately the data of the LMC existing in the literature does not permit one to obtain interesting limits upon the X-ray luminosity of Sgr A*. However, *XMM-Newton* observations of the iron K_{α} -line in the direction towards massive gas complexes in the LMC should make it possible to improve these limits.

In chapter 3 it has been demonstrated that there are two viable observational strategies for constraining the past X-ray luminosity of galactic nuclei with the next generation of X-ray telescopes. One is to search for scattered AGN radiation in the spectral continuum at high energies $E \gg kT(1+z)$, and the other one is to perform imaging in bright resonance X-ray lines. The first approach appears to be particularly promising for studying distant (at $z \gtrsim 0.5$) powerful quasars and their environments.

Furthermore, it has been shown that the relative contribution of scattered radiation is typically larger by a significant factor of 3–10 in a resonance line than in the neighbouring continuum.

Finally, the level of constraints that could be derived from future observations on the past X-ray luminosity of the nearby M87 and Cyg A active galaxies has been estimated. The upper limits imposed by the available *XMM-Newton* and

Chandra X-ray continuum data are typically 1–2 orders of magnitude weaker.

In this respect, it should be noted that the same method can also be applied to groups of galaxies and isolated giant elliptical galaxies, which also are large reservoirs of hot ionised gas capable of scattering AGN radiation. The main advantage of clusters is the larger extent of intracluster gas, which makes it possible to study past galactic activity on longer timescales (up to a few times 10^6 years for the richest clusters) than in the case of groups of galaxies and early-type galaxies (up to a few times 10^5 years). On the other hand, the latter two classes of objects have their own advantage that the typical gas temperatures for them are $kT \sim 1$ keV and that the factor $\exp(E/kT)$ becomes significant already in the standard X-ray band (< 10 keV). In particular, one can use the K_α -line of He-like iron at 6.7 keV. Indeed, the corresponding ions (Fe XXV) are still abundant at such low temperatures, but collisional excitation of the ions leading to emission in the line is already inefficient.

Although only the case was considered where the AGN is an isotropic source, in reality angular anisotropy at some level is expected. Therefore, the contribution of scattered emission from the AGN to the surface brightness may be larger or smaller in some regions than predicted assuming source isotropy. In this respect reference is made to the papers by Gilfanov et al. (1987a) and Wise & Sarazin (1990b) as well as chapter 4 of this work for a detailed discussion of scattered surface brightness profiles that may arise in the case of beamed source emission.

In the discussion of the simulations for the M87 and Cyg A galaxies and the associated clusters of galaxies a fiducial value of 10% as the minimum detectable contribution of scattered AGN emission to a resonance line was used. Obviously, significant efforts will be required to achieve this or better detection level experimentally. One difficulty is that the measured surface brightness is the integral of emission (thermal plus scattered) along a given line of sight, and there may be present gas with different temperatures and element abundances along this line of sight. Both types of variations will have an effect on the equivalent line width. In principle it should be possible to determine and subtract the underlying temperature and abundance radial trends from a careful analysis of the spectral-imaging data. The remaining uncertainties are expected to be largest for cluster central regions, where both the gas temperature and element abundances vary significantly, for example in the M87 case. On the other hand, this problem is not expected to be severe outside cluster cores. For example, in the Cyg A cluster the gas appears to be nearly isotropic outside the central ~ 200 kpc (see Smith et al. (2002)), whereas the equivalent width of the 6.7 keV iron emission line changes by only $\sim 10\%$ when the gas temperature varies by 0.5 keV around $kT \sim 7.5$ keV. Therefore, achieving the 10% detection level appears realistic.

It is obvious that the potential of the method developed in chapter 3 can be

6 Concluding remarks

fully realized only when it is possible to resolve the interesting resonance lines from neighbouring lines. Indeed, lines other than resonance lines can contribute significantly to the intrinsic emission of the gas, but little to the scattered AGN emission. Moreover, it is desirable that all important lines in blends be resolved, such as the permitted, intercombination and forbidden lines in the complex around the 6.7 keV (Fe XXV K_{α}) line. Even a small contribution of scattered emission from the AGN could then be made manifest by comparing the surface brightness profiles measured in these lines. Future high-energy astrophysics missions such as *Astro-E2*, *Constellation-X* and *XEUS* will provide the required energy resolution (\sim a few eV).

Finally, it should be noted that the constraints on the past AGN X-ray luminosity could be further improved by means of X-ray polarimetry, especially if it became possible to measure polarisation in X-ray resonance lines. The radiation of a central source gets strongly polarised upon scattering in a beta-cluster (with a typical resulting degree of polarisation $P \sim 60\%$, Sunyaev (1982)), whereas the intrinsic emission of the intracluster gas in X-ray resonance lines is also polarised but to a much lesser degree ($P \lesssim 10\%$, Sazonov et al. (2002a)). Thus, even a few per cent contribution of scattered AGN radiation to the surface brightness in a resonance line would be manifest in polarimetric observations.

In chapter 4 I have tried to assess the possibility of constraining the parameters of relativistic extragalactic jets, especially the inclination angle of the jet with respect to the observer and the Lorentz factor of the matter flowing through the jet, by means of a model for the radiation field produced by such jets. On the basis of this model I have illustrated and discussed the scattered radiation produced by a single pair of blobs being ejected along oppositely directed axes out of the nucleus of an AGN. In a second part I have studied the distribution of the scattered surface brightness produced by multiple blob pairs.

The results of these two sections have been used in a final section of this chapter, where I have tried to derive independent constraints for the jet of M87 based on the observed jet to counterjet flux ratio, and based on the surface brightness in two specific regions on the side of the counterjet. I have found that the presently most popular model for the jet of M87, i.e. an inclination angle of about 30° to 40° with respect to the line of sight and a Lorentz factor in the range of 3 to 5, lies well within the derived constraints. However, a combination of a very large Lorentz factor and a large inclination angle does not seem to be consistent with the observational limits.

Lorentz factors of up to 10 have been detected in extragalactic jets. As is apparent from the results of chapter 4, any extragalactic jet located in a cluster with a high electron density might be a promising target for the method presented in this chapter. However, motions with apparent superluminal velocities have

been observed in galactic objects as well. For instance the two microquasars GRS 1915+105 and GRO J1655-40 (Mirabel & Rodriguez (1994); Hjellming & Rupen (1995)) have an inferred bulk Lorentz factor of 2.5. However, for these cases, the observations suggest that the single blob scenario should be more appropriate.

Observations of Gamma-Ray Bursts strongly indicate, and theoretical models for these objects advocate, the presence of relativistic, well collimated outflows in GRBs. The radiating matter is believed to move initially with Lorentz factors up to $10^2 - 10^3$. From the perspective of the results of chapter 4 these objects are very interesting in that their inclination angle is most probably very well constrained, since these objects are believed to be observed very close to the line of sight. In this context it should be stressed, that in principle the method studied in this chapter to constrain relativistic, well collimated outflows is not restricted to radio wavelengths.

In chapter 5 a possible explanation for a relation between the Thomson depth and the CMB decrement caused by the Sunyaev-Zel'dovich Effect (SZE) as found in studies of dark matter N-body simulations of clusters of galaxies was presented. It was shown that such a scaling relation arises if the intracluster gas is distributed similar to the dark matter density described by the NFW-profile and if the finite spatial resolution of the numerical simulation is taken into account. It was furthermore investigated whether the $\Delta T_r \propto \tau_T^2$ relation holds for analytical models of an isothermal gas sphere in the gravitational potential of a dark matter halo distributed according to the NFW-profile, the available experimental data of SZE observations and recent results from cosmological gas-dynamic simulations of clusters of galaxies.

Furthermore, an attempt has been made to search for hints for the existence and slope of such a relation in other samples of clusters of galaxies. Constructing clusters with a more realistic description of the gas density distribution resulted in a steeper slope of the relation. From the data for the observed and simulated clusters one cannot confirm a relation, although a certain trend is discernible, indicating a much shallower slope. Future observations and numerical simulations should allow one to test, whether such a relation still holds at, and how it extends down to smaller Thomson depths. Although this relation awaits a firm establishment, it is important to mention possible applications.

A relation between the SZ decrement and the Thomson depth would imply, if clusters are close to isothermal, a relation between T_e and τ_T or equivalently between ΔT_r and T_e . A relation like this would enable one to estimate the temperature of the cluster from the observed SZ decrement. Combining this relation with the mass temperature relation one could derive a $M_{\text{vir}} - \tau_T$ or equivalently $M_{\text{vir}} - \Delta T_r$ relation for clusters of galaxies, which is rather important since the virial mass is an important but difficult quantity to determine. This might become

6 Concluding remarks

especially important for high redshift clusters, which are too faint in X-rays.

The results obtained in chapter 5 can be greatly improved with upcoming observational data of the SZ effect as will be provided by the *Planck* satellite to be launched in 2007 as well as more sophisticated simulations of clusters of galaxies.

References

- Alcock, C., Hatchett, S. (1978), *The effects of small-angle scattering on a pulse of radiation with an application of X-ray bursts and interstellar dust*, ApJ, 222, 456
- Aldrovandi, S. M. V., Pequignot, D. (1973), *Radiative and dielectronic recombination coefficients for complex ions*, A&A, 25, 137
- Anders, E., Grevesse, N. (1989), *Abundances of the elements - meteoritic and solar*, Geochimica et Cosmochimica Acta, 53, 197
- Andreani, P., Böhringer, H., Dall'Oglio, G., Martinis, L., Shaver, P., Lemke, R., Nyman, L.-A., Booth, R., Pizzo, L., Whyborn, N., Tanaka, Y., Liang, H. (1999), *The Enhancement and Decrement of the Sunyaev-Zel'dovich Effect toward the ROSAT Cluster RX J0658-5557*, ApJ, 513, 23
- Arnaud, K. A. (1996), *XSPEC: The First Ten Years*, Astronomical Data Analysis Software and Systems V, eds. Jacoby G. and Barnes J., ASP Conf. Series Volume 101, 17
- Arnaud, M., Rothenflug, R. (1985), *An updated evaluation of recombination and ionization rates*, A&AS, 60, 425
- Baganoff, F. K., Maeda, Y., Morris, M., Bautz, M. W., Brandt, W. N., Cui, W., Doty, J. P., Feigelson, E. D., Garmire, G. P., Pravdo, S. H., Ricker, G. R., Townsley, L. K. (2003), *Chandra X-ray Spectroscopic Imaging of Sgr A* and the Central Parsec of the Galaxy*, ApJ, 591, 891
- Bahcall, J. N., Kirhakos, S., Saxe, D. H., Schneider, D. P. (1997), *Hubble Space Telescope Images of a Sample of 20 Nearby Luminous Quasars*, ApJ, 479, 642
- Bartelmann, M. (1996), *Arcs from a universal dark-matter halo profile*, A&A, 313, 697

References

- Binney, J., Merrifield, M. (1998), *Galactic Astronomy*, Princeton University Press, Princeton
- Binney, J., Tabor, G. (1995), *Evolving Cooling Flows*, MNRAS, 276, 663
- Biretta, J. A. (1993), *The jet of M87*, Astrophysical Jets, eds. Burgarella D., Livio M. and O’Dea C.P., Cambridge University Press, 225
- Biretta, J. A., Owen, F. N., Cornwell, T. J. (1989), *A search for motion and flux variations in the M87 jet*, ApJ, 342, 128
- Biretta, J. A., Stern, C. P., Harris, D. E. (1991), *The radio to X-ray spectrum of the M87 jet and nucleus*, AJ, 101, 1632
- Biretta, J. A., Zhou, F., Owen, F. N. (1995), *Detection of proper motions in the M87 jet*, ApJ, 447, 582
- Birkinshaw, M. (1999), *The Sunyaev-Zel’dovich Effect*, Physics Reports, 310, 97
- Blandford, R. D., McKee, C. F., Rees, M. J. (1977), *Super-luminal expansion in extragalactic radio sources*, Nature, 267, 211
- Blandford, R. D., Rees, M. J. (1974), *A ‘twin-exhaust’ model for double radio sources*, MNRAS, 169, 395
- Blitz, L., Williams, J. P. (1999), *Molecular Clouds*, The Origin of Stars and Planetary Systems, eds. C. J. Lada and N. D. Kylafis, 3
- Böhringer, H., Belsole, E., Kennea, J., Matsushita, K., Molendi, S., Worrall, D. M., Mushotzky, R. F., Ehle, M., Guainazzi, M., Sakelliou, I., Stewart, G., Vestrand, W. T., Santos, S. D. (2001), *XMM-Newton observations of M87 and its X-ray halo*, A&A, 365, 181
- Boyce, P. J., Disney, M. J., Blades, J. C., Boksenberg, A., Crane, P., Deharveng, J. M., Macchetto, F. D., Mackay, C. D., Sparks, W. B. (1998), *HST Planetary Camera images of quasar host galaxies*, MNRAS, 298, 121
- Bridle, A. H., Perley, R. A. (1984), *Extragalactic Radio Jets*, ARAA, 22, 319
- Burderi, L., King, A. R., Szuszkiewicz, E. (1998), *Does the Thermal Disk Instability operate in Active Galactic Nuclei?*, ApJ, 509, 85
- Carilli, C. L., Harris, D. E., Pentericci, L., Röttgering, H. J. A., Miley, G. K., Kurk, J. D., van Breugel, W. (2002), *The X-Ray-Radio Alignment in the z=2.2 Radio Galaxy PKS 1138-262*, ApJ, 567, 781

-
- Carlstrom, J. E., Joy, M. K., Grego, L., Holder, G. P., Holzapfel, W. L., Mohr, J. J., Patel, S., Reese, E. D. (1999), *Imaging the Sunyaev-Zel'dovich Effect*, Particle Physics and the Universe, Physica Scripta and World Scientific, eds. L. Bergstrom, P. Carlson and C. Fransson
- Cavaliere, A., Fusco-Femiano, R. (1976), *X-rays from hot plasma in clusters of galaxies*, A&A, 49, 137
- Cavaliere, A., Fusco-Femiano, R. (1978), *The Distribution of Hot Gas in Clusters of Galaxies*, A&A, 70, 677
- Chandrasekhar, S. (1950), *Radiative Transfer*, Clarendon Press, Oxford
- Ciotti, L., Ostriker, J. P. (1997), *Cooling Flows and Quasars: Different Aspects of the same Phenomenon? I. Concepts*, ApJ, 487, 105
- Ciotti, L., Ostriker, J. P. (2001), *Cooling Flows and Quasars: II. Detailed Models of Feedback-modulated Accretion Flows*, ApJ, 551, 131
- Cooray, A. R. (1999), *An SZ temperature decrement-X-ray luminosity relation for galaxy clusters*, MNRAS, 307, 841
- Couderc, P. (1939), *Les auréoles lumineuses des novae*, Ann. d'Astrophys., 2, 271
- Cramphorn, C. K. (2001), *A scaling relation between the SZ decrement and Thomson depth in clusters of galaxies*, AstL, 27, 135
- Cramphorn, C. K., Sazonov, S. Y., Sunyaev, R. A. (2004), *Scattering in the vicinity of relativistic jets: a method for constraining jet parameters*, A&A, in press
- Cramphorn, C. K., Sunyaev, R. A. (2002), *Interstellar gas in the Galaxy and the X-ray luminosity of Sgr A* in the recent past*, A&A, 389, 252
- Crawford, C. S., Lehmann, I., Fabian, A. C., Bremer, M. N., Hasinger, G. (1999), *Detection of X-ray emission from the host clusters of 3CR quasars*, MNRAS, 308, 1159
- Dame, T. M. (1993), *The distribution of Neutral Gas in the Milky Way*, Back to the Galaxy, eds. S. S. Holt and F. Verter, 267
- Dame, T. M., Hartmann, D., Thaddeus, P. (2001), *The Milky Way in Molecular Clouds: A New Complete CO Survey*, ApJ, 547, 792
- Diaferio, A., Sunyaev, R. A., Nusser, A. (2000), *Large-Scale Motions in Superclusters: Their Imprint in the Cosmic Microwave Background*, ApJ, 533, 71

References

- Dickey, J. M., Lockman, F. J. (1990), *HI in the Galaxy*, ARAA, 28, 215
- Ebisawa, K., Maeda, Y., Kaneda, H., Yamauchi, S. (2001), *Origin of the Hard X-ray Emission from the Galactic Plane*, Science, 293, 1633
- Evrard, A. E., Metzler, A. C., Navarro, J. F. (1996), *Mass Estimates of X-Ray Clusters*, ApJ, 469, 494
- Fabian, A. C., Crawford, C. S., Ettori, S., Sanders, J. S. (2001), *Chandra detection of the intracluster medium around 3C 294 at $z=1.786$* , MNRAS, 322, 11
- Fang, T. D., Davis, D. S., Lee, J. C., Marshall, H. L., Bryan, G. L., Canizares, C. R. (2002), *A Chandra High-Energy Transition Grating Spectrometer Observation of the Quasar H1821+643 and its surrounding Cluster*, ApJ, 565, 86
- Finoguenov, A., Matsushita, K., Böhringer, H., Ikebe, Y., Arnaud, M. (2002), *X-ray evidence for spectroscopic diversity of type Ia supernova: XMM observation of the elemental abundance pattern in M87*, A&A, 381, 21
- Frenk, C. S., White, S. D. M., Bode, P., Bond, J. R., Bryan, G. L., Cen, R., Couchman, H. M. P., Evrard, A. E., Gnedin, N., Jenkins, A., Khokhlov, A. M., Klypin, A., Navarro, J. F., Norman, M. L., Ostriker, J. P., Owen, J. M., Pearce, F. R., Pen, U.-L., Steinmetz, M., Thomas, P. A., Villumsen, J., Wadsley, J. W., Warren, M. S., Xu, G., Yepes, G. (1999), *The Santa Barbara Cluster Comparison Project: A Comparison of Cosmological Hydrodynamics Solutions*, ApJ, 525, 554
- Garcia, M. R., Murray, S. S., Primini, F. A., Forman, W. R., McClintock, J. E., Jones, C. (2000), *A First Look at the Nuclear Region of M31 with Chandra*, ApJ, 537, 23
- Genzel, R., Eckart, A., Ott, T., Eisenhauer, F. (1997), *On the nature of the dark mass in the centre of the Milky Way*, MNRAS, 291, 219
- Ghez, A. M., Klein, B. L., Morris, M., Becklin, E. E. (1998), *High Proper-Motion Stars in the Vicinity of Sagittarius A*: Evidence for a Supermassive Black Hole at the Center of Our Galaxy*, ApJ, 509, 678
- Gilfanov, M. R., Sunyaev, R. A., Churazov, E. M. (1987a), *Powerful Radio Sources in Clusters of Galaxies - the Origin of Jet like Structures*, SvAL, 13, 233
- Gilfanov, M. R., Sunyaev, R. A., Churazov, E. M. (1987b), *Radial Brightness Profiles of Resonance X-Ray Lines in Galaxy Clusters*, SvAL, 13, 3

-
- Grimm, H.-J., Gilfanov, M. R., Sunyaev, R. A. (2002), *The Milky Way in X-rays for an outside observer. Log(N)-Log(S) and Luminosity Function of X-ray binaries from RXTE/ASM data*, A&A, 391, 923
- Hardcastle, M. J., Birkinshaw, M., Worrall, D. M. (2001), *A Chandra detection of the radio hotspot of 3C 123*, MNRAS, 323, 17
- Hardcastle, M. J., Worrall, D. M. (1999), *ROSAT X-ray observations of 3CRR radio sources*, MNRAS, 309, 969
- Harris, D. E., Nulsen, P. E. J., Ponman, T. J., Bautz, M., Cameron, R. A., David, L. P., Donnelly, R. H., Forman, W. R., Grego, L., Hardcastle, M. J., Henry, J. P., Jones, C., Leahy, J. P., Markevitch, M., Martel, A. R., McNamara, B. R., Mazzotta, P., Tucker, W., Virani, S. N., Vrtilik, J. (2000a), *Chandra X-Ray Detection of the Radio Hot Spots of 3C 295*, ApJ, 530, 81
- Harris, D. E., Owen, F. N., Biretta, J. A., Junor, W. (2000b), *A comparison of the extra nuclear X-ray and radio features in M87*, preprint, astro-ph/0002464
- Hernquist, L. (1989), *Tidal triggering of starbursts and nuclear activity in galaxies*, Nature, 340, 687
- Hines, D. C., Owen, F. N., Eilek, J. A. (1989), *Filaments in the radio lobes of M87*, ApJ, 347, 713
- Hjellming, R. B., Rupen, M. P. (1995), *Episodic ejection of relativistic jets by the X-ray transient GRO J1655-40*, Nature, 375, 464
- Hooper, E. J., Impey, C. D., Foltz, C. B. (1997), *Hubble Space Telescope Imaging of $z \geq 0.4$ Quasar Galaxies selected by Quasar Radio and Optical Properties*, ApJ, 480, 95
- Horner, D. J., Mushotzky, R. F., Scharf, C. A. (1999), *Observational Tests of the Mass-Temperature Relation for Galaxy Clusters*, ApJ, 520, 78
- Kaaret, P. (2001), *Chandra X-Ray Point Sources, including Supernova 1979C, in the Spiral Galaxy M100*, ApJ, 560, 715
- Kaastra, J. S. (1992), *An X-Ray Spectral Code for Optically Thin Plasmas*, International SRON-Leiden Report, updated version 2.0
- Kormendy, J., Bender, R. (1999), *The Double Nucleus and Central Black Hole of M31*, ApJ, 522, 772

References

- Kormendy, J., Gebhardt, K. (2001), *Supermassive Black Holes in Galactic Nuclei*, 20th Texas Symposium on relativistic astrophysics, eds. Wheeler J.C. and Martel H., AIP conference proceedings, Vol. 586, 938
- Koyama, K., Maeda, Y., Sonobe, T., Takeshima, T., Tanaka, Y., Yamauchi, S. (1996), *ASCA View of Our Galactic Center: Remains of Past Activities in X-Rays?*, PASJ, 48, 249
- Koyama, K., Makishima, K., Tanaka, Y. (1986), *Thermal X-ray emission with intense 6.7-keV iron line from the Galactic ridge*, PASJ, 38, 121
- Lee, Y., Stark, A. A., Kim, H. G., Moon, D. (2001), *The Bell Laboratories CO Survey: Longitude-Velocity Maps*, ApJS, 136, 137
- Lin, D. N. C., Shields, G. A. (1986), *Accretion disks and periodic outbursts of active galactic nuclei*, ApJ, 305, 28
- Macchetto, F. D., Marconi, A., Axon, D. J., Capetti, A., Sparks, W. B., Crane, P. (1997), *The Supermassive Black Hole of M87 and the Kinematics of its associated Gaseous Disk*, ApJ, 489, 579
- Madau, P., Blandford, R. D., Rees, M. J. (2000), *Compton Echoes from Gamma-Ray Bursts*, ApJ, 541, 712
- Makino, N., Sasaki, S., Suto, Y. (1998), *X-Ray Gas Density Profile of Clusters of Galaxies from the Universal Dark Matter Halo*, ApJ, 497, 555
- Marconi, A., Axon, D. J., Macchetto, F. D., Capetti, A., Sparks, W. B., Crane, P. (1997), *Is there really a supermassive black hole in M87?*, MNRAS, 289, 21
- Mather, J. C., Fixsen, D. J., Shafer, R. A., Mosier, C., Wilkinson, D. T. (1999), *Calibrator Design for the COBE Far-Infrared Absolute Spectrophotometer (FIRAS)*, ApJ, 512, 511
- Matsushita, K., Belsole, E., Finoguenov, A., Böhringer, H. (2002), *XMM-Newton observation of M87. I. Single-phase temperature structure of intracluster medium*, A&A, 386, 77
- McKee, C. F., Ostriker, J. P. (1977), *A theory of the interstellar medium - Three components regulated by supernova explosions in an inhomogeneous substrate*, ApJ, 218, 148
- McLure, R. J., Dunlop, J. S. (2001), *The cluster environments of powerful radio-loud and radio-quiet active galactic nuclei*, MNRAS, 321, 515

-
- McLure, R. J., Kukula, M. J., Dunlop, J. S., Baum, S. A., O'Dea, C. P., Hughes, D. H. (1999), *A comparative HST imaging study of the host galaxies of radio-quiet quasars, radio-loud quasars and radio galaxies. I.*, MNRAS, 308, 377
- Meisenheimer, K., Röser, H.-J., Schlötelburg, M. (1996), *The synchrotron spectrum of the jet in M87*, A&A, 307, 61
- Mewe, R., Gronenschild, E. H. B. M., van der Oord, G. H. J. (1985), *Calculated X-radiation from optically thin plasmas. V.*, A&AS, 62, 197
- Mineshige, S., Shields, G. A. (1990), *Accretion disk thermal instability in galactic nuclei*, ApJ, 351, 47
- Mirabel, I. F., Rodriguez, L. F. (1994), *A superluminal source in the galaxy*, Nature, 371, 46
- Morrison, P., Sartori, L. (1969), *The Light of the Supernova Outburst*, ApJ, 158, 541
- Morrison, R., McCammon, D. (1983), *Interstellar photoelectric absorption cross sections, 0.03-10 keV*, ApJ, 270, 119
- Murakami, H., Koyama, K., Maeda, Y. (2001a), *Chandra Observations of Diffuse X-Rays from the Sagittarius B2 Cloud*, ApJ, 558, 687
- Murakami, H., Koyama, K., Sakano, M., Tsujimoto, M., Maeda, Y. (2000), *ASCA Observations of the Sagittarius B2 Cloud: An X-Ray Reflection Nebula*, ApJ, 534, 283
- Murakami, H., Koyama, K., Tsujimoto, M., Maeda, Y., Sakano, M. (2001b), *ASCA Discovery of Diffuse 6.4 keV Emission near the Sagittarius C Complex: A New X-Ray Reflection Nebula*, ApJ, 550, 297
- Murphy, B. W., Chernoff, D. F. (1993), *Polarized Scattering in the Vicinity of Galaxies*, ApJ, 418, 60
- Navarro, J. F., Frenk, C. S., White, S. D. M. (1995), *Simulations of X-ray clusters*, MNRAS, 275, 720
- Navarro, J. F., Frenk, C. S., White, S. D. M. (1997), *A Universal Density Profile from Hierarchical Clustering*, ApJ, 490, 493
- Nieten, C. (2001), *Properties of molecular gas and interstellar dust in M31*, PhD Thesis, University of Bonn

References

- Norman, M. L., Daues, G., Nelson, E., Loken, C., Burns, J., Bryan, G., Klypin, A. (2000), *Simulated Cluster Archive: A Computational Catalog of X-Ray Clusters in a Lambda-CDM Universe*, Large-Scale Structure in the X-Ray Universe, Atlantisciences, Athens, eds. M. Plionis and I. Georgantopoulos
- Owen, F. N., Eilek, J. A., Kassim, N. E. (2000), *M87 at 90 Centimeters: A Different Picture*, ApJ, 562, 449
- Pence, W. D., Snowden, S. L., Mukai, K., Kuntz, K. D. (2001), *Chandra X-ray Sources in M101*, ApJ, 561, 189
- Peterson, B. M. (1993), *Reverberation mapping of active galactic nuclei*, PASP, 105, 247
- Rees, M. J. (1967), *Studies in radio source structure - I. A relativistically expanding model for variable quasi-stellar radio sources*, MNRAS, 135, 345
- Rees, M. J. (1978), *The M87 jet - Internal shocks in a plasma beam*, MNRAS, 184, 61
- Rees, M. J. (1988), *Tidal disruption of stars by black holes of $10^6 - 10^8$ solar masses in nearby galaxies*, Nature, 333, 523
- Reese, E. D., Mohr, J. J., Carlstrom, J., Joy, M., Grego, L., Holder, G. P., Holzapfel, W. L., Hughes, J. P., Patel, S. K., Donahue, M. (2000), *Sunyaev-Zel'dovich Effect-derived Distances to the High-Redshift Clusters MS 0451.6-0305 and CL 0016+16*, ApJ, 533, 38
- Rephaeli, Y. (1995), *Comptonization Of The Cosmic Microwave Background: The Sunyaev-Zel'dovich Effect*, ARAA, 33, 541
- Rottmann, H., Mack, K.-H., Klein, U., Wielebinski, R. (1996), *The radio lobes of Virgo A at 2.8 cm wavelength*, A&A, 309, 19
- Rybicki, G., Lightman, A. (1979), *Radiative Processes in Astrophysics*, John Wiley & Sons, Princeton
- Ryle, M., Longair, M. S. (1967), *A possible method for investigating the evolution of radio galaxies*, MNRAS, 136, 123
- Sarazin, C. L., Wise, M. W. (1993), *BL Lacertae objects, Fanaroff-Riley type I radio sources, cluster cooling flows*, ApJ, 411, 55

-
- Sazonov, S. Y., Churazov, E. M., Sunyaev, R. A. (2002a), *Polarization of resonance X-ray lines from clusters of galaxies*, MNRAS, 333, 191
- Sazonov, S. Y., Sunyaev, R. A., Cramphorn, C. K. (2002b), *Constraining the past X-ray luminosity of AGN in clusters of galaxies: The role of resonant scattering*, A&A, 393, 793
- Schade, D. J., Boyle, B. J., Letawsky, M. (2000), *Hubble Space Telescope observations of X-ray-selected active galactic nuclei*, MNRAS, 315, 498
- Scheuer, P. A. G. (1974), *Models of extragalactic radio sources with a continuous energy supply from a central object*, MNRAS, 166, 513
- Schulz, N. S., Canizares, C., Huenemoerder, D., Kastner, J. H., Taylor, S. C., Bergstrom, E. J. (2001), *Chandra Observations of Variable Embedded X-Ray Sources in Orion. I. Resolving the Orion Trapezium*, ApJ, 549, 441
- Shakura, N. I., Sunyaev, R. A. (1973), *Black holes in binary systems. Observational appearance*, A&A, 24, 337
- Shibata, R., Matsushita, K., Yamasaki, N. Y., Ohashi, T., Ishida, M., Kikuchi, K., Böhringer, H., Matsumoto, H. (2001), *Temperature Map of the Virgo Cluster of Galaxies Observed with ASCA*, ApJ, 549, 228
- Shirey, R., Soria, R., Borozdin, K., Osborne, J. P., Tiengo, A., Guainazzi, M., Hayter, C., Palombara, N. L., Mason, K., Molendi, S., Paerels, F., Pietsch, W., Priedhorsky, W., Read, A. M., Watson, M. G., West, R. G. (2001), *The central region of M 31 observed with XMM-Newton. I. Group properties and diffuse emission*, A&A, 365, 195
- Sholomitskii, G. B., Yaskovich, A. L. (1990), *Cosmological Halos - a New Test for Intergalactic Gas*, SvAL, 16, 383
- Shull, J. M., van Steenberg, M. (1982), *The ionization equilibrium of astrophysically abundant elements*, ApJS, 48, 95
- Siemiginiowska, A., Czerny, B., Kostyunin, V. (1996), *Evolution of an Accretion Disk in an Active Galactic Nucleus*, ApJ, 458, 491
- Skibo, J. G., Johnson, W. N., Kurfess, J. D., Kinzer, R. L., Jung, G., Grove, J. E., Purcell, W. R., Ulmer, M. P., Gehrels, N., Tueller, J. (1997), *OSSE Observations of the Soft Gamma-Ray Continuum from the Galactic Plane at Longitude 95 degrees*, ApJ, 483, 95

References

- Smith, D. A., Wilson, A. S., Arnaud, K. A., Terashima, Y., Young, A. J. (2002), *A Chandra X-Ray Study of Cygnus A. III. The Cluster of Galaxies*, ApJ, 565, 195
- Smith, M. S., Kawano, L. H., Malaney, R. A. (1993), *Experimental, computational, and observational analysis of primordial nucleosynthesis*, ApJS, 85, 219
- Sofue, Y., Kato, T. (1981), *Neutral Hydrogen in M31 - Part One - the Distribution of HI Gas and Spiral Arms*, PASJ, 33, 449
- Solomon, P. M., Rivolo, A. R. (1989), *A face-on view of the first galactic quadrant in molecular clouds*, ApJ, 339, 919
- Solomon, P. M., Rivolo, A. R., Barrett, J., Yahil, A. (1987), *Mass, luminosity, and line width relations of Galactic molecular clouds*, ApJ, 319, 730
- Sparks, W. B., Fraix-Burnet, D., Macchetto, F., Owen, F. N. (1992), *A counterjet in the elliptical galaxy M87*, Nature, 355, 804
- Sugizaki, M., Mitsuda, K., Kaneda, H., Matsuzaki, K., Yamauchi, S., Koyama, K. (2001), *Faint X-Ray Sources Resolved in the ASCA Galactic Plane Survey and Their Contribution to the Galactic Ridge X-Ray Emission*, ApJS, 134, 77
- Sunyaev, R. A. (1982), *Intergalactic Gas in Galaxy Clusters - Scattering and Polarization of the Radio Emission of a Central Source*, SvAL, 8, 175
- Sunyaev, R. A., Churazov, E. M. (1996), *Scattering of X-ray emission lines by neutral and molecular hydrogen in the solar atmosphere and in the vicinity of active galactic nuclei and compact X-ray sources*, AstL, 22, 648
- Sunyaev, R. A., Churazov, E. M. (1998), *Equivalent width, shape and proper motion of the iron fluorescent line emission from molecular clouds as an indicator of the illuminating source X-ray flux history*, MNRAS, 297, 1279
- Sunyaev, R. A., Gilfanov, M. R., Churazov, E. M. (1998), *The 6.4 keV fluorescent emission from the Galactic Center molecular clouds*, Highlights in X-ray Astronomy, eds. B. Aschenbach and M. Freyberg, 102
- Sunyaev, R. A., Markevitch, M., Pavlinsky, M. (1993), *The center of the Galaxy in the recent past - A view from GRANAT*, ApJ, 407, 606
- Sunyaev, R. A., Uskov, D. B., Churazov, E. M. (1999), *Scattering of X-ray emission lines by molecular hydrogen*, AstL, 25, 199

-
- Sunyaev, R. A., Zel'dovich, Y. B. (1972), *The Observations of Relic Radiation as a Test of the Nature of X-Ray Radiation from the Clusters of Galaxies*, *Comments Astrophysics and Space Physics*, 4, 173
- Sunyaev, R. A., Zel'dovich, Y. B. (1980), *Microwave background radiation as a probe of the contemporary structure and history of the universe*, *ARAA*, 18, 537
- Tonry, J. L. (1991), *Surface brightness fluctuations - A bridge from M31 to the Hubble constant*, *ApJ*, 373, 1
- Vainshtein, L. A., Sunyaev, R. A. (1980), *The K_{α} -Lines in the Background X-Ray Spectrum and the Interstellar Gas in Galaxies*, *SvAL*, 6, 353
- Valinia, A., Marshall, F. E. (1998), *RXTE Measurement of the Diffuse X-Ray Emission from the Galactic Ridge: Implications for the Energetics of the Interstellar Medium*, *ApJ*, 505, 134
- van der Laan, H. (1963), *Radio galaxies II*, *MNRAS*, 126, 535
- Verner, D. A., Ferland, G. J. (1996), *Atomic Data for Astrophysics. I. Radiative Recombination Rates for H-like, He-like, Li-like, and Na-like Ions over a Broad Range of Temperature*, *ApJS*, 103, 467
- Verner, D. A., Verner, E. M., Ferland, G. J. (1996), *Atomic Data for Permitted Resonance Lines of Atoms and Ions from H to Si, and S, Ar, Ca, and Fe*, *Atomic Data and Nuclear Data Tables*, 64, 1
- Voronov, G. S. (1997), *A Practical Fit Formula for Ionization Rate Coefficients of Atoms and Ions by Electron Impact: $Z = 1-28$* , *Atomic Data and Nuclear Data Tables*, 65, 1
- White, D. A. (2000), *Deconvolution of ASCA X-ray data - II. Radial temperature and metallicity profiles for 106 galaxy clusters*, *MNRAS*, 312, 663
- Williams, J. P., Blitz, L., Stark, A. A. (1995), *The Density Structure in the Rosette Molecular Cloud: Signposts of Evolution*, *ApJ*, 451, 252
- Wilson, A. S., Yang, Y. (2002), *Chandra X-Ray Imaging and Spectroscopy of the M87 Jet and Nucleus*, *ApJ*, 568, 133
- Wise, M. W., Sarazin, C. L. (1990a), *Electron scattering and the distance to cluster cooling flows*, *ApJ*, 363, 344

References

- Wise, M. W., Sarazin, C. L. (1990b), *X-Ray spectra and Opacity Effects in Cluster Cooling Flows*, ApJ, 395, 387
- Worrall, D. M., Birkinshaw, M., Hardcastle, M. J., Lawrence, C. R. (2001), *Chandra measurements of the X-ray core and cluster of 3C 220.1*, MNRAS, 326, 1127
- Yang, Y., Wilson, A. S., Ferruit, P. (2001), *Chandra X-ray Observation of NGC 4151*, ApJ, 563, 124
- Yaqoob, T., Serlemitsos, P. (2000), *A Broad Fe K_{α} Emission Line in the X-Ray Spectrum of the Quasar 3C 273*, ApJ, 544, 95
- Young, A. J., Wilson, A. S., Shopbell, P. L. (2001), *A Chandra X-Ray Study of NGC 1068. I. Observations of Extended Emission*, ApJ, 556, 6
- Young, A. J., Wilson, A. S., Terashima, Y., Arnaud, K. A., Smith, D. A. (2002), *A Chandra X-Ray Study of Cygnus A. II. The Nucleus*, ApJ, 564, 176
- Zombeck, M. V. (1990), *Handbook of Astronomy and Astrophysics*, Second Edition, Cambridge University Press

Danksagung

Ein großes Dankeschön gilt meinem Doktorvater Rashid A. Sunyaev für die freundliche Aufnahme in der von ihm geleiteten, überaus aktiven Arbeitsgruppe “High Energy Astrophysics” mit ihren ausgezeichneten Arbeitsbedingungen sowie seine hilfreiche Unterstützung während meiner ganzen Zeit am MPA, die maßgeblich zum Gelingen dieser Arbeit beigetragen haben. Rashid hat mich an seinem enormen Wissen auf nahezu jedem Gebiet der Astrophysik teilhaben lassen, war stets darum bemüht, mir den Blick für das Wesentliche zu öffnen, und hat mir gezeigt, was es heißt, astrophysikalisch zu denken.

Ferner möchte ich mich bei Sergey Yu. Sazonov für die fruchtbare Zusammenarbeit bedanken, deren Ergebnisse ihren Niederschlag in den Kapiteln 3 und 4 dieser Arbeit gefunden haben.

Ein weiterer Dank gilt all denen, deren Bekanntschaft ich während meiner Zeit am MPA habe machen dürfen und mit denen ich die Freude hatte, auch abseits der Astrophysik die ein oder andere Untiefe des Lebens auszuloten.

Ganz besonders danken möchte ich meinen Eltern und meiner Schwester. Ihr habt mich zu jeder Zeit rückhaltlos unterstützt, mir Sicherheit gegeben und mir insbesondere während der letzten Phase dieser Arbeit des öfteren wohlwollend ins Gewissen geredet sowie tatkräftig unter die Arme gegriffen. Dafür und für noch soviel mehr möchte ich Euch von ganzem Herzen danken.

Danksagung

Lebenslauf

PERSÖNLICHE DATEN

Conrad K. Cramphorn
geboren am 18. Januar 1971 in Dundee/GB, ledig

SCHULAUSBILDUNG

Aug. 1977 – Juni 1981	Grundschule Süd, Hude
Aug. 1981 – Juni 1983	Orientierungsstufe, Hude
Aug. 1983 – Juni 1990	Altes Gymnasium, Oldenburg, Abitur

WEHRDIENST

Jan. 1999 – Okt. 1999	Fliegerhorst, Erding
-----------------------	----------------------

STUDIUM

Okt. 1990 – Juni 1992	Studium der Physik an der Georg-August-Universität Göttingen
Sep. 1992 – Juli 1993	Studienjahr an der Universität von Kalifornien, Santa Cruz, Vereinigte Staaten von Amerika
Okt. 1993 – Okt. 1995	Studium der Physik an der Georg-August-Universität Göttingen
Okt. 1995 – Okt. 1996	Diplomarbeit an der Universitätssternwarte Göttingen mit dem Thema: "Magnetohydrostatisches Gleichgewicht ruhender Protuberanzen"
1. November 1996	Diplom in Physik, Georg-August-Universität Göttingen
Jan. 1997 – Aug. 2001	Promotionsstipendium am Max-Planck-Institut für Astrophysik, Garching